Quantum Technologies Lab
TUM School of Natural Sciences
Technical University of Munich

Dissertation

Optomechanics with high-stress silicon nitride resonators

David Christopher Julian Hoch

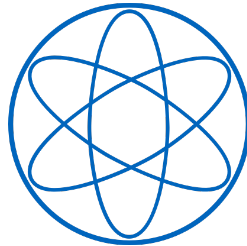

Technische Universität München
TUM School of Natural Sciences

Optomechanics with high-stress silicon nitride resonators

David Christopher Julian Hoch

Vollständiger Abdruck der von der TUM School of Natural Sciences der Technischen Universität München zur Erlangung des akademischen Grades eines
Doktors der Naturwissenschaften (Dr. rer. nat.)
genehmigten Dissertation.

Vorsitz:
Prof. Dr. Frank Pollmann
Prüfer der Dissertation:
1. Prof. Dr. Menno Poot
2. Prof. Dr. Alexander Holleitner

Die Dissertation wurde am 16.06.2023 bei der Technischen Universität München eingereicht und durch die TUM School of Natural Sciences am 30.11.2023 angenommen.

Abstract

In the field of optomechanics, resonators made out of high-stress silicon nitride serve as a highly interesting platform, both in research and for applications. The extremely high quality factors that have been demonstrated in such devices allow them to serve, e.g. as highly sensitive sensors or even quantum storage devices. In this thesis, I will explain the fabrication of such devices and describe the setups built for their characterization. The *chip-integrated* devices with dimensions in the micron regime are made using state-of-the-art nanofabrication techniques in a clean room environment as commonly used in the semiconductor industry. The nanofabrication is described in detail using the example of a tunable directional coupler, a so-called H-resonator, which can be utilized in optical quantum circuitry, in particular for improving CNOT gates.

The three setups described in this work were built in the course of the project. One of these is designed to measure optomechanical devices integrated into photonic circuitry under ambient conditions and perform optical transmission measurements by doing, e.g. wavelength sweeps in the telecom range around 1550 nm. The second setup is built in a similar fashion but placed in a vacuum chamber to perform dynamic measurements on the optomechanical devices in the absence of air damping. Here, measurements are typically performed by network or spectrum analyzers. The third setup is as well made for measurements of integrated resonators in vacuum, however, the interferometric read-out includes a laser focused onto a suspended resonator which forms - together with its substrate - a Fabry-Pérot cavity. While the first two are based on fiber optics and photonic integrated circuitry (PIC), the latter utilizes free-space optics components.

These setups enable many experiments such as those performed within the two projects discussed in depth in this work. One covers the study of the geometric tuning of stress in silicon nitride beam resonators. By displacing the beam at its center by design and subsequently releasing it from its substrate, the high intrinsic stress of the beam partially relaxes. The dynamics of these stress-tuned beams are read out via integrated Mach-Zehnder interferometers. As the remaining stress strongly influences the energy dissipation, a model from the literature is improved for the lower-stress regime and applied to our data. The second project focuses on the development of a method to efficiently map the mode shapes of micromechanical devices utilizing a phase-lock loop, robust against phase changes at the nodal lines of the mode shapes. With this technique, complex modes of suspended silicon nitride membranes are studied. Both studies are affirmed by measurements on beams integrated into a racetrack design as a reference.

The results of this work make an important contribution to the field of optomechanics and the study of the dynamics of silicon nitride resonators.

Zusammenfassung

Im Feld der Optomechanik bilden Resonatoren aus unter hoher Spannung stehenden Siliziumnitrids eine spannende Plattform, sowohl in der Grundlagenforschung als auch in der industriellen Anwendung. Durch ihr Potential, sehr hohe Qualitätsfaktoren zu erreichen, können sie als sehr sensible Detektoren oder sogar zur Speicherung von Quanteninformation dienen. In dieser Arbeit werde ich die Fabrikation solcher Bauelemente beschreiben und Messaufbauten für deren Charakterisierung beschreiben. Hergestellt werden solche in Mikrochips *integrierte* Bauelemente in der Größenordnung einiger Mikrometer mit Hilfe von modernen Nanofabrikationstechniken in Reinraumumgebung, wie sie aus der industriellen Halbleiterfertigung bekannt sind. Die Nanofabrikation wird am Beispiel eines abstimmbaren optischen Richtkopplers, dem sogenannten H-Resonator beschrieben. Dieser Koppler kann unter anderem für die Verbesserung von CNOT Gattern in optischen Quantenschaltkreisen verwendet werden.

Drei Messaufbauten werden beschrieben und wurden im Laufe dieser Arbeit aufgebaut. Einer ist konstruiert, um optomechanische Elemente, welche in optische Schaltkreise integriert sind, unter Umgebungsbedingungen zu vermessen. Während beispielsweise die Wellenlänge im Telekombereich um 1550 nm durchgestimmt wird, kann mit diesem Aufbau die optische Transmission gemessen werden. Der zweite Messaufbau ist ähnlich zum ersten aufgebaut, allerdings in einer Vakuumkammer integriert. Somit kann die Dynamik der Bauelemente bei geringer Luftdämpfung gemessen werden. Üblicherweise werden solche Messungen mit Hilfe von Netzwerkanalysatoren oder Spektrumanalysatoren durchgeführt. Auch der dritte Aufbau ist für Messungen an integrierten Resonatoren unter Vakuum designt. Hier jedoch bildet der Resonator gemeinsam mit dem Substrat eine Fabry-Pérot Kavität. Ein Laser wird auf den Resonator fokussiert und somit wird die Bewegung des Resonators interferometrisch ausgelesen. Während die ersten beiden Aufbauten auf Faseroptik und integrierten photonischen Schaltkreisen basieren, beruht letzterer auf Freistrahloptik.

Diese Aufbauten ermöglichen viele unterschiedliche Experimente, so wie die, welche in der vorliegenden Arbeit im Rahmen von zwei Projekten ausführlich diskutiert werden. Eines befasst sich mit der Studie von Balkenresonatoren aus Siliziumnitrid, deren Spannung geometrisch gestimmt wird. Mit Hilfe eines versetzten Zentrums des Balkens im Design und anschließendes Loslösen vom Substrat kann die hohe intrinsische Spannung teilweise relaxieren. Die Dynamik solcher Balken, deren Spannung gestimmt werden kann, wird mit integrierten Mach-Zehnder Interferometern gemessen. Die verbleibende Spannung hat großen Einfluss auf die Dissipation der Energie. Darüber hinaus wurde ein Modell aus der Literatur an den Bereich geringer Verspannungen angepasst und an unsere Daten angelegt. Das zweite Projekt beschäftigt sich mit der Entwicklung einer Methode, um die mechanischen Moden mikromechanischer Bauelemente effizient zu vermessen. Hierfür wird eine Phasenregelschleife verwendet, welche robust gegenüber Phasenveränderungen an den Schwingungsknoten der Moden ist. Mit Hilfe dieser Technik wurden komplexe Moden von Siliziumnitridmembranen analysiert. Die Diskussion beider Projekte wird von Messungen an in Ringresonatoren integrierte Balkenresonatoren begleitet, welche als Referenz einiger der vorgestellten Messungen dienen sollen.

Die Ergebnisse dieser Arbeit bilden einen wichtigen Beitrag im Feld der Optomechanik und der Analyse der Dynamik von Siliziumntridresonatoren.

Contents

Abstract . . . i
Zusammenfassung . . . ii
1 Introduction . . . 1
2 Optomechanics with photonic devices . . . 5
2.1 Introduction to Optomechanics . . . 6
2.2 Silicon nitride . . . 7
2.3 Photonic circuitry . . . 8
2.3.1 Optical waveguides . . . 9
2.3.2 Grating couplers . . . 9
2.4 Integrated mechanical resonators . . . 11
2.4.1 Membrane modes . . . 14
2.4.2 Nonlinearities . . . 15
2.4.3 Electrical crosstalk . . . 15
2.4.4 Dissipation . . . 17
2.5 Measurements and data processing techniques . . . 18
2.5.1 Detection methods . . . 18
2.5.2 Response function and fitting . . . 19
2.5.3 Measurements of integrated MZIs . . . 21
2.5.4 Transduction calibration via thermal motion . . . 23
3 Device Fabrication . . . 27
3.1 Introduction . . . 28
3.2 Process steps . . . 28
3.2.1 Wafer preparation . . . 28
3.2.2 Lithography steps . . . 30
3.2.3 Evaporation . . . 31
3.2.4 Photonic and mechanical structures . . . 33
3.2.5 Reactive ion etching . . . 34
3.2.6 Release . . . 35
3.2.7 Electron beam writing . . . 36
3.2.8 Inspection . . . 38
3.3 Optimization of nanofabrication . . . 40
3.3.1 Wafer dicing . . . 40
3.3.2 Precision of the marker positions . . . 40
3.3.3 Descum . . . 41
3.3.4 Reactive ion etcher . . . 41
3.3.5 Optimization of process flows . . . 42
3.4 Post-fabrication . . . 44
3.5 Devices . . . 44
4 Setups . . . 49
4.1 Introduction . . . 51
4.2 Measurement devices . . . 51

4.3 Quick Measurement Setup . . . 52
4.4 Large Vacuum Chamber . . . 56
4.4.1 Concept and functionality . . . 56
4.4.2 Attenuator . . . 57
4.5 Square Vacuum Chamber . . . 58
4.5.1 Concept and functionality . . . 58
4.5.2 Beam path . . . 58
4.6 Piezoelectric actuator . . . 59
4.7 Temperature control . . . 60
4.8 Stages . . . 62
4.8.1 Stepper motors . . . 62
4.8.2 Picomotors . . . 63
5 Efficient optomechanical mode-shape mapping of micromechanical devices . . . 65
5.1 Introduction . . . 67
5.2 Nanofabrication . . . 67
5.2.1 Surface quality . . . 68
5.2.2 Reflectivity . . . 71
5.3 Mode properties . . . 71
5.3.1 Response and mode shape . . . 71
5.3.2 Demodulation . . . 73
5.3.3 Harmonic oscillator response . . . 73
5.4 PLL mode mapping . . . 75
5.4.1 Comparison of different methods for mode mapping . . . 75
5.4.2 Mode maps . . . 78
5.4.3 Variation of the measurement scheme . . . 79
5.5 Thermal motion . . . 79
5.6 Temperature dependence . . . 81
5.7 Beyond membranes . . . 84
5.8 Summary . . . 84
6 Geometric tuning of stress in pre-displaced silicon nitride resonators . . . 87
6.1 Introduction . . . 89
6.2 Sample and Setup . . . 89
6.3 Beam shapes . . . 93
6.4 Simulations . . . 94
6.5 Relaxation and stress tuning . . . 95
6.5.1 Stress relaxation in released beam . . . 95
6.5.2 Influence of the beam parameters on the relaxation . . . 95
6.6 Dynamic beam analysis . . . 97
6.7 Dissipation . . . 99
6.7.1 Dissipation mechanisms . . . 99
6.7.2 Dissipation in stress-tuned Sbeams . . . 100
6.7.3 Influence of D_0 on the dissipation . . . 105
6.7.4 Influence of L on the dissipation . . . 105
6.8 Influence of the beam shape . . . 108
6.9 In- and out-of-plane Q_{bending} . . . 109
6.10 Nonlinearity . . . 110
6.11 Design considerations . . . 113
6.12 Summary . . . 114
7 Conclusion and Outlook . . . 115
Appendix A Dissipation of beams . . . 119
Appendix B Surface quality . . . 123

List of Figures . . . 129
List of Tables . . . 141
List of Publications . . . 143
Acknowledgements . . . 145
References . . . 149

CHAPTER 1

Introduction

The field of optomechanics [1–6], which studies the interaction between light and mechanical resonators, offers plenty of opportunities for applications both in cutting-edge science and industry: from the exploration of quantum effects [7] to the development of highly sensitive sensors [8]. The underlying principle has been developed already in the year 1873 by Maxwell, postulating radiation pressure forces [3, 9]. One can even look further back in history, to find the first hints of these forces: in the year 1619 Kepler describes his observation of dust trails of comets pointing away from the sun [3]. It took until 1901 for Lebedew to experimentally demonstrate the effect of radiation pressure forces on a light mill [9]. Over the next decades, several big breakthroughs were reported, including trapping of atoms and feedback cooling in the late 1970s by Ashkin [10]. Nowadays, the arguably most well-known optomechanical cavity is the Laser Interferometer Gravitational-Wave Observatory (LIGO) in Hanford and Livingston. This interferometer is providing astonishing proof of the ultra-high sensitivity of optomechanical cavities by detecting signals as tiny as gravity waves [11]. While this detector requires kilometer-long arms in the interferometer, cavity optomechanical systems can also be realized in table-top experiments [12]. Such setups typically utilize *high-finesse* optical cavities with the light bouncing back and forth between their end mirrors (or end facets) [3]. If one of the end mirrors is suspended, the momentum transferred by the light changes the cavity dimensions. This influences the effective spring constant of the suspended mirror and therefore its resonance frequency. As a consequence, the optical properties of the cavity change as well. This influence on the mechanical frequency of a suspended mirror or resonator is called the optical-spring effect [3]. The mirrors in such cavities do not necessarily have to be of macroscopic dimensions. Optomechanical cavities can as well be integrated on microchips in the form of *microtoroids*, *photonic crystal cavities*, or *ring resonators* [3] as is dealt with in this work. They are orders of magnitude smaller, providing the opportunity to fabricate them on large scale in portable devices at low costs. This makes them a great tool in the realization of sensors, combining their high sensitivity with the size and cost-effectiveness of chip-based technology. Micro-electro-mechanical systems (MEMS) sensors are already well applied for several decades, e.g. as acceleration sensors in cars to fast and reliably trigger airbags in case of accidents [13] and are even integrated into wearables as fall protection [14]. Optomechanical sensors are also developed to serve a huge variety of tasks, such as force, inertia, acoustic, chemical, and thermal sensing [8]. Frequency conversion with the help of optomechanical cavities is reaching the 5G band in mobile communication [15]. Even in the absence of a cavity, the dynamics of integrated optomechanical devices can be sensed, e.g. by utilizing *integrated Mach-Zehnder interferometers* [16].

So far, such devices are majorly applied in a pure classical way. However, in their incentive to shift the limits of the performance of optomechanical devices, many researchers have taken optomechanics down to the quantum level in the past years. Quantum optics by itself, again,

is a rather old discipline: Planck's work on black body radiation from the early 20th century is building the foundation of the quantum theory of light, together with Einstein's description of the photoelectric effect [17]. One of the most important achievements in quantum optics - which can be said has changed the world - was the invention of the laser in the year 1958 by Shawlow and Townes [18]. And another breakthrough might be in sight: integrated quantum photonics is a candidate for winning the competition for realizing quantum computers [19]. Since Feynman described the idea of a quantum computer in the year 1986 [20], several leading platforms for quantum computing have been developed. Quantum computing may be based on superconducting circuits, neutral atom arrays, trapped ions, or photonic systems [21]. *Superconducting quantum circuits* are based on the collective motion of electrons in electrical oscillators, which can be described as LC circuits. Here, large numbers of atoms are involved such that these circuits are macroscopic systems. Josephson junctions transform the circuit into an artificial atom, allowing ground and excited states. The Josephson effect adds nonlinearity to this system without introducing dissipation or dephasing [22]. *Neutral atom arrays* are arrays of single particles, trapped using magnetic fields or optical tweezers. The control of quantum states is realized by driving atomic transitions between hyperfine levels using laser beams or by microwaves [23]. *Trapped ions*, in contrast, are confined in radiofrequency traps. Their shared motional modes are utilized as a quantum bus which can lead to entanglement. Quantum bits out of trapped ions typically have strong ion-ion interactions and a long state coherence [24]. While light is often used to control quantum systems, *photons* can also be used directly as quantum systems. Photons are potentially free from decoherence, however, this comes at the cost of low photon-photon interaction. The qubit state can be encoded in the polarization of the photons or in their path [25]. It is still unclear, which one of these quantum systems will make the race, or if maybe several of them will coexist - each being optimized for their own specific task. One may be the system of choice for computational tasks, one ensures long coherence times for the storage of quantum information, and another is used for the transport of quantum information to interconnect remote quantum computers. One or more may be based on photonic qubits, especially the transport of quantum information over long distances is almost predestined for its realization via photons due to their high speed and low interaction with the environment. Already quantum key distribution both via fiber networks [26] and satellites [27] is investigated. It is thus very likely, that photons will play an essential role in a potential future quantum internet [28]. This argument is backed, by photonic integrated circuits (PICs) being successfully investigated as a platform for quantum circuitry [29, 30]. Besides integrated single photon sources and single photon detectors, quantum PICs are further based on classical integrated optical components, such as waveguides and directional couplers, that can be utilized for qubit routing and the realization of quantum gates. A photonic quantum computer, however, that is based on path-encoded optical low-loss qubits requires fast and precise switches for the routing of photons and stabilizing the quantum gates. And here comes the connection of quantum optics and optomechanics into play. As *optical microelectromechanical (MEMS)*, also known as *microoptoelectromechanical (MOEMS)* systems have a huge potential in PICs [31] as well as optical networks and communication [32, 33] and they might be as well promising candidates for tasks in the quantum regime [34]. For example as an optical switch, based on microelectromechanical cantilevers [35] or the Hdirectional device, introduced in Chapter 3 of this thesis.

However, optomechanics cannot only be used for quantum optics control, such devices can be of quantum mechanical nature itself. The development of the above-mentioned gravitational wave detectors was driving this field from its early times. After years of research, the entanglement between a mode of macroscopical mechanical resonators and the light field inside a cavity [36] or even with single photons [37] became possible by the means of radiation pressure. Optomechanical interaction via single photons can even create entangled cat states between two mechanical resonators in separated optomechanical cavities [7]. Such connection of different quantum systems does offer many opportunities including the study of light-matter interactions

and builds a potential platform for such quantum state transfer [38]. Many hybrid quantum systems with coupling between these different systems have been developed [39]. One of these is the microwave-to-optics conversion while preserving the quantum state by the means of a mechanical resonator [39–42]. Integrated resonators, however, cannot only transfer quantum information but even have the opportunity for the storage of quantum information [43]. For the storage of quantum information, the resonators need to be able to perform multiple coherent oscillations. To do so, these resonators need to have exceptionally high Qf-products, where Q is its quality factor at the fundamental resonance frequency f. The relation $Qf \gg k_B T_{bath}/h$ (where T_{bath} is the temperature of the mechanical environment) has to hold, for observing quantum effects in optomechanical systems [44]. Thus the Qf-product must be $\sim 6.2 \cdot 10^{12}$ Hz at ambient temperatures of 300 K. Inside a dilution refrigerator with typical temperatures around 20 mK a Qf-product of $\sim 4.1 \cdot 10^{8}$ Hz is necessary.

Another essential requirement for the preparation of mechanical quantum states is the so-called *strong coupling*. The observation of such *strong coupling* between a micromechanical resonator and an optical cavity field has first been reported in the year 2009 by Gröblacher *et al.* [45]. While until the year 2012 only a "small number of systems" have satisfied the above-mentioned relation for observing optomechanical quantum effects [46], by now this has been achieved in many more experiments. E.g. by the localization of modes by phononic bandgaps, a Qf-product above 10^{14} Hz has been achieved, resulting in "many" coherent oscillations at room temperature [47]. For SiN strings at cryogenic temperatures of 4 Kelvin also Qf-products of about 10^{14} allowing for about 1000 quantum coherent oscillations have been reported. It is claimed that at the above-mentioned dilution refrigerator temperatures of a few tens of milliKelvin mechanical quantum state lifetimes on the order of a second are expected [48]. To reach and overcome this goal, the energy dissipation has to be reduced as much as possible for a given frequency regime. Losses can be reduced by a lot, which is typically done by working with high-stress amorphous materials and a mechanism called dissipation dilution [49, 50]. In this mechanism, the tension in the resonators is enhanced to greatly reduce the internal losses. A deep understanding of dissipation mechanisms is thus crucial for the development of increasingly better devices. Several techniques have been developed to utilize dissipation dilution, such as hierarchical structuring [51]: in an integrated approach utilizing string networks, thermal-noise-limited force sensitivities of $1.3\,\mathrm{aN}/\sqrt{\mathrm{Hz}}$ for a 226 kHz perimeter mode with quality factors of $1.5 \cdot 10^{9}$ at room temperature have been reported [52]. Another example of the utilization of dissipation dilution are GeOI microbridges with a periodic array of lateral corrugations that are defining a distributed feedback cavity (DFB) [53]. The key in the urge for record-high quality factors lies in increasing the stress in the resonator. Several ideas have been realized to tune the stress in mechanical resonators, e.g. bending of the whole chip [54] or clamp tapering [55], and, recently, our geometric tuning of stress [16]. Other ways to reduce dissipation is the suppression of energy radiating into the bulk, e.g. by phononic crystal patterning [56–58].

While the above experiments are often performed on nanostrings, also two-dimensional resonators like membranes are implemented into quantum experiments [59–62]. On resonance, these membranes take on specific mode shapes, depending on their design and mode number, but also more complex influences like the superposition of various modes [63]. The actual mode shape such two-dimensional resonators are forming is of great interest, for example when photonic metasurfaces are applied onto membranes for mode engineering [64]. In the literature, several techniques to gain mode maps of two-dimensional resonators such as membranes, cantilevers, or trampolines are introduced. Such techniques for the visualization of mechanical modes are optical interferometry [65–67], heterodyne detection [68, 69], dark field imaging [65, 70], force microscopy [71–74], and the application of a phase-lock loop to an optomechanical cavity [63]. Altogether, the field of optomechanics is a thriving field that regularly impresses with new results and insights. This work will deal with experiments on optomechanics based on integrated high-stress silicon nitride resonators. Further, the fabrication of the devices will be discussed, as

well as the measurement environment used for characterization.

In Chapter 2, I will start to introduce the background and concepts of the field of optomechanics, which are important for the understanding of the subsequent chapters. I will talk about Si_3N_4 - our material of choice - and its outstanding properties. Then, I will continue with explaining the basics of integrated optics circuitry and micromechanical resonators. The concept of motion sensing in our different setups will be explained in detail. To extract important information from the gained data, the measured response has to be fitted. Which fit functions are used throughout this work will be shown as well as how to deal with crosstalk and nonlinearities. The chapter will be concluded with a discussion of the dissipation mechanisms present in micro- and nanomechanical devices.

Chapter 3 leads the reader through our nanofabrication methods. From a plain and polished wafer to a finished and functional device on a chip, I will discuss each step to be done. As many of these steps had to be optimized to meet our requirements, these procedures together with issues and solutions will also be covered in this chapter.

Chapter 4 is dedicated to the setups that were built and characterized during the time of this work. They were all set up from scratch and build the foundation of the projects worked on in our group. The Quick Measurement Setup (QMS) is designed for transmission measurements of integrated optics circuitry under ambient conditions. If these circuits also include mechanical devices they will be subsequently studied in the Large Vacuum Chamber (LVC) after a first characterization in the QMS. Here, the dynamics of the devices can be studied under controlled conditions regarding temperature and pressure. The third setup discussed in this work is the Square Vacuum Chamber (SVC). In contrast to the aforementioned setups, it is not designed for integrated photonics circuitry but utilizes free-space optics to interferometrically measure the dynamics of integrated mechanical devices under controlled conditions, such as in the LVC.

In Chapter 5, I present the application of a phase-lock loop for efficient mode shape mapping integrated into the SVC setup. The capabilities of this method are proven by the study of the modes of a membrane. A mode triplet is analyzed closer. The advantage of this method over a variety of others is shown by comparing measurements performed by each method. Further characteristics of the membrane, like measurements of the temperature dependence of its dynamics and its thermal motion, are concluding the chapter.

In the final chapter, I present a technique to tune the stress in beam resonators independent of the deposition process. The stress is geometrically tuned on-chip by pre-displacing the beams. They straighten during release and relax to their final stress, dependent on their geometry. The beam dynamics are measured by means of integrated Mach-Zehnder interferometers. Both the geometric and dynamic results nicely match our finite element simulations. A model for the dissipation in these beams is improved and adapted for the low-stress regime and applied to our data. The chapter concludes by looking at the influence of altered beam shapes on their dynamics and dissipation. This works finishes with a summary and outlook.

CHAPTER 2

Optomechanics with photonic devices

This chapter gives an introduction to the field of optomechanics and integrated photonic circuitry with the intention to provide the reader with the theoretical background for the discussion of the experimental results in this thesis. I will start introducing some concepts and figures of merit in optomechanics and continue describing the outstanding properties of silicon nitride, our material of choice. I will further provide an introduction to photonic integrated circuitry and the integration of mechanical resonators into on-chip cavities. The detection mechanisms applied in this work are described in detail, as well as information on how to interpret the obtained data will be given. Parts of the contents of this chapter are reprinted from [63] and [16].

2 Optomechanics with photonic devices . . . 5
- 2.1 Introduction to Optomechanics . . . 6
- 2.2 Silicon nitride . . . 7
- 2.3 Photonic circuitry . . . 8
  - 2.3.1 Optical waveguides . . . 9
  - 2.3.2 Grating couplers . . . 9
- 2.4 Integrated mechanical resonators . . . 11
  - 2.4.1 Membrane modes . . . 14
  - 2.4.2 Nonlinearities . . . 15
  - 2.4.3 Electrical crosstalk . . . 15
  - 2.4.4 Dissipation . . . 17
- 2.5 Measurements and data processing techniques . . . 18
  - 2.5.1 Detection methods . . . 18
  - 2.5.2 Response function and fitting . . . 19
  - 2.5.3 Measurements of integrated MZIs . . . 21
  - 2.5.4 Transduction calibration via thermal motion . . . 23

2.1 Introduction to Optomechanics

In the introduction, an overview of the field of optomechanics was given. In the following, it will be described in more detail how optics and mechanics work together on a chip and the necessary background for the projects discussed in Chapter 5 and Chapter 6 will be given.

For the utilization of optomechanical effects or the measurement of the resonator motion via the optical signal, there needs to be optomechanical coupling, i.e. an influence of mechanical motion on ligth and vice versa. Optomechanical cavities can reach exceptionally high sensitivities of e.g. 10^{-19} m/$\sqrt{\text{Hz}}$ in case of a gravitational wave detector [75]. This means that a displacement of the resonator of 10^{-19} m can be measured with a signal-to-noise ratio (SNR) of 1 in a one Hertz output bandwidth[1] in these km-long devices. Still, also tiny on-chip cavities like silica toroids can reach extremely good sensitivities at the order of 10^{-3} fm/$\sqrt{\text{Hz}}$ [76]. Another important measure is the optomechanical coupling strength $g_{OM} = \partial\omega_c/\partial u$, quantifying how much the resonator displacement u changes the cavity frequency ω_c. ω_c is the resonance (angular) frequency at which light is efficiently coupled into the cavity, i.e. when the cavity dimensions are multiples of the laser wavelength. The radiation pressure of the photons alters ω_c by displacing a suspended end mirror or a "membrane in the middle" [77], while a change in ω_c changes the amount of light (which is typically set at a fixed laser frequency) that couples into the cavity. A sketch of a cavity with suspended end mirror can be found in Fig. 2.1(a).

There are various types of cavities that can serve for optomechanical experiments [3]. A type of low Finesse Fabry-Pérot cavity is realized in our project on mode shape mapping (see Chapter 5). Here, we are studying the dynamics of a membrane suspended over the chip substrate, forming the end mirror of the cavity. In such cavities, the coupling constant can be obtained via $g_{OM} = -\omega_c/L$ with cavity length L [2]. Our project on racetrack cavities with integrated beams (see Fig. 2.1(b) and Sec. 3.5)) in contrast, utilizes ring resonators with a coupling constant of $g_{OM} = -\frac{\omega_{cav}}{\bar{n}_{eff}}\frac{L_{beam}}{L_{RT}}\frac{\partial n_{beam}}{\partial u}$, where ω_{cav} is the cavity frequency, $\bar{n}_{eff}$ is the effective refrective index, L_{beam} is the length of the suspended beam, L_{RT} is the length of the racetrack, and $\frac{\partial n_{beam}}{\partial u}$ is the change of the refractive index of the beam n_{beam} with its displacement u.

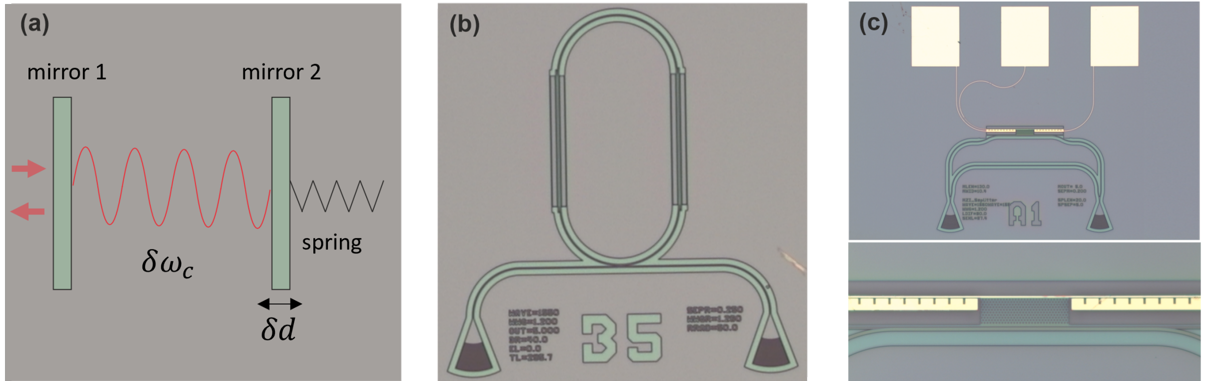

Figure 2.1: Implementations of optomechanical coupling. (a) Sketch of a Fabry-Pérot cavity with movable end mirror. (b) Microscope image of a racetrack cavity with integrated suspended beams. (c) Mach-Zehnder interferometer with a mechanical device - here, a H-resonator - next to one arm of the interferometer.

Usually, it is desired to utilize large coupling strengths, to reach high signal-to-noise ratios (SNR) or for example to controll and detect non-classical states of mechanical motion [2]. Such large optomechanical coupling has been achieved, e.g. by placing two waveguides in close vicinity to each other. Here, symmetric and anti-symmetric optical modes form with a mode volume of the order of λ^3. The coupling in this technique is about $g_{OM} \sim \omega_c/\lambda$ [56, 78]. In pairs of

[1]An output bandwidth of 1 Hertz corresponds to half a second of integration time.

silica discs, coupling of $2\pi \cdot 33$ GHz/nm [79] and in photonic crystal cavities coupling of even $2\pi \cdot 123$ GHz [78] have been achieved.

2.2 Silicon nitride

All devices described in this thesis are made of silicon nitride. The physical properties of Si_3N_4 make it an outstanding material for chip-based photonics and optomechanics [80]. This section provides an overview of these properties and the various deposition techniques. For on-chip devices, SiN is typically deposited as a thin film of several hundred nanometers on the substrate material, often with a cladding layer in between. We will in the following look at both its optical and mechanical properties.

SiN is a ceramic material with many interesting properties. In industry, SiN is used to build gas injectors or punching dies due to its high rigidity and high thermal robustness [81]. In general, silicon nitride can be used in a wide range of crystal structures or compositions, such as porous, dense, powder, or combined with further materials like in the form of SiAlON. Its crystal structure is (α, β) hexagonal [82]. However, we utilize amorphous Si_3N_4 applied on the wafer by low pressure (10-1000 Pa) chemical vapor deposition (LPCVD). Amorphous SiN, which is generally nonstoichiometric can besides LPCVD also be applied by atmospheric pressure CVD or plasma enhanced CVD. The advantages of SiN are its low permeability toward elements like sodium, oxygen, H_2O, or hydrogen. Further benefits are its high electrical resistivity (10^{12} Ωm), hardness, and good chemical resistance. [82]. The electronic band structure of α-Si_3N_4 has an indirect band gap of 4.5 eV [83] resulting in the high electrical resistivity which allows us to directly apply electrodes for actuation or heating purposes on the material.

The film stress σ_{film} of SiN largely depends on the deposition process and stochiometry and is 1050 MPa for our amorphous LPCVD films[2]. Without further tuning of the stress, we reach quality factors of several hundred thousand as will be discussed in the following chapters. By the utilization of dissipation dilution quality factors above 10^9 have been reported for SiN resonators [50, 51, 84]. Its Young's modulus E is thickness dependent with about $230 - 265$ GPa for thicknesses of $0.2 - 0.3$ μm and 290 GPa for 0.5 μm [85]. For our film thicknesses of 330 nm we expect a Young's modulus of 250 GPa and Poisson ratio ν of 0.23 [86]. Furthermore SiN has a density ρ of 3.10×10^3 kg/m^3 [86] and a coefficient of thermal expansion (CTE) of $2.3 \times 10^{-6}\,\mathrm{K}^{-1}$, however, the latter is slightly temperature dependent. Its hardness or mechanical strength makes the mechanical devices robust and reliable, and its high yield strength of 13 GPa [87] allows to utilize the effect of dissipation dilution, gaining extremely high quality factors. That enables to enter the quantum regime with the motion of resonators based on SiN [88]. In the year 2004, Norte *et al.* report Qs of 10^8 on tethered membranes out of SiN, sufficient to enter quantum regime at room temperatures [89]. By now, SiN resonators reaching such high and even higher quality factors have expanded to designs such as photonic crystal patterned nanobeams and strain engineered nanobeams [52], or topology optimized trampoline structures [90]. The good chemical resistance of SiN results in good stability in rough environmental conditions, e.g. when applied as a sensor, but also causes a good selectivity to our SiO_2 cladding layer when the devices are released in hydrofluoric acid [91, 92].

With an effective refractive index of about 1.5 at wavelengths around 1550 nm in isolated slot waveguides [80] SiN is very well suited for the propagation of optical modes over a wide range of wavelengths. Due to its large bandgap SiN is transparent both in the visible and infrared (IR) regime [93, 94] with reported optical losses as low as 1.0 dB/m [95]. For us, the visible regime is important as measurements in our square vacuum chamber (SVC) are performed with a HeNe laser at $\sim$ 630 nm. Also for our hybrid approach of aluminum nitride integration on silicon nitride photonic circuits [96] to utilize on-chip nonlinear optics a high transmission in the visible

[2]Note that this is the film stress, i.e. the SiN is connected to the SiO_2 cladding layer. The release of suspended beams without further stress tuning leads to a relaxed stress of 850 MPa (see Sec. 6.5).

regime is imperative [97]. One of the first reported waveguides were SiN on SiO_2 single mode waveguides with propagation losses of 1-2 dB/cm [98,99]. Improvements included improved CVD processes and a reduced waveguide roughness after etching and resulted in propagation losses of 0.1 dB/cm. Later, high aspect ratio cores, minimizing sidewall scattering allowed losses as low as 0.045 dB/m [100]. Today, there are three types of waveguides with variations in their core geometries and in the fabrication process [98]. These types are single stripe waveguides with ultra-low propagation loss and optimized fiber coupling [100, 101], multilayer structures allowing tight bends [102, 103], and highly confined buried waveguides [102]. Ultra-high optical quality factors of several 10s of million in planar Si_3N_4 ring resonators on Si substrates have been reported [94]. Our linear optics (quantum) circuitry and optomechanics operate near the telecom wavelength of 1550 nm. This wavelength is also widely used in industry and telecommunication [104]. We thus meet an advanced technology that makes a future integration into a larger framework straightforward. SiN is also a candidate for the utilization of Kerr nonlinear processes [105] enabling switching functionalities in integrated photonic circuitry.

2.3 Photonic circuitry

We have seen above that amorphous SiN is an excellent material for both integrated photonics and mechanics. In this section the basic elements of integrated photonic circuits, namely optical waveguides and grating couplers are explained. In contrast to free space optics or fiber optics, in photonic integrated circuitry the light propagates through waveguides integrated into chips [106]. As in these platforms, also in integrated optics the light can be routed and manipulated. To ensure a certain functionality different components than in free-space optics are used. The integrated equivalent of a free space beam splitter is called a directional coupler [80]. Here, two waveguides are brought into close vicinity of each other such that the light can couple to one another with a certain ratio. This coupling ratio is fixed for static directional couplers and largely depends on the dimensions of the coupler. In the following chapter, an electromechanically tunable directional coupler will be introduced - the so-called Hdirectional - which allows active routing of the light and even the tunability of integrated optics quantum gates. The integrated version of a 50 : 50-beam splitter can be realized by dividing a waveguide into two waveguides separating (or combining) the light (see Fig. 3.14(a)-(c), showing a variety of our realized devices). In the case of laser light, each waveguide will then propagate 50% of the intensity[3]. With such splitters, integrated Mach-Zehnder interferometers (MZIs) can be implemented, which will be the foundation of the measurements in Chapter 6 (also see Fig. 2.1(c), showing an imgage of a so-called Hresonator device placed next to a MZI). Another type of integrated device is the ring resonator. Here, light couples from the feeding waveguide to another waveguide forming a closed ring. The light will cycle around in the ring and eventually either get scattered, i.e. lost, or couples back into the feeding waveguide and can be detected. As only wavelengths with an integer fraction of the ring circumference can couple into the ring, wavelength sweeps will return a transmission pattered with narrow resonances. From the properties of these fringes, such as their extinction, free spectral range (FSR), or linewidth one can learn a lot about devices integrated into the ring, such as mechanical resonators (see Fig. 2.1(b) showing such a ring resonator with two integrated suspended beams) or waveguide crossings [107]. Such studies can be performed by utilizing only the linear characteristics of light. While SiN does exhibit only weak nonlinear optical properties [108], strong nonlinear materials like AlN can be applied to the ring, and their functionality exploited, such as their ability to generate single photons [109]. Of course, integrated photonics does also offer a huge variety of further functionality, that, however, shall not be part of this work. However, the functionality of photonics circuitry is based on waveguides that confine the light in two dimensions and leave one free dimension to define the

[3]If single photons are propagating, they will be in a superposition of both waveguide modes, each with a 50% probability.

propagation direction.

2.3.1 Optical waveguides

Dielectric waveguides as described in this section are based on a high contrast between the refractive indices of the core (SiN) and the cladding layer (SiO_2)[4]. The typically strong confinement of the light in waveguides ensures small losses in waveguide bends which allows very narrow bends with radii that can be as low as only a few microns. Furthermore, the light intensity in the core is very high which allows making use of nonlinear properties when appropriate materials are integrated into the circuitry [110]. We use so-called ridge waveguides, where the material around the waveguide is removed and the waveguide is only connected via the cladding layer to the substrate as can be seen in Fig. 3.6 showing a scanning electron image of the cross-section of two waveguides. An analysis of the influence of the waveguide dimensions on the supported optical modes and properties like the effective refractive index and the group velocity is given in the work of Xiaohe Bai [111].

When switching from laser light to single photons, one basically switches from analyzing intensities to analyzing probabilities [112, 113]. On the single photon level a lot of research is done on integrated photon sources [114, 115] and detectors [116, 117]. However, we couple light from an external fiber-coupled laser onto the chip and after the light passes through the circuitry, it is coupled back into a second fiber leading to a photodetector. The challenges and their solutions are discussed in the next section.

2.3.2 Grating couplers

One issue when coupling light from the laser, e.g. via an optical fiber, to the waveguide is the mode size mismatch. The waveguide has a width of about 1 μm while the fiber core dimensions are typically around 10 μm. Solutions include tapered fibers, edge couplers, or grating couplers (GCs), with their respective pros and cons discussed in detail in the review by Cheng *et al.* [118]. In this section it is described how the light is coupled onto and off a chip in our labs. For us, the grating couplers are the best option as we need fast and easy coupling as we have several 100 devices on each chip. Edge couplers are quite intolerant towards spatial mismatch and also more complicated to fabricate [118]. We thus implement grating couplers with adiabatic taper. GCs on silicon nitride can reach high efficiencies above 60 % [119].

To utilize the diffraction effect, which the grating couplers are based on, the period of the grating pattern, i.e. the refractive index variation, needs to be larger than the wavelength of the light [118]. The light is coupled in the direction of the index variation and works both ways, independent of whether coupling the light in or out. Our fiber is tilted at an angle of $\theta = 8°$ with respect to the normal axis of the chip. This is as perpendicular alignment of the fiber array would cause strong back reflections [118], thus chip-to-fiber grating couplers are typically based on the 2nd order diffraction peak [110]. From the grating, the light is then led via an adiabatic taper into the waveguide (see Fig. 2.2(a)). Specifically, we use a focusing grating coupler with curved grating lines.

The coupling itself is based on fulfilling Bragg's condition for constructive interference [110]. The parameters that can be varied in a basic grating coupler are the grating period and its filling factor[5]. Furthermore, the etch depth does play a role, as well as the length of the tapering region. This tapering region is taking a large space on the chip as the taper angle θ_{taper} has to fulfill the condition of being smaller than $\frac{\lambda}{2Wn_{\text{eff}}}$, with the varying waveguide width W and mode effective index n_{eff}. The taper length, however, can be shortened by applying a curved grating to focus the light onto the waveguide [118]. The relation between the various parameters reads for such

[4]Note, that fibers, on the contrary, have a small index contrast [110].
[5]The filling factor is defined as the ratio of the width of a ridge over the period.

a focusing grating coupler [118]:

$$m\lambda = n_{\text{eff}}\sqrt{x^2 + y^2} - xn_0 \sin\theta, \tag{2.1}$$

with the integer for each grating line m, the fiber tilt angle θ, and the refractive indices of the cladding layer and the GC, n_0 and n_{eff}, respectively. The curved grating lines thus have the form of ellipses having a common focal point. As there are quite some parameters to tweak, an optimized design is typically obtained by finite-element (FEM) simulations.

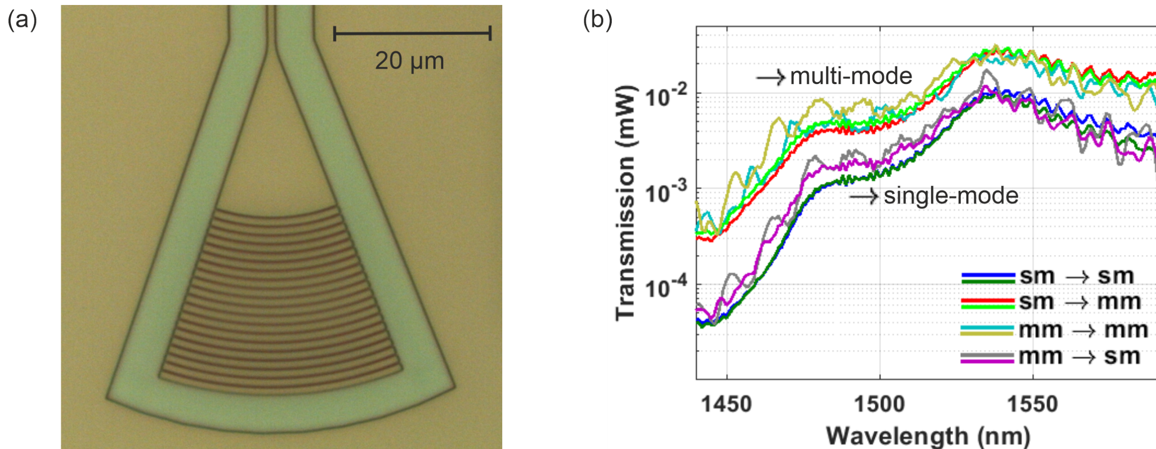

Figure 2.2: (a) Optical microscope image of a grating coupler. (b) Transmission profile of a calibration device over the wavelength. The individual measurements were done with different combinations of input and output fibers (sm: single-mode fiber, mm: multi-mode fiber).

The coupling efficiency of the GC is wavelength dependent as can be seen in Fig. 2.2(b) showing experimental data. Here, wavelength sweeps on calibration devices[6] with different combinations of input and output fibers are shown. The fibers can either support a single (sm-fiber) or multiple modes (mm-fiber) of the light depending on the core diameter. All measurements have their peak close to our desired wavelength of 1550 nm but differ in their transmission profile. Measurements with single-mode input fibers show a nice and smoothly varying shape. Those with multi-mode input fibers display strong wiggles in their profile as they create a speckle pattern on the grating. Although their transmission is quite high, we prefer the smooth background. When looking at the influence of the type of output fibers, the multi-mode fibers ensure a higher transmission for all wavelengths than the single-mode fibers due to their higher collection efficiency of the light scattered by the GC without fine structure. In our setup both types of fibers were used. The ideal combination is thus a single-mode input fiber with a multi-mode output fiber, ensuring both high efficiencies and a smooth transmission profile as can be seen in Fig. 2.2.

Figure 2.3 shows measurements on calibration devices with different design parameters. The paramterers swept in this experiment are the grating period and filling factor. The chip with these devices was measured in our so called quick meeasurement setup, that will be introduced in Cha. 4. I did these measurements at an early stage of my work myself, however, these particular were performed again by Giulio Terrassanta when the setup was changed to its current state with a sweep laser integrated instead of a step laser. The transmission profile is as shown in Fig. 2.2 and for every device the max was extracted. In panel (a) the maximum measured transmission for the two design parameters is displayed. Visible is a band of the grating period of highest transmission through the filling factor. The transmission increases towards larger filling factors. Panel (b) shows the wavelength of the highest transmission in dependence on the sweep parameters. For the desired wavelength of 1550 nm again a narrow band in the grating

[6]These calibration devices consist of two grating couplers connected by a waveguide as described in Sec. 3.5.
[7]Measured on sample WSN03_77.

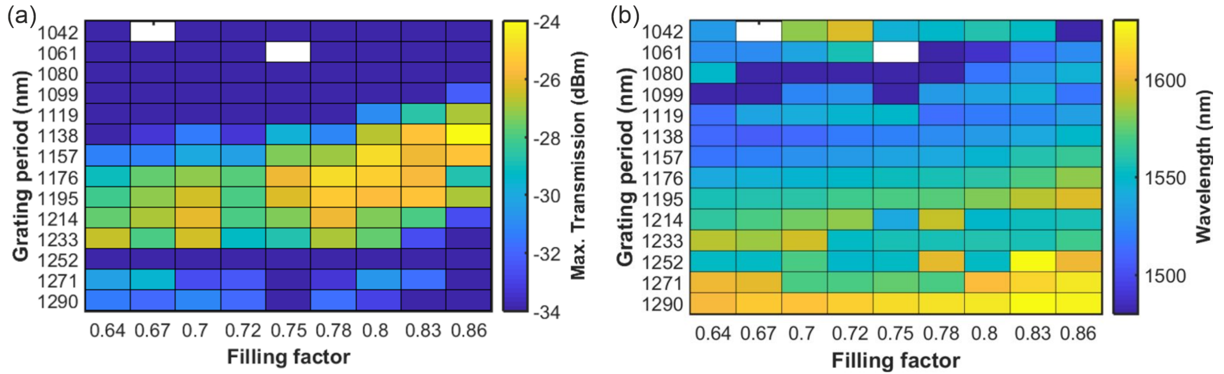

Figure 2.3: Measurements on calibration devices, i.e. a single waveguide connecting the input and output grating coupler (similar to the device in Fig. 3.14(h)). The device parameters of the grating couplers are swept. (a) Maximum transmission versus the grating period and filling factor of the grating couplers. (b) The wavelength of maximum transmission versus the grating period and filling factor of the grating couplers. For the white data points no data is available. Measurements are taken by Giulio Terrassanta[7].

period is visible, here only weakly dependent on the filling factor. Based on earlier experiments, our design parameters of choice were 1148.6 nm[8] for the grating period and 0.75 for the filling factor. This is close to the result of the measurements shown above, which return 1138 nm and 0.86 for the filling factor as ideal design parameters [109].

The coupling efficiency is also strongly dependent on the alignment of the fiber array over the GC. In the chapter introducing the setups, the automatic positioning of the sample under the fiber array for optimized transmission will be described. Here, we will look at the dependence of the transmission on the horizontal (x-y) position which is shown in Fig. 2.4(a) and (b). The measurements are again taken on calibration devices, here with single-mode to single-mode fibers and single-mode to multi-mode fibers, respectively. It can be seen that a clear peak exists with several side peaks appearing in the y-direction, which is the direction along the symmetry axis of the GC. As expected, the pattern along the symmetric x-direction is symmetric as well. These measurements were taken at a single wavelength of 1550 nm. Panels (c) and (d) show further measurements with the fiber settings of (a) and (b), respectively. Here, the stage was scanning along the y-direction only, but now sweeping the wavelength at each point. These measurements show that the ideal y-position is very similar for the whole wavelength range. The shape and intensity of the side peak are strongly wavelength-dependent. These measurements confirm the result of those in Fig. 2.2, showing that the multi-mode output fiber ensures the highest transmission and that this is valid for the full x-y-map.

Although, there are many ways to further increase the coupling efficiency, like using innovative and more complex design structures of the grating we note that our designs are good enough for the measurements we perform. Furthermore, techniques have been developed like adding a Poly-Si overlay onto the grating or integrating reflectors below the grating coupler. The reflectors can consist of metal (e.g. Au/Al), a distributed Bragg reflector, or a silicon grating. A discussion of these methods can be found in the work of Cheng *et al.* [118].

2.4 Integrated mechanical resonators

Not only the optics circuitry described above, but also mechanical resonators on the nano- or micro-scale can be integrated into the chip. This includes beams [16], membranes [63], or hybrid

[8]The grating period in μm of our design is calculated via $0.870^{-3} \cdot \lambda(nm) - 0.1999$.

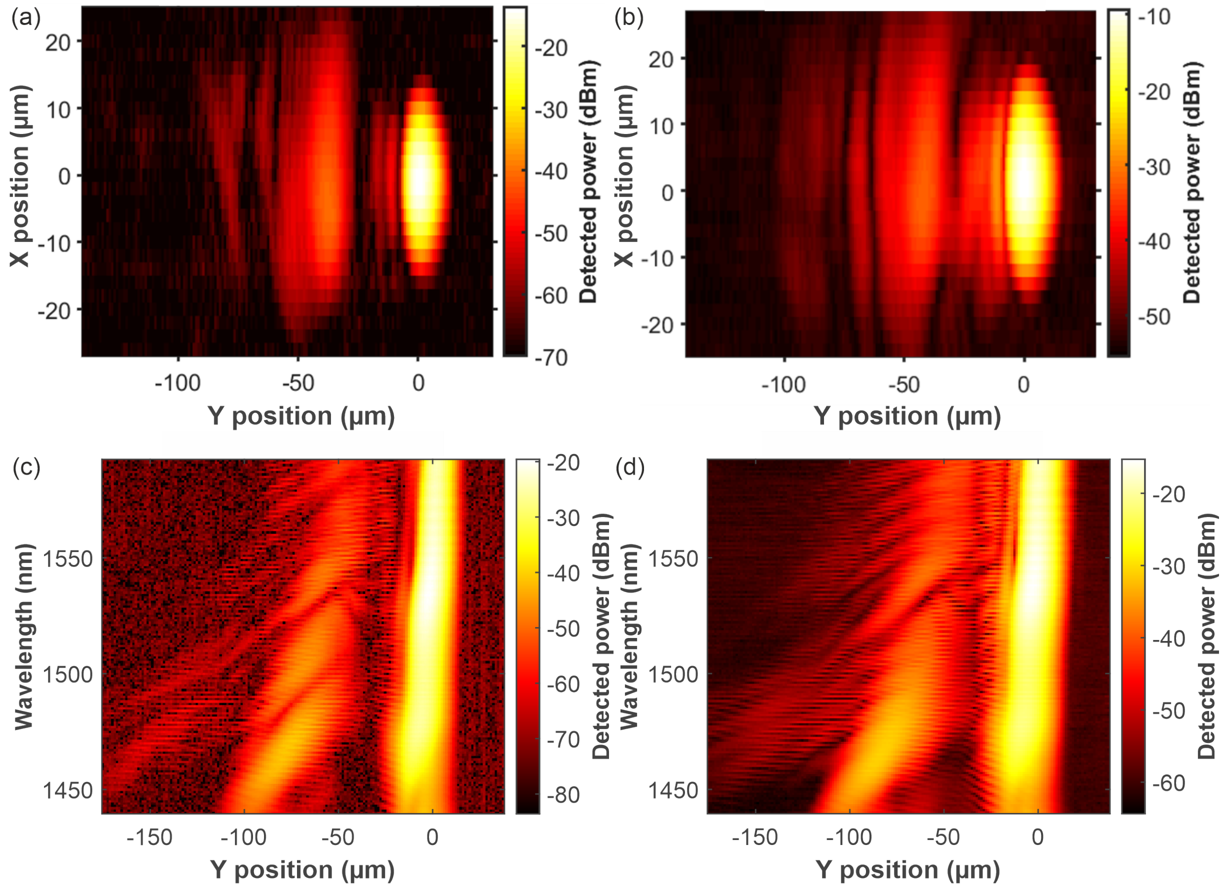

Figure 2.4: Top: maps of the detected power when scanning with the fiber array over a grating coupler. The input and output fibers are single-mode to single-mode (a) and single-mode to multi-mode (b). Bottom: detected power of wavelength scans when scanning from top to bottom over the grating coupler. The input and output fibers are single-mode to single-mode (c) and single-mode to multi-mode (d). Note that the x and y directions are swapped in the top panels for better comparison with the lower panels. These measurements were performed by Menno Poot.

photonic and mechanics devices, such as the so-called Hresonator [120]. As an introduction, in this section, the equations of motion of a plate resonator and a nonstandard beam resonator will be discussed as an introduction to the studies in Chapter 5 and Chapter 6, respectively. As well the relevant parameters in the field of continuum mechanics will be introduced.

The following discussion is based on Ref. [121] and [2]. In continuous materials, the stress σ is the quantity describing the *internal forces* between neighboring particles. The strain γ in contrast is a measure of the *deformation* of the material. Both are closely related to each other: a change in one of them leads to a change in the other. The stress-strain curve describes the relation between the two parameters, which is linear in the elastic regime, i.e. for low strains. Increasing the strain will eventuallly bring the material to the yield point, from where the deformation changes from elastic to plastic. Below that point, the device will return to its original dimensions when the stress is removed, while above that point, the deformations will be permanent. Eventually, fracture will appear in the device. In the linear regime, the relation is mathematically expressed by the elasticity tensor $\boldsymbol{E}$, a fourth-rank tensor of the form $\sigma_{ij} = E_{ijkl}\gamma_{kl}$. Due to its symmetry, the 81 elements of this tensor reduce to 21 independent elements and can be expressed by a 6-by-6 matrix. The inverse of $\boldsymbol{E}$ is the compliance tensor $\boldsymbol{C}$. In an isotropic material only two independent parameters remain, the Young's modulus E

and the Poisson's ratio ν. E describes the tensile or compressive relation between stress and strain, i.e. its "lengthwise stiffness". ν in contrast describes the expansion or contraction of the material in the directions perpendicular to the direction of the applied stress. In the example of pulling on a thin beam with length L with a resulting change of its length ΔL, it acounts $\frac{\Delta L}{L} = \gamma_{xx} = \frac{\sigma_{xx}}{E} = \frac{F/A}{E}$. For the height h this results in $\frac{\Delta h}{h} = -\nu \cdot \frac{\Delta L}{L}$. The relation $\frac{E}{2+2\nu}$ is called the shear modulus G and describes the "shear stiffness" of the material. The elasticity tensor now reads:

$$[E] = \frac{1}{(1+\nu)(1-2\nu^2)} \begin{bmatrix} E(1-\nu) & E\nu & E\nu & 0 & 0 & 0 \\ E\nu & E(1-\nu) & E\nu & 0 & 0 & 0 \\ E\nu & E\nu & E(1-\nu) & 0 & 0 & 0 \\ 0 & 0 & G & 0 & 0 & \\ 0 & 0 & 0 & G & 0 & \\ 0 & 0 & 0 & 0 & G & \end{bmatrix} \tag{2.2}$$

For example, the beams discussed later in Chapter 6, feel a high (intrinsic) tensile stress σ_{xx} before release and are thus stretched along the x-direction, i.e. along the beam. The resulting strain γ_{xx} induces stress in the y- and z-direction as resulting from E. When the beams are released, i.e. the cladding layer between beam and substrate is removed (see Chapter 3), the stress in x, can actually in turn lead to strain in y and z and the beam - now free in these directions - shrinks in these directions. This relaxes the stress σ_{xx} and is the reason why the tensile stress even of a straight beam reduces after release (see Sec. 6.5). This will be discussed in more detail, including the more complex and thus more interesting situation of pre-displaced beams.

If the mechanical device is stretched or compressed along the tensile direction one speaks of the tension T as the restoring force acting along the device. Such as the device cannot just be stretched without investing energy, it also cannot be bent without applying extra energy as bending stretches parts of the material and compresses others. This rigidity is called the bending rigidity D. T and D sometimes work against each other, e.g. in our pre-displaced beams, where the finite rigidity prevents the beams from fully straightening even though there is tension left (see Fig. 6.7 displaying the stress and displacement before and after release with respect to different design parameters). In formerly straight beams an effect called *buckling* can appear. When there is compressive strain exceeding a critical value larger than the bending rigidity, the beams deform against their tendency to keep their initial form. More about buckling can be read in [122].

With these ingredients Ref. [2] derives the equations of motion of a variety of (micro)mechanical systems. With the displacement field u the equation of motion of a thin plate reads:

$$\rho h \frac{\partial^2 u}{\partial t^2} + \left(D\nabla^4 - \frac{\partial}{\partial x_\alpha} T_{\alpha\beta} \frac{\partial}{\partial x_\beta} \right) u(x,y) = F(x,y), \tag{2.3}$$

where ρ is the density of the material, h is the thickness of the plate, t is the time, T is the displacement-dependent tension, and the rigidity D equals $Eh^3/12(1-\nu^2)$. F is the external force acting on the device.

The equation of motion of thin beams, the so-called Euler-Bernoulli equation with tension reads:

$$\rho A \frac{\partial^2 u}{\partial t^2} + D\frac{\partial^4 u}{\partial x^4} - T\frac{\partial^2 u}{\partial x^2} = F, \tag{2.4}$$

where A is the cross-section of the beam and the bending rigidity $D = EI$. I is the second moment of inertia, which equals $h^3 w/12$ for a rectangular beam and $\pi r^4/4$ for a cylindrical beam.

By the equations of motion, the frequency and the displacement profile of particular modes can be obtained. By expanding the displacement in the basis formed by the eigenfunctions ξ,

such as

$$u(x,t) = \sum_n u^{(n)}(t)\xi_n(x), \tag{2.5}$$

it can be shown that each mode of the mechanical device can be described as a harmonic oscillator [2,122]. By taking the Fourier transform of the equation of motion, the transfer function[9] $H_{HO}(\omega)$ can be obtained [123]:

$$H_{HO}(\omega) = k_0 \frac{u(\omega)}{F(\omega)} = \frac{\omega_0^2}{\omega_0^2 - \omega^2 + i\omega\omega_0/Q}, \tag{2.6}$$

with the spring constant k_0, frequency ω, resonance frequency ω_0, and quality factor Q. The phase and amplitude of the modes of a harmonic oscillator can be seen in Fig. 2.10. Especially the second panel in the top row shows a nice example with low noise and no external influences such as the crosstalk discussed below. For driving frequencies far below the resonance frequency, the oscillator follows the driving force adiabatically and both amplitude and phase are small. Note that in our systems, the driving signal applied by the network analyzer first drives the piezo, which is then exciting the resonator and the absolute phase shown in the plots is thus often shifted as discussed in sec. 2.5.2. Approaching the resonance frequency of the device, the amplitude increases towards its maximum, and the phase response lags behind the driving force by $-\pi/2$. Exceeding the resonance frequency, the device cannot follow the driving force any longer and the amplitude reduces again, as well its motion is now out of phase with the applied force by 180°. From the full width at half maximum (FWHM) of the peak the damping $\gamma = \omega_R/Q$ can be obtained, which will play an important role in the further scope of this thesis.

2.4.1 Membrane modes

In the previous section it was shown how mode properties can be deduced from the equation of motion in the general case (see also Eq. (2.10)). In particular the out-of-plane modes of a square membrane with side lengths a under uniform tension can be calculated analytically [124]. The normalized mode shapes are:

$$\xi_{m,n}(x,y) = \sin(\pi m x/a)\sin(\pi n y/a), \tag{2.7}$$

so that the local displacement is [2] $u_{m,n}(x,y) = U_{m,n}\xi_{m,n}(x,y)$. The modes are labeled using two integers m and n that count the number of anti-nodes in the x and y direction, respectively. The (m,n) mode, thus, has $m-1$ $(n-1)$ vertical (horizontal) nodal lines. At the anti-nodes, $\xi_{m,n} = 1$ and the amplitude is $U_{m,n}$. The corresponding eigenfrequencies are:

$$f_{m,n} = f_{1,1} \times \left(\frac{m^2+n^2}{2}\right)^{1/2}; \qquad f_{1,1} = \frac{1}{2a}\left(\frac{2\sigma}{\rho}\right)^{1/2}. \tag{2.8}$$

For the membrane studied in Chapter 5, ρ is the mass density of Si_3N_4 [125] and σ is the film stress in our wafers, yielding $f_{1,1} = 1.48\,\mathrm{MHz}$ for $a = 275\mu m$.

Experimentally, the eigenfrequencies appear as a series of sharp resonances, such as shown later in Fig. 5.8 where an overview spectrum over several resonances of a membrane is displayed. There, the first peak is at 1.46 MHz, close to the result from Eq. (2.8), which also shows that once $f_{1,1}$ is known, the other eigenfrequencies can be calculated [16]; their values (dashed lines) nicely match the observed peaks so that resonances can be identified. For example, the peak at 2.92 MHz matches $f_{2,2}$. On the other hand, the one at 3.26 MHz coincides with both (1,3) and (3,1). Theoretically, a perfectly square membrane has degenerate modes, i.e. $f_{m,n} = f_{n,m}$ but, in practice, small imperfections can break the degeneracy. When zooming in, two peaks with $\sim 1\,\mathrm{kHz}$ splitting are visible as shown in Fig. 5.10. Still, from their frequencies alone these

[9] The transfer function generally speaking describes the output of the mechanical device resulting from a certain input and returns the amplitude and phase of the motion.

cannot be identified. Instead, their mode shape should be measured to unambiguously determine which peak corresponds to which mode. This will be the topic of Chapter 5.

2.4.2 Nonlinearities

The linear response of a resonator follows a Lorentzian mode shape as shown in Fig. 2.7(a). However, nonlinearities cause deviations from the Lorentzian response. In general, there are several potential sources of nonlinearity [126]. These will be introduced in this section together with a discussion of whether they have a relevant influence on the resonators presented in this work. *Material nonlinearity* comes from a nonlinear relation between stress and strain. As a consequence plasticity is occurring for large strain. The threshold where this is playing a role is - as no surprise - a material parameter. The yield strength of LPCVD Si_3N_4 is reported as 13 GPa [87]. We are operating at intrinsic stresses below the film stress of 1050.1 MPa and, importantly, the experiments are reproducible. The latter strongly indicates that even at higher excitation, we do not reach the regime of plastic deformation and this type of nonlinearity can be neglected. *Detection nonlinearity* plays a role if a nonlinear conversion between displacement and measured voltage is present. This is not affecting the dynamics of the resonator and is only present in the detected signal. In our case the conversion is linear (c.f. Sec. 2.5.3) and we thus do not observe this kind of nonlinearity in our measurements. *Nonlinear damping* is affecting the dissipation of the resonator and still largely unclear [126]. The study of the role of nonlinear damping for the dynamics of integrated resonators can be of large interest in the future, however, we have not found indications of it in the data discussed in this work. *Actuation nonlinearity* is related to a nonlinear response of the piezo (the actuation) to the linear NWA excitation. At high excitations, piezoelectric ceramics are known to exhibit nonlinear behaviour [127], however, we do not expect this to play a role in the range of relatively low excitations we are applying with the NWA. *Geometric nonlinearity* results from elongation of the resonator due to its deflection. This results in an increase of the longitudinal stress and thus a frequency shift. This effect is appearing in our data when strongly driving the resonator (see Fig. 2.7(i)). For sufficiently high excitation powers, this actuation nonlinearity in the resulting oscillatory motion takes place, which deviates from the linear response (Fig. 2.5(a)). In the following discussion, we will focus on the nonlinearity of third power appearing in the equation of motion, the so-called duffing nonlinearity. This can either result in an increase or a decrease in the spring constant. The first is referred to as spring hardening and the latter as spring softening. The effect of spring hardening results in an increase in the resonance frequency when the oscillation amplitude increases (Fig. 2.5(b)). Whereas spring softening causes the resonance frequency to decrease when the oscillation amplitude increases (Fig. 2.5(c)) [128]. Both effects appear simultaneously (Fig. 2.5(d)) but usually one of these dominates over the other [129]. It can be seen in panels (a) and (b) that a certain driving frequency can result in up to three values for the amplitude of oscillation, in panel (d) it shows even up to five values. Of course, in reality, all these values do not take place at the same time. Which response is appearing in the experiment strongly depends on the sweep direction of the frequency. This is visualized in Fig. 2.6(a) for the sweep-up case and in (b) for the sweep-down case. In this work exclusively sweep-up measurements are shown which results from the functionality of our measurement framework. In Sec. 2.5.2 it will be shown that the duffing nonlinearity can still be fitted. Later in the discussion of the dynamics of pre-displaced beams, the appearance of both spring softening and spring hardening is shown.

2.4.3 Electrical crosstalk

Besides the nonlinearities discussed above also electrical crosstalk causes deviations from the Lorentzian response. The crosstalk strongly alters the obtained response making it impossible to fit it with the pure standard harmonic oscillator fit (Fig. 2.7(e)). The interference of the

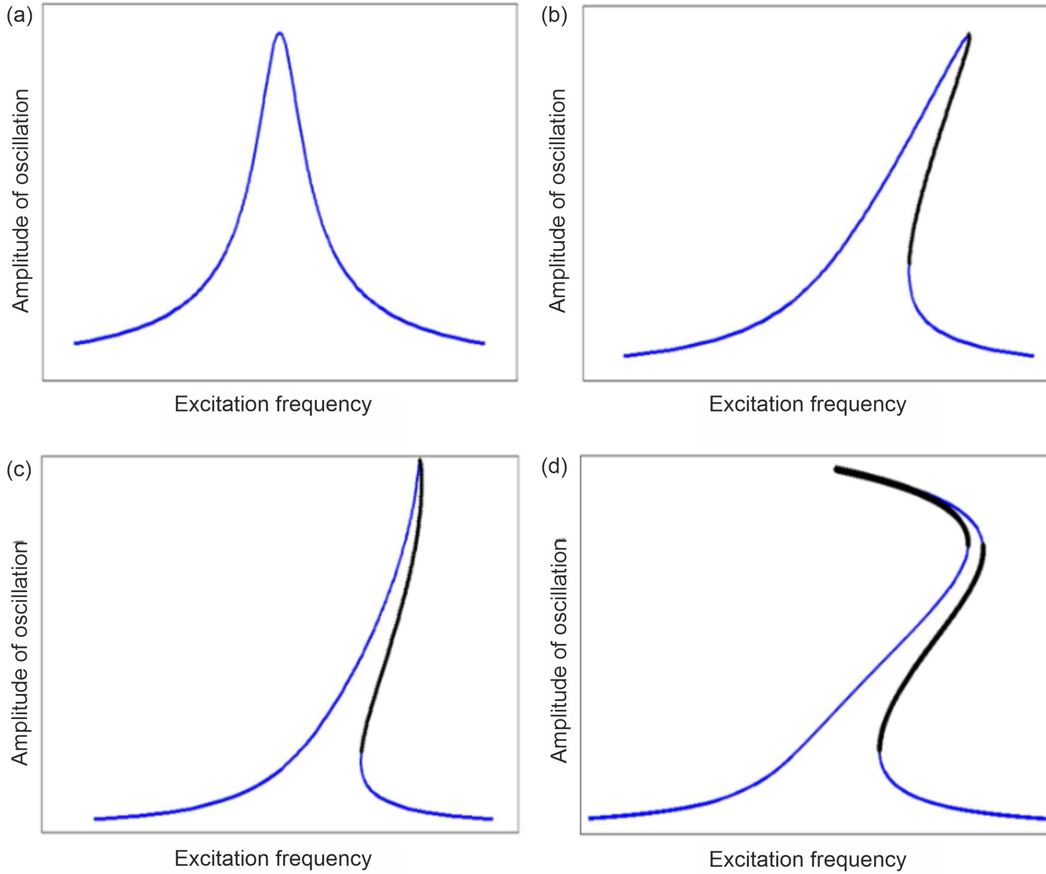

Figure 2.5: Typical response of a MEMS resonator when the hardening behavior is dominant (the black traced segments are unstable regions): (a) The response when the resonator is in the linear region, (b) the response when the amplitude of oscillation is small but the hardening phenomenon is observed, (c) the response when the amplitude of oscillation is higher than that in (b) and softening just starts to occur over and above the hardening that is already there, and (d) the response when the amplitude of oscillation is very high and softening and hardening are clearly noticeable. Figure and caption adapted from [129] © 2011 IEEE.

response of the device with the electrical crosstalk leads to the Fano-like mode shapes [130]. Panel (f) and (g), however, show that the correction term $z_x e^{i\phi_x}$ in the fit function can solve this issue (see Eq. (2.11)). Still, crosstalk leads to unstable operation of the phase-lock loop discussed in Chapter 5 and results in distorted mode maps as discussed by Sommer *et al.* [131] further analyzing the PLL setup described in this work. While mode mapping worked well for the measurements discussed in the following chapters, crosstalk becomes more prominent at higher frequencies, i.e. at higher modes or smaller and stiffer membranes that were fabricated together with the discussed membrane. The reason is that there is an additional pathway from excitation to detection than the one via the piezo, resonator, and photodetector, which is of electrical nature. For smaller signals (higher modes are much less pronounced also for the membrane discussed later) the influence of crosstalk becomes more strongly visible in the data but the crosstalk itself increases with frequency as well. Sommer *et al.* show a method to successfully compensate for the crosstalk while taking the mode maps [131]. There it is also discussed that there is not one single pathway for the electrical crosstalk but several parallel pathways that sum up to the total crosstalk. It is (so far) not possible to eliminate the crosstalk by making small changes to the setup or by exchanging a potential source of the crosstalk such as individual measurement devices. Further investigation might be able to reduce the crosstalk actually present

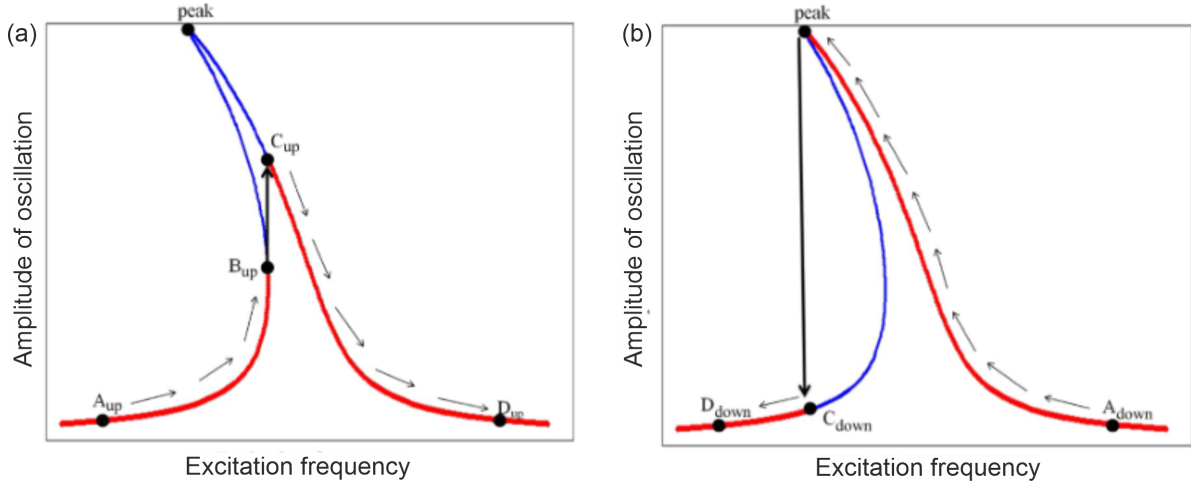

Figure 2.6: (a) Sweep-up case. Note how a *jump* exists from point "B_{up}" to point "C_{up}" without passing by point "peak." (b) Sweep-down case. Note how a *jump* exists from point "peak" to point "C_{down}" spontaneously. Figures and captions adapted from [129] © 2011 IEEE.

in the setup. However, both the correction term in the fit function and the compensation method applied to the PLL successfully solve the issues with crosstalk in current measurements.

2.4.4 Dissipation

The quality factor was already mentioned above and will be further discussed in this section. It is a measure of the dissipation of energy in the resonator. However, it can be defined in several different ways. Quite often it is described as the number of oscillations until the oscillation fades out, i.e. the amplitude is reduced by the factor $1/e$. One other definition goes via the spectral purity of the resonator motion: $Q = \frac{f_0}{w}$, the ratio of the resonator's resonance frequency f_0 over its FWHM w [49]. A definition equivalent to the former two is the ratio of the stored total energy vs. the energy lost during one cycle of vibration $Q = \frac{W}{\Delta W}$. The latter shall imply the idea of dissipation dilution [50, 132] which is of high relevance for the study of stress-tuning in pre-displaced beam resonators that will be discussed in depth in Chapter 6. The various sources of dissipation can be broken up into energy loss due to the surrounding *medium*, phonons traveling into the bulk via the *clamping* points, *surface losses*, the for us most relevant *intrinsic loss*, and some *others*, like *thermoelastic damping (TED)* or *Akhiezer damping* that shall not be of further interest in the context of this work. When obtaining the overall quality factor we can look at the different sources of dissipation individually and finally build the sum over all the contributions [126]:

$$\frac{1}{Q} = \frac{1}{Q_{\text{medium}}} + \frac{1}{Q_{\text{clamping}}} + \frac{1}{Q_{\text{surface}}} + \frac{1}{Q_{\text{intrinsic}}} + \frac{1}{Q_{\text{other}}} \tag{2.9}$$

Losses due to the *surrounding medium*, such as liquid or gas can be quite extreme at ambient conditions as the mass of this medium has to be removed or dragged during each cycle of oscillation. This is shown in Fig. 4.6(b) where the Quality factor of a Hresonator is plotted against the pressure of the medium. There it can be seen that the quality factor goes from the fluidic regime to the ballistic regime when the pressure is reduced. In the first one, the resonator is larger than the mean free path of the molecules and air can be modelled as a viscous fluid. In the latter, the damping comes from the momentum transfer from the resonator to the colliding gas molecules [126]. Usually, the desired regime is the ballistic regime where Q is rather constant over the pressure. Thus we perform our dynamic measurements in vacuum. Still, it can be thought of examples where the influence of the surrounding medium is utilized: if the resonator

serves, e.g. as a gas sensor, the influence of the medium on the resonator is of interest [133]. Hollow resonators have been built where a fluid flows through the device itself and its properties or contamination alters the resonator motion [134, 135].

Energy can radiate from the resonator into the environment, i.e. the bulk, via the clamping points, the so-called *clamping losses*. Clamping losses are strongly dependent on the geometry of the resonator [126]. To overcome these often the design can be optimized. One can decouple the chip from the substrate [136] or integrate a phononic shield (phononic band gap structure) into the bulk around the clamping points [47].

As the limiting factor in our resonators, we observe the *intrinsic losses* which can be divided into friction losses and fundamental losses [126]. Friction losses result from the lag of the induced strain behind the applied stress which is not in phase and thus irreversible motion of the atoms takes place. For thin resonators with a high surface-to-volume ratio, surface friction can become dominant over the friction within the bulk of the resonator. Fundamental losses are non-reversible heat flow in the resonator, examples of which are TED and phonon-phonon interaction (Akhiezer damping). TED is related to thermal relaxation between strain-induced temperature differences in different spacial areas in the solid. During the vibration of the resonator, one side is under compression while the other side is under tension. The first is becoming warmer while the latter becomes colder resulting in a temperature gradient causing energy loss. Akhiezer damping in contrast is related to the interaction of the oscillation strain field (low frequency) with the atomic thermal motion (high frequency) in the lattice. This mechanism starts to play a role in the GHz-regime of resonator vibrations [126]. Strategies to reduce energy dissipation are cooling of the resonator, altering the device design, and dissipation dilution. The latter utilizes the increase in tensile stress and leads to extremely high quality factors. It will be further discussed later in the Chapter 6 about geometric stress tuning in beam resonators. In the next chapter, the nanofabrication processes to build our resonators are described. Not only the device design defines the dynamics of the resonators and their dissipation, but also details in nanofabrication have a strong influence, so is, e.g. surface friction caused by adsorbates on the surface, the surface roughness, or surface impurities which can be targeted by variations in the nanofabrication processes.

2.5 Measurements and data processing techniques

In the previous sections, the mechanics of integrated devices and the coupling between optics and mechanics have been discussed. It was also focused on the response of driven devices at their resonance frequency and how the obtained data can be fitted, especially for the more complex situations in the presence of nonlinearities or electrical crosstalk. Next, I will describe how the optomechanical measurements are actually performed and evaluated both on integrated Fabry-Pérot cavities in our phase-lock loop (PLL) setup and on photonic circuits in our LVC.

2.5.1 Detection methods

As mentioned at the beginning of this chapter, to detect the mechanical properties of integrated resonators, their motion has to be translated into an optical signal. Many methods for this translation have been developed, such as utilizing on-chip cavities (e.g. ring resonators, Fabry-Pérot cavities, and photonic crystal cavities), Mach-Zehnder interferometers, transmission modulation, capacitive detection, piezoelectricity, flux-based methods, or level spectroscopy [2]. In this work, three different methods of transduction are applied. The first one is based on the principle of a Fabry-Pérot cavity and applied in the SVC (c.f. Sec. 4.5). It is very well suited to measure the motion of "2-dimensional" devices like membranes, wide cantilevers, or trampolines, which will be demonstrated in Chapter 5.

The significance of the reflectivity of these devices becomes apparent when looking at the

measurement principle. As illustrated later in Fig. 4.8 showing a sketch of our PLL setup, the lock-in amplifier (LIA) outputs a voltage at (angular) frequency ω with amplitude V_{out}: $V_{\text{output}}(t) = V_{\text{out}} \cos(\omega t)$. This is applied to the piezo the sample is mounted on. The actuation of the piezo results in an oscillating inertial force on the membrane, which induces vibrations. These result in a modulation of the reflected power as the interference of the laser light depends on the distance of the membrane surface to the Si substrate, as illustrated in Fig. 5.5 showing a sketch of the cross-section of a membrane. The reflected power is detected using the photodetector and converted to a voltage by the low-noise amplifier. This voltage goes to the input of the LIA and contains the same frequency as the output: $V_{\text{input}}(t) = V_{\text{in}} \cos(\omega t + \phi)$. Here, V_{in} is the amplitude at the excitation frequency ω and ϕ is the phase difference between output and input signals.

Another way to detect mechanical motion is the utilization of the resonances of photonic microring resonators. A ring resonator is brought in close vicinity of a feeding waveguide, such that light can couple into the ring. Due to the specific circumference of the ring, only light with a wavelength that is an integer fraction of this circumference can couple into the ring. When performing wavelength sweeps, this results in very narrow ring resonances at the output of the feeding waveguide. The properties of these resonances, like their extinction or linewidth, depend on the coupling of the ring and feeding waveguide (external losses) and the losses inside the ring (internal losses). These properties can be altered by changing the ring circumference, which can be done by changing the temperature of the device or else by integrating a mechanical resonator inside the ring (or in close vicinity). The latter is applied for the racetrack devices of our synchronization project, which will be part of various discussions later in this work and is nicely introduced by Xiong Yao [137] and Agnes Zinth [138]. This method can also be used to study purely optical properties, such as those of AlN-covered rings [109].

The way, the mechanical motion is extracted from the above-mentioned transmission measurements, is analogous to that of the third detection method, which utilizes integrated Mach-Zehnder interferometers (MZI) instead of rings. Here, instead of ring resonances, the transmission spectrum of wavelength sweeps shows the interference pattern of the MZI, due to the recombination of two waveguides with different lengths (c.f. Fig. 2.9(b)). The transmission is dynamically altered when the light in one of the arms picks up an additional phase, introduced by an object that oscillates in its vicinity, as explained in the next section.

2.5.2 Response function and fitting

When measuring the resonance frequencies the response is often not just a sharp peak at the frequency discussed above but can have a more complex shape. We measure the dynamics of the resonators typically with a network analyzer (NWA) or lock-in amplifier (LIA), as described in more detail in the next section. There we see distinct peaks in the frequency response whenever the device is driven on one of its resonances as described above. See Fig. 5.8 for an overview spectrum of the first 39 modes measured on a membrane together with their calculated frequencies marked. Zooming into these resonances with higher resolution, we gain further information about these modes. Examples can be seen in Fig. 5.9 where nine modes out of the previously mentioned overview spectrum are measured with high resolution and presented with their fit. There are several values, like the quality factor, linewidth $w = f_0/Q$, or peak height z_{mech}, that we want to extract from the data. This is done by fitting the data. However, the measured frequency response does not always follow the Lorentzian shape expected from the harmonic oscillator model (e.g. Fig. 2.7(a)). Electrical crosstalk (Sec. 2.4.3) or nonlinearities (Sec. 2.4.2) can cause strong deviations from this model (e.g. Fig. 2.7(e,i), respectively). This does not necessarily mean, that the desired information cannot be extracted. By choosing an appropriate fit function, that can account for these influences, we will still get this information. The four fit functions (eq. (2.10)-(2.13)) that are used for the measurements of this work are explained in the following. Figure 2.7 visualizes these fits applied on measurements on a cantilever (1st row), on a membrane (2nd row), and on a displaced beam (3rd row). It can be seen that none of

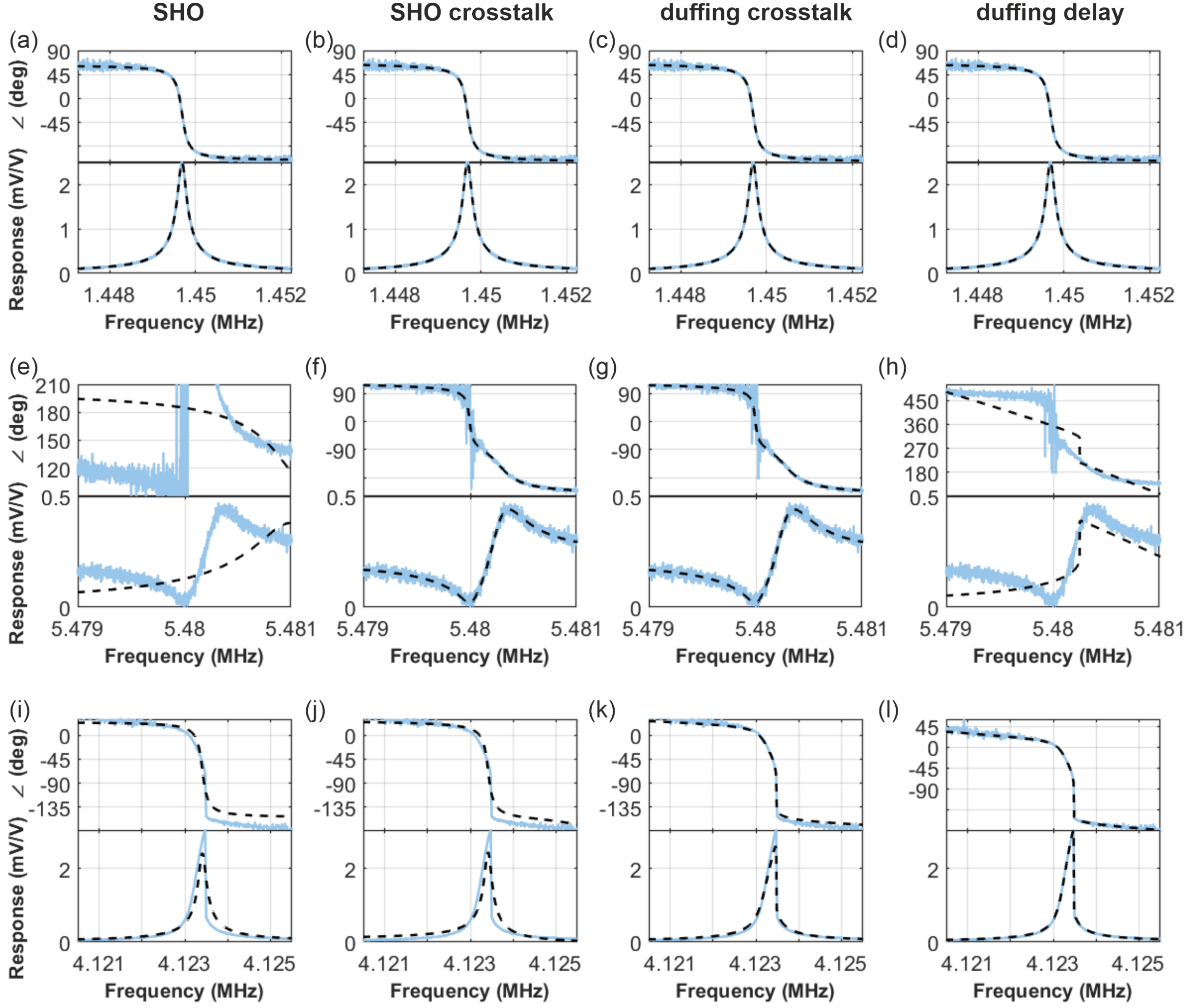

Figure 2.7: Measurement on three different devices fitted with four different functions, each. Panels (a-d) display a measurement in the linear regime on the cantilever discussed later in Sec. 6.9. Panels (e-h) display the results of a measurement on a membrane also in the linear regime but with strong crosstalk described in Sec. 2.4.3. Panels (h-j) display a measurement in the nonlinear regime on the Sbeam discussed in Sec. 6.10. Column one is fitted with the pure standard harmonic oscillator function "SHO" (Eq. (2.10)), column two with the standard harmonic oscillator function including crosstalk "SHO crosstalk" (Eq. (2.11)), column three with the complex duffing fit including crosstalk "duffing crosstalk" (Eq. (2.12)), and column four is fitted with the complex duffing fit including delay "duffing delay" (Eq. (2.13)).

the fit functions resembles the mode shape correctly in all the cases and thus have to be chosen carefully for each measurement.

The fit for the standard harmonic oscillator (SHO) resembles the Lorentzian behavior of the resonator when no disturbing influences like crosstalk or nonlinearities are present:

$$Z(f) = z_{mech} e^{i\psi} \frac{f_0 w}{f_0^2 - f^2 + ifw}, \tag{2.10}$$

with z_{mech} the peak value of the mechanical response, ψ the overall phase offset (for the SHO the phase angle is $\psi - \pi/2$), f_0 the frequency at resonance, f the frequency, $w = 2\pi FWHM$ the damping rate. To fit Eq. (2.10) to the complex measured response, the real and imaginary parts of the response were fitted simultaneously, and the magnitude and phase of the resulting curve

were calculated for the plots.

If (electrical) crosstalk is present and interferes with the oscillator response, the obtained mode can strongly deviate from the Lorentzian shape which is further discussed in Sec. 2.4.3. In that case, a correction term accounting for the crosstalk needs to be added to the fit function:

$$Z(f) = z_{mech} e^{i\psi} \frac{f_0 w}{f_0^2 - f^2 + ifw} + z_x e^{i\phi_x}, \tag{2.11}$$

with z_x the magnitude and ϕ_x the phase of the crosstalk.

In addition to the crosstalk also duffing nonlinearity may be present and leads to hysteresis for upward and downward sweeps as discussed in Sec. 2.4.2. The standard harmonic oscillator fit including duffing nonlinearity and crosstalk is written as:

$$Z(f) - Z_x(f) = Z_{mech}(f) = z_{mech} / \left(i + \frac{f_0 - f + \frac{3}{4}\alpha |Z_{mech}(f)|^2}{w/2\pi} \right) \tag{2.12}$$

with $Z_x(f) = z_x e^{i\phi_x}$ the contribution of the crosstalk, $Z_{mech}(f)$ the contribution of the resonator, f_0 the frequency at resonance, f the frequency, α the duffing nonlinearity parameter in units of Hz/(V/V). The amplitude $Z_{mech}(f)$ stands on two sides of the equation. The equation can be solved by finding the roots of a third order polynomial. From the sign of α and the sweep direction it can be deduced whether the fitted value belongs to the upper or the lower branch of the hysteresis.

A time delay that leads to a mismatch between the control data and measured data is unavoidable in real systems. This is because there is always some time spent, e.g. in the calculation and execution of the excitation (i.e. the control forces), as well as in computation [139]. Also the amount of cable causes delay due to the finite speed of the signal. If the time delay becomes significant it can as well be reflected in the fit function. The standard harmonic oscillator fit including duffing nonlinearity with delay reads:

$$Z(f) = z_{mech} / \left(i + \frac{f_0 - f + \frac{3}{4}\alpha |Z(f)|^2}{w/2\pi} \right) \times e^{-i\tau(f-f_0)+i\psi} \tag{2.13}$$

with the phase being $e^{-i\tau(f-f_0)+i\psi}$, τ the delay time, and ψ the overall phase offset. A measurement that is affected is fitted without and with time delay in Fig. 2.7(k) and (i), respectively, where the latter fit nicely resembles the data while the first does show deviations.

2.5.3 Measurements of integrated MZIs

A Mach-Zehnder interferometer [140] can be realized in different ways. While we work with its integrated version, the working principle originates from experiments in free space optics, where beam splitters introduce an additional pathway for the light and rejoin it with the reference path [141]. For completeness, it shall be mentioned, that Mach-Zehnder interferometers cannot only be applied in optics experiments, but e.g., also electronic MZIs have been realized [142].

The content of this section focuses on integrated MZIs and is partially adapted from [16] and shall be seen as a preparation for Chapter 6. As mentioned above, the interference pattern of a MZI is influenced by introducing an additional - time-dependent - phase in one of its arms. This typically happens by a local change in the effective refractive index, which can be done by bringing an object (such as a mechanical resonator) into the vicinity of the MZI waveguide, such that it overlaps with the evanescent field of the light mode traveling through the waveguide. The change of the effective refractive index depends on the separation of the object and the waveguide, as shown in Fig. 2.8(a). As a consequence of the change in the effective refractive index, the interference fringes of the MZI do shift and thus the measured transmission at a specific wavelength does as well. This is illustrated in Fig. 2.8(b). For fringes with high

extinction and narrow linewidths, a small shift of the fringes (horizontal arrow) results in a high variation of the transmission (vertical arrow) and enables high sensitivities. This is utilized in the project on the geometric tuning of stress, discussed in Chapter 6. This method is applied in the Quick Measurement Setup, discussed in Chapter 4.3, as well as in the Large Vacuum Chamber, described in Chapter 4.4.

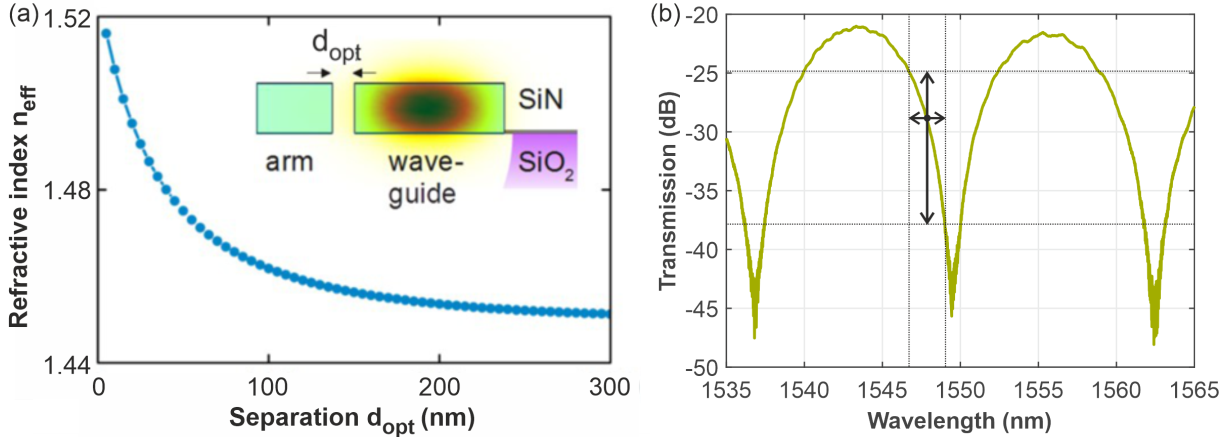

Figure 2.8: (a) Effect of a SiN object (arm) in the vicinity to the waveguide on the effective refractive index n_{eff} in dependence of its distance d_{opt}. The inset shows a sketch of the device. The light mode is symbolized by a change in color in an oval fashion in the waveguide. Adapted from [143]. (b) Principle of the detection mechanism of an integrated Mach-Zehnder interferometer. A small shift of the interference fringes (horizontal arrow) results in a high variation of transmission (vertical arrow) and enables high sensitivities.

In our projects, we typically use MZIs to sense the mechanical response of 1-dimensional resonators, such as strings[10]. The full measurement principle is as follows: laser light is coupled in and out of a chip via a fiber array placed above the grating couplers of the integrated device. The input waveguide splits into two waveguides with equal splitting ratios. The upper waveguide passes the resonator and rejoins with the reference waveguide before connecting to the output grating coupler. The different lengths of the two waveguides result in a wavelength-dependent phase shift, resulting in interference fringes (Fig. 2.9(b)). If the resonator is close to the upper waveguide, the light traveling through this arm picks up an additional phase shift due to a distance-dependent effective refractive index $n_{\rm eff}$ in the interaction region [144]. As the resonator-waveguide distance is modulated by driving the former with the piezo, its motion translates into fast changes in the interference in the MZI output and subsequently in the electrical signal generated by the photodetector (PD) as read out by the NWA. When the resonator is driven over its resonance frequency, this leads to a distinctive peak in the response measured by the NWA. This is visible in Fig. 2.9(a) for several resonances of the Sbeam (marked by the vertical lines) and as well in Fig. 2.10 showing an individual zoom into each of the resonances together with the obtained phase.

These measurements, however, do not only contain information about the pure motion of the resonator under test. They typically also show signatures which do not origin from the resonator. Especially in the overview of the driven response shown in Fig. 2.9(a), a noise-like background is visible. To understand these fluctuations, we typically compare network analyzer measurements on different types of devices as shown in Fig. 2.9. Besides the data taken on a regular device which shows the mechanical resonances, we repeat measurements on a number of calibration devices: on a calibration device with an MZI but without a mechanically active part,

[10]An exception is the Hresonator, extending in two-dimentions, that can also be measured with MZIs. Still, the detection principle remains the same and the MZI senses the motion of the one resonator arm in its vicinity.

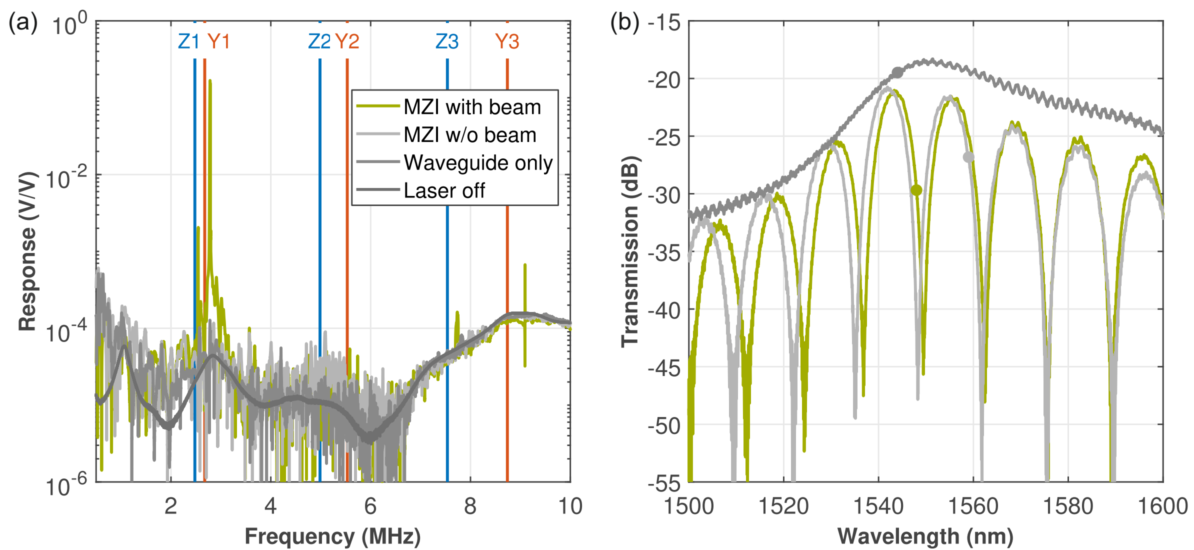

Figure 2.9: (a) Network analyzer traces measured under different conditions. The green curve is measured on a regular Sbeam device with a mechanical resonator. The simulated flexural modes are indicated by the vertical lines, labeled by their polarization and mode number (in-plane in orange; out-of-plane in blue). The other curves are taken on a Mach-Zehnder interferometer device without a beam (light gray), a calibration device with a waveguide directly connecting the input and output grating couplers (gray), and one where the laser was off (dark gray), respectively. (b) Transmission through the devices (colors as in (a)) vs. wavelength. The markers in each curve denote the wavelength selected for the NWA measurements of (a). The overall transmission profile is similar for all devices and is that of the grating couplers. The dips visible in the MZI devices are the typical interference fringes expected in such devices.

on a device with only a waveguide connecting the input and output grating coupler (i.e., with neither a Mach-Zehnder interferometer nor a resonator), as well as one with the laser turned off. The latter measurement shows that even without an optical signal, a background is present. This is the electrical cross talk [63, 145] in the setup and its shape is recognizable in all measurements (c.f. Sec. 2.4.3). However, unlike the other measurements, this is a smoothly varying contribution. The other measurements were all taken with the laser on and are not smooth, but show noise-like fluctuations. However, these fluctuations are reproducible - i.e., not noise - and we attribute these to eigenmodes of the piezo element that is used to actuate the mechanical resonators [145]. Since these are also present in the "waveguide only" measurement, it is likely that these appear because the vibrations of the piezo dynamically change the distance between the grating couplers and the fiber array, thus resulting in a modulation in the amount of light transmitted through all the optical devices.

The individual resonances as shown in the example of Fig. 2.10 are fitted with the harmonic oscillator response function $H(f)$ taking the crosstalk into account [145]. As shown in Fig. 2.10, Eq. (2.10) fits the driven response of all modes well and the resulting values and uncertainties of the most relevant fit parameters - as well as derived quantities, such as Q - are listed later in Table 6.3 when the results of these measurements are discussed in further detail. Overall, Mach-Zehnder interferometers are a powerful tool to extract information from the motion of our integrated devices and we utilize them in a variety of our projects.

2.5.4 Transduction calibration via thermal motion

An important property, related to the detection methods is the transduction, describing how a certain displacement u of the resonator corresponds to the obtained voltage V. Figure 2.11

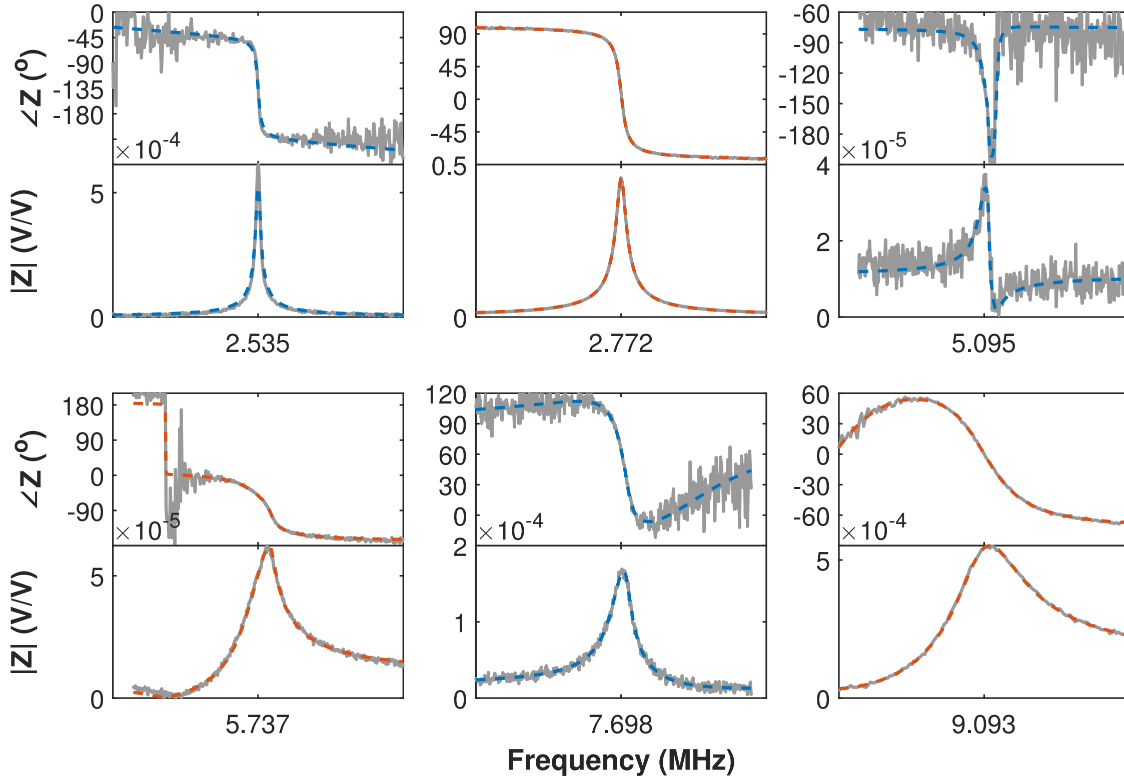

Figure 2.10: Frequency response of the modes marked in Fig. 2.9(a), together with the respective phase $\angle S$. The span is 2 kHz in all panels. The dashed lines are the fits of Eq.(2.10) to the data.

displays this relation at the measurement on a string resonator. Higher excitations lead to a higher displacement of the resonator and thus a larger voltage at the detector. For low excitationthe signal-to-noise ratio (SNR) strongly decreases such that detection and fitting of the mode become more difficult. The transduction can be obtained by measuring the thermal motion of the resonator with a Spectrum Analyzer (SPA). Here, the resonator is not actively driven, but the power spectral density of its thermal motion is measured. Figure 2.12 shows the thermal motion of the fundamental mode of a string integrated into a racetrack cavity (see Sec. 3.5). The transduction factor $\frac{dV}{du}$ can be calculated as follows:

$$\frac{dV}{du} = \sqrt{\frac{A(2\pi f_0)^2 m}{k_B T}}, \tag{2.14}$$

with the area under the thermal motion peak $A = 16.8\ \mathrm{V}^2$, resonance frequency f_0, the mass of the resonator $m = 1.02 \cdot 10^{-13}$ kg, resonator temperature T, and Boltzmann constant k_B. The transduction factor of the string from Fig. 2.12 is 480 kV/m. Further measurements of the thermal motion on a membrane can be found in Sec. 5.5. Having discussed the background of optomechanical devices and the related measurements, the next Chapter explains how these devices are fabricated by state-of-the-art nanofabrication techniques.

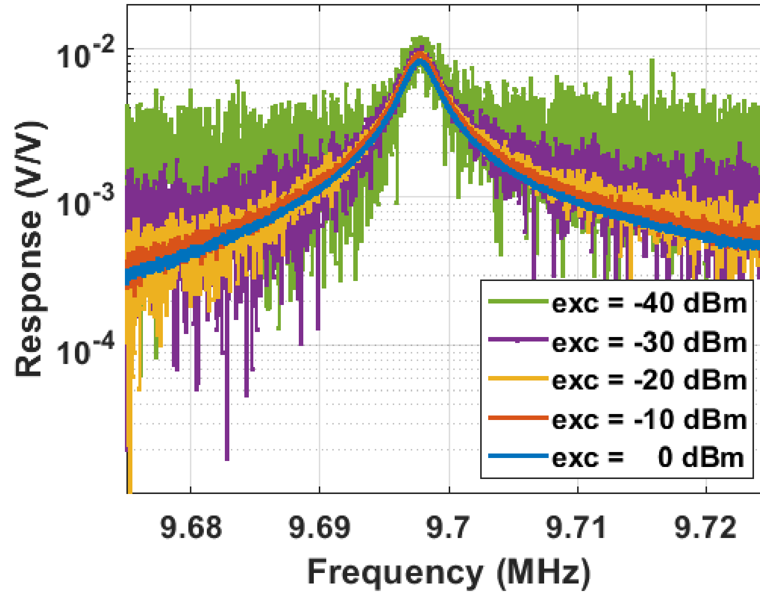

Figure 2.11: Amplitude response of a string near 9.7 MHz for different excitation powers.

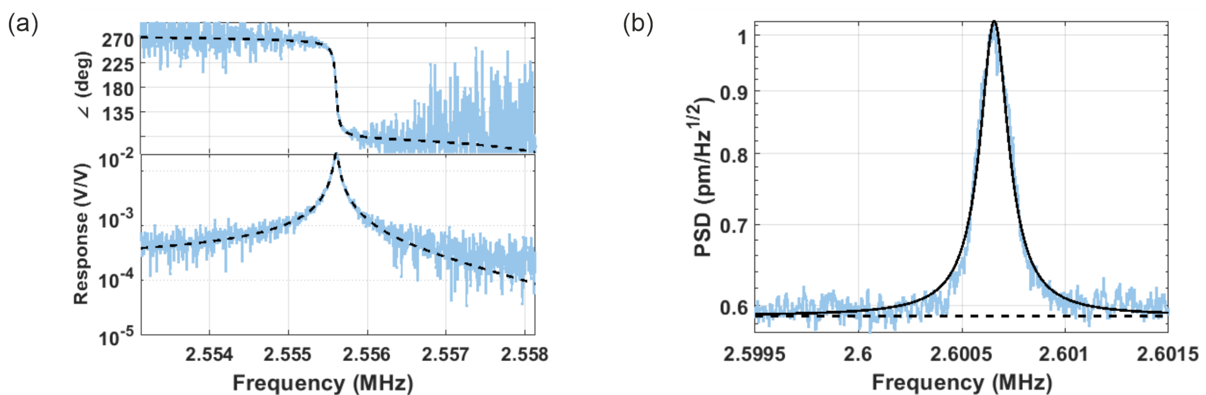

Figure 2.12: (a) Network analyzer measurement of the fundamental mode of a racetrack device with integrated suspended beam. (b) Thermal motion measurements of the same mode with a spectrum analyzer. The resonance frequency has drifted by 55 kHz between these two measurements.

CHAPTER 3

Device Fabrication

This chapter explains the nanofabrication processes that were applied to build the devices that we measure in our labs.

My personal contribution to the content of this chapter is the integration of the described steps into the clean room environment. This includes calibrations of the process parameters, like dose tests, testing, and optimizing of the parameters on various machines, e.g. the electron beam writer, evaporator, or reactive ion etcher (RIE). I took over the responsibility for the RIE, including maintenance and providing it to the clean room community. At the nanobeam, I performed alignment precision tests and the optimization of the parameter set. I worked on the device design and applied all the described fabrication steps for making chips for the study in the lab. Some of the devices were fabricated by students under my supervision. Furthermore, my contribution includes the documentation of the nanofabrication processes.

3.1 Introduction 28
3.2 Process steps 28
3.2.1 Wafer preparation 28
3.2.2 Lithography steps 30
3.2.3 Evaporation 31
3.2.4 Photonic and mechanical structures 33
3.2.5 Reactive ion etching 34
3.2.6 Release 35
3.2.7 Electron beam writing 36
3.2.8 Inspection 38
3.3 Optimization of nanofabrication 40
3.3.1 Wafer dicing 40
3.3.2 Precision of the marker positions 40
3.3.3 Descum 41
3.3.4 Reactive ion etcher 41
3.3.5 Optimization of process flows 42
3.4 Post-fabrication 44
3.5 Devices 44

3.1 Introduction

We use state-of-the-art nanofabrication techniques to fabricate the devices studied in our labs. These techniques are well-known in semiconductor industries and have been developed over several decades. Today, the "5 nm"-process[1] limit has been reached, expected to be overcome soon [147]. We utilize these techniques to make integrated photonic (quantum) circuitry and optomechanics devices. For fabrication, we use the clean room facilities of the Center for Nanotechnology and Nanomaterials (ZNN) and the Walther-Meißner-Institute (WMI). All process steps are performed in-house, apart from dicing the 4-inch wafers into the individual chips of 6x10 mm, which we commission the company "CrysTec GmbH Kristalltechnologie" to. The arguably most important and crucial steps for making high-quality integrated circuits and nanomechanical devices are pattern generation, electron beam lithography, and both dry and wet etching. The patterns are designed with MATLAB® based on a gdsii toolbox from Ulf Griesmann which is further developed for our needs within the EQT-group. Electron beam lithography is performed at a "nanobeam nb5" from "NanoBeam Limited" and for dry etching a "Plasma Pro 80 Cobra" RIE with inductively coupled plasma (ICP) from "Oxford Instruments" is used. The most complex devices that we currently fabricate contain electrical contacts, optical circuitry, and mechanical devices. Each of them is defined in an individual lithography step including the corresponding preparations and subsequent fabrication steps. This chapter starts by explaining in Sec. 3.2 how we apply the nanofabrication methods to build such a device in the example of the so-called H-directional for which I developed the nanofabrication. The H-directional is a tunable directional coupler designed for quantum optics circuitry. Tuning is realized by altering the distance of two adjacent waveguides by applying a voltage to the electrodes of the device. Measurements on the H-directional are not discussed in this work, but it shall serve as an example in this chapter, as it includes almost all nanofabrication steps, that we have in our portfolio. As part of this work, I developed the nanofabrication for the H-directional. A finished device is displayed in Figure 3.7. Most of our devices, however, only contain some - but not all - of these steps. While working on the projects for this thesis some of the process steps have been reevaluated and changed or optimized. At the very first, none of these steps were applied by our group to this clean room environment, such that all of them were first tested and optimized as part of this work. "Optimizing" ranges from switching to different machines - as for example done for the electron beam writing and evaporation - over switching to other chemicals or adding marker protection to adjusting details in the process parameters - electron beam currents and trimming values - with sometimes large effects on the outcome. In Sec. 3.3 the most relevant optimizations, including their motivation and outcome are discussed. Some different types of samples - such as membranes for the test of mechanical properties or ring resonators for the purpose of 2nd harmonic generation of single photons - include a sputtering step of AlN. The manufacturing of superconducting nanowire single-photon detectors (SNSPD) in contrast requires sputtering of materials like NbTiN. Applying these processes is currently in progress and will not be described in this thesis. The chapter closes with Sec. 3.4 by describing the steps to mount and connect the finished chips on a printed circuit board (PCB) for optomechanics measurements in the vacuum chambers.

3.2 Process steps

3.2.1 Wafer preparation

We start the fabrication of our chips with a 4-inch *wafer*. The substrate material of the chips covered in this thesis is a 525 μm layer of silicon. Both sides have a 3300 nm cladding layer of

[1]Note, that "5 nm" does not stand for an actual dimension but serves as a term for the current limit in semiconductor manufacturing [146].

SiO_2 grown and on top a 330 nm layer of Si_3N_4 - our material of choice for the photonic and mechanical devices. The deposition is done via LPCVD and the wafer is double-side polished. We purchase these wafers from "Active Business Company GmbH". Our samples typically have a size of 6×10 mm and can be diced from the wafer, either manually by scratching the cut lines with a diamond scratch and subsequent breaking of the wafer (which will result in a cut along the scratch), or by getting the whole wafer diced with a wafer saw. The latter is our preferred method, not only because dicing the chips manually is quite time-consuming and produces scraps whenever a cutline has not been scratched properly; but the professionally diced chips are also very precise in their dimensions - which is crucial whenever they have to fit in a matching holder, e.g. during electron beam lithography or evaporation - and the side faces are perpendicular to the surface. The latter clearly improves the grip when handling the chips with a tweezer and reduces the risk of damaging the chips during the process. We send the wafers to "CrysTec GmbH Kristalltechnologie" for dicing. Before we do so, the full wafer is **patterned** with gold structures and covered with S1805 resist to protect the delicate surface. The patterning of the gold structures works as described below for the application of the electric parts to the chip. These structures are shown in Figure 3.1 and serve several purposes: crosses between the chips mark the cut lines for dicing the chips. A triangle marks the lower left corner of the chips to define its orientation. Each chip has a name referring to the wafer it's coming from and a unique number. In this step also the markers for positioning during the various lithography steps are applied. They have a square shape with a side length of 20 μm. In each of the four corners of the chip are three markers for redundancy. In each corner also a cross-shaped structure is applied, to evaluate the alignment precision of the individual lithography steps. For completeness also the frame and logo shall be mentioned here.

The writing time on PMMA resist for a full wafer with a dose of 9.0 C/m^2 and beam current of 3 nA takes over 10 hours for basically two reasons. Firstly, the total area to be written is very large compared to the patterns usually written on single chips, and secondly, the pattern is divided into so-called main fields - square areas with a typical size of 400 μm to 500 μm^2 - and has to mechanically move to each main field with a pattern in it. For example, writing a full wafer with $\sim$ 120 chips with a main field size of 500 μm takes nearly 8.5 hours of writing time and around two hours for moving and settling the stage. The latter cannot be efficiently reduced as one can either increase the main field size or rearrange the pattern such that fewer main fields contain a pattern. Both are already optimized for low beam deflection[3] and reduced main field stitching[4]. The writing time, however, can be drastically reduced by writing the large and not crucial areas like visual markers and text with high beam currents - e.g. 20 nA - and only the markers used for aligning the different subsequent lithography steps with the lowest possible beam current $\sim$ 1.3 nA, i.e. highest precision. This reduces the total writing time to $\sim$ 3 h for the visual pattern and $\sim$ 2 h for the markers (15 min exposure time). The writing time should not only be reduced as these kinds of machines are usually heavily used by many groups and users but more importantly, as effects like mechanical drift of the stages, thermal drift, and other instabilities are reduced. This is beneficial, especially for the crucial patterns, which are thus written all together in the same step. Only subsequently the remaining time-consuming steps, like the huge visual markers, are written and sped up by increasing the beam current.

Development is performed by placing the wafer for two minutes in a solution of 3 parts de-ionized (DI) water and 1 part Isopropanol (IPA), cooled down to $5°C$. Onto the wafer a 5 nm

[2]The maximum possible size at this machine is 1000 μm, however giving rise to imprecisions due to the large deflection of the beam.

[3]Ideally, the beam hits the sample along its normal axis to minimize focus errors and the proximity effect. The larger the main field size, the larger the beam angle close to the edges. It is thus favorable to set the field size rather small.

[4]When writing the contents of a new main field, the stage has to mechanically move to the new position. This implies the risk of introducing tiny positioning errors between neighboring main fields, so-called stitching. It is thus favorable to set the main fields large enough, such that no critical structures cross the boundaries.

adhesion layer of Chromium and 50 nm layer of gold are **evaporated** and subsequently **lifted off** in a bath of heated Acetone (Ac). The details are described in the following paragraphs about evaporation and liftoff.

Before the wafer is covered with **protective resist** S1805 and sent out for dicing, the markers are covered with **SU8 resist** to protect the gold markers during RIE etching. Chips that undergo several lithography steps will be etched in one step and later the same markers are used to align the different layers with respect to each other. Etching unprotected markers gives rise to potential misalignment of the different layers (see Figure 3.2).

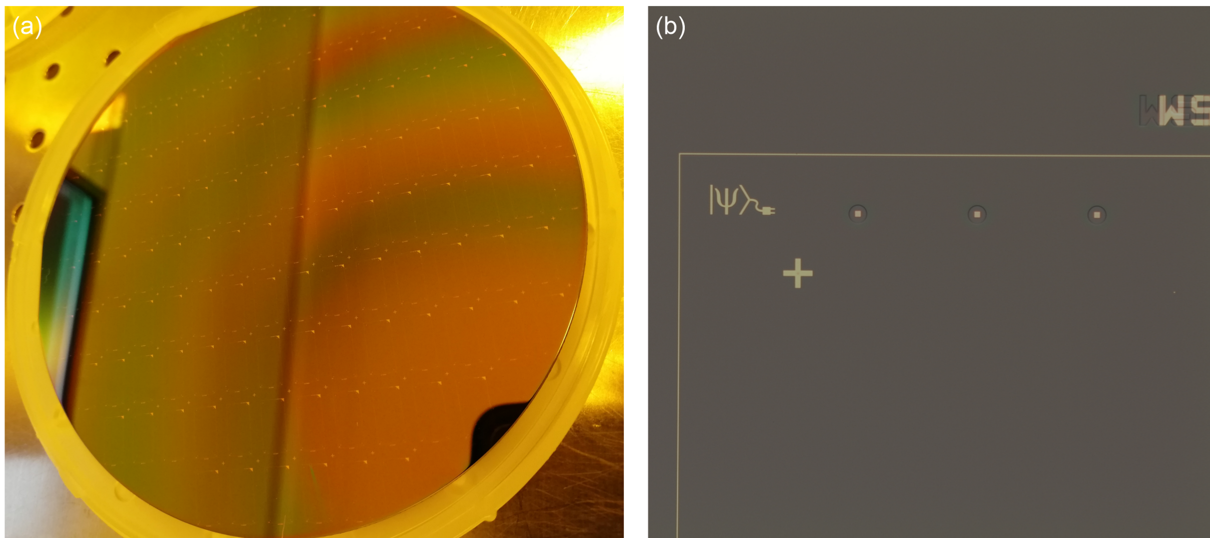

Figure 3.1: (a) Image of the full wafer in its transport box, ready to be sent out for dicing. The gold patterns defining the chips are visible. (b) Upper left corner of an empty chip with the gold pattern. Visible in this detail are the frame, square e-beam markers, an alignment cross, our group logo, and parts of the unique chip name. When looking closely, the SU8 covering the markers can be resolved as well.

3.2.2 Lithography steps

Figure 3.3 shows the main process steps of the Hdirectional. Panel (a) symbolizes a chip that is taken from the wafer box with diced chips and prepared by **stripping** it from its protective resist in an ultrasonic bath with Acetone. The chip is dried and cleaned from organic residues for three minutes in an Oxygen plasma in a plasma asher. This can in principle also be done by placing the chip for 10 minutes on a hotplate at 180 °C. **Coating** is done by applying a few droplets of PMMA resist to fully cover the chip and then spinning the chip on a spin coater for two minutes at a speed of 4000 rpm. Then the resist is baked for 2 minutes at 180 °C on a hotplate to harden the compounds.

In Figure 3.3(b) the **pattern** for the gold electrodes is written. The writing step is performed as described above for the full wafer. To place the pattern inside the golden frame, alignment is done with respect to four of the square markers, shown in Fig. 3.1(b), each in one corner of the chip. After manually driving to these markers, each of them is precisely located and focused by the nanobeam. The lower left marker defines the position of the pattern on the chips, the lower right marker defines its rotation, and the two upper markers correct for shear and keystone. In this step, the electrodes, contact pads (to later apply a voltage via an electrical probe), wires (to connect the electrodes with the contact pads), and additional markers are written. Additional markers are needed, as the region around the markers used in this step will be developed as well and subsequently covered with gold, thus cannot be used anymore in the following lithography steps. One cannot simply use one of the two spare sets of markers as it is imperial to have a very

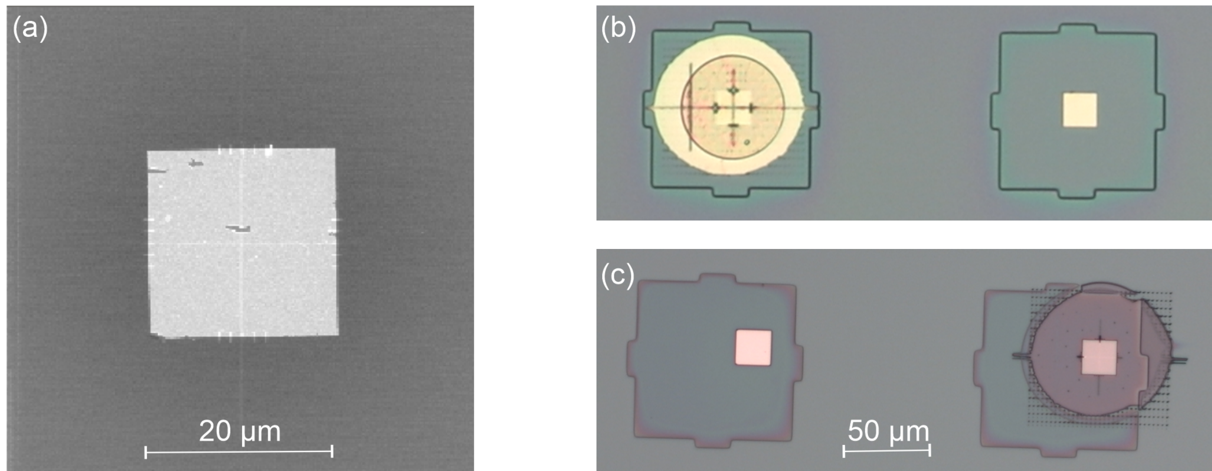

Figure 3.2: (a) Gold marker unprotected during reactive ion etching. The five linear signatures crossing each edge result from the automatic marker search and focusing of the e-beam writer. (b) Unetched gold markers covered with SU8. The left marker was used to align the pattern, later used for evaporating the metal pattern, and is thus covered with gold in the exposed region. The right marker was not exposed in this lithography step and the gold (applied during this second evaporation step) lifted off completely. (c) Gold markers protected with SU8 during reactive ion etching. The left marker was not exposed to the electron beam and was additionally covered with ZEP resist. The right marker was used for alignment and only protected by the SU8, still, the gold is undamaged. Note that the alignment between SU8 and marker is not perfect, however within tolerance as the marker is fully covered.

precise alignment of the different lithography steps, and the different sets of markers might have a tiny mismatch. Thus, in the following alignment steps, only the additional markers written in this very step will be used.

The electron beam writer requires several settings, optimized for the specific task, that have high impact on the outcome of the pattern. These will be described in detail in Sec. 3.2.7.

Development of the exposed PMMA is done as for the full wafer by placing the chip in a cooled developer (1:3 IPA-DI water) and then rinsing it with IPA and blow drying the chip with N2 gas. A developed pattern is shown in Figure 3.4.

3.2.3 Evaporation

The next step is the **evaporation** of the metallic components, here electrodes, wires and contact pads (and the additional alignment markers) out of gold. This is sketched in Figure 3.3(c). To improve adhesion, we first evaporate a sticking layer of 5 nm Chromium onto the SiN. Only then the gold layer with a thickness of 50 nm is evaporated. Besides Cr also Ti is often used as an adhesion material, however it is not resistive against hydrofluoric acid that we use to release the mechanical structures which is why we decide for Cr in our process.

The Cr-Au layer is now covering the whole chip - either on top of the PMMA or sticking to the chip following the defined pattern. By placing the chip into a heated bath of Acetone - the so-called **liftoff** step - the PMMA goes off and removes the unwanted gold. The process is accompanied by sonication in an ultrasonic bath. This is done until one can visually see that the gold is fully lifted off. This process typically takes only minutes but can take hours or days if the Acetone is not effectively dissolving the PMMA. It is important to choose a low enough ultrasonic power and time to lower the risk of damaging the remaining gold structures, but long enough to make sure all the other gold and PMMA came off. Once the sample is taken out of the bath, any remaining gold sticks to the surface and cannot be removed later. Figure 3.5(a) shows an example of a too-short liftoff where gold residues are still sticking onto the wires on

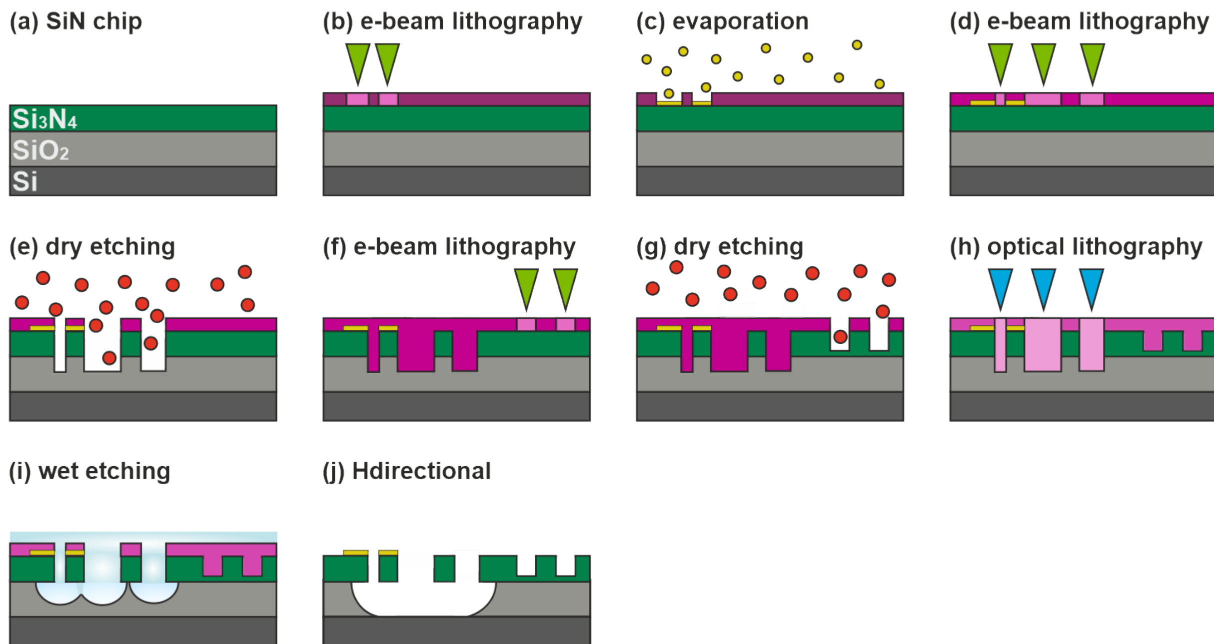

Figure 3.3: Schematics of the main nanofabrication steps for the Hdirectional. (a) The blank chip after being stripped from the protective resist with layers of 330 nm Si_3N_4 (green), 3300 nm SiO_2 (light gray) on Si substrate (dark gray). (b) Electron beam lithography on PMMA resist to create the mask for metallic structures. (c) Evaporation of gold to create metallic structures, e.g. electrodes. (d) Electron beam lithography on ZEP resist to create the etch mask of the simultaneously photonic and mechanical structures. (e) Dry etching with ICP assisted RIE through the 330 nm thin layer of Si_3N_4 around 70 nm into the SiO_2 cladding layer. (f) Electron beam lithography on ZEP resist to create the etch mask of the purely photonic structures. (g) Dry etching with ICP assisted RIE around 300 nm into the Si_3N_4 layer. (h) Optical lithography on AZ resist to create etch masks for the subsequent wet etch. (i) Wet etch with buffered oxide etch (BOE) to release the mechanical structures defined in step (e). (j) The finished sample, ready to be studied.

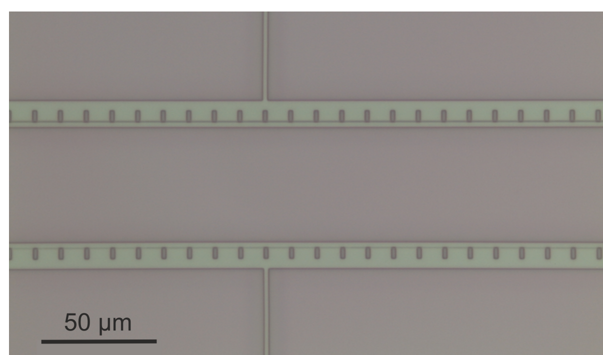

Figure 3.4: Optical micrograph of a developed pattern. Shown are the structures of the two future electrodes of a H-directional device written on PMMA.

the chip. Panel (b), in contrast, shows broken wires. The gold either came off due to too strong sonication or was never applied - which can happen if the PMMA was not properly developed before evaporation. Then a few nm thin layer of PMMA might still be present on the surface before the gold is applied and subsequently removed together with the gold during liftoff. This can be avoided by adding a descum (c.f. Sec. 3.3.3) step after development.

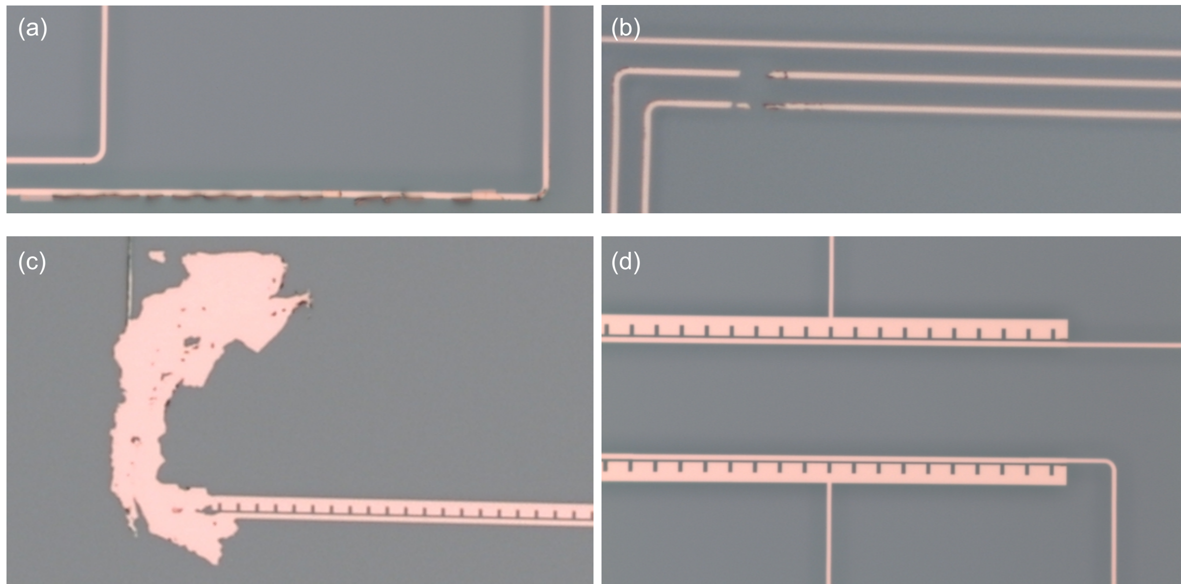

Figure 3.5: Gold structures after liftoff. (a) Wires sonicated too short: some gold is still sticking to the wires. (b) Broken wires, no electrical connection will be possible. (c) Unwanted gold that could not be removed during liftoff is remaining on the sample, covering the wires and electrodes. This is creating a short in the circuits and will prevent mechanical structures from proper release. (d) Electrodes and wires are properly lifted off, and no damage is visible. The width of the wires is $1\,\mu$m.

As mentioned above, the gold markers used for aligning the gold pattern are now also covered with gold. That is the reason why in the previous step also new markers were applied that will be used for alignment in the following lithography steps. In this example, two crucial lithography steps, each followed by reactive ion etching follow. Thus, as done for the full wafer the new markers will also be protected with SU8. SU8 is an optical resist and this step is not crucial in terms of alignment, such that it can easily be performed via an optical maskless aligner (MLA), which is much lower in resolution and precision than the e-beam writer. The only requirement is, that the markers are fully covered. Even though we have extra markers on each chip for redundancy, we avoid using a different set of markers in different lithography steps (unless they are applied in one of these steps as done here) to ensure the best possible alignment between the individual layers. Applying the **marker protection** includes the **spinning**, **writing**, **post-exposure bake**, and **developing of the SU8**.

3.2.4 Photonic and mechanical structures

After the gold structures are applied, the remaining steps concern the application of the photonic and mechanical structures. The photonic structures typically consist of grating couplers, waveguides, and interaction regions. The latter may, e.g. be photonic crystals or tapered waveguides. Many of our devices also contain movable parts (i.e. mechanical structures). The movable parts may be integrated into the photonic circuit, i.e. simultaneously serve as a waveguide. This is realized in Hdirectional or Racetrack-Synchronization devices (see Fig. 3.14(a) and (i), respect-

ively). But the movable parts can as well be placed only close to the waveguide and interact with the photons but (ideally) don't guide them, e.g. in the case of our Sbeams. Integrated optomechanical devices, like our membranes or cantilevers, are connected to free-space optics and do not involve integrated photonic circuitry but only contain the movable, mostly resonating, structure. The following nanofabrication steps describe the procedure for the Hdirectional, including both photonic and mechanical structures. These are typically formed in separate lithography steps, named "masked" and "through", respectively. The latter defines the mechanical structures by **reactive ion etching** fully through the silicon nitride into the cladding layer (Figure 3.3(e)) and thus allows the later release by underetching the mechanical parts (Figure 3.3(i)). The masked step, in contrast (Figure 3.3(f,g)), leaves about 30 nm of silicon nitride to protect these structures from being released. This is ensured due to the high selectivity of silicon nitride to silicon dioxide when exposed to buffered hydrofluoric acid, which is 128 in our case.

Another way to protect purely photonic structures from being released is by defining "etch-windows" in an optical resist that cover all structures to be protected and only exposes the structures to BOE in the "window" regions (Figure 3.3(h)). This is especially useful when the remaining silicon nitride ended up too thin and may break through in the etchant or when the masked and through steps are combined into a single step by etching all the structures through and then defining the windows for the structures to be released. It is not mandatory for the masked and through steps to do them in a certain order or to combine them. Each way has different pros and cons and may differ from device to device. This is discussed later in 3.3.5.

Both the masked and through lithography steps follow the same procedure and only differ in the etching time during reactive ion etching. They begin with **coating** the chip with ZEP520A resist for electron beam writing. It is - as the PMMA - a positive resist, meaning the exposed areas will be removed during development. The chip is prepared the same as for the PMMA coating by plasma ashing or dehydrating and is then spin-coated with ZEP at a speed of 4000 rpm for two minutes and then baked at 180° C for another three minutes. Visual inspection under the microscope tells if the coating is even and clean. **Writing** again takes place at the nanobeam (Figure 3.3(d) through, (f) masked). In comparison to writing the metal pattern, ZEP needs a different dose of $2.0\,\mathrm{C/m^2}$ and maybe an adjusted beam current, depending on the size of the structures. Trimming turned out to be not necessary and thus the trimming factors for both main-field and sub-field trimming are set to 1.0000. We use Xylene as **developer** and hold the chip with a tweezer into the chemical. For one minute the chip is gently stirred. Then it is rinsed with - and subsequently stirred in IPA for about 20 s to rinse off the developer. The chip is then blown dry with N_2.

3.2.5 Reactive ion etching

Reactive Ion etching (Figure 3.3(e) through, (g) masked) is done with a recipe based on SF6 and CHF3 chemistries and optimized for our SiN structures. Optimized means, that the structures shall have vertical side walls, sharp edges, and smooth surfaces. Parameters to tweak are the gas composition and pressure, power settings of the RIE and ICP generators, but also the table temperature and etching time. This recipe is quite stable and has not to be adjusted between different runs. The etch rate for SiN, however, which is about 2 nm/s (c.f. Fig. 3.12), varies slightly and has to be adjusted. The machine is heavily used by different user groups, each working with different chemistries and materials. It is imperial that gas compositions and materials that can damage the machine or impact the functionality of our devices do not enter the chamber. Still, even the permitted materials influence the subsequent processes. This can be reduced (besides by running cleaning recipes) by running conditioning processes before etching the samples. Conditioning means, that the recipe runs for some time on the empty chamber to "condition" the chamber, e.g. this coats the chamber side walls with the desired atoms. However, the conditions will never be exactly the same, however during this conditioning run,

the subsequent etch rate can be estimated by comparing the so-called DC bias[5] with our database and using it to decide on the right etching time. Often, the DC bias during the following etch run is slightly higher than during conditioning by about 2 V which translates to about 5 to 10 nm deeper etch into the SiN for the masked etch. Figure 3.6 shows a scanning electron microscope (SEM) image of the cross-section of two adjacent waveguides.

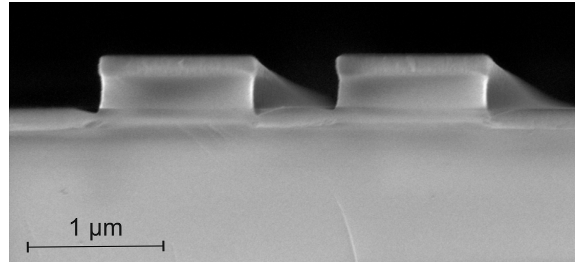

Figure 3.6: Scanning electron image of the cross-section of two adjacent waveguides out of SiN, here with a layer of AlN deposited on top. Figure taken by Timo Sommer.

The resist serves as the mask during etching and needs to be removed afterwards, a process called **stripping**. The sample is placed in a beaker with a strong solvent, like "ZDMAC", and sonicated for about 10 minutes at bath temperatures of 30 to 50 degree centigrade. Then, the chips are transferred to another beaker with Acetone while being rinsed with Acetone out of a wash bottle. It is again sonicated for a few minutes and then transferred to a third beaker filled with IPA for a last $\sim$ 1 min sonication. During the transferal, the sample is first rinsed with Acetone and then with IPA. Finally, the sample is taken out while being rinsed with IPA to remove the last remaining debris or ZEP residues and blown dry with a N_2-gun. After visual inspection under the optical microscope (OM), the sample is ready for the next steps, may it be another lithography step, release, or finally measuring the sample in the lab.

3.2.6 Release

As described above, it can be useful to define windows for the wet etch by a **maskless aligner** (Figure 3.3(h)). This protects surfaces that shall not be in contact with the etchant. Whether with or without further protection, we **release** the mechanical structures in buffered hydrofluoric acid (BOE) with surfactant 7:1, ensuring a constant HF concentration during the release. This step is sketched in Figure 3.3(i). The etchant etches SiN with a rate of 0.57 nm/min and SiO_2 with a rate of 76.5 nm/min.

After being taken out of the etchant, the sample is subsequently rinsed in two different beakers with deionized (DI) water to remove the etchant and is placed in a transport beaker with DI water. It is crucial, that the sample does not get dry at the surface, as the surface tension of the drying water implies the risk to destroy the delicate structures. A solution is the so-called **critical point drying**. The sample is placed in a chamber filled with Ethanol and is dried in several cycles of heating and cooling and filling the chamber with CO_2 under pressures of up to 50 bar. The goal is to bring the Ethanol from its liquid to its gaseous state without crossing the line of direct liquid-gas transition in its phase diagram. This is done by moving it around the critical point (hence the name) via its phase of supercritical fluidity. The highest risk in this step is contamination as dirt in the chamber or on the sample will be all over the devices after the process. Working very cleanly in this step is extremely important. This is usually the last step in sample fabrication before the finished sample can be admired and measured, and destroying the sample in this last step can hurt a lot.

[5]The DC bias is the bias between the upper electrode, applying the HF field, and the lower electrode, i.e. the sample table. It is measured by the machine and results from the machine enforcing the set recipe parameters.

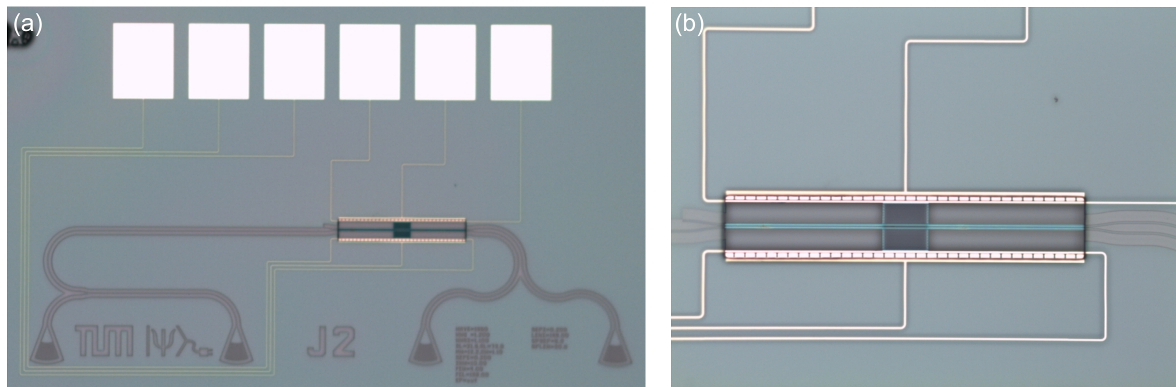

Figure 3.7: Finished Hdirectional device. (a) The full device, (b) zoom into the directional coupler region. The distance between the grating couplers is 250 μm and the length of the coupling region is 168 μm.

3.2.7 Electron beam writing

Before we conclude the description of the fabrication steps, let us take a closer look at the electron beam lithography step, introduced above. The electron beam writer enables us to write structures of the size of several hundred micrometers down to a few 10s of nanometers. Besides the resist, also the type and size of structures influence the best set of process parameters. The ideal dose, measured in C/m^2, is obtained by a dose test: a test structure is written with a large range of different doses and then developed. Under the optical microscope, it will become visible which dose suits best. For an increasing dose, large structures first become fully developed as many stray and secondary electrons will take part in the exposure of the desired structures. But they also cross at the boundaries, at the edge of the structures, which shall be sharp in the ideal case. Thus, increasing the dose even further leads to less pronounced edges. Small structures, however, have their transitions from under, over ideal, to perfect exposure at little higher doses. Underexposure at the boundaries of sub-structures, written consecutively[6] can for example lead to ridges in thin structures, like electrical wires or grating couplers (Fig. 3.8(c)). This can be solved by tweaking the trimming value. A trimming value of 1 leads to writing the structure exactly to the edge of a sub-structure. If there is a small mismatch when writing these sub-structures one after the other, the structures might not be perfectly connected. Trimming values larger than 1 lead to exposure slightly over the edge. In contrast, stray electrons might anyways expose further than the boundary and lead to badly pronounced edges. In this case, a trimming value smaller than 1 corrects for it. The right settings depend on the specific structure to be written and have to be tweaked if necessary. Trimming values can be set for each, the main field and the subfield. Usually, it is sufficient to find a good compromise for the ideal dose. If further precision is needed it can make sense to use additional software (a powerful tool, that we have at hand is the Genesys Beamer Software) for Proximity Effect Correction (PEC). The pattern will be fractured into small sub-patterns, each with an adjusted dose, to reflect the effect of stray electrons on the resist, not to be exposed.

The selected dose is reached by exposing the structure with the chosen beam current for a certain time. The higher the beam current, the lower the exposure time. It is still not beneficial to always go for high currents ($\sim 10-20$ nA). Small structures and structures that are in close proximity of each other will not be properly defined if the beam current is too high. In our case, this leads to non-circular, shaped holes for the photonic crystal, such as those implemented in the block part of the Hdirectional devices, instead of the desired circles. An example is shown in

[6]Keep the words main field and subfield in mind. What that means will be revealed below.

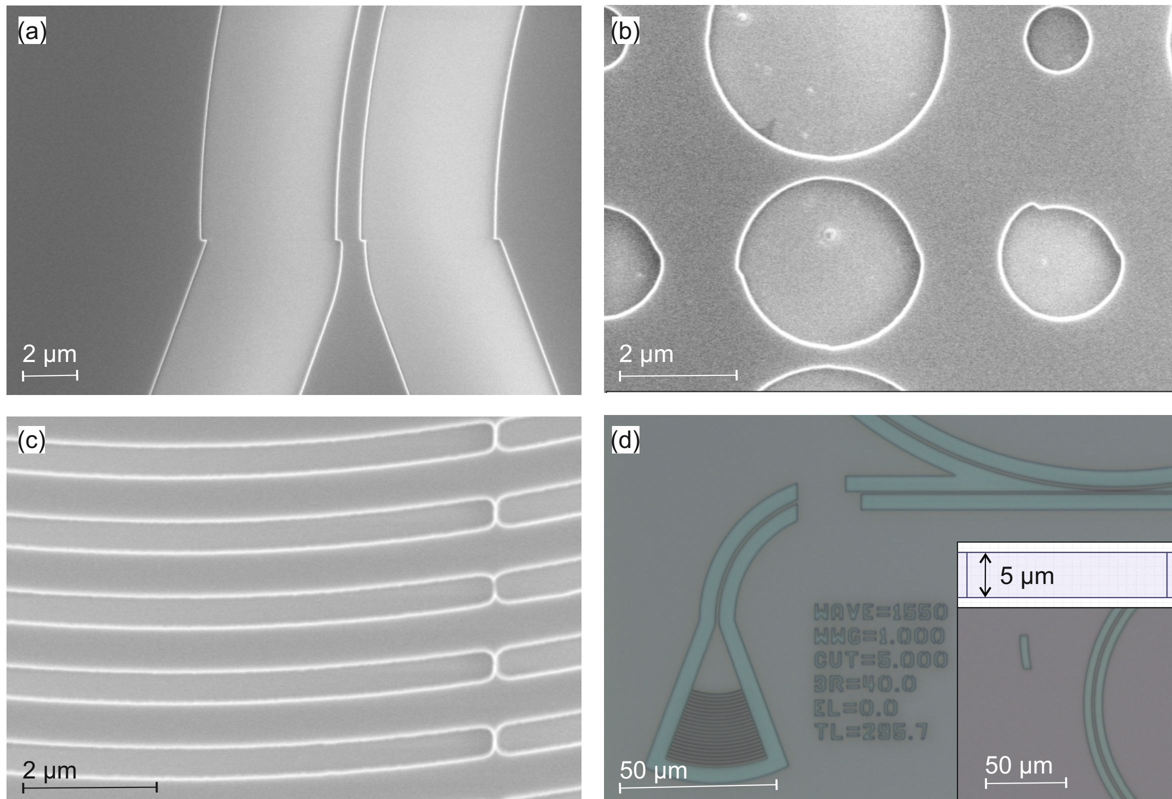

Figure 3.8: Potential issues in electron beam writing. (a) Stitching errors between neighboring main fields result in a horizontal shift between the grating coupler and waveguide. (b) Non-circular photonic crystal holes due to too high beam currents. (c) Ridges in the grating coupler structure due to underexposure. (d) Missing subfields due to 1-dimensional structures in the pattern file, not corrected by the merge function. Insets: (top) One-dimensional structure as appearing in the gds file on the gap next to a waveguide. The features in this image have been enhanced for clarity. (bottom) Example of such a subfield written at a random location on the chip instead.

Fig. 3.8(b). The solution is to select the lowest possible beam current ($\sim 1\,\mathrm{nA}$) at the expense of writing time. Which currents are available varies from run to run and depends on the calibration of the machine, done right before writing the chips. A detail, that shall not be further explained here, is the alignment of the beam, which can be optimized for small stitching errors (vertical beam landing) or low off-axis deflection aberrations ("optical" beam landing). The latter option is preferable for small structures and is available for small beam currents in the database of the machine. Switching to small currents with optical beam landing solved our issues with the non-circular photonic crystal holes.

As mentioned above, the full structure is fractured into smaller sub-structures: the main fields and subfields. While writing, the electron beam is deflected to follow the pattern. In the center of a main field, the beam hits perpendicular to the sample surface. The further the beam is deflected towards the edges of the main field, the higher is the angle. When a full main field is written, the stage mechanically moves to center the beam over the next main field. A typical main field size is around $400\,\mu\mathrm{m}$. If possible, a structure on the chip should not cross the borders of a main field, as this is a typical source for misalignment when the stage does not perfectly settle at the next position. We are talking about the precision of several 10s of nm reached by a mechanical stage! The main field is further divided into subfields. After one subfield is fully written, the beam deflects to the next. Here, the stage is not moving. A typical size for subfields is $20\,\mu\mathrm{m}$. Our devices are much larger than that (two grating couplers have a distance of $250\,\mu\mathrm{m}$), thus crossing many subfields. This is unavoidable and usually not a major problem, but so-called subfield stitching errors can appear if the neighboring subfields are not perfectly aligned with respect to each other. To reduce the risk, subfields should only cross, e.g. a waveguide, and not divide it along its length. It is possible to tweak the sizes of the (square) main fields and subfields and apply an offset with respect to the $(0,0)$-location.

We create our patterns with Matlab in the gdsii file format (.gds). To make it readable by the electron beam writer, we first have to convert it with the software "nbpat" to a so-called pattern file (.npf). With this software, e.g. the layers to be written in this run and the main field and subfield dimensions are selected. Another important functionality is the so-called "merge". Our gds files contain many 1-dimensional structures, i.e. lines, (see inset of Fig. 3.8(d)) that in principle should not influence the pattern to be written. However, the more of these structures are present, the higher likely it is that a few of them create issues as shown in Fig. 3.8(d), i.e. subfields are not written at the correct but random nearby location. The appearance of this error can be drastically reduced by "merging" the structures, separated by these lines. After applying this functionality, the number of remaining unwanted lines is strongly reduced. Figure 3.4 shows a pattern that does not suffer from any of the above-mentioned issues and came out very nicely.

3.2.8 Inspection

Inspecting the devices helps to target issues in the fabrication process and faulty devices and helps to learn which steps can be improved. Doing so after every nanofabrication step avoids the situation that one keeps fabricating a chip that should have been discarded earlier within the process because some mistake was made and a step did go wrong. The fabrication processes are quite complex and delicate, so this happens regularly. The fastest and most often performed analysis method is the inspection under the **optical microscope** (Fig. 3.9(a)). These images can be taken fast with usually sufficient resolution. It can be done easily between different nanofabrication steps and reveal contamination, broken devices, or issues in the pattern.

Also measurements with the **reflectometer** (Fig. 3.9(d)) are done regularly. This gives information about the thicknesses of the SiN and SiO_2 layers. This information is very useful to check the etch depth after etching with the RIE and tells if re-etch is necessary or if etch windows need to be applied to avoid breakthrough during BOE.

Another useful device is the **profilometer** (Fig. 3.13). It measures the sample profile by scanning over it with a sharp tip and gives information about step heights, gaps, and gets the

profile of structures. This can either confirm the results from reflectometry or be used when reflectometry cannot be performed, e.g. when a refractive index is not well known or the feature size is smaller than the spot size.

Scanning electron microscopy (Fig. 3.9(c)) provides beautiful (as well as very insightful) images of the micro- and nano-world. We use it to visualize the device surface and cross-section. Especially when looking at the released and therefore delicate optomechanical structures, SEM tells us if there is structural damage and if devices are fully released. It furthermore gives information about contamination of the devices and we can measure the device dimensions. The latter gives us a number at hand for lateral etching during the RIE process and provided essential information on the stress relaxation of our Sbeams, discussed in detail in chapter 6. We aim for obtaining SEM images only after the chip has been measured in one of our setups as SEM holds the risk of electrical charging and carbon depositions that might influence the dynamics of the devices.

Atomic force microscopy (Fig. 3.9(b)) also provides information about the surface structure and roughness of the sample. E.g. for comparing the influence of the wet etch on the smoothness of the different surfaces.

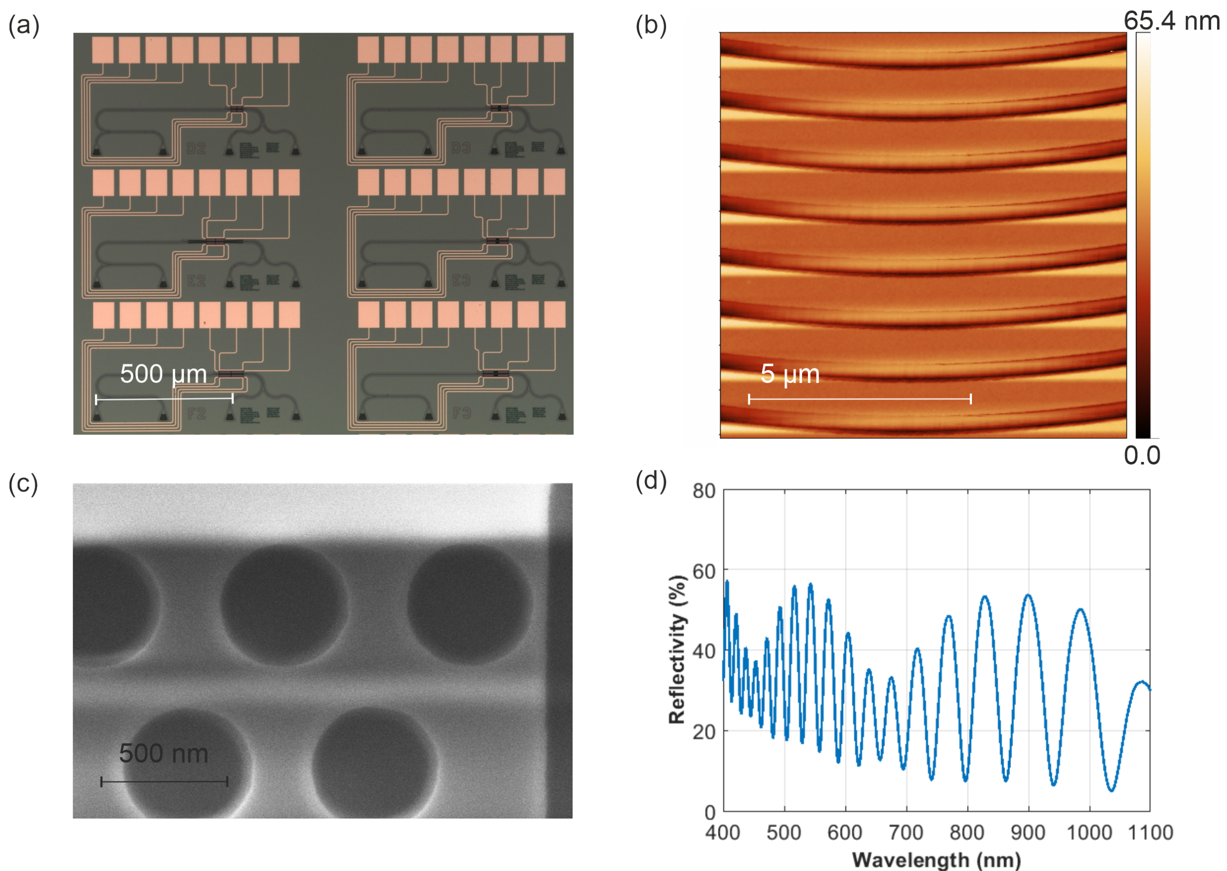

Figure 3.9: Sample analysis using different techniques. (a) Optical microscope image of an overview over several full scale devices. (b) AFM image zooming into a part of a grating coupler providing information of the height profile. (c) SEM image of the holes of a photonic crystal pattern of a Hdirectional device. (d) Reflectometer measurement of a SiN layer on SiO_2 on Si substrate. Displayed is the reflectivity of this layer stack over the wavelength.

3.3 Optimization of nanofabrication

The nanofabrication processes need to be regularly re-evaluated and optimized to get high-quality devices. For example, the optimal dose can change over time. Aging resist can change its viscosity and thus its thickness after spinning. This might require an adjusted spinning speed or dose. New bottles of resist might as well have slightly different properties and require adjustments in the respective process parameter. But also other nanofabrication steps have been optimized over time. In this section, new findings and "lessons learned" that lead us to improve the processes over time are described.

3.3.1 Wafer dicing

Dicing the wafer is best done by a professional company. A 4-inch wafer gives us roughly 100 chips with our preferred size of 10×6 mm. The costs lie well below 100 € per wafer. Dicing the wafer manually is very time-consuming and the result is never as good as when it is done with a wafer saw. The break-line is first scratched with a diamond scribe. This can be done at a cutting table, with a stage, positioning screws, and a mounted scribe, or with a similarly well outcome with a triangle ruler and a handheld scribe. In both cases, the wafer or piece of the wafer is broken along the scratch. This mostly works properly, but whenever it does not, scraps are produced. As breaking the wafer requires applying some pressure, there is a relatively high risk that these scraps damage the delicate sample surface even though it is covered with protective resist. And the sample dimensions are typically not as precise as when diced professionally, however, the tolerance of the nanofabrication machines is typically big enough, such that this is not a major problem. Another benefit of a wafer saw is the resulting perpendicular edges, which makes the sample much handier to grab with tweezers. Broken edges typically have an angle and the risk of losing the sample or flipping it when moving it in or out of a beaker is strongly enhanced. Anyone who lost an almost finished sample after days of fondly preparing it in one of the last steps appreciates a good grip with the tweezers.

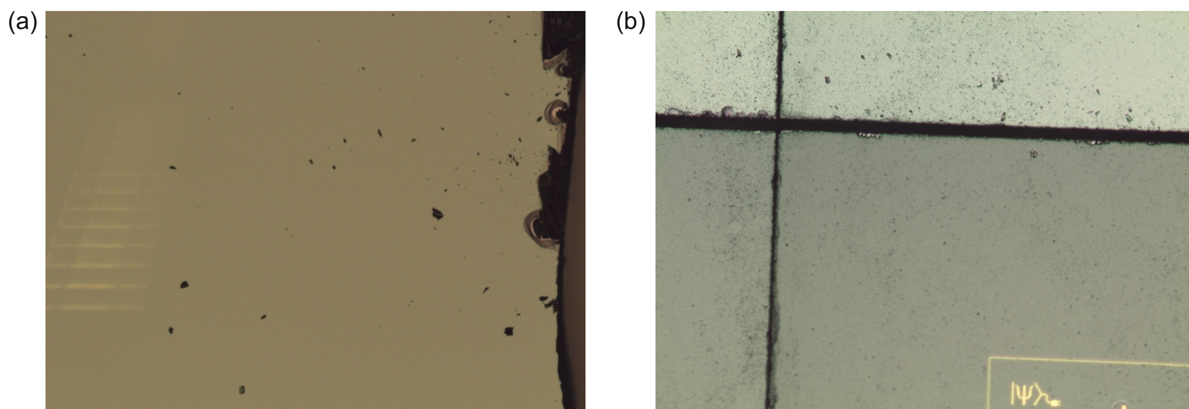

Figure 3.10: Chip diced (a) manually with a diamond scribe and (b) with a wafer saw.

3.3.2 Precision of the marker positions

The alignment of the pattern of subsequent lithography steps is done by automatically positioning and focusing the square gold markers. This needs high precision to get the best possible alignment of the different layers. In some patterns the route of the photons consists of waveguides written in different steps (e.g. when parts of the path are released), a tiny mismatch between the layer can thus dramatically increase the scattering and loss of the light at the interfaces. We thus always use the same set of markers in subsequent writing runs to avoid mismatch in case the

different sets of markers are not perfectly aligned with respect to the other. The precision of different positioning attempts can be read from the logfiles that are created by the machine and scaling, shear, and keystone of the pattern can be obtained. A test run[7] with repeated positioning shows a maximum mismatch[8] of only 8 nm for the worst marker when performing 10 subsequent runs. The deviation of the autofocus of these runs corresponds to $\sim 500\,\mathrm{nm}$ which is four times better than what is considered as "good" by the machine manual[9]. The precision of different runs can also be checked with an optical microscope or an SEM as shown in Fig. 3.11 for very good precision (a) and large mismatch (b). An analysis with the SEM where the deviation of an auxiliary pattern (written together with the devices) from the gold crosses (written together with the alignment markers) was performed as well[10]. A cross is present in each corner of the chip and surrounded by the auxiliary pattern of two different lithography runs. The mismatch in some regions was low enough to be unresolvable with the SEM, while the largest observed mismatch was 380 nm, which is quite large, given that the waveguide width is typically $1\,\mu$m and for some chips, the waveguides of two different runs have to align with each other. A way to improve the alignment is the protection of the markers during dry etch. If the pattern shows different deviations at the crosses in different corners, this is a sign not only of a shift in the pattern but also of rotation, shear, or keystone. An analysis returned a stretching of the pattern over the whole width of the chip of up to $13\,\mu$m[11]. The pattern deviated from a perfect rectangle (orthogonal x- and y-axis) by 0.34 degree. The maximum measured rotation of the pattern with respect to the crosses was less than 0.8 degree. As a further consequence of the variations in the quality of alignment, which often turned out very well but sometimes rather bad, we applied an additional step to the fabrication routine of our wafers and cover the markers with SU8. But not only imperfections in the alignment and imperfections in the alignment markers play a role in the mismatch. The temperatures before and after the lithography runs were tracked and gave an expected thermal expansion of the distance between two horizontal markers of up to 13 nm. The thermal expansion can play a role, both when writing the actual devices, but also already when the markers are written on the whole wafer. In the latter, the exposure time is much longer and a thermal expansion of half a micron over the whole wafer was estimated. This can be reduced by writing the extensive visual layers of the gold pattern in a different step than the gold markers. Thus the gold markers are written in a much shorter time period and experience less thermal expansion. This is by now applied to the fabrication routine.

3.3.3 Descum

As Fig. 3.5 showed, the evaporation and liftoff of the gold are also not trivial. Panel (b) shows the situation where parts of the gold wires came off, electrical contact via these wires is not possible anymore. The reason can be, that after development, a thin layer of resist of just a few nanometers might remain on the surface and keeps the gold from sticking properly. It can thus be a good idea to add a descum step between the development and the evaporation. This is simply an ashing step with oxygen plasma of a few seconds and removes any thin layer of organic residues on the SiN surface.

3.3.4 Reactive ion etcher

Reactive ion etching is done by running a recipe, optimized for the specific material and structure. The recipes typically follow a certain structure. They start with a pump-down step, providing a proper vacuum of around 10^{-5} mbar followed by a step of letting the gases into the chamber,

[7] The test was performed on sample WSN03_67.
[8] The mismatch was calculated from the position parameters, returned by the machine.
[9] Version v2018-08-27.
[10] These tests were performed on the chips SN034 and SN053.
[11] This analysis was performed on the chips WSN03_29 and WSN03_58.

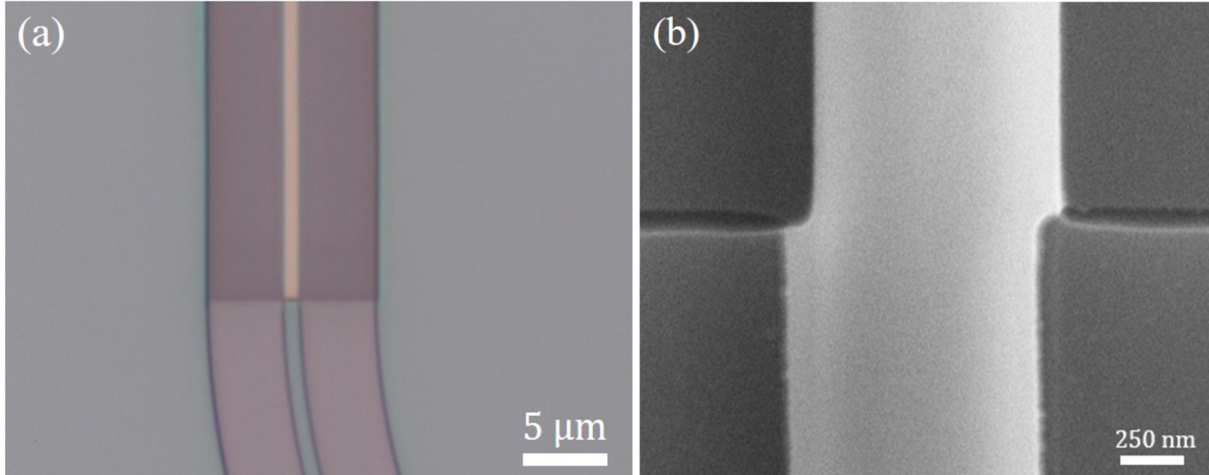

Figure 3.11: Alignment of the ring resonator and suspended beam (i.e. the through and masked layer) on our racetrack devices. (a) No mismatch of the layers is visible. The figure is taken with an optical microscope. (b) Large lateral shift between the layers. The figure is taken with an SEM. Both panels are taken from [137].

stabilizing the gas flow. Often a "strike" step is necessary to ignite the plasma. This is not always needed, if the powers and gas pressures of the etching recipe are high enough, the plasma ignites anyways but if not, a few seconds of striking are needed. The strike step has in principle the same process parameters as the etch step, but with higher power and/or gas pressures, before regulating them down to the values of the recipe. The process parameters and gas chemistries are optimized for the materials and structures they shall etch. In this work, we stick to one recipe, optimized for integrated photonic and mechanical structures out of SiN on SiO_2. The etch depth is set by setting the proper etch time. The etch depths over time for SiN and SiO_2, respectively, are plotted in Fig. 3.12, once measured by the ellipsometer (a) and once measured with the profilometer (b). Both results match nicely. It becomes clear from the plots that both materials have different etch rates. The etch rate of the recipe on SiN is $\sim 2\,\mathrm{nm/s}$ and of SiO_2 is $\sim 1\,\mathrm{nm/s}$. As mentioned above, the exact etch rate depends on the usage of the machine before the run, i.e. which other materials and chemistries have been etched before. This influence can be reduced by running chamber cleans and conditioning runs. Another influence on the etch rate is the thermal conduction to the table. The table is cooled by a constant He gas flow. The sample can be either just placed on the table, however, it is recommended to add a thermal connection. As often done in reactive ion etching, we use a droplet of Fomblin oil, that we place below the sample. The amount of oil slightly differs between different runs, which has little influence on the etch rate. If one wants to further reduce the variation, one can consider using a thermally conducting sticky tape instead of the Fomblin.

3.3.5 Optimization of process flows

Devices with both optical and mechanical structures undergo several lithography steps, namely, "masked" (used for photonic structures, not fully etched through the SiN layer), and "through" (used for mechanical structures, etched into the cladding layer). Optionally lithography steps to apply metallic structures (used for electrodes) and for the opening of etch windows (optical lithography, protecting structures during BOE or RIE) are performed as well. There are several options to structure the process flow: start with the masked and continue with through, or vice versa. Optionally windows can be applied next. Or, if all structures (both optical and mechanical) are etched through, the windows step is mandatory. The latter prevents mismatch between the masked and through layer due to different alignment at the electron beam writer. Using the

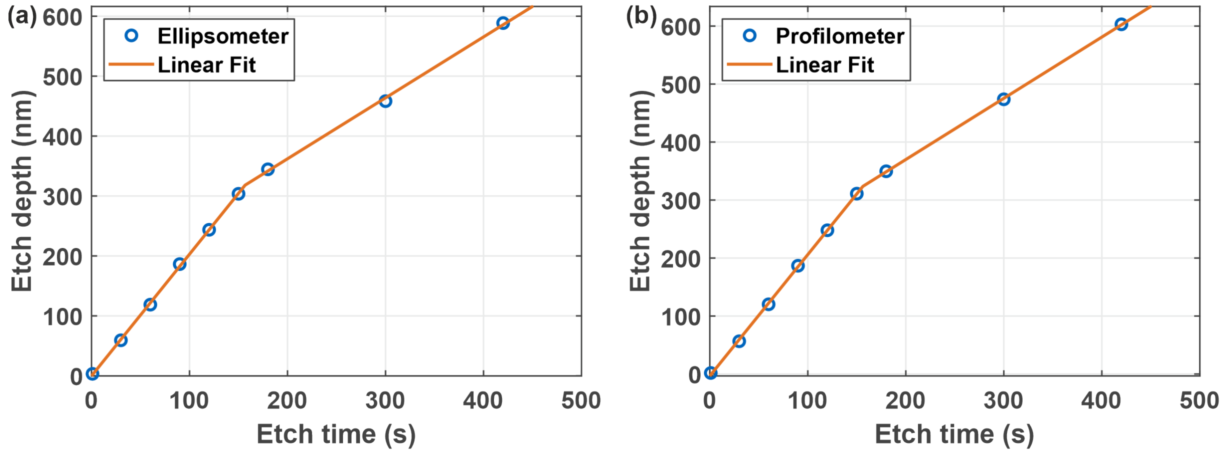

Figure 3.12: Etch rates of our inductively coupled plasma-assisted reactive ion etching recipe optimized for optical and mechanical structures on a SiN platform. Plotted is the etch depth into the material versus time, measured with (a) an ellipsometer and (b) a profilometer. The trend is linear with a little offset, due to the strike step, having a higher etch rate for a few seconds in the beginning. The kink in the data appears when the SiN layer is fully etched through and the SiO_2 starts being etched. The measurements and analysis were performed by Burak Yildiz [148].

same alignment markers in both steps, however, turned out to provide proper alignment. There is no final answer to which of these process flows provides the best outcome, it has to be decided for the individual task. In the case of beams integrated into racetrack cavities, it turned out to be favorable to first do the through and then the masked step. The reason is, that if the structures are already etched (masked), the resist is not evenly covering these structures. During the subsequent longer etch (through), the resist can break through at the edges of waveguides which then deteriorate. Hdirectional devices, in contrast, gave better outcomes when first doing the masked and then the through step. Here, the argument is, that if the through step was done first, the trenches next to the gold electrodes are such deep that in the following lithography run (masked), the resist does not cover the edges of the gold (55 nm above the SiN surface) thick enough, to protect them during the masked etch and the gold becomes deteriorated during RIE etching. Besides the additional gold layer on the Hdirectional devices, a further difference between these two projects is that a different bottle of electron beam resist (ZEP 520A) was used. The resist for the latter turned out to be slightly less viscous, leading to a different profile at the edges of the fabricated structures. This relatively small difference in fabrication made it necessary to swap the two lithography steps. Additionally, the relation between the spinning speed and the profile of the ZEP resist over already applied structures was studied. Figure 3.13 displays two measurements of this study. During the fabrication of the Hdirectional device, profilometer measurements were taken. The electrodes are already applied and the “through” etch is performed. Then ZEP is applied for the “masked” step with a spinning speed of 3000 rpm (panel (a)) and 2000 rpm (panel(b)). At the regular spinning speed of 3000 rpm the coating is very thin close to the edges of the electrodes and is expected to break through during the next etch. At the smaller spinning speed, the thickness is much larger especially close to critical structures.

It is in principle possible to also follow the “re-etch” scheme, where first, all structures (both optical and mechanical) are etched masked, and then optical photoresist windows are opened over the mechanical structures and re-etched (hence the name) in the RIE. This method avoids lateral mismatch between the masked and through layers (they are written in the same run), but as the structures to be released are not protected during the re-etch, they are also etched and create a vertical step at the boundary. Thus the latter method turned out to be not preferable.

More detailed discussions of the process flows can be found in the Master’s theses of Xiong

Yao [137] and Sarath Chandran [149].

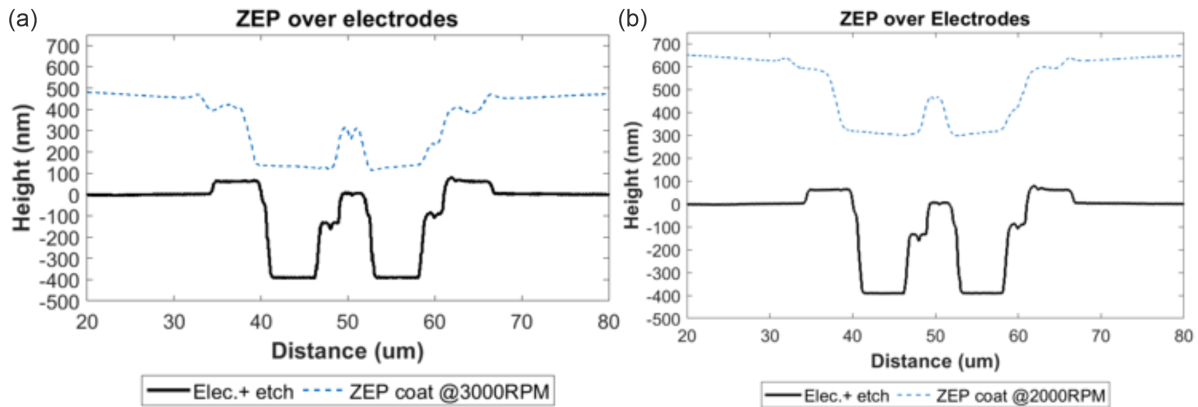

Figure 3.13: Profilometer measurements on a Hdirectional device covered with ZEP taken during fabrication. The electrodes are applied and the through etch is performed. Black: profile taken on the blank surface, blue: profile taken with ZEP applied at 3000 rpm (a) and 2000 rpm (b). The figure is taken from [149].

3.4 Post-fabrication

The finished chip is now ready for measurements in ambient conditions. It can directly be placed on the QMS setup and after approaching and aligning an optical fiber array (FA) optical transmission spectra like wavelength sweeps can be taken. If the sample, however, is to be placed in a vacuum chamber and mechanically actuated, it is mounted on a printed circuit board (PCB). In Figure 4.5(c), a close-up view of a chip on a PCB, mounted in a vacuum chamber is shown together with the arm of a fiber array placed over it. The actuation is done via a piezo element - a thin plate made of piezoelectric ceramics at about the size of the sample. This plate is covered with a thin layer of gold to facilitate the wire bonding and is electrically contacted from both the top and the bottom and placed underneath the sample. An RF signal applied to the electrical contacts is translated into the motion of the plate and "shaking" the sample and thus driving the mechanical devices of interest (more details in Sec. 4.6). This is realized by first gluing the piezo element onto the PCB with conducting silver paste. Then the sample is glued again with silver paste on top of the piezo. It is crucial to use such little of the silver paste that there is no electrical contact between the top and the bottom of the piezo to avoid a short. After each of these two steps, the silver paste is dried by placing the PCB on a hotplate and heating it at 100 °C for several hours. While the bottom of the piezo is glued to an electrically conductive area on the PCB, the top part is contacted by bonding a wire to both the piezo and the PCB. The electric signal can then be applied via an RF connector. To perform the measurements the whole PCB is screwed onto the sample stage inside one of the vacuum chambers. How these setups are designed and how measurements are performed is described in the following chapter.

3.5 Devices

This chapter is concluded with a brief introduction of the devices mentioned above while describing the nanofabrication steps. Two of these devices will be discussed in depth in the following chapters: membranes are discussed in Chapter 5 together with the application of the SVC for the efficient and robust mode shape mapping based on a phase-lock loop. Pre-displaced beams for the study of geometrical tuning of stress in these resonators are discussed in Chapter 6. Some of the other devices will come back in the following chapter, describing the setups, to indicate which

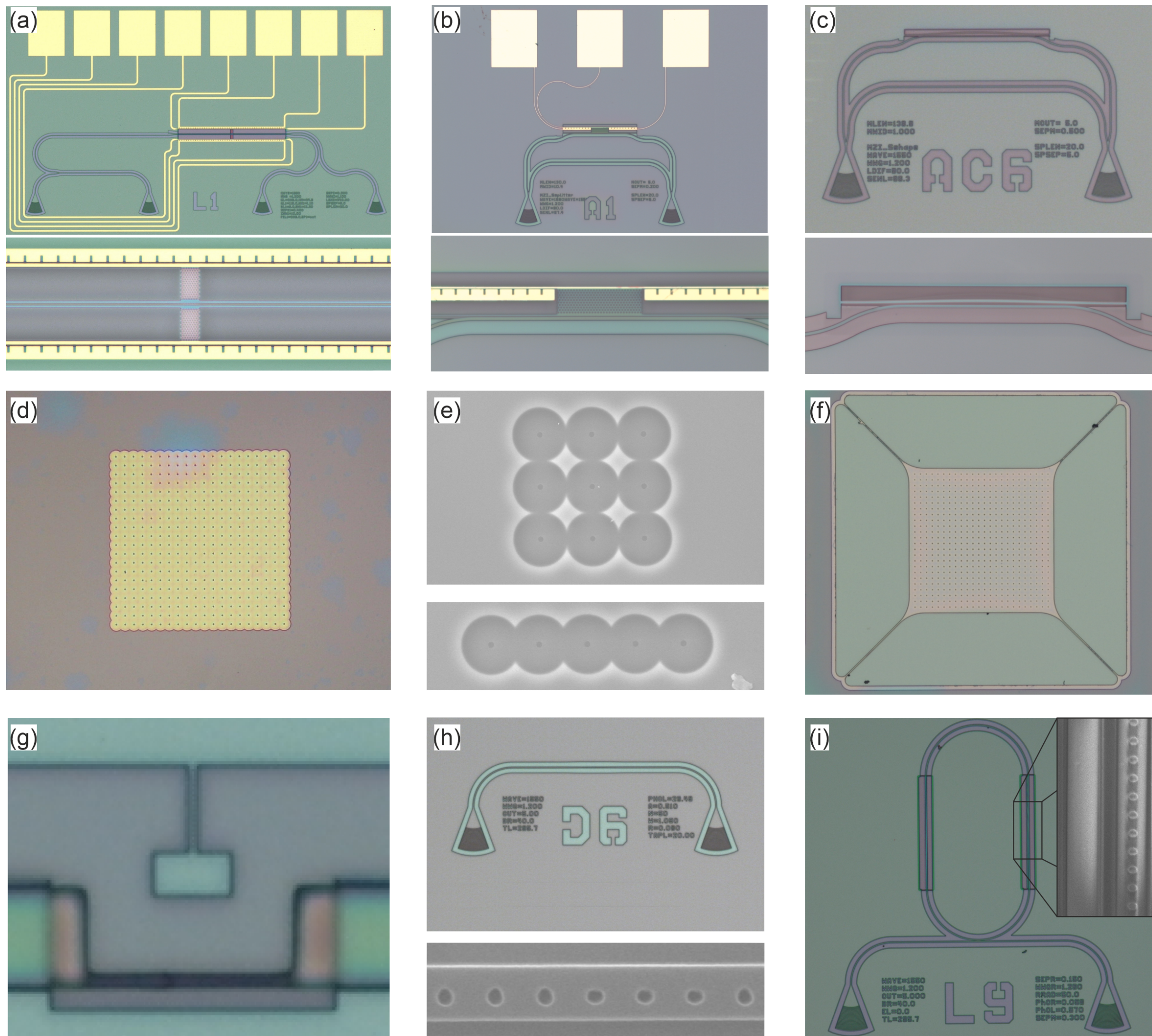

Figure 3.14: Devices that will be mentioned throughout this thesis. (a) Hdirectional, (b) Hresonator, (c) Sbeam, (d) membrane, (e) two-dimensional drum array (top) and one-dimensional drum array (bottom), (f) trampoline, (g) cantilever, (h) photonic crystal beam, (i) racetrack. The bottom panels in (a,b,c,h) show a zoom into the functional region of the respective device. The device dimensions are described in the text.

setup is the right tool to characterize the specific devices. The racetrack device already served in the previous chapter as an example when some principles of optomechanical measurements have been discussed. It will also be used as a complementary example when discussing some of the measurements in the following chapters.

Figure 3.14 displays the images of many of the devices studied in our group, however, it only displays a selection and is not complete. The Hdirectional (a) has been introduced above and is an electro-mechanically tunable directional coupler. A directional coupler is the integrated pendant to a beam splitter and allows to couple the light field (or single photons) from the original to an adjacent waveguide. The coupling ratio (probability)[12] is mainly dependent on the length of the interaction region of the waveguides and their distance. Also, the tapering region and mode confinement do play a role. When a medium that allows for propagation of the light reaches into the evanescent field of the mode coupling takes place. The coupling ratio is fixed

[12]When going from a light field to single photons the concept of the coupling ratio is replaced by coupling probabilities, for simplicity, in the following I will only use the term coupling ratio.

for simple static directional couplers. Placing heaters next to the waveguides, allows to tune the coupling ratio, however, suffers, e.g. from a low switching speed [150][13]. Instead, we are working on the Hdirectional for fast and repeatable switching (MHz regime). As already introduced earlier in this chapter the Hdirectional consists of two independent optomechanical devices, each in the form of an H. One arm serves as a waveguide and the other arm has gold evaporated on top to move the device in-plane by electrostatic forces. The two arms are connected with a photonic crystal patterned block. The photonic crystal is designed, such that it forms a band gap around the targeted wavelength of 1550 nm to ensure that light is not leaking from the waveguide arm into the block. To contact the electrodes by an electrical probe, contact pads (rectangular gold structures in the image) are placed above the device. Two of these devices are placed in a mirrored fashion, such that their waveguides are in close vicinity and build a directional coupler. Applying a voltage to the electrodes will push (pull) the waveguides closer together (apart). The bottom panel of (a) shows a zoom into the functional region of the directional coupler. In any device including grating couplers, the distance between two of the latter is 250 μm. Panel (b) shows a Hresonator device. The principle is very similar to the Hdirectional [144], however, only one H-shaped device is used and placed, e.g in the vicinity of one arm of an integrated Mach-Zehnder-interferometer. As visualized in Fig. 2.8(a), when the arm is reaching the evanescent field of the light passing through the waveguide, the effective refractive index, that the light "feels" changes, and the light passing this arm of the Mach-Zehnder-interferometer picks up an additional phase. This causes a change in interference when both arms recombine. Driving the device, i.e. periodically changing its distance to the waveguide, dynamically influences the intensity of the detected signal which allows measuring, e.g. resonance frequencies and quality factors. Placing particles, e.g. microspheres, on the resonator block, changes its dynamics and allows to sense these particles and to draw conclusions, e.g. about their mass. The bottom panel shows a zoom into the interaction region of the MZI and the Hresonator. Panel (c) displays the Sbeam device. The detection principle of the dynamics of this curved beam is analogous to that of the Hresonator. The bottom panel again shows a zoom towards the mechanical device. This device is the main actor of its own project on geometric stress tuning, extensively discussed in Chapter 6. Panel (d) shows a membrane consisting of an underetched SiN layer. The membrane is perforated with holes that serve as origins for the etching process. This membrane has a side length of 275 μm and will extensively be studied in Chapter 5. Panel (e) displays a two-dimensional (top panel) and one-dimensional (bottom panel) array of overlapping drums. The fabrication principle is analogous to that of the membrane, however, the distance between the etch holes is so far away that after the wet etch, they are not fully released and the boundaries of the drums are still connected to the substrate. Thus, such devices allow the study of the coupled modes of many drums, up to much larger arrays than displayed here. The diameter of each drum is 20 μm. Panel (f) shows a trampoline device, an underetched block, only held by four strings at its corners, connecting it to the bulk. The width of the block is 200 μm. In panel (g) a cantilever device can be seen. Exfoliating flakes of transition-metal dichalcogenide monolayers and placing them on the paddle allows for experiments on exciton generation. The dimensions of the paddle are 5 times 10 micron and its connection to the bulk is 1 times 10 micron large. A typical calibration device is shown in panel (h). It consists of two grating couplers connected by a waveguide with a width of 1 μm. As each chip is fabricated a tiny bit differently, also the transmission profiles of the grating couplers (see Fig. 2.2) will be different on each chip. Such devices are added to each chip and additionally allow for the compensation of the grating coupler transmission profile of the measured data of more complex devices [80]. The bottom panel shows that the specific device displayed here is not a pure calibration device but has photonic crystals integrated into the waveguide. The purpose is to study their band gaps and utilize them for

[13] A discussion of different types of tunable directional couplers and phase shifters can be found in the work of Sebastian Müller [150].

other devices like the racetrack device in panel (i)[14].

This racetrack device is basically a ring resonator with two beams integrated into the waveguides. The purpose is to study the dynamics of these beams and couple them purely by the optical field and finally synchronize their motion. In a first attempt, we aimed to use the ridge below the beams, which remains when releasing the beams for just the right time, for the optomechanical coupling. We learned that the coupling is not strong enough to observe the optical spring effect and initiate synchronization, so we next placed an extra beam in the near vicinity of each of the integrated ones. To avoid the leakage of light into the bulk, these auxiliary beams are patterned with a photonic crystal. For choosing the right design parameters, the above-mentioned study on the patterned calibration devices was instrumental [138].

The next chapter will explain the design, construction, and characterization of the setups, which allow us to study the devices, whose fabrication was introduced above.

[14] A good discussion of the appearance of band gaps by the integration of photonic and phononic crystal patterns into our waveguides can be found in the work of Burak Yildiz [148] and Julia Lamprich [151], respectively.

CHAPTER 4

Setups

In this chapter, the setups used for the measurements of the projects presented in this work are described and their main characterizations are shown.

My personal contribution to the content of this chapter, i.e. the building of the three setups described in the following, is:

- quick measurement setup: setting up parts of the setup, like the stages and stage controllers, and performing transmission tests on grating couplers and a variety of devices. Some characterizations have been taken over by students under my supervision.
- large vacuum chamber: planning and setting up of the chamber and its components. This includes the soldering of connections, applying fibers, performing pressure tests, and initial transmission tests for the proof of principle. I also built the electronics environment to integrate an attenuator for the attenuation of the excitation powers. Students took over, e.g. the integration of the pressure meters into the framework.
- square vacuum chamber: planning of the optical paths and setting up parts of it. Several students strongly assisted with the characterization of the optical components.

Furthermore, I worked on the integration of measurement devices into the Labview environment and the improvement of VIs.

---

4 Setups 49
 4.1 Introduction 51
 4.2 Measurement devices 51
 4.3 Quick Measurement Setup 52
 4.4 Large Vacuum Chamber 56
  4.4.1 Concept and functionality 56
  4.4.2 Attenuator 57
 4.5 Square Vacuum Chamber 58
  4.5.1 Concept and functionality 58
  4.5.2 Beam path 58
 4.6 Piezoelectric actuator 59
 4.7 Temperature control 60
 4.8 Stages 62

4.8.1 Stepper motors 62
4.8.2 Picomotors 63

4.1 Introduction

The measurements presented in this work were performed on various setups built by our group. They are designed for our specific needs and are constantly improved and extended. Measurements that don't require low pressures, i.e. the characterization of photonic devices, are performed in the so-called "quick measurement setup" (QMS). It enables measurements under ambient conditions, i.e. at ambient pressure and temperature, however, the stage has an integrated heating element. Typical measurements are wavelength sweeps in the near-infrared (NIR) regime. An electrical probe allows contacting electrical devices. For measurements on mechanical devices we have two vacuum chambers available, each reaching the low 10^{-5} mbar regime to allow for high quality factors. In this thesis, they are referred to as "square vacuum chamber" (SVC) and "large vacuum chamber" (LVC). The former is designed for free-space optical measurements on integrated optomechanical cavities. The latter is connected - similar to the QMS - with fiber optics and allows measurements on integrated optomechanical circuits, typically realized via an integrated Mach-Zehnder interferometer or a ring/ racetrack cavity. The mechanical devices are driven via a piezo element which in turn is actuated via an NWA. An electrical probe can be used to electrically contact the devices and actuate them capacitatively. The samples in both chambers are mounted on x-y-stages and can be actively heated or cooled. Besides the NWA, other measurement devices e.g. SPA, LIA, or spectrometer can be used in these setups. All setups are mounted on optical tables to decouple the measurements from environmental vibrations. LabVIEW is used to control the - to a large extent - automatized measurement procedures and obtain the data. As all setups were built from scratch during the time of this work, I will present the main aspects of their functionality and characterization in this chapter.

4.2 Measurement devices

For the acquisition of the data on the different setups, we have several measurement devices at hand, each serving specific tasks. Low-frequency sweeps are recorded with a data acquisition system (DAQ) and read by Labview and its results are written into a data file such that the sweep parameters are connected to the data acquired by the DAQ. Such measurements are performed at the QMS and LVC and typically are wavelength or laser power sweeps. In the SVC the low-frequency data is extracted from the signal by a bias tee and recorded with a picoampmeter. This way the optical transmission through the beam path can be measured and utilized to align the setup. This data also serves to record the reflectivity maps of devices while taking the two-dimensional mode maps. Driven dynamic measurements on our optomechanical devices are typically taken with an NWA. As described above, the NWA sends a signal into the system to be measured and records the amplitude and phase response. The signal is mostly sent to the piezo to drive the sample but can also be applied to electrodes (e.g. at the Hresonator or Hdirectional) integrated on the chip. Some choices have to be made when setting the measurement parameters: firstly the frequency range (span) has to be chosen, which in our case lies in the low MHz regime and depends on whether an overview scan over several modes or high resolution zooms into individual modes shall be performed. The resolution is influenced by the set number of data points and segments, which the range is divided into. The intermediate bandwidth (IFBW) has a strong influence on the quality of the data. A lower IFBW results in better resolution and SNR at the expense of longer measurement times as smaller chunks of the span are measured at a time [152]. The excitation power as well influences the SNR. Too low powers lead to small excitation of the device that might not at all or hardly stand out from the noise. A high SNR is favorable with the limitation that too high powers lead to nonlinear driving of the resonator which typically shall be avoided. The best IFBW and excitation powers depend on the individual device to be measured.

Additionally to the NWA the SVC has a LIA connected that can also take frequency sweeps

but is mainly used to lock to specific modes and measure the response exactly there. This is utilized in the PLL setup described in Chapter 5. Up to six modes can be locked simultaneously by locking to their phases that have been obtained before the measurement. This allows for fast measurements of the mode on a large number of locations on the device as required for two-dimensional mode maps.

The SPA does not drive the devices but measures the frequency spectrum of the input signal. That way the power spectral density can be acquired and used to e.g. measure the thermal motion of the device (see Sec. 5.5) [153]. Here an important parameter to select is the resolution bandwidth (RBW) which is a measure of the minimum required separation between two frequency components to visually separate them. The setting of the RBW affects the frequency resolution of the trace and the measurement speed. There is a trade-off between the resolution and the measurement speed. If the measurement takes too long, the mode might drift in frequency during the measurement and result in a distorted mode with increased linewidth and less precise location in frequency space. These measurement devices are integrated into the larger frame of setups described in the following.

4.3 Quick Measurement Setup

The QMS is the most frequently used setup in our lab environment. As the name indicates, it is quick to place a sample and start the measurement. No pump-down of a vacuum chamber or cooling to cryogenic temperatures is necessary. For most measurement schemes the measurements run fully automatized and all data is readily collected when coming back to the setup after a few hours[1]. Integrated photonics circuitry, like ring resonators or directional couplers, is measured with this setup. But also integrated optomechanical devices are characterized before they are extensively measured in the LVC (see Sec. 4.4). It is of interest to compare the photonic behavior of the devices before and after release, i.e. with and without the cladding layer beneath the mechanically active devices. Without much hassle, the chip can be measured in between the nanofabrication steps, before and after release. It can also be verified, that - at least from a photonics point of view - the devices are working properly before the chip is mounted into the vacuum chamber and brought to vacuum.

The setup, as sketched in Fig. 4.1 is able to measure integrated photonic devices by coupling the laser into the circuitry via a FA-to-grating coupler interface. The measurement scheme typically includes one single-mode input fiber (yellow fiber in the sketch) and one to three multimode output fibers (blue fibers in the sketch)[2]. See Sec. 2.3.2 for the discussion about the ideal combination of single-mode and multi-mode fibers. As mentioned above, the setup is automatized, by moving from device to device on the chip and fulfilling the measurement procedure on each device. Moving to the next device is done by moving the sample holder with an x-y-stage (more about the stages in Sec. 4.8) until the (fixed[3]) fiber array is placed above the next device. This can be done by tracking the transmitted light while moving the stage and registering the next device by the signal surpassing a certain threshold. Another way is by using the anchoring functionality: Before starting the measurement, at least four devices in each corner of the chip are positioned manually and their locations are saved. By providing the design file[4], the locations of all devices are calculated and can directly be addressed by the stages. Either way, after the device is (roughly) placed below the fiber array, the sample moves repeatedly in x- and

[1] Exceptions from the full automation are, when devices shall be measured repeatedly with different settings of non-automatized components.

[2] The input fiber is a single-mode fiber to ensure a well-defined mode being coupled onto the chip. The output fibers, collecting the light from the output grating couplers are typically multi-mode fibers as of their better collection efficiency.

[3] The fiber array is fixed in the x-y-direction and manually adjustable in the z-direction.

[4] The design file (.dev) is created together with the .gds file when compiling the Matlab script with the pattern for the lithography steps.

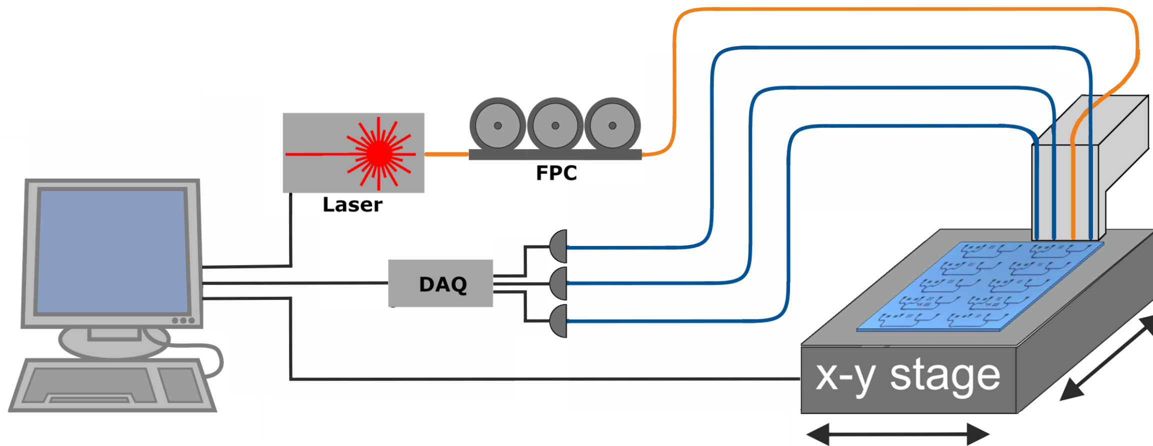

Figure 4.1: Sketch of the QMS setup shown in Fig. 4.2. FPC: fiber polarization controller, yellow line: input fiber guiding the laser light onto the sample, blue lines: output fibers, collecting the light transmitted through the device. The output fibers end in photodetectors, connected to a DAQ. The motorized x-y stage and laser are Labview controlled. The data coming from the DAQ is also read by Labview. Figure adapted from [143].

y-direction over the transmission peak, and the transmission profile is tracked to optimize for the location with the highest transmission. The stage control and data collection are done via a Labview interface. A detailed description of the virtual instruments (VIs) shall not be part of this work. Only so much: The control consists of various interconnected (sometimes independent) VIs, that are constantly improved and added with new functionality by members of our group. The VIs are also controlling the measurement devices, like the laser or temperature control, and are responsible for writing the obtained data into the final data file. The different components of the setup shall now be explained in the order of the path, the light travels through the setup - from the laser to the detector.

As a light source, any fiber-based laser (or free-space laser with fiber coupling) can be connected. Initially a HP8168F step laser[5] was used. We later connected a Santec TSL550 sweep laser[6], which is capable of much higher measurement speeds. The first was very well suitable to measure devices, like directional couplers, photonic crystals, and setup or grating coupler characterizations. There, typically measurements of one data point per nanometer are sufficient. However, as it steps through the wavelengths, this laser takes unreasonably long to measure, e.g. ring resonators or racetrack cavities, where typically $10 - 100$ thousand data points are taken over the wavelength range. Thus, to properly resolve the ring resonances, which have a linewidth of a few 10s of pm for high-quality devices, the fast sweep laser, as it - as the name tells - sweeps through the wavelengths with high resolution. Figure 4.2(a) shows a photograph of the setup sketched in Fig. 4.1, with the sweep laser to the right (white device cover).

The light travels through the fiber polarization controller (FPC). The FPC consists of three 3D-printed paddles that can be rotated, as shown in Fig. 4.3(a). The fiber describes three windings in each paddle. By adjusting the rotation of the paddles, the polarization direction (not the polarization itself) can be selected, comparable to a $\lambda/2$-plate in free-space optics. The polarization is adjusted, such that the transmission through the device is optimized (i.e. obtaining the highest signal from the detector). This is necessary as the efficiency of the grating couplers is very much polarization dependent and a wrong setting can cause a drop in coupling intensity by several 10s of dB. After the FPC, the fiber is connected to a FA. The fiber array guides the

[5]The laser has a wavelength range of $1450 - 1590$ nm with 1 pm wavelength resolution. Source: Internal HP8168F specification sheet.

[6]The laser has a wavelength range of 1480 - 1640 nm with 0.1 pm wavelength resolution. Source: TSL-550 Operation Manual.

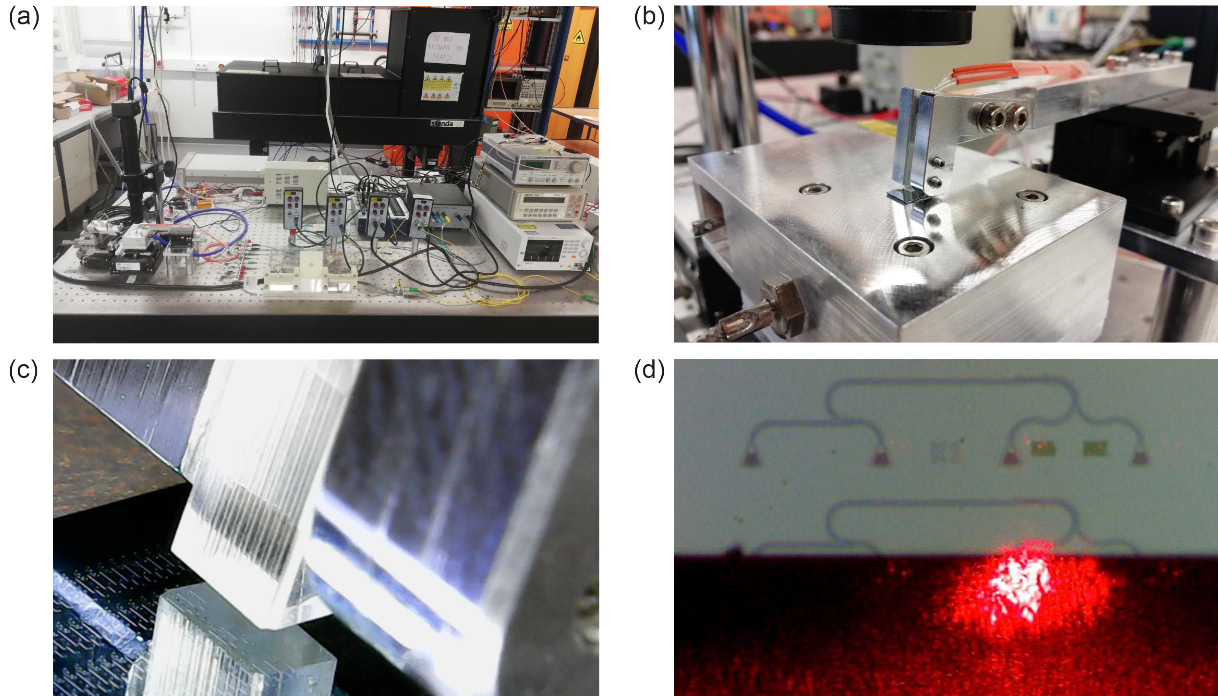

Figure 4.2: QMS setup. (a) Overview of the whole setup. (b) Sample holder and arm holding the fiber array. A sample is placed below the fiber array. At the top of the image, the camera objective for the observation optics is visible (black part). (c) Zoom towards the fiber array and sample. The devices on the sample are visible. The fiber array is reflected on the sample surface. (d) View through the observation camera onto the sample with devices on it. The red light is sent through one of the fibers and projected onto the sample. This is not the measurement laser (NIR) but a test laser in the visible regime used to align the grating couplers of the devices below the fibers.

light onto the integrated grating couplers and is mounted on an aluminum arm over the sample (Fig. 4.2(b,c)). In panel (c), a mirrored image of the fiber array is visible on the sample surface. The distance between the real array and the image is a measure of its distance to the sample surface during alignment. The structures, that appear on the chip, are the fabricated devices to be measured. The fiber array is tilted with an angle of 8° with respect to the normal axis of the sample, which ensures high coupling between the FA and the grating coupler. The distance between FA and grating coupler can be changed by moving the aluminum arm up and down with a micrometer screw. The coupling is not only dependent on the x-y-position (see Sec. 2.3.2) but also on the z-position. In general, the highest transmission is ensured, when the FA is as close as safely possible (without physically touching the sample surface) over the sample and the x-y-position is optimized. The FA consists of four single-mode and four multi-mode fibers, as mentioned above, the single-mode fibers are typically used for the light coming from the laser and the multimode fibers are used for the light collected from the output grating couplers. Which grating coupler is used for input and output is defied by the propagation direction of the light, the grating couplers themselves do not differ in any way, whether they are used as input or output couplers. The grating couplers of some devices, that shall be tested on their symmetry of transmission, like 4-port-devices or directional couplers, actually are altered in their function as input or output couplers.

After being transmitted through the device, the light led into a New Focus NF 2053 photoreceiver[7], which converts its intensity into a voltage. The detector- and setting-specific gain value

[7]The detector covers a wavelength range of $900 - 1700$ nm and has an adjustable transimpedance gain from 626 to 18.810^6 V/A. Source: Users' guide 10-MHz Adjustable Photoreceivers Models 2051 and 2053.

in V/mW has to be entered into the VI before the measurement, as well as the detector offset, i.e. voltage measured when the laser is turned off. The voltage signal from the detector is fed into a DAQ from National Instruments. The obtained data is now transferred via a USB cable to the VI on the measurement computer and finally written into the data file (.dat), which can be read and evaluated with our pool of Matlab-based data processing scripts that are constantly improved and expanded.

Optional features of the setup are the heating element and temperature read-out integrated into the sample holder, which can as well be addressed via Labview. The temperature is either stabilized on the desired value or swept as a measurement parameter. The sample is placed onto a small hole in the holder, which is connected to a small vacuum pump to ensure, that the sample is not moving or rotating after it has been aligned. If the grating couplers are rotated with respect to the fiber array, the input and output grating couplers and respective fibers are not in line anymore, reducing the coupling efficiency.

In Fig. 4.2(d) the view through the observation camera (the bottom part of the objective can be seen at the top of panel (b)) is shown. The devices are those of panel (c) and can be seen in much more detail, now. They are the directional coupler devices described in Sec. 3.2. The black bar at the bottom of the image is the fiber array. When aligned to the grating couplers, the fiber array is covering parts of the device, currently measured. It can be clearly seen, that the devices are nicely aligned with respect to the FA, in terms of rotation. The red spot comes from an alignment laser in the visible regime connected to one of the output fibers. It is used to get a first feeling of the alignment between the device and fiber array on a newly positioned chip, as the measurement laser does not lie in the visible regime and makes it hard to align without further reference.

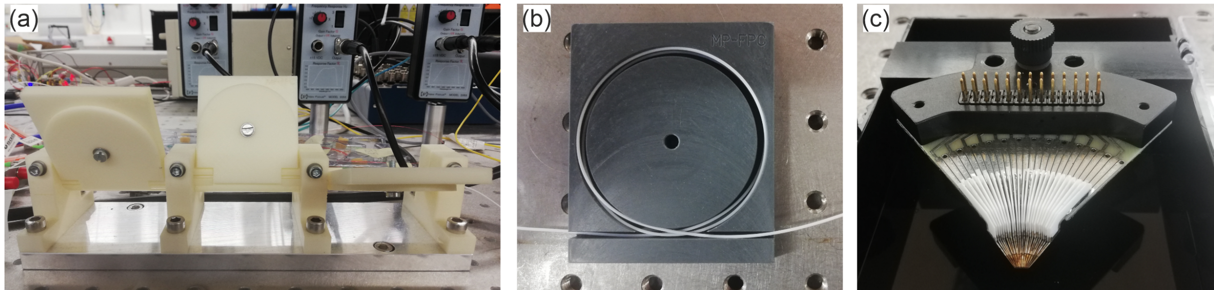

Figure 4.3: Individual parts of the QMS. (a) Fiber polarization controller. (b) View into an opened FPC paddle with the winded fiber visible. (c) Electrical probe.

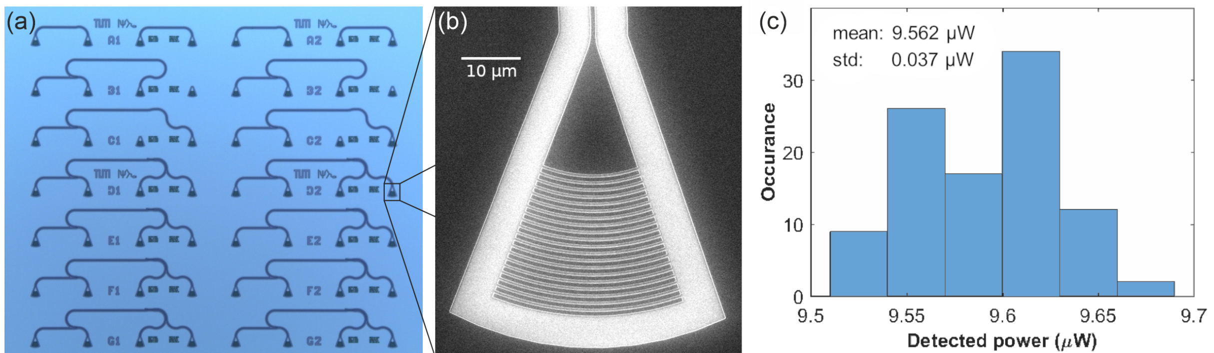

Figure 4.4: (a) Microscope image of the sample with devices on it. (b) Scanning electron micrograph of a grating coupler. (c) Histogram of the detected power for 100 optimizations of the chip position underneath the fiber array. Figure adapted from [143].

Once visually aligned with the help of the red laser, as seen in Fig. 4.2(d), the sample is aligned

with much more precision by the automatic positioning algorithm, tracing the transmission through the device. Fig. 4.4(a) again shows a microscope image of the sample, not taken with the observation optics but with a high-resolution optical microscope. Panel (b) zooms into one of the grating couplers and displays a scanning electron micrograph. The functionality of the grating coupler as well as characterization measurements have been described in Sec. 2.3.2. In the lower part of the device, the grating for coupling the light on and off the waveguide to free space is visible followed by the taper and the waveguide can be seen. Such a device has been automatically optimized 100 times and the detected power was recorded. Panel (c) shows the histogram of the occurrence of the detected power after optimization. At a mean transmission of $9.562\,\mu$W, the standard deviation is only $0.037\,\mu$W, proving the very good repeatability of the optimization procedure.

Some devices need to be electrically contacted. This can be a device with heating elements, i.e. gold structures next to a waveguide or a directional coupler. It is further applied to measure electro-mechanically actuated devices, like Hdirectionals or Hresonators (see Fig. 3.14(a) and (b), respectively). The electric current or voltage is fed into the gold wires on a chip by an electrical probe as shown in Fig. 4.3(c). The needles are placed onto contact pads, i.e. relatively large golden structures on the sample, connected to the wires.

4.4 Large Vacuum Chamber

4.4.1 Concept and functionality

The Large Vacuum Chamber is a measurement setup that is very similar to the QMS - but in vacuum. It is designed for integrated photonics circuitry that includes mechanically active devices. One of the key figures of merit of a mechanical device is its quality factor. The first and easiest method to increase the quality factor by orders of magnitude is by reducing the air damping, present in any ambient setup (c.f. Fig. 4.6(b)). The LVC consists of an aluminum chamber, a photograph of which is shown in Fig. 4.5(a), with various feedthroughs to connect the inside with the outside world. For our devices, we are typically interested in their dynamics in the low MHz regime. We drive the devices and measure their response. Driving is done by gluing the sample on a piezo-electric actuator which is electrically connected to the output of a NWA and "shakes" the sample. The response of the device is read by the laser light and translated back to a voltage by the detector. This voltage is finally fed into the NWA, recording both the drive and the measured signal. Alternatively, a SPA can be connected to, e.g. do measurements on the thermal motion of the devices. A sketch of how a measurement is set up for the example of geometrically tunable beams, read by an integrated Mach-Zehnder interferometer is provided in Chapter 6 in Fig. 6.2(b).

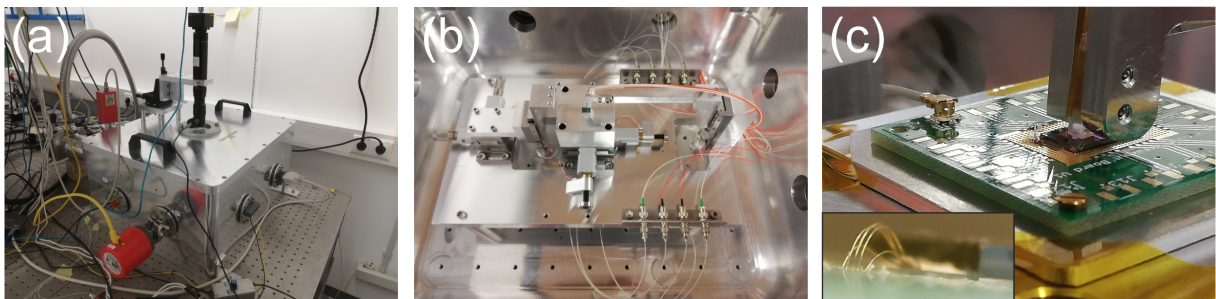

Figure 4.5: (a) Outside view of the LVC. (b) View inside the chamber. (c) Close view of the PCB and fiber array. Inset: Bonded wires connecting the RF connector with the piezo.

The vacuum is provided by a pump system consisting of a turbo pump and a pre-pump. A pump-down curve is shown in Fig. 4.6(a). Our systems ultimately reach pressures close to

10^{-5} mBar which is supposed to be sufficient to get below the air damping limited regime as can be seen in Fig. 4.6(b)).

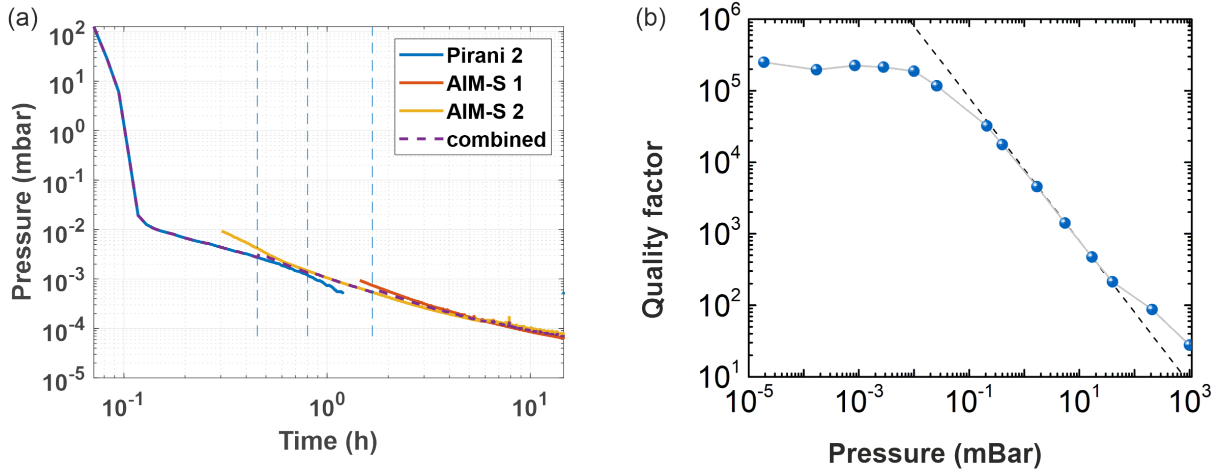

Figure 4.6: (a) Pressure versus time during pump-down of the LVC. The pressure was obtained by gauges with different measurement ranges, a Pirani gauge (blue) and two AIM-S gauges (red and yellow). The purple dashed line is laid onto the data for the full range, combining the data of all three gauges in their respective measurement ranges. (b) Quality factor of a Hresonator device (c.f. Fig. 3.14(b)) versus the pressure inside a vacuum chamber[8]. Panel taken from [143].

As for the QMS, an electrical probe can be installed to electrically contact the devices on the sample. In the case of the QMS on-chip heating elements (e.g. placed at directional couplers for tuning of the coupling ratio) or switches (e.g. Hdirectional, c.f. Fig. 3.14(a)), are usually DC actuated. The reduced air damping in the LVC allows for an AC drive of the mechanical devices at much higher frequencies (e.g. Hresonator, c.f. Fig. 3.14(b) or the aforementioned Hdirectional if fast switching is desired).

4.4.2 Attenuator

Typically, we want to excite the piezo with powers such that the resonator motion stays in the linear regime as explained in Sec. 2.4.2. With the Network analyzer HP E5100B, however, we stayed deep in the nonlinear regime and did not reach the linear motion[9]. The solution was to integrate an attenuator into the setup and place it between the NWA output and the feedthrough, leading to the piezo inside the chamber. The attenuator is a HP33321SC (Fig. 4.7(a)) and can attenuate the applied HF signal between 0 and 70 dB in steps of 10 dB. Switching is done by applying a voltage to a specific combination of inputs, which is done by a relais board. This in turn is controlled via an Arduino that receives its commands from a Labview VI, integrated into the larger framework of our Labview measurement control. That way we are able to take dynamic measurements on our resonators in the linear regime. This transition from measurements deep in the nonlinear to the linear regime can be seen in Fig. 4.7(b). Further measurements by sweeping the attenuation can be found in Sec. 6.10.

[8]Note: this measurement was not taken in the LVC.
[9]The power range of this NWA is −23 to +11 dBm.

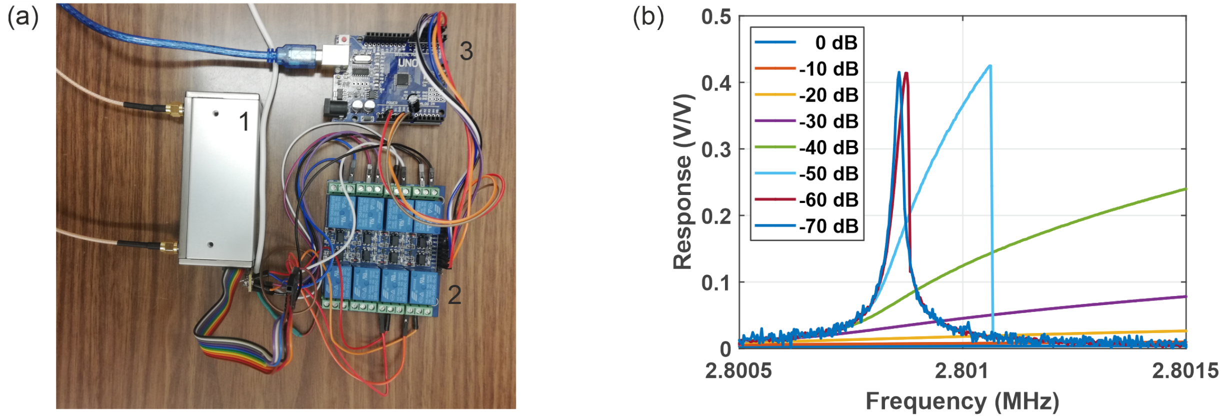

Figure 4.7: (a) Photograph of the attenuator with control electronics. (1) Attenuator HP 33321SC, (2) Relais board, (3) Arduino. (b) Response of a Sbeam device at an excitation power of 10 dBm set by the NWA but different settings of the attenuator. Correction of the response for the attenuation is done during data processing. The legend displays the respective attenuator setting.

4.5 Square Vacuum Chamber

4.5.1 Concept and functionality

The square vacuum chamber is the only free-space optics setup in our portfolio. As it is designed to characterize the dynamics of mechanical structures, mainly in the low MHz regime, the measurements take place in vacuum. As the LVC, pressures of the low 10^{-5} mBar regime can be reached. The structures that we measure form a cavity between the resonator and the sample substrate. When laser light shines from the top onto the resonator, some of the light is reflected from its surface, while some is transmitted and then reflected at the bottom of the cavity, i.e. the Si substrate. The fraction of this reflected light, that now passes the resonator again and leaves the cavity, interferes with the light reflected on its surface in the first place. The principle is illustrated in Fig. 5.5 in Chapter 5.

4.5.2 Beam path

The reflectivity of the structure depends on the distance between the device (e.g. membrane, cantilever, trampoline,...) and Si substrate, enabling interferometric measurements of the resonator displacement using the setup shown in Fig. 4.8 and 4.9. For this, a HeNe laser is led through a beam expander, for an improved focal spot on the sample, a polarizing beam splitter (PBS), to separate the beam paths towards the sample from the reflected signal, and a quarter wave plate. The latter turns the formerly linearly polarized light into circularly polarized light in case of the light being sent towards the sample and vice versa for the reflected signal. Thus, the PBS will separate these two beam paths and guide the signal toward the detector. Then the beam is passing a 90:10 beam splitter (BS) and is focused using a 10x microscope objective with a 32 mm working distance and NA=0.28. The BS is combining (separating) the laser and the light used for illumination (observation). The high reflectivity vs. transmittance ensures a good yield of the reflected signal. The objective has a fixed position[10] outside the vacuum chamber, which is mounted on a motorized x-y stage that can scan with steps of 1.25 μm while measuring the reflected light using a photodetector. Characterizing measurements of the individual components in the beam path - in particular the verification of the Gaussian beam shape at the focal spot on the device surface - are presented in [154] and [155]. For excitation and detection, either a

[10]The objective is fixed in the x-y-direction and can be aligned in z.

network analyzer (HP 4396A) or lock-in amplifier (Zurich Instruments HF2) can be used. Their output goes to the piezo-electric actuator to excite the membrane. Its vibrations modulate the light on the photodetector, which turns the optical signal into an electrical one. This electrical signal is split by a bias tee into its dc and ac parts. The dc reflection is recorded by a picoamp current meter and can be used to align the beam path for an optimized reflection, but also to take reflectivity maps like the one shown in Fig. 5.6. The ac part is again detected with the NWA or LIA. A detailed description of the analysis of the signal is given in Chapter 2, Sec. 2.5.1.

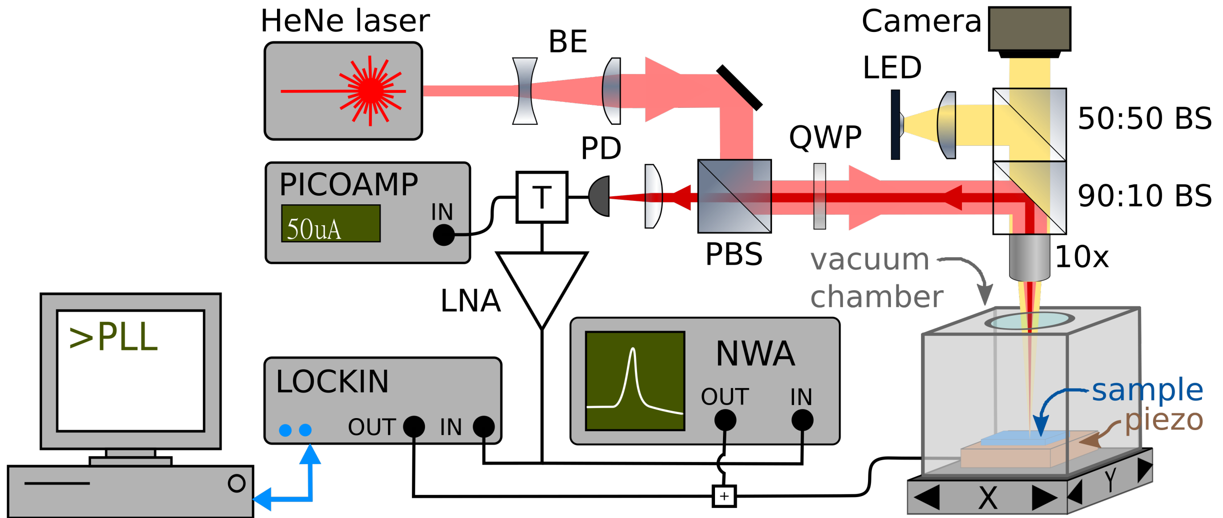

Figure 4.8: (b) Schematic overview of the measurement setup. BE: beam expander, (P)BS: (polarizing) beam splitter, QWP: quarter wave plate, PD: photodetector, LNA: low-noise amplifier, NWA: network analyzer, T: bias tee, +: combiner, LED: light emitting diode for illumination.

Figure 4.10(a) shows the main part between laser objective and detector. The laser is located outside, i.e. "below" the figure. At the far end of the figure, right before the vacuum chamber, a mirror reflects the light upwards, where it is reflected by another mirror (not in this image) towards the 90:10 beam splitter displayed in Fig. 4.8 and the microscope objective, shown in Fig. 4.10(b). In the latter panel, the objective can be seen with the vacuum chamber underneath. Below the viewport, the sample is visible and mounted on a PCB and connected to an RF cable for the piezoelectric actuation. Panel (c) shows this PCB with the piezo element and sample glued onto it with silver paste. In the bottom right, the HF connector is mounted, used for applying the actuation signal to the piezo. If further zooming into the figure, the bonded gold wire connecting the connector with the piezo would become visible.

4.6 Piezoelectric actuator

As mentioned above, the RF output signal of the NWA or LIA is applied to a piezo-electric actuator (throughout this thesis mostly addressed as "piezo") mounted on the PCB below the sample. The actuation of the piezo drives the (opto-)mechanical device on the chip which alters the optical signal which in turn is transferred back into a voltage by a photodetector and fed back into the measurement device (also see explanation in Sec. 5.3.1). Thus the units in the typical frequency response shown in this work are displayed in V/V, i.e. the detected voltage over the excitation voltage is not directly describing the isolated resonator motion.

The thickness of the piezo[11] is 0.1 mm, resulting in a fundamental thickness-mode resonance at 21.3 MHz. This mode, as well as its third higher harmonic, are shown in Fig. 4.11. In piezoelectric plates, the fundamental thickness mode and its odd harmonics are most easily

[11]"plate c252 x40 y9 t0,1 eCuNi" from Physik Instrumente GmbH & Co. KG.

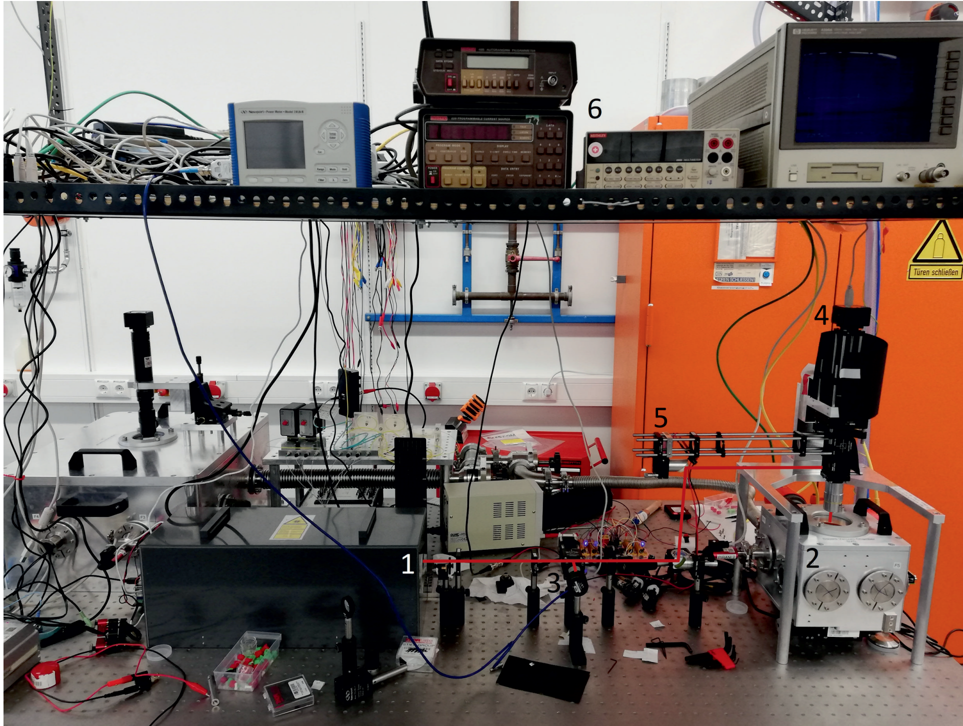

Figure 4.9: View on the SVC setup at an early stage, where calibrations were performed (here, an optical power meter is connected to a detector to measure and characterize the beam alignment). The optics are placed on the optical table with the HeNe laser placed inside the gray box (1) and the vacuum chamber (2) visible in the lower right corner of the image. The optical path is indicated by red lines, also visible are the photodetector (3), the observation camera (4), and the illumination source (5). The control electronics stand on the rack above (6).

excited while the even harmonics require very strong electric fields (in the ideal case they are not excited at all) [156]. The modes of the devices discussed in this work typically lie in the regime of several hundred kHz to about 20 MHz and all lie within the excitation bandwidth of the piezo.

4.7 Temperature control

In the QMS a thermocouple is used to measure the temperature, while for the LVC and SVC the temperature sensor Pt1000 (Fig. 4.12(b)) is used as of its smaller size. Furthermore, the thermocouple turned out to be less reliable and accurate than the Pt1000 as it sometimes returns incorrect values due to ground loops and interferences. To alter the temperature in the QMS simply a resistor is used and the stage thus can only be heated. In contrast, the LVC and SVC utilize a Peltier element (Fig. 4.12(a)) that is placed directly underneath the PCB. It can be used both for heating and cooling, depending on the polarity of the connected current source. Fig. 4.12(c) shows the relation between applied current and temperature. The current was increased from 0 to 0.5 A in steps of 0.025 A every 30 minutes and then again reduced. The temperature reduces from the ambient temperature inside the chamber of $\sim$ 32 degree to $\sim$ 16 degree and rises again when the current is reduced. Only small hysteresis is visible. Panel (d) shows the same measurement but displays the temperature versus time. To see how the temperature saturates after a new current setting, a zoom into the time dependence of the temperature is shown in panel (e). After a new current value is set, the temperature drops quickly within about 5 minutes and then saturates much slower. After about 15 minutes the temperature stays constant until the current changes again. In this range, the temperature drops

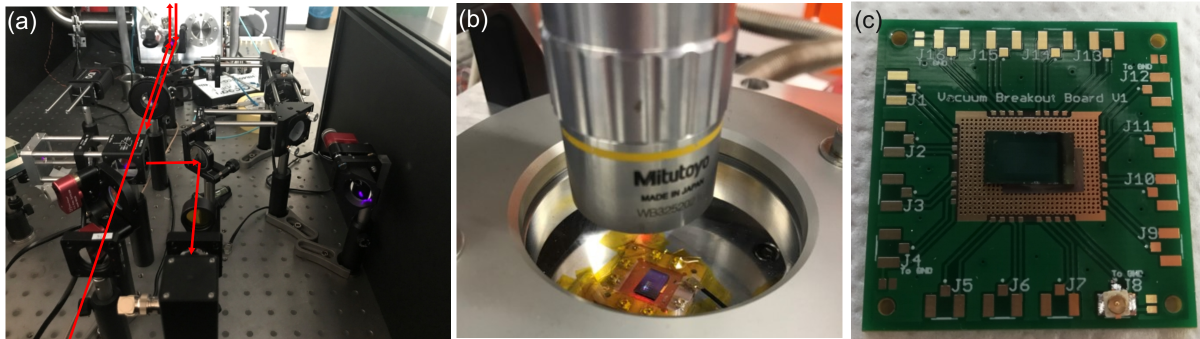

Figure 4.10: (a) Main part of the beam path between laser, objective, and detector. (b) View inside the vacuum chamber through the viewport. Visible are the microscope objective mounted over the viewport and the sample mounted on a PCB inside the chamber. (c) PCB with the actuating piezo and sample mounted onto it. In the lower right corner, the connector for applying HF signals to the piezo is visible.

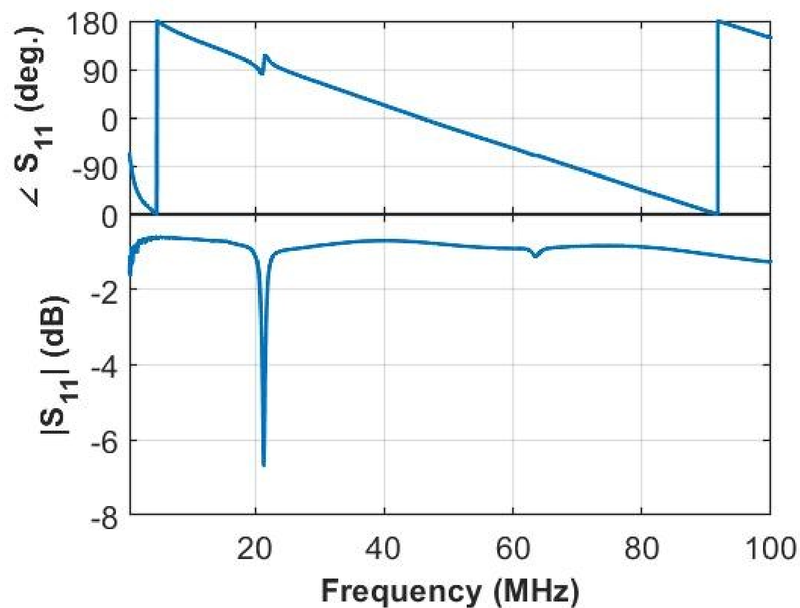

Figure 4.11: Magnitude (bottom panel) and phase (top panel) of the frequency response of a piezo element actuating the sample. Visible is the fundamental thickness mode of the piezo at about 20 MHz and its third higher harmonic close to 60 MHz.

by nearly one degree when the current is increased by 0.025 A. Refer to Fig. 5.16 to Fig. 5.18 to see the application of the temperature control during measurements on mechnaical devices.

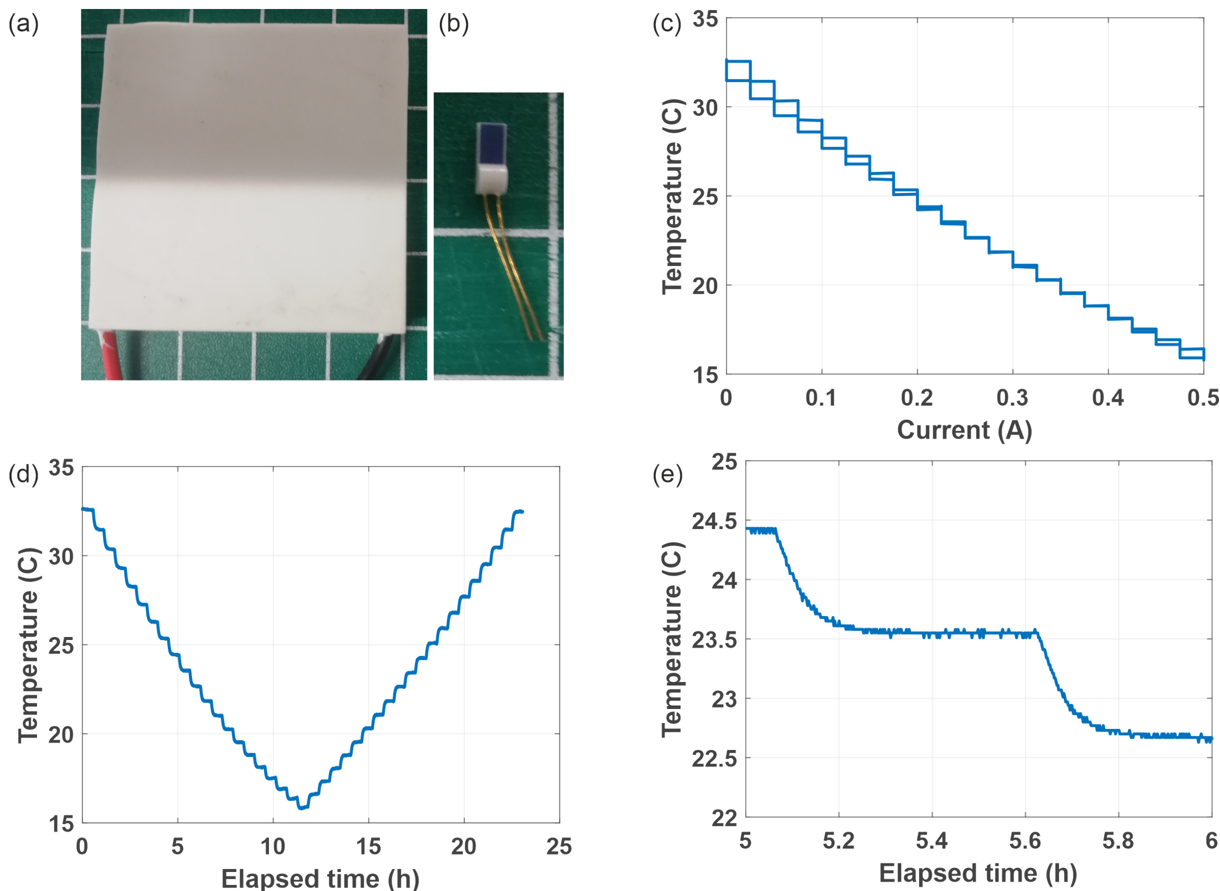

Figure 4.12: (a) Photograph of a Peltier element (side length: 40 mm) and (b) temperature sensor Pt1000 (the image of the Pt1000 is enlarged by a factor of 2 with respect to the Peltier element in panel (a)). (c) Measured temperature vs. current sent through the Peltier element. (d) Measured temperature vs. time in the measurement of (c). (e) Zoom into panel (d).

4.8 Stages

Each setup is equipped with stages to move the sample under the detecting laser. This way the individual devices on a chip can be addressed and the optical transmission optimized. For some devices, such as 4-port-devices[12] the fiber array needs to be laterally shifted for subsequent measurements on the same device. The SVC setup is able to perform 2-dimensional scans on suspended devices and needs a small and repeatable step length. In the following, the two concepts that we have integrated into our setups are described.

4.8.1 Stepper motors

Despite their different measurement concept, the QMS and the SVC both use the same type of stages. Each setup uses two stages from Newport that are positioned perpendicular to each other to address any point in the x-y-plane with the measurement laser. The stages are driven by self-made stage controllers, based on an Arduino plus stepper motor shield. The Arduino

[12]These devices are designed to measure the symmetry of, e.g. directional couplers and have four integrated grating couplers (four ports), each of which can serve as input or output grating coupler.

is communicating with Labview for an automatized positioning and returns its positions to the program. The step size is 1.25 μm and can in principle be further reduced. However, reducing the step size further makes use of fractions of full steps of the motor which is less stable and might cause glitches, and is as well less powerful. The latter is especially important for the SVC as the stages carry the full vacuum chamber and have to drag the rather stiff metal hose connecting the chamber with the vacuum pump. Here, the stages move the chamber below the detection laser. In the case of the QMS, the stages carry the much lighter sample stage, which basically consists of a small Aluminum block. Stage precision, hysteresis, and repeatability have been thoroughly studied by Christopher Waas [157]. When several devices shall be addressed one after each other with measurements performed on each of them the stages need to move to the next device and automatically align the position. On integrated devices this was originally done to move the stages towards the next device until it is detected: when the device just measured is moving away from the input fiber, the transmitted signal is quickly reduced and stays low until the next device approaches the fiber. Then the signal rises again and the maximum is registered. For each chip, specific settings for threshold values of the detection have to be given to Labview. Further, the required settings are the number of devices to be measured in each column and row. Ideally, the vertical sweep direction is bottom-up to avoid the algorithm locking to the secondary peak visible in each grating coupler (see Sec. 2.3.2). A drawback of the described strategy is, that broken or contaminated devices will not be registered and a device (or full row) will be skipped. The consequence is a wrong naming of the data files (this can manually be corrected, as a picture is taken over each device, which is correctly named on the chip) and the loss of the correct reference at the end of a row (the algorithm expects one more device as one has been skipped and will drive away until the timeout applies). For chips with imperfections, this leads to quite some manual work and can significantly increase the measurement time. By the time the algorithm has been improved. When generating the .gds file with the pattern information for the electron beam writer, also a .dev file is generated by Matlab. This file contains information on the positions of each device and can be loaded into Labview. Now, only the position of four devices (ideally in the corners of the chip) need to be located on the stage as reference (so-called anchoring) and together with the information from the design file, each device can be addressed individually and does not require the device search via the transmission. Thus the positioning is now robust against device damage. Once roughly positioned that way, the exact position is optimized as before by moving both horizontally and vertically over the device and locating the maximum.

4.8.2 Picomotors

The sample stage in the LVC in contrast is driven by the “picomotors” from New Focus whose driving is based on piezos. These are vacuum compatible as they are placed inside the chamber. The chamber of the LVC setup is much larger than the SVC as of the larger complexity of the inside components and thus too heavy to be moved like the SVC. This comes at the cost that the step size of this type of motor is not reproducible and thus the positioning via anchors as described above is not an option. Here, the original approach to finding the next device by tracking the optical transmission is used. Anyways, the measurements typically performed in this chamber are much more complex and require much more interaction by the operator, such that individual devices are often extensively measured without a fully automatized approach. The dynamic measurements usually start with obtaining an overview spectrum with the NWA to identify potential modes which are then selected for individual high-resolution spectra (refer, e.g. to Fig. 6.8(a) and (b), respectively, for such measurements obtained on Sbeam devices). Individual decisions like the correct excitation powers and laser wavelengths have to be taken. This has been started to be automatized with Labview as well, however, at the current state, the manual approach is still the strategy of choice. Once positioned, further measurements might be

excitation or laser power sweeps[13] with the NWA or thermal motion measurement (see Sec. 2.12) with the SPA.

The setups described in this chapter allow for realizing the projects, some of which already have been mentioned above. In the coming chapters, two of these projects will be discussed in depth.

[13]Laser power sweeps are relevant, e.g. in the synchronization project to utilize the optical spring effect.

CHAPTER 5

Efficient optomechanical mode-shape mapping of micromechanical devices

This chapter covers the measurements of micro membranes out of silicon nitride. To measure the mode shape of these and other micromechanical devices a new setup was developed and built. The benefits of this new setup based on a phase-locked loop in comparison with other techniques are emphasized.

This chapter is largely based on material published in Micromachines, Special Issue Physical Microelectromechanical Systems (MEMS): Design, Modeling, Fabrication, and Characterization).
David Hoch, Kevin-Jeremy Haas, Leopold Moller, Timo Sommer, Pedro Soubelet, Jonathan J. Finley, and Menno Poot. Efficient optomechanical mode-shape mapping of micromechanical devices. *Micro-machines, 12(8), 2021* DOI:10.3390/mi12080880 [63].
Reprinted by permission via Creative Commons Contribution Licence.
My personal contribution to the content of this chapter is the device design and fabrication of several batches of chips. I strongly contributed to the planning and building of the setup. Furthermore, I performed many of the measurements discussed below either by myself or guided the students when obtaining the measurements.

5 Efficient optomechanical mode-shape mapping of micromechanical devices 65
5.1 Introduction 67
5.2 Nanofabrication 67
5.2.1 Surface quality 68
5.2.2 Reflectivity 71
5.3 Mode properties 71
5.3.1 Response and mode shape 71
5.3.2 Demodulation 73
5.3.3 Harmonic oscillator response 73
5.4 PLL mode mapping 75
5.4.1 Comparison of different methods for mode mapping 75
5.4.2 Mode maps 78
5.4.3 Variation of the measurement scheme 79
5.5 Thermal motion 79
5.6 Temperature dependence 81

5.7 Beyond membranes 84
5.8 Summary 84

5.1 Introduction

Visualizing eigenmodes is crucial in understanding the behavior of state-of-the-art micromechanical devices. Here, I demonstrate a method to optically map multiple modes of mechanical structures simultaneously. The fast and robust method, based on a modified phase-lock loop, is demonstrated on a silicon nitride membrane and shown to outperform three alternative approaches. Line traces and two-dimensional maps of different modes are acquired. The high-quality data enables us to determine the weights of individual contributions in superpositions of degenerate modes.

In recent years, there have been many applications for integrated opto- and electromechanics extending from e.g. mobile communication [71] and highly sensitive sensors [70, 158–163], including recording the nano motion and "sound" of single bacteria on nanodrums [164], to position detection close to the quantum limit [74, 165, 166]. In the development of such devices, an efficient method for mode characterization is instrumental and, hence, a number of techniques including optical interferometry [65–67], heterodyne detection [68,69], dark field imaging [65,70], and force microscopy [71–74] have been developed to visualize mechanical modes. However, most of these have one or more drawbacks, such as poor sensitivity, lacking phase information, low spatial resolution, or long measurement times. Here, we demonstrate an experimental method that combines the high sensitivity of the optical interferometric techniques with demodulation and frequency tracking to offer rapid and robust imaging of multiple modes simultaneously. The advantages of the technique, combining high resolution and sensitivity, as well as its robustness against sign changes of the mode shape at the nodal lines while tracking the resonance frequency via a phase-lock loop (PLL), are illustrated by mapping the eigenmodes of a square SiN membrane. With this method, the eigenmodes of the membrane can not only be unambiguously identified but also their mode composition can be determined quantitatively and insights into clamping losses are provided.

5.2 Nanofabrication

Before discussing the results of our method in depth, first, the fabrication of the devices the following discussion is based on is explained in this section. The SiN membranes are made on chips with 330 nm high-stress Si_3N_4 [16, 96, 143]. Release holes are defined using electron-beam lithography followed by a fluorine-based reactive ion etch, exposing the underlying SiO_2 [167]. The membranes are released using buffered hydrofluoric acid followed by critical-point drying. The reflectivity of the structure depends on the distance between the membrane and Si substrate, enabling interferometric measurements of the membrane displacement using the setup explained in Chapter 4. In Fig. 4.8 a sketch of the setup, including the vacuum chamber, the beam path, and measurement devices has already been shown.

The sample as shown in Fig. 4.10(c) appears to be not much more than a piece of silicon the size of a fingernail. So let us now zoom in and take a look at what reveals at the micro-scale. Figure 5.1(a) displays the optical micrograph of the membrane discussed in the following. It has a side length of 275 μm and is about 180 nm thin. Its thickness is not constant and depends on the distance to the holes etched through the membrane (gray dots). This can be seen in panel (b) which is zooming into the upper left corner of (a) and reveals a change in the color of the membrane, repeating with the holes. This is a consequence of the fabrication process discussed below. While this work mainly builds on the results of that particular membrane, also membranes of different sizes were fabricated and measured. Panel (c) shows an example of a much smaller membrane. The large membranes can very well be approximated by a rectangular shape. Due to a different ratio of the membrane area and circumference, the circle elements at the edges of small membranes result in higher deviations between the shape of the real membrane and the rectangular approximation. Thus the comparison between theory and measurement needs more

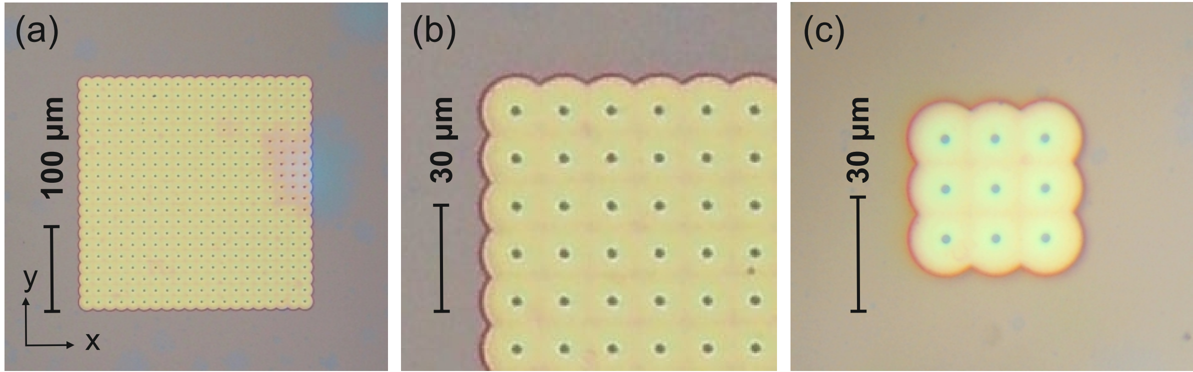

Figure 5.1: Optical micrographs of differently sized membranes. (a) Membrane with a side length of 275 μm, discussed in this work. (b) Zoom into the membrane of (a). The holes (gray dots) are dry etched through the SiN layer, each being the starting point for the 10 μm wet etch in a circular fashion. (c) Example of a small membrane realized on the chip.

care for small membranes. Besides membranes, also drums and drum arrays were realized on the chip. Such as single drums with increasing hole size - the most extreme devices appear rather alike circular rims than drums. Other devices are one- and two-dimensional drum arrays with different lengths and overlaps. They are not discussed in this work, however, they may answer interesting questions in terms of the coupling behavior of the many modes appearing in these arrays. Technically our membranes are two-dimensional drum arrays with full overlap, resulting in a fully released membrane. In the following, it is explained, how the devices are made. Figure 5.2 explains the sample fabrication steps. First, a 6×10 mm chip is diced from a 4" wafer with 330 nm LPCVD Si_3N_4 on 3300 nm SiO_2 on a Si substrate (a) and is cleaned. Electron-beam resist (ZEP 520A) is applied and the holes of the membrane are patterned by electron beam lithography using a Nanobeam nB5 (b). Next, the holes are dry etched $\sim 70\,\mu$m into the SiO_2 layer using reactive ion etching (c) with a SF_6/CHF_3 inductively-coupled plasma. The membrane is released (d) by wet etching with buffered hydrofluoric (BHF) acid for 130 min with a rate of 77 nm/min. This ensures that the circular cavities around the holes are fully overlapping and that the Si layer is fully exposed. Note that BHF has good selectivity to Si [168], that is expected to result in a smooth surface underneath the membrane as will be proven in Sec. 5.2.1. Then, the chip is transferred into water and subsequently into Isopropanol, and finally dried using a critical point dryer. As shown in Fig. 5.2(e), the SiN membrane (green) is now free-hanging above the silicon substrate (dark gray). Between the released membrane and the substrate, a low-finesse optical cavity is formed whose resonance wavelength depends on the separation between these two layers, giving rise to the displacement-dependent reflection utilized for measuring the mode shapes. The fabrication process has a high yield and is very repeatable; different samples have very similar resonance frequencies and quality factors for nominally identical devices.

5.2.1 Surface quality

The SiN surface is exposed to BOE for more than two hours during release and despite the high selectivity of 128:1 for SiO_2:SiN it is slowly etched as well [169]. During the release, when 10 μm of SiO_2 is etched, the top surface of the membrane is equally etched by 76 nm. The surface appears still quite smooth under the optical microscope even though some areas show discolorations, as can be seen for example in the upper right corner of Fig. 5.1(a). Reflectometer measurements show a different etch depth in these locations. Here, the remaining SiN is 10 to 15 nm thicker than on the rest of the chip [170]. A reason might be that in these areas possibly some e-beam resist remained and delayed the time until the BOE reached the SiN surface. Figure 5.3 takes a closer look at the membrane surface. The image in panel (a) is obtained by an SEM on a

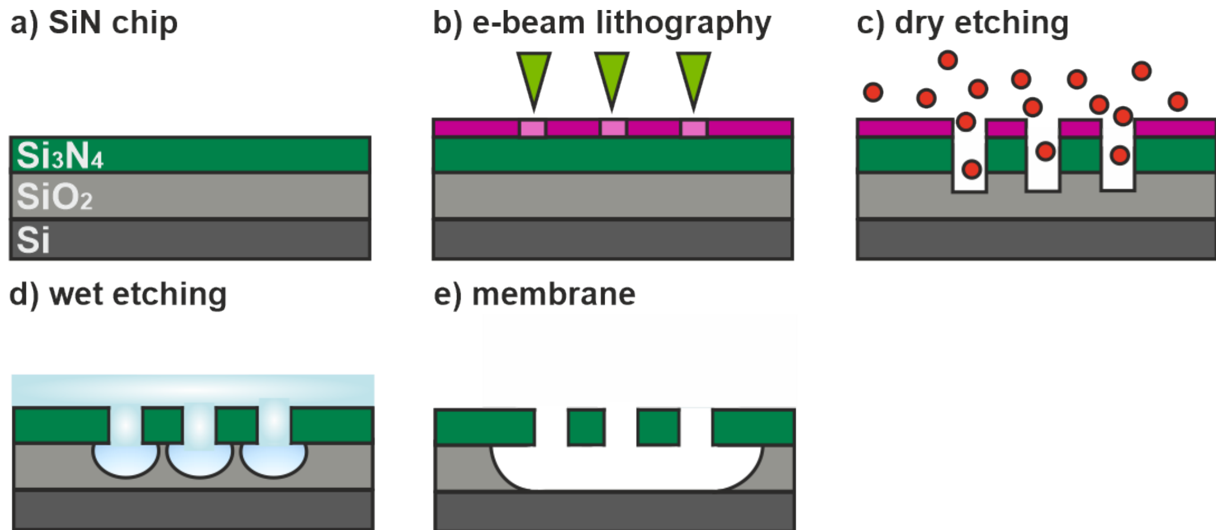

Figure 5.2: Schematic illustration of the nanofabrication process flow of the sample. (a) The sample is diced from a wafer with 330 nm Si_3N_4 on 3300 nm SiO_2 on a Si substrate. (b) The holes of the membrane are patterned by electron beam lithography. (c) The holes are dry etched by reactive ion etching. (d) The membrane is released by wet etching with buffered hydrofluoric acid (light blue). (e) Under the released membrane a cavity is formed, resulting in the interference utilized for measuring the mode shapes.

coupled drum array. Here, the distance of the holes is larger than for the membranes, such that the drums overlap - but not fully. Thus the areas with still SiO_2 underneath are clearly visible in the image and appear brighter than the released areas. Next to the holes, horizontal features are visible, which are artifacts resulting from the horizontal scan direction. The surface appears quite smooth overall, however randomly distributed dots seem to be visible. And indeed, the image in panel (b), obtained by an atomic force microscope (AFM) shows this roughness as well (red dots on yellow background). The inset shows a region without holes and thus provides a zoom into the scale bar. The grain-like surface structure becomes clearer now and shows a peak-to-valley of 50 nm. The RMS roughness is about 6.7 nm. Even though taken by a completely different technique than (a), also here the artifacts near the holes become visible. Here, the scanning direction was again horizontal. In contrast to the image in panel (a), the one in panel (b) was taken on a fully released membrane. However, not only the top side of the SiN membrane is exposed to BOE - as soon as the SiO_2 below the membrane is etched away in a circular fashion from the center, these areas on the bottom side of the membrane are also exposed. Near the holes, for almost the whole time, thus almost the same amount of SiN is etched away as from the top. This exposure time becomes shorter and shorter further away from the holes. The measured thickness is typically ~ 225 nm, due to the finite spot size of the reflectometer, only the average thickness of a region on the membrane can be measured[1]. Still, the thickness of the membrane is not equal at every location but changes in a repeated fashion with the periodicity of the holes. This becomes visible in Fig. 5.1(b,c) by a change in the color of the SiN surface. Due to the overlap of the etched areas between neighboring holes, any region is exposed for some time from underneath, only at the edge of the membrane, the exposure time reduces to zero, appearing as the largest change in color at the edge around the membrane. Figure 5.3(c) shows reflectivity measurements taken by a reflectometer on the SiN surface of several locations on the sample. The reflectivities taken on similar parts of the sample, i.e. either exposed to BOE but not under etched (supported) or exposed and underetched (released) match very well and can

[1]Note: The limited resolution of the reflectometer does not allow to target a precise position, e.g. close to or further away from a hole.

hardly be distinguished in the figure. Another measurement was taken on a reference sample that was not exposed to BOE [171]. The results of the different types of measurements appear sinusoidal-like with an offset in their wavelength dependence. The periodicity in the supported case is higher than in the released case. On average, the reflectivity of the released regions is highest. When there is the SiO_2 layer in between, as both in the supported and reference case, the reflectivities are lower. Interestingly, the reflectivity is lowest on the reference sample which is supposed to have the smoothest surface. This might result from less scattering at the SiN surface and thus higher transmission into the SiO_2 layer, where it is partially absorbed. The reflectivities at a wavelength of 632.8 nm, which is the wavelength of the HeNe laser of the setup, are indicated in the plot. At this very wavelength, the released surfaces have the highest reflectivity (44.5 %), then comes the reference sample, which is here close to a peak, with 29.5 %, and lowest are the supported areas, here, close to a minimum, with a reflectivity of 16.4 %. The measured reflectivities as a function of the wavelength match well with their fits as can be seen in Appendix B.

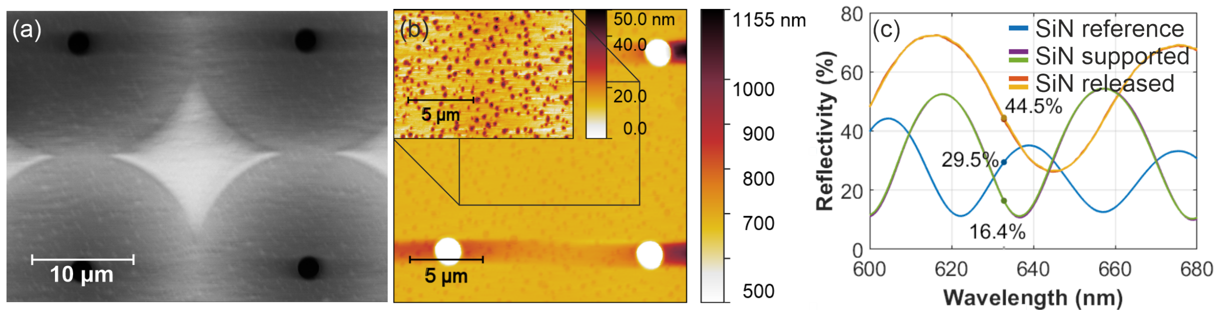

Figure 5.3: Measurement of the surface properties of SiN after being exposed to BOE for about two hours. The measurements were taken by SEM (a), AFM (b), and reflectometry (c). The measurements were taken on different parts of the SiN surface, while (b) and (c) show measurements on a fully released membrane, is (a) showing a pattern where the holes have a larger distance and thus form coupled drums after the given time for the wet etch instead of a fully released membrane. The horizontal features next to the holes in panels (a) and (b) are artifacts, resulting from the horizontal scan direction. The inset in (b) shows a part of the SiN surface without holes and thus a much smaller range of the scale bar to make smaller features on the surface visible. (c) Shown are five measurements, one on an unetched reference sample (blue), two measurements on locations that were exposed to BOE only at the upper side (supported: purple, green), and two measurements on locations that were exposed to BOE both at the upper and lower side, i.e. a released membrane (released: red, yellow). The two supported (and the two released) measurements match very closely and can hardly be distinguished in the figure. The numbers indicate the reflectivity at the laser wavelength used in the setup, i.e. 632.8 nm. A figure showing the full wavelength range of this data can be found in Appendix B.

The motion of the membrane is measured interferometrically and therefore the light is not only reflected at the SiN surface, but it is also reflected at the bottom of the cavity formed by the Si substrate as sketched below in Fig. 5.5. As the Si substrate is also exposed to the etchant, it thus makes sense to take a closer look also at its surface quality. Figure 5.4(a) is an SEM image of an area on the chip where the substrate was exposed to the etchant. The surface looks very smooth and hardly any variation over the surface is visible. The AFM measurement in panel (b) confirms that the maximum height from hill to valley in the measured area is 2 nm with an RMS roughness of about 154 pm. How good is that surface now in terms of its reflectivity of the measurement laser? Panel (c) compares the reflectivity of the “etched” silicon (red) with a polished reference piece of silicon (blue). Both reflectivities match extremely well over the full obtained wavelength range from 400 nm to 1000 nm and both show a reflectivity of 34.8% at 632.8 nm, i.e. the wavelength of the HeNe laser used in the setup. This shows, that even though

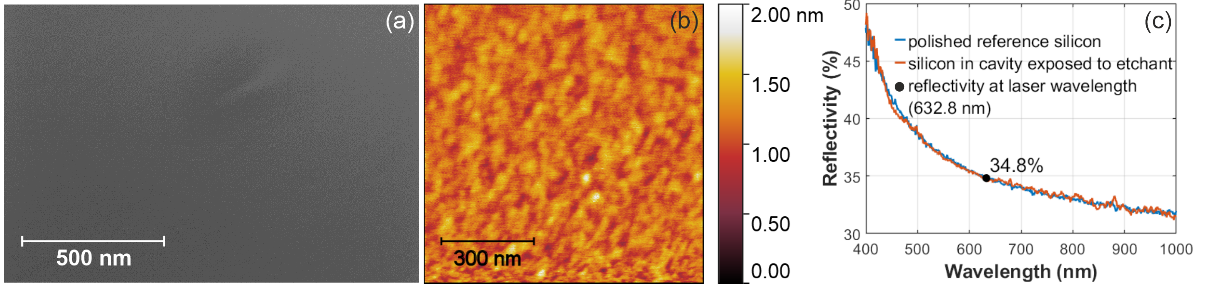

Figure 5.4: Measurement of the surface properties of the Si substrate after the SiO_2 layer has been etched away. The measurements were taken with an SEM (a), an AFM (b), and a reflectometer (c). The reflectometer measurements were taken on a polished reference Si sample (blue) and on the Si surface exposed to BOE (red). The black dot indicates the reflectivity of both samples at 632.8 nm, i.e. the laser wavelength of our setup. The measurements of (a), (b), and (c) were taken on close by, but not exactly the same parts of the Si surface.

being exposed to the etchant, the silicon substrate which serves as the end mirror of the cavity is of high quality as the polished reference silicon.

5.2.2 Reflectivity

It was already explained in Sec. 2.5.1 that the power of the reflected light depends on the distance of the membrane to the substrate. Fig. 5.5 visualizes the underlying interferometric principle. In panel (a) the geometry of the membrane and the cavity it forms with the substrate is visible. As the etchant starts to remove the SiO_2 at the holes, the SiN layer is exposed there the longest and an angled pattern is formed underneath the membrane as sketched. This is visible in the reflectivity map in Fig. 5.6 where not only the holes can be resolved but one can also see the change in reflectivity near and further away from the holes. Figure 5.5(b) illustrates the surfaces where the rays in this Fabry-Pérot-cavity reflect and interfere. Note, that the light hits the sample more or less perpendicular to its surface with a maximum angle of 16.3 degree due to the numerical aperture (NA) of the microscope objective of 0.28, as indicated in Fig. 4.8. A comparison of the reflectivities of supported and released SiN measured by a reflectometer has been shown in Fig. 5.3(c).

5.3 Mode properties

Having explained how the membranes are fabricated, in the following sections it will be discussed how the measurements with the lock-in amplifier are performed and how the resonances of the membranes are extracted from the measured data.

5.3.1 Response and mode shape

In the linear response regime used in our experiments, the measured signal $V_{\text{input}}(t)$ is proportional to the drive amplitude V_{out}. Hence, the responses are normalized by V_{out} and their units are, thus, V/V. In particular, we define $Z \equiv X + iY \equiv V_Z/V_{\text{out}}$. This overall system response can be written as a product of the frequency responses of the individual components: $Z(\omega) = G(\omega)R(\omega)\, \partial P/\partial U_{m,n}\, H_{m,n}(\omega)A(\omega)$. Here, A, R, and G are the responses of the piezo transduction (“actuation”), photodetector (“responsivity”), and amplifier (“transimpedance gain”), respectively. This relation is sketched in Fig. 5.7. Although on larger scales, signatures of the frequency-dependent piezo response can be seen [16], in a narrow span around the resonance frequency of interest, ω_0, all these responses are approximately constant and the ω

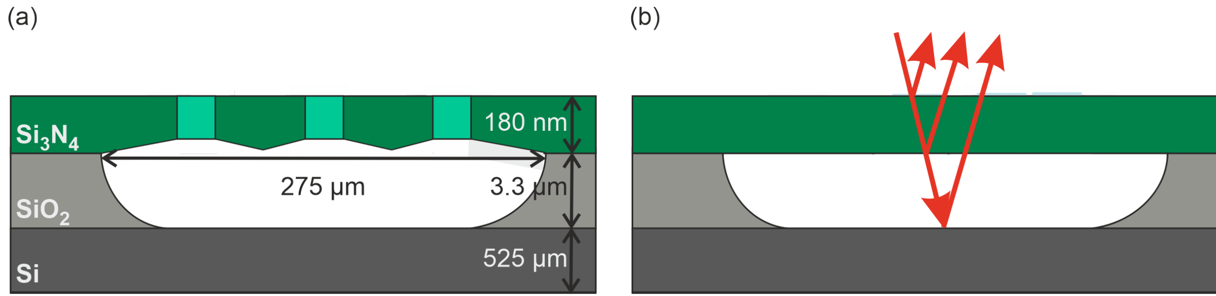

Figure 5.5: (a) Sketch of the cross-section of a membrane device. The light green areas in the SiN layer indicate that the membrane includes a series of holes. As the underetching starts at the holes and continues until the full membrane is released, different parts on the bottom of the membrane are in contact with the etchant for different times and the thickness is thus not constant all over the membrane. If the light is partially or fully hitting a hole, the reflected signal becomes even more complex and differs from reflections at unperforated parts of the membrane. This becomes visible in both the reflectivity maps (Fig. 5.6) and mode maps (Fig. 5.12). (b) Interferometric principle of the measurement setup. When actuated, the distance between Si_3N_4 and Si changes dynamically. This results in a time-dependent interference pattern of the light reflected at the membrane and the light reflected at the substrate (red arrows). For clarity, the light path is drawn with an angle while the light is actually hitting the membrane perpendicular to its surface with a maximum angle of 16.3 degree due to its numerical aperture of 0.28. The layer stack is SiN on air on silicon.

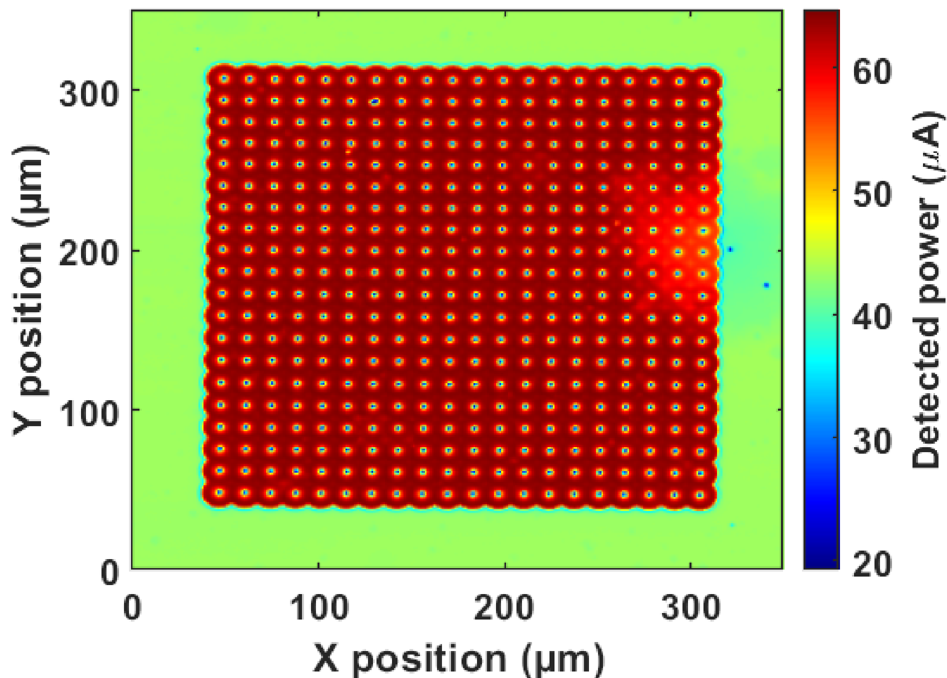

Figure 5.6: Reflectivity map of a membrane with a side length of 275 μm. The data was taken in the same measurement as Fig 5.14.

dependence is omitted. In contrast, $H_{m,n}(\omega)$ is the harmonic oscillator response function that transduces the piezo vibrations via the inertial force into the vibrational amplitude $U_{m,n}$ of the (m, n) mode, which varies strongly near the eigenfrequency $\omega_0 = \omega_{m,n}$.[2] Finally, $\partial P/\partial U_{m,n}$ is the change of the reflected laser power with the displacement of the entire mode $U_{m,n}$ [2]. Importantly, this quantity depends on the position of the laser spot: it is largest at anti-nodes and zero at a node. Using Eq. (2.7) introduced in Chapter 2 and applying the chain rule, it can be rewritten as $\partial P/\partial U_{m,n} = \partial P/\partial u \times \xi_{m,n}(x, y)$, where $\xi_{m,n}(x, y)$ is the normalized mode shape. Now $\partial P/\partial u$ is independent of the position as it quantifies the change in reflected power P for a given displacement u *at the readout position* (x, y)[3]. Combining all this, gives $Z(x, y, \omega) = Ce^{i\psi}H_{m,n}(\omega)\xi_{m,n}(x, y)$ for some proportionality constant C and complex angle ψ. This shows that the mapped normalized demodulated signal at constant frequency $Z(x, y \mid \omega)$ is directly proportional to the mode shape $\xi_{m,n}(x, y)$. Measuring Z as a function of the readout position (x, y) using any of the different methods presented later in this work thus enables mapping the mode shape $\xi_{m,n}$.

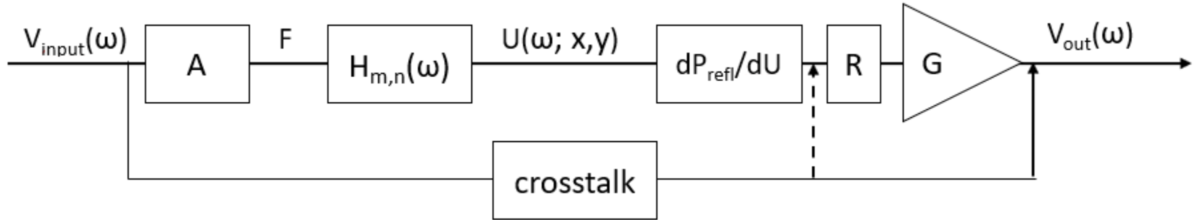

Figure 5.7: Sketch of the overall system response. $V_{input}(\omega)$ is the driving voltage from the NWA or lock-in amplifier output, A is the response of the piezo transduction, R is the response of the photodector, G is the response of the amplifier, $\partial P/\partial U_{m,n}$ is the change of the reflected laser power with the displacement of the entire mode $U(\omega; x, y)$, and $V_{out}(\omega)$ is the voltage as measured by the NWA or lock-in amplifier. The "crosstalk" symbolizes possible pathways of the electical crosstalk in the setup.

5.3.2 Demodulation

The demodulated signal $V_Z(t)$ has to be calculated to obtain the mode properties. Demodulation with the LIA can be seen as a calculation of the quadratures V_X and V_Y using $V_Z(t) = \langle 2V_{\text{input}}(t) \exp(-i\omega t)\rangle \equiv V_X + iV_Y$. Here, the angled brackets indicate low pass filtering using the demodulation bandwidth. The complex demodulated voltage $V_Z(t)$ can also be expressed in its magnitude and phase $V_Z(t) = |V_Z(t)| \exp(i\angle V_Z(t))$, where $\angle$ denotes the argument of a complex number. For the aforementioned signal $V_{\text{input}}(t) = V_{\text{in}} \cos(\omega t + \phi)$, one obtains $V_X = V_{\text{in}} \cos(\phi)$ and $V_Y = V_{\text{in}} \sin(\phi)$ so that $|V_Z(t)|$ is V_{in} and $\angle V_Z(t) = \phi$. Due to the low-pass filtering, the demodulated signals ("quadratures") are only slowly (compared to ω) varying in time; their sampled values are indicated with the index n.

5.3.3 Harmonic oscillator response

The harmonic oscillator response function $H(\omega)$ has the largest magnitude at the resonance frequency $\omega = \omega_0$ [2]. There, its phase is $\angle H(\omega_0) = -\pi/2$ so that on resonance, the total phase of $Z(\omega_0)$ becomes $\alpha - \pi/2 \mod \pi$ where the last term comes from the sign of $C\xi_{m,n}(x, y)$. This

[2]In principle, the response would be a sum over all modes $H_{\text{total}}(\omega) = \sum_{m,n} H_{m,n}(\omega)$ but for simplicity it is assumed here that only a single mode (m, n) gets excited. In Fig. 5.10 and Fig. 5.13(a) the combined responses of two and three modes, respectively, are fitted to the data.

[3]Further refinements in the readout model could include the finite spot size of the laser by writing $\partial P/\partial U_{m,n}$ as a two-dimensional convolution of the beam shape and the mode shape.

phase is typically used as the setpoint for the PLL introduced later in Sec. 5.4, ϕ_{sp}, as it locks ω to ω_0, thereby maximizing the magnitude of the signal. For this reason, the value of α is needed for every mode, which is determined by fitting the driven frequency response $Z(\omega \mid x, y)$ measured at a fixed position. In particular, they were fitted using the expression (c.f. Eq. (2.11)):

$$Z(\omega) = z_{\text{mech}} e^{i\psi} \frac{\omega_0 \gamma}{\omega_0^2 - \omega^2 + i\omega\gamma} + z_x e^{i\phi_x}, \tag{5.1}$$

where z_{mech} is the peak value and γ is the damping rate which is related to the quality factor $Q = \omega_0/\gamma$. The z_x term includes a small amount of electrical crosstalk [16, 145] (cf. the gray line in Fig. 5.8), which result in Fano-like resonances. More information about the electrical crosstalk can be found in Sec. 2.4.3.

Both during the demodulation (as a setting in the LIA), as well as in postprocessing, an additional "analyzer" phase α can be set. In the former case, this corresponds to $\exp(-i\omega t) \rightarrow \exp(-i\omega t - \alpha)$ for the aforementioned calculation of the quadratures. We use the latter, though, which performs the transformation

$$\begin{pmatrix} X' \\ Y' \end{pmatrix} = \begin{pmatrix} \cos\alpha & \sin\alpha \\ -\sin\alpha & \cos\alpha \end{pmatrix} \begin{pmatrix} X \\ Y \end{pmatrix}. \tag{5.2}$$

By setting the analyzer phase equal to the setpoint of the phase-lock loop, $\alpha = \phi_{sp}$, the X' quadrature (cf. the real part of Z') contains the mode shape, whereas Y' (cf. the imaginary part of Z') is related to the error e_j.

So far, the analysis has been for a single frequency ω. The Zurich Instruments HF2 lock-in amplifier with multi-frequency kit option can, however, generate an excitation signal with six different frequencies and subsequently demodulate the input signal at all of these. This enables measurements on six modes *simultaneously*, as employed in, for example, Fig. 5.12.

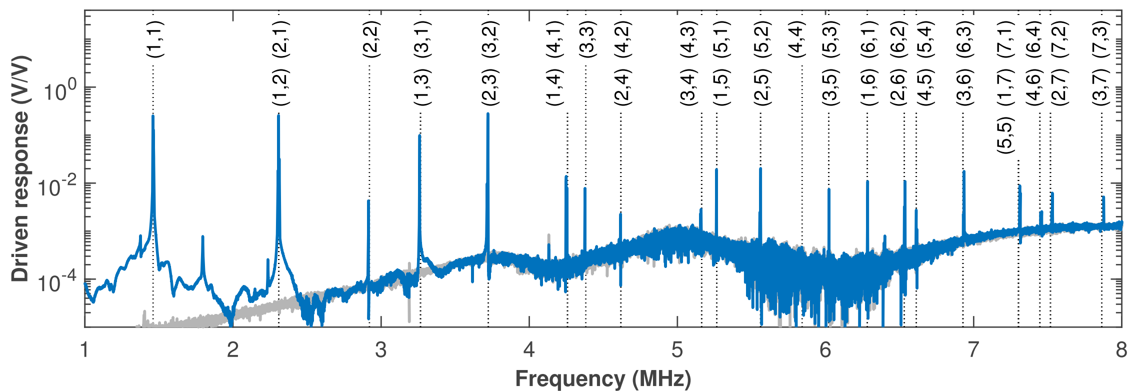

Figure 5.8: Driven response of the membrane measured using the NWA (blue) with the calculated frequencies (Eq. (2.8)) as black dashed lines and the mode numbers indicated. The gray trace is the instrument background.

An overview of the measured modes of the membrane displayed in Fig. 5.6 can be found in Fig. 5.8. It shows the driven response of the membrane (blue) measured with the NWA. The gray trace is the instrument background from which several peaks of the blue trace clearly stand out. The vertical dashed lines mark the frequencies of the calculated modes together with their mode number. They match very nicely with the measured peaks and thus allow us to identify the latter. Figure 5.9 shows zooms measured with the LIA of some of the modes in the overview spectrum and Table 5.1 lists their properties. A zoom of the response near the (3,1) and (1,3) modes is again shown in Fig. 5.10. It is noted that due to temperature variations in the lab, the values for the exact resonance frequencies may differ slightly between measurements. This drift, in combination with the relatively long duration of response function measurements, resulted in

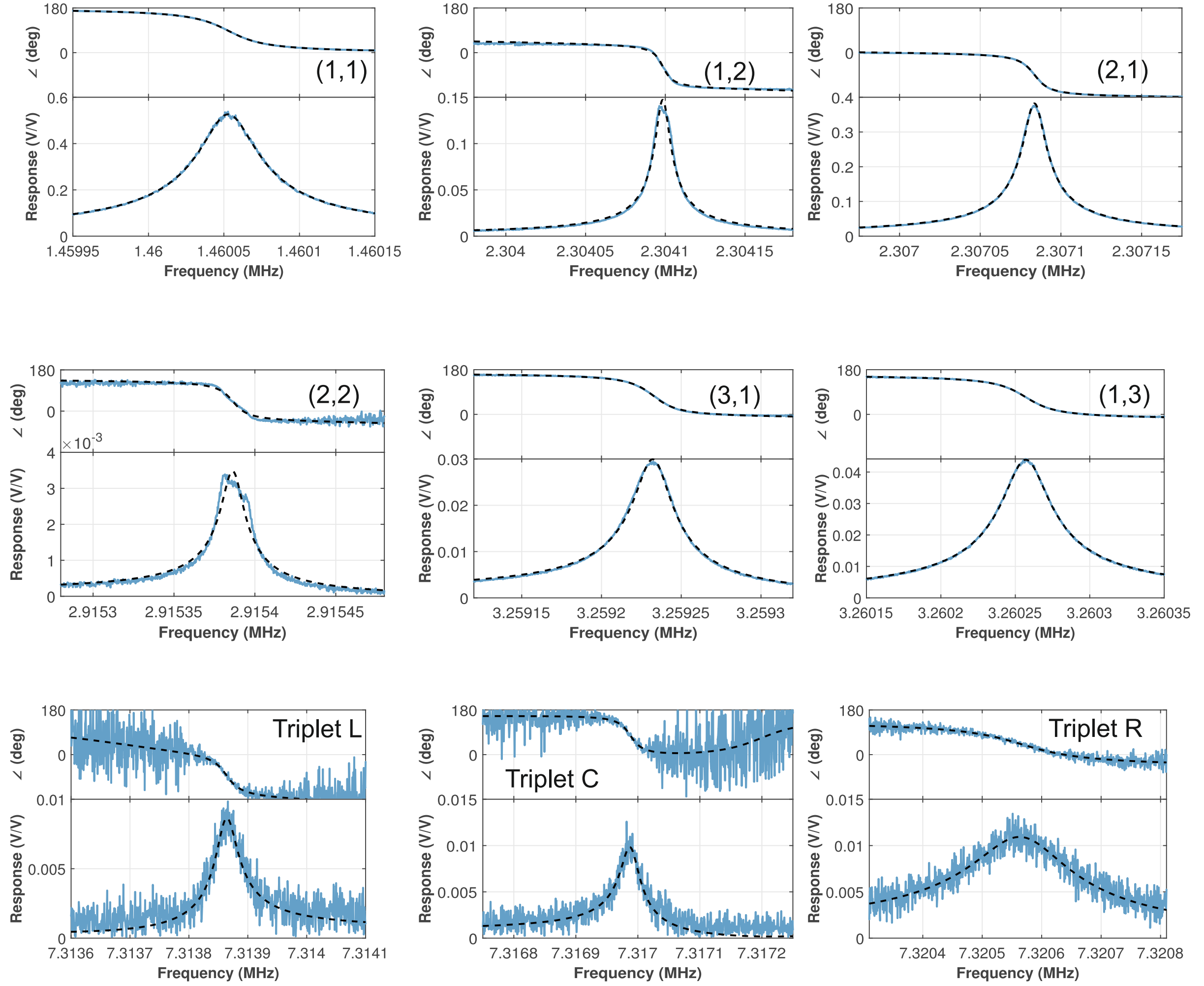

Figure 5.9: Driven responses of the modes described in this chapter. For the first 6 modes, the span is 200 Hz, whereas for the triplet the span is 500 Hz. The blue curves are measured using the LIA, whereas the black dotted lines are the fits of Eq. (5.1) to the data. The measurement settings and fit results are indicated in Table 5.1.

a clear distortion of the (2,2) resonance. A similar measurement with the NWA showed a regular response and yielded $\gamma/2\pi = 5.22 \pm 0.02\,\text{Hz}$, which corresponds to $Q = 559\text{k}$.

5.4 PLL mode mapping

5.4.1 Comparison of different methods for mode mapping

Before presenting the full two-dimensional mode maps obtained with our PLL setup, I will first compare in Fig. 5.11 line traces taken with different methods to show the robustness and efficiency of ours. The membrane is scanned in the y direction while sequentially acquiring the signal of the (1,3) mode at 3.260 MHz using four different methods. First of all, Fig. 5.11(a) shows the dc reflection, which overlaps for all methods. The suspended membrane has a higher reflectivity compared to the supported regions as discussed above and the holes are visible as small dips in the signal.

Now, method (i) for obtaining a mode shape (dark blue lines in Fig. 5.11) is to simply

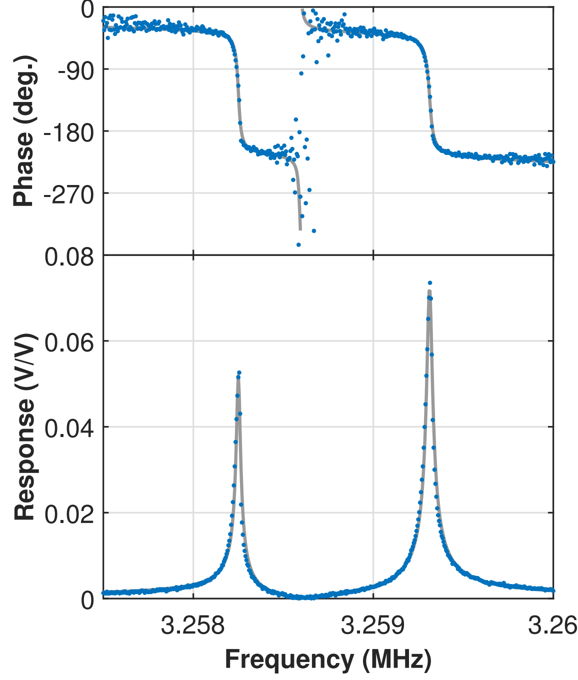

Figure 5.10: Network analyzer measurement of the driven response near the (3,1) and (1,3) eigenfrequencies. Two separate resonances with a spacing of 1.06 kHz can be seen. As discussed in the text, the left and right resonance correspond to the (3, 1) and (1,3) modes, respectively.

Table 5.1: Overview of the excitation power, setpoint, and fit parameters (see Fig. 5.9) for the modes discussed in this work. The fit uncertainty in the resonance frequency is below 3 Hz for all modes, but the exact value drifts over the course of time.

Mode	**Excitation** (dBm)	**Frequency** (MHz)	**Q** (10^3)	$\gamma/2\pi$ (Hz)	z_{max} (V/V)	α (rad)	ϕ_{sp} (°)
(1,1)	-45	1.460 053	39.0 ± 0.1	37.42 ± 0.05	0.527	3.111 ± 0.001	87
(1,2)	-50	2.304 098	250.0 ± 2.4	9.22 ± 0.09	0.149	0.594 ± 0.007	-68
(2,1)	-50	2.307 084	167.4 ± 0.4	13.78 ± 0.04	0.384	0.012 ± 0.002	-98
(2,2)	-35	2.915 386	208.3 ± 3.9	14.00 ± 0.26	$3.5 \cdot 10^{-3}$	2.283 ± 0.014	-104
(3,1)	-35	3.259 232	140.2 ± 0.6	23.24 ± 0.09	0.030	2.856 ± 0.003	-111
(1,3)	-40	3.260 257	104.7 ± 0.2	31.14 ± 0.05	0.044	2.788 ± 0.001	-20
Triplet L	-35	7.313 864	199.8 ± 9.6	36.61 ± 1.76	$9.1 \cdot 10^{-3}$	0.172 ± 0.037	-68.8
Triplet C	-35	7.316 988	238.0 ± 12.2	30.74 ± 1.58	$9.7 \cdot 10^{-3}$	2.842 ± 0.039	-263.3
Triplet R	-35	7.320 566	45.0 ± 1.3	162.81 ± 4.66	0.011	2.262 ± 0.029	49.8

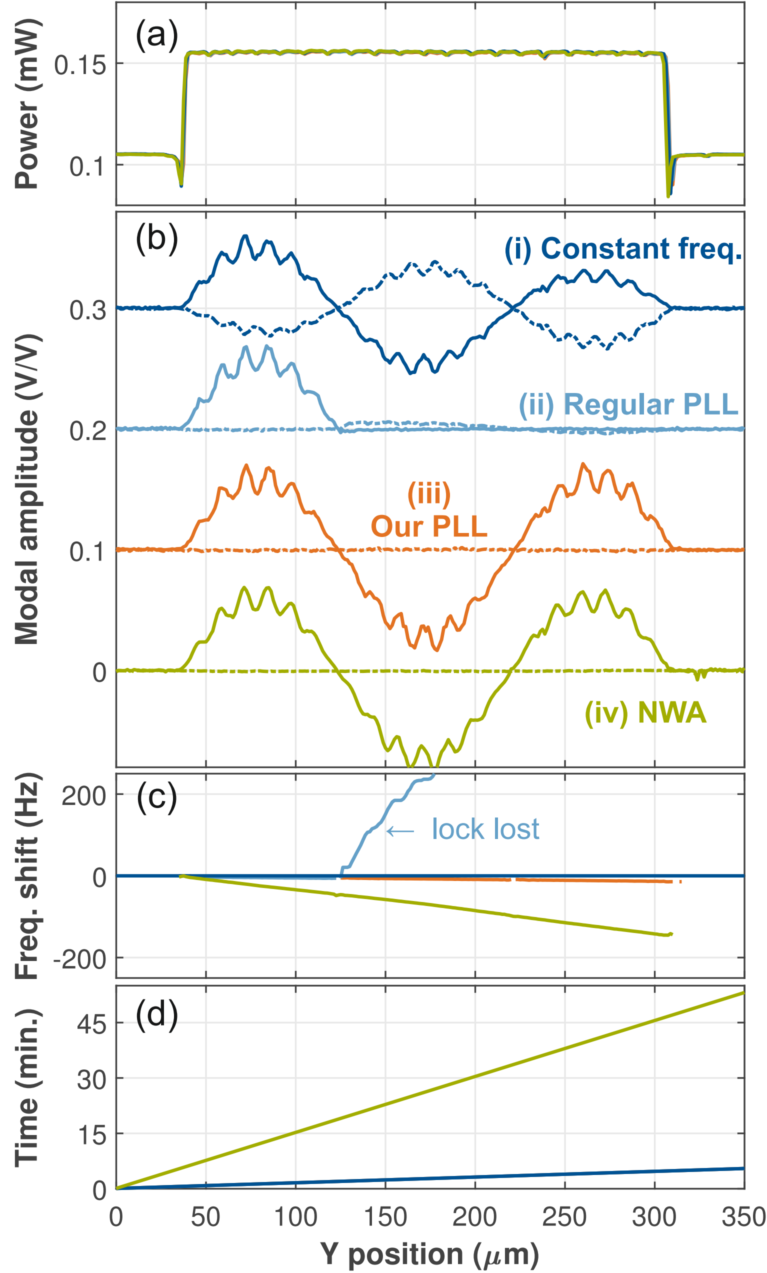

Figure 5.11: Line traces over the membrane for (i) constant frequency (dark blue), (ii) regular PLL (light blue), (iii) the modified PLL with mod 180° (orange), (iv) data measured using a network analyzer (green). (a) Reflected laser power. (b) The mode profile of the (1,3) mode near 3.26 MHz. Solid (dashed) lines indicate the real (imaginary) part. The curves are offset for clarity. (c) Frequency change during the measurement. For (i)-(iii), this was the actuation f, whereas for (iv) the resonance f_0 was extracted from the NWA traces. By definition, the frequency was constant in (i). (d) Elapsed time since the start of the trace.

drive the mechanical resonator at that resonance frequency and record the amplitude [172]. Figure 5.11(b) shows that the suspended part of the membrane has a clear response with small modulations due to the holes. There are two nodes in the modal amplitude vs. y, indicating that this is the (1,3) and not the (3,1) mode, which was not clear from the frequency response alone. Taking a closer look shows that, unlike the theoretical prediction of Eq. (2.7), the anti-nodes have unequal magnitudes. Also, the modal amplitude shows an imaginary part (see Sec. 5.3.2 for details) that grows with time. This indicates that the resonance frequency drifted from the

(fixed) driving frequency during the measurement. This means that the naive approach (i) does not yield accurate mode shapes.

A standard approach to track a resonance is a phase-lock loop [162,173]. Here, it is a software-implemented PI-controller in LabVIEW in combination with digital demodulation in the LIA[4]. The PI-controller updates the driving frequency f to keep the phase ϕ at the setpoint ϕ_{sp} using:

$$f_{n+1} = f_1 + Pe_n + I\sum_{j=1}^{n} e_j. \tag{5.3}$$

Here, $e_n = \phi_n - \phi_{\mathrm{sp}}$ is the error in the n-th sample, and P and I are the proportional and integral gain, respectively. Fig. 5.11(b) shows that with this regular PLL (method (ii), light blue), the first anti-node has a lower imaginary part compared to the previous method. However, as also indicated by the sudden large shift in Fig. 5.11(c), the PLL loses lock after the node where the mode changes sign, resulting in a π jump in ϕ. This problem that almost all off-the-shelf PLL-based systems have, motivates our improvements to the regular PLL. For our method (iii), we, first of all, added a modulo operation: $e_n \to e_n \mod \pi$. This way, the PLL can handle the sign flips and will remain locked irrespective if the motion is in phase or in anti-phase. A second addition is to turn the PLL off until a minimum signal magnitude is reached. This maintains the frequency while scanning e.g. over the nodes. The orange curve in Fig. 5.11(b) shows the result of our new method: The anti-nodes are now equal in magnitude and the imaginary part stays very small. Our robust method (iii) thus faithfully maps the mode, even in the presence of frequency drifts, nodes, and sign changes.

The fourth mode-mapping approach, method (iv), is performed with the NWA [67]. Here, a full frequency response is measured at every point of the line trace, and its fitted maximum and phase (Sec. 5.3.2) are used to reconstruct the modal amplitude. Similar to our improved PLL (cf. method (iii)), method (iv) is also capable of mapping a drifting mode accurately (Fig. 5.11(b,c), green). However, as Fig. 5.11(d) shows, the NWA method is about ten times slower compared to all other methods. Although it can be considered the gold standard, method (iv) is too slow to do e.g. full 2D mode maps efficiently. After comparing the results from the line traces taken under realistic conditions with the different methods, it is clear that our method (iii) is the preferred technique. The response of measurements on a single location on the membrane have been discussed in the previous section. To further demonstrate the use of our PLL setup, we will now turn our attention to the measurements of two-dimensional mode maps.

5.4.2 Mode maps

Using our method, the first six modes were measured simultaneously while scanning the membrane in the x and y direction, resulting in the 2D mode maps shown in Fig. 5.12. The first mode in Fig. 5.9 at 1.46 MHz is indeed the (1,1) mode, and the second one at 2.30 MHz is the (1,2) mode. Although some modes are slightly distorted compared to Eq. (2.7), one can still easily recognize them. Also note that fine details, such as the release holes (1 μm radius) are clearly visible in these high-resolution maps.

It can be obtained from the mode maps that $f_{1,2} < f_{2,1}$ whereas $f_{1,3} > f_{3,1}$. This means that the breaking of the degeneracy between the (m, n) and (n, m) modes for $m \neq n$ is not caused by different side lengths of the membrane (cf. a rectangular instead of a square shape) and that more subtle effects play a role here. As mentioned above, some of the maps do not show completely straight nodal lines as expected from the theory. This may be an effect of the finite bending rigidity of the membrane [174] and is confirmed using finite-element simulations. A discussion of the properties of the other detected modes in the range of about $1 - 20$ MHz on

[4]Note, that it is also possible to perform this task using the digital signal processor in the lock-in amplifier [120, 140], which can further improve the operation speed.

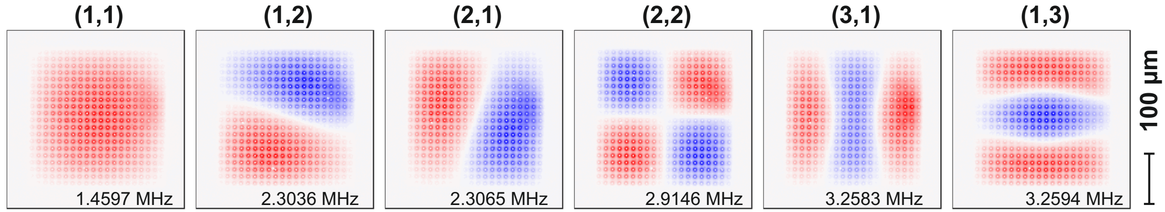

Figure 5.12: Normalized mode maps (real part) of the first six modes of the square SiN membrane acquired in a single, simultaneous, measurement with the method described in this chapter. The release holes are visible as an array of dots across the entire surface of the structure. Starting frequencies are indicated in each map; further properties are listed in Table 5.1.

this membrane as well on differently sized membranes can be found in [152] and [175].

When modes are degenerate, a superposition of them is also an eigenmode and, a priory, it is not clear what their modes would look like. Mode mapping is thus crucial to understand the nature of the resonance. Eq. (2.8) shows that the (5,5), (1,7), and (7,1) modes are triple degenerate and that these are expected around 7.3 MHz. Figure 5.13(a) shows three distinct peaks near this frequency. Their mode maps in Fig. 5.13(b) indicate that, unlike the modes in Fig. 5.12, their shapes are not directly given by Eq. (2.7); instead, they show a much richer spatial structure. With the resolution of our mapping, it is possible to quantitatively determine the contributions of each individual mode to the superpositions. For this, the mode shape is written as $u(x, y) = w_{5,5}\xi_{5,5}(x, y) + w_{1,7}\xi_{1,7}(x, y) + w_{7,1}\xi_{7,1}(x, y)$ and the weights $w_{m,n}$ are determined by linear fitting to the experimental mode shapes. The results in the bottom row of Fig. 5.13(b) show good agreement with the experiment, including the structure of nodal lines (white) and the variation in amplitude at the different anti-nodes. Finally, note that the modes have very different damping rates γ, as seen from the peak width in Fig. 5.13(a) (see also Table 5.1). It is known that the clamping losses depend on the displacement field near the edge [70, 167, 176, 177]. Looking at the first two mode shapes shows alternating positive (red) and negative (blue) displacements near the edge of the membrane, whereas the third one (cf. the one with increased damping) has the same sign everywhere along the edge (red only); the radiation of acoustical energy into the supports would be very different. This explanation for their different linewidths would be difficult to obtain without our high-resolution mode maps with phase information.

5.4.3 Variation of the measurement scheme

Higher modes can be quite difficult to lock to due to their fast drift and often loose lock during the measurement. As discussed in the comparison of the different mode mapping techniques, we have observed that the modes drift over time, making the phase locking technique inevitable when performing long measurements. The fundamental and higher modes, however, have a certain frequency ratio and this ratio remains constant while the modes are drifting (see Fig. 5.14). This is as this ratio only contains m and n, while being independent of changes in σ and L. This enables us to only lock to the fundamental mode and update the information for the higher modes by the known frequency ratio without having to lock to all of them individually. This helps to also measure the above mentioned modes that are otherwise challenging to lock to.

5.5 Thermal motion

The transduction factor and thermal motion of nanomechanical resonators have been introduced earlier in Sec. 2.5.4. Here the thermal motion measurement on a membrane is shown. Figure 5.15(a) displays the driven fundamental membrane mode obtained with the NWA. This

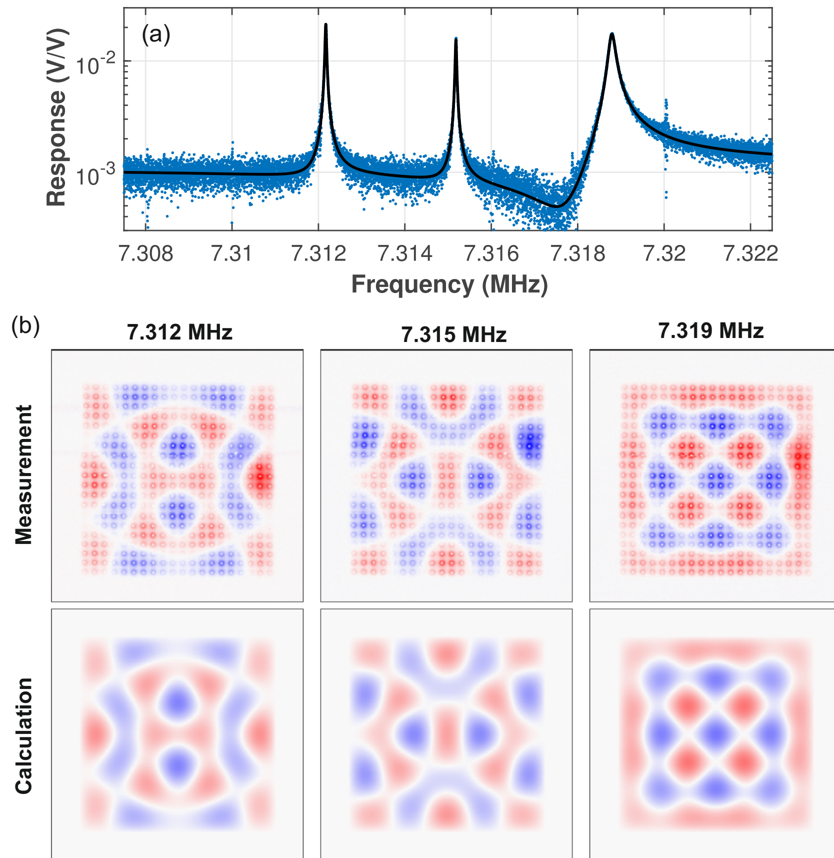

Figure 5.13: (a) Driven response near $f_{5,5} = f_{1,7} = f_{7,1}$. The triplet is fitted using three standard harmonic oscillator responses taking crosstalk into account (Sec. 5.3.2) [145] (black line). (b) Measured (top) and calculated (bottom) mode maps. The weights from the linear fitting are $\{w_{5,5}, w_{1,7}, w_{7,1}\} \propto \{0.561, -0.506, 0.656\}$, $\{0.817, 0.260, -0.515\}$, and $\{0.105, 0.694, 0.712\}$ for the left, middle, and right peak, respectively. The fit uncertainty in the weights is 0.002.

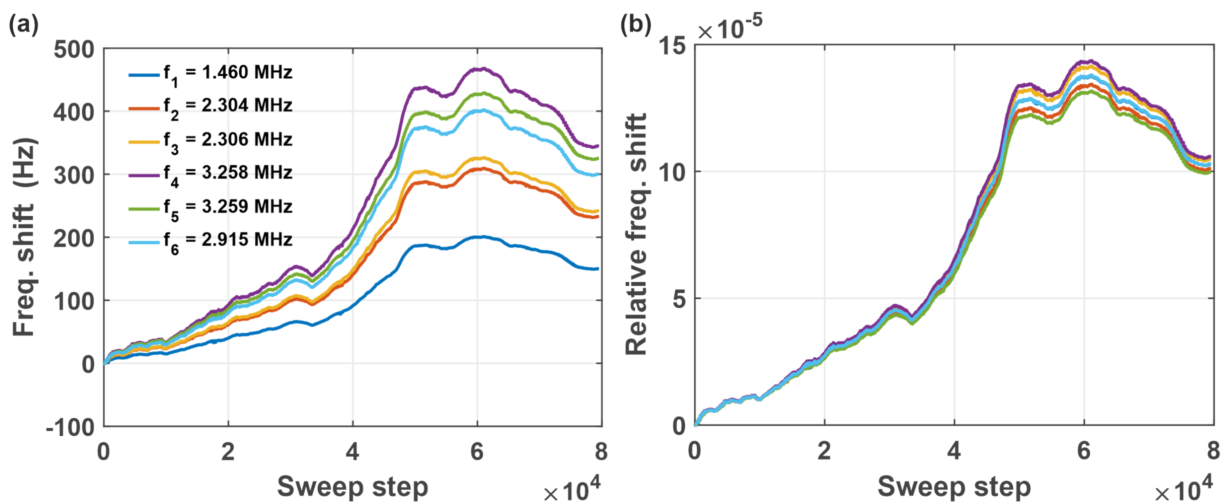

Figure 5.14: (a) Shift of the resonance frequencies of the first six modes over time (sweep steps). (b) Frequency shift of (a), relative to the shift of the first mode.

measurement is typically done right before the thermal motion measurement with the SPA as it returns the resonance frequency and thus tells at which frequency to search for the much less pronounced thermal motion peak. Due to the drift of the resonance frequency with temperature both the driven and undriven modes only align in frequency if measured shortly one after another. Panel (b) displays the thermal motion measurement. From this measurement, a transduction factor $\frac{dV}{du}$ of 67 kV/m with a noise floor of 456 $\mathrm{fm}/\sqrt{\mathrm{Hz}}$ was calculated using eq. (2.14). The SNR could be further improved by averaging over a longer measurement time. However, this improvement is at the expense of the sharpness of the peak as the mode is expected to drift over time.

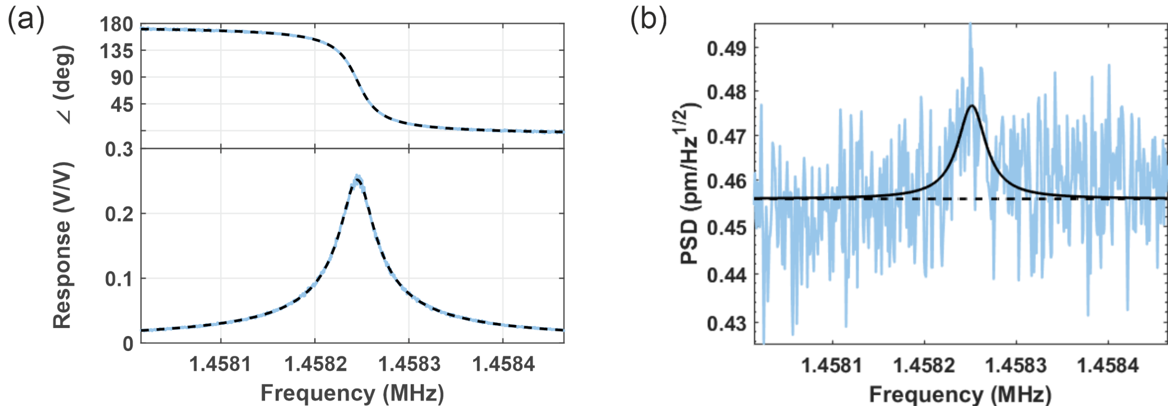

Figure 5.15: (a) Measurement of a fundamental membrane mode with the NWA. (b) Thermal motion measurement of the mode of (a) with a SPA.

5.6 Temperature dependence

We have seen above that the resonance frequencies drift over time. This became apparent most prominently in method (i) and caused it to fail. Such drifts are often caused by small variations in temperature which can depend on such simple but unavoidable parameters as the time of the day and the outside temperature or the amount of direct sunlight shining into the lab[5]. How do the mode properties react to much higher changes in temperature? The setup allows to actively change (or stabilize) the temperature over a wide range as described in Sec. 4.7. The membrane was cooled (heated) step-wise from the ambient[6] temperature inside the chamber of about 32 °C to ∼ 17 °C (∼ 62 °C) and then heated (cooled) back to ambient. At each new setting, several hundred measurements were taken to give the temperature time to settle.

The observed trends as well as overshoot and hysteresis, both for the cooling and the heating experiment, are consistent over several runs of this measurement (independent of the sweep number), as well as with the very different devices, namely racetracks with mechanical parts introduced in Sec. 3.5)[7] on another chip [178], measured in the LVC setup[8]. Despite the differences in the design, the racetrack devices are also made out of SiN in a similar sandwich structure and the fundamental mode of the mechanical resonators has a frequency of ∼ 2.5 MHz and is thus

[5]Temperature control (air conditioning, optical shielding) can lower or even suppress these effects, still heating of the devices by the measurement laser and subsequent drift of the resonance frequencies will still be present.

[6]Note that ambient temperature does not refer to the temperature in the lab but the temperature inside the vacuum chamber. The latter lies at around 32 °C due to the high power consumption of the stages which dissipate heat into the vacuum chamber.

[7]Remember, the racetrack devices are ring resonators with suspended beams implemented in the flat regions and suspended beams patterned with photonic crystals in their vicinity.

[8]As explained in Chapter 4. Even though the LVC setup is a quite different setup, it has the same type of temperature control implemented as discussed in Sec: 4.7.

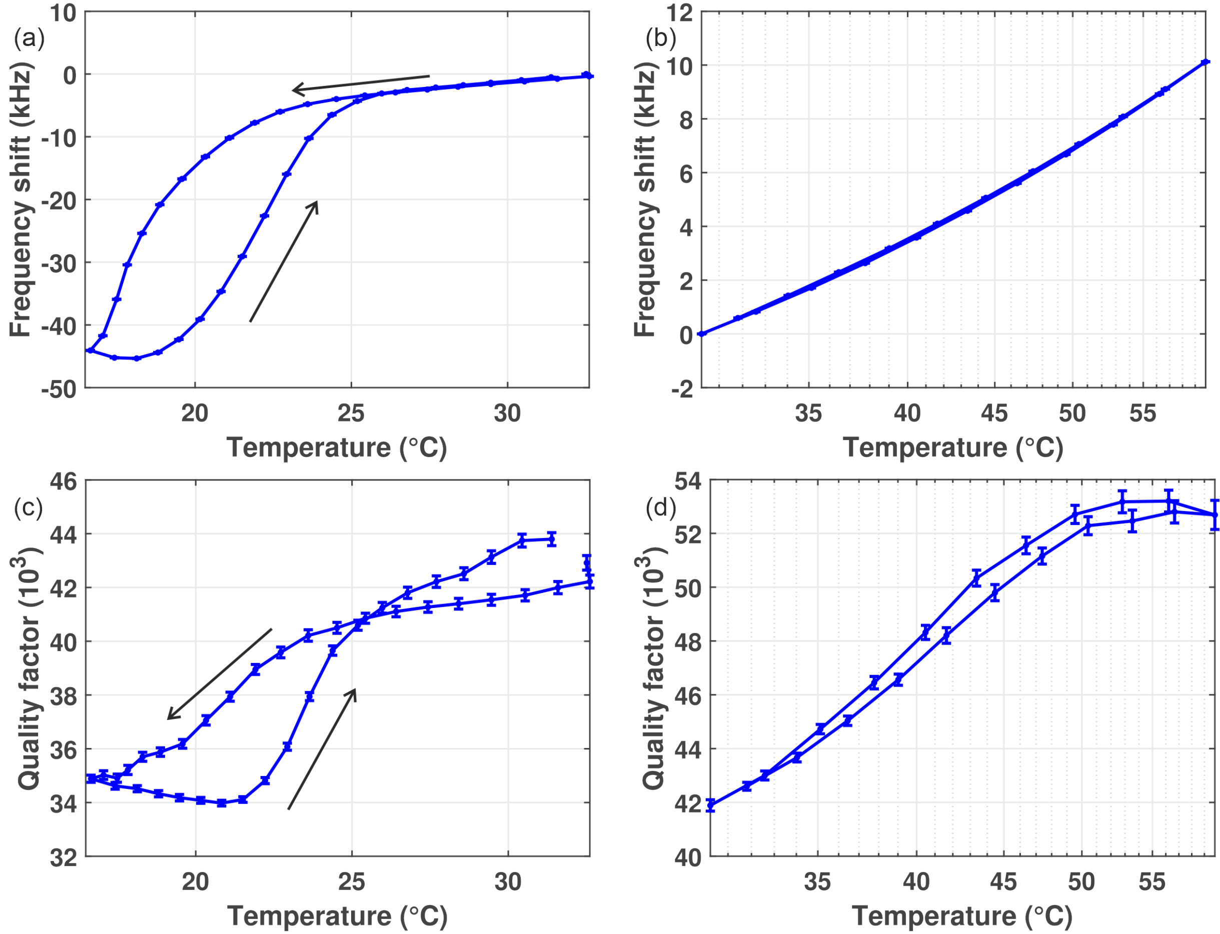

Figure 5.16: Temperature sweep: Resonance frequency shift (top panels) and quality factor (bottom panels) of the fundamental mode when the temperature is changed. (a,c) The sample was cooled below ambient temperature and warmed up back to ambient. At each new setting of the current through the Peltier element, 500 traces were taken to let the temperature settle. In the plot, the result of the last trace at each setting is shown. The black arrows indicate the sweep direction. (b,d) The sample was heated above the ambient temperature and let to cool back to ambient. At each new setting of the current through the Peltier element, 300 traces were taken to let the temperature settle. In the plot, the result of the last trace at each setting is shown.

similar to that of the membranes. Fig. 5.18 shows the result of the temperature sweep on such a device. In the measurement of panel (a) the temperature is increased by the laser power instead of by the Peltier element. Increased laser power sent into the racetrack heats the beams and causes thermal expansion of the mechanical resonators. As a consequence, the intrinsic stress is reduced and thus the resonance frequencies go down[9]. This is also reflected in the measurement. The frequency of the fundamental mode of a racetrack beam is reduced by about 7 kHz for an increase in temperature by $\sim 20\,^\circ$C. The shift of the adjacent photonic crystal beam is much lower and only reduced by less than 1 kHz. This is because this beam does not serve as a waveguide and is thus much less affected by laser heating. As a reminder, the photonic crystal is designed such that it forms a band gap around 1550 nm and does not support the light mode. In panel (b) the temperature is changed via the Peltier element. The increase in temperature by about $35\,^\circ$C causes an increase of the resonance frequency by ~ 18 kHz, resulting in $\frac{\Delta f}{\Delta T}\frac{1}{f} = 2.1 \cdot 10^{-4}/^\circ$C,

[9]Note, not only the mechanical devices expand due to heating, but the whole ring resonator does and changes its circumference. Thus, the ring resonances also experience a shift with respect to the laser wavelength.

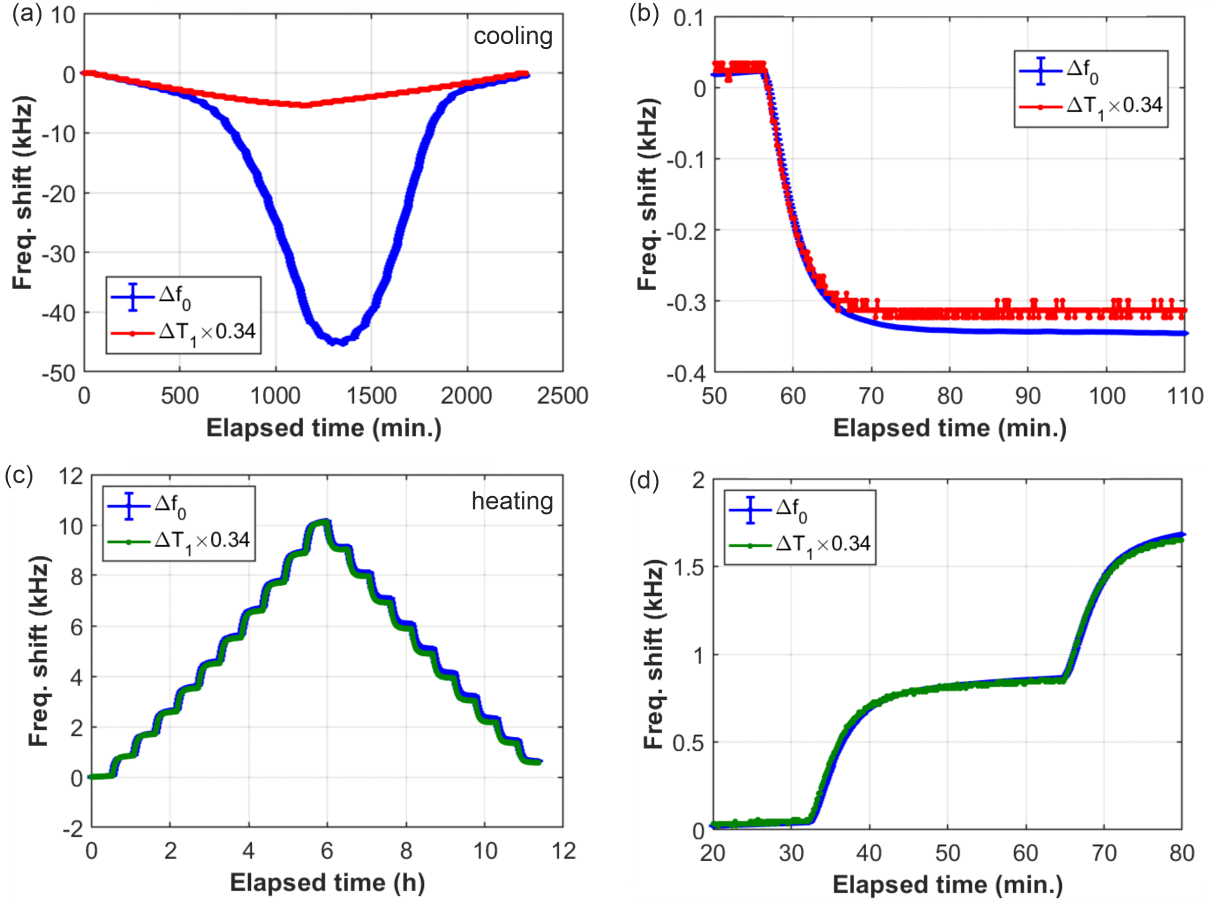

Figure 5.17: Overlay of the measurement of the temperature and the observed shift in resonance frequency versus time. (a) The stage was cooled below ambient temperature and heated up again with a zoom shown in (b). (c) The stage was heated above ambient temperature and cooled down again with a zoom shown in (d). The temperature was scaled with a factor of 0.34 kHz/° C. The data was obtained in the same measurements as that in Fig. 5.16. Panels made by Menno Poot.

which is consistent with the observation on the membranes (Fig. 5.16). In contrast to (a), the frequency rises with the temperature as the whole chip is heated. This is a strong indication that the thermal expansion of the bulk is larger than that of the beams and increases the strain in the beam. The behavior of both beams coincides here, again as the whole chip is heated and not only one of the beams. The hysteresis is rather small for both beams.

As detailed in Ref. [179], for the simpler case of SiN strings on Si substrate, the increase in resonance frequency with increasing temperature, which we observe here is expected. The thermal expansion coefficient of Si ($\alpha_{Si} = 2.6\,\text{ppm/K}$ [180]) is larger than that of SiN ($\alpha_{SiN} = 1.67 - 2.3\,\text{ppm/K}$ [85]). Heating the sample thus results in a larger expansion of the substrate with respect to the resonator, which, as a consequence will be stretched and the increasing stress results in a higher resonance frequency. For strings this can be calculated as follows [179, 181]:

$$f_0(T) = \frac{n}{2L}\sqrt{\frac{\sigma_0 - E(\alpha_{str} - \alpha_{sub})(T - T_0)}{\rho}}. \tag{5.4}$$

With the mode number n, string length L, stress σ_0, Young's modulus E, the thermal expansion coefficient of the string and the substrate α_{str} and α_{sub}, respectively, mass density ρ, temperature T and reference temperature T_0 (corresponding to stress σ_0). The change in frequency thus results from a temperature-induced change in stress. A temperature difference of 30 °C in a 100 μm long beam should thus cause a shift in frequency of the fundamental mode by 7.3 kHz. This

differs by about a factor of 2 to the shift of ~ 16 kHz obtained in case of strings implemented in racetracks. This is as the derivation does not include the thermal expansion of the SiO_2 cladding layer ($\alpha = 0.55$ ppm/K [182]). This now is significantly smaller than that of SiN and is expected to add more complexity. Also, the quality factor (Fig. 5.16(c,d)) is reduced at lower temperatures, indicating a temperature related reduction in strain.

So far, measurements of the temperature dependence have been performed on a single location on the membrane. The setup provides a great tool to obtain the full mode maps at different temperatures. This can reveal a potential temperature dependence of the mode shapes and might give further insight into the mechanisms playing a role in the temperature dependence of the mode properties.

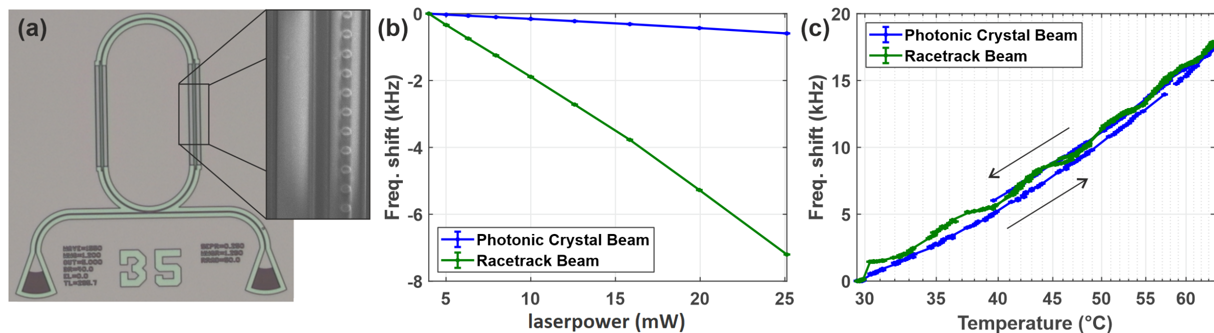

Figure 5.18: Racetrack device with photonic crystal beam in the vicinity of the suspended beams integrated into the racetrack. (a) Frequency shift vs. laser power sent into the device (blue: photonic crystal beam, green: beam integrated into the racetrack). (b) Frequency shift measured during a temperature sweep, as in Fig. 5.16(b). The black arrows indicate the sweep direction.

5.7 Beyond membranes

Beyond the SiN membranes, extensively studied in this work, a large variety of other optomechanical devices can be studied with the setup. For example, we also measured devices like trampolines and cantilevers. Figure 5.19 gives a glance at the measurements of these devices. (a,b,c) show the reflectivity maps of a trampoline, a cantilever, and an AlN-covered membrane, respectively. As mentioned in the introduction of this chapter, such devices can be used in sensing and detection by applying materials on them and carefully observing the resulting changes in the dynamic properties, like resonance frequencies, mode shapes, and quality factors. A set of membranes has been covered with layers of AlN of varying thicknesses and the aforementioned properties have been studied. The AlN was applied by Giulio Terrassanta in collaboration with the WMI [96,97,109]. The results have been published in [183] and [131]. The cantilever shows a pattern that already appears like a higher mode. This, however, is not true, the pattern results from the strong bending of the cantilever. The magnitude ranges over several periods of the interference pattern and is thus visible in the reflectivity map. Panels (d,e,f) show the (1,1), (1,3), (1,3) modes of the respective devices. The quality factors are 32.6k, 6.76k, 76.9k, respectively. Panels (g,h,i) are the PLL maps of these modes.

5.8 Summary

In conclusion, I have presented a fast method to map the amplitude and phase of vibrational modes under realistic conditions. Our method is based on an improved PLL and is robust against frequency drift, phase jumps, and nodal lines and outperformed traditional methods. The novelty and advantage lie in the combination of high resolution, sensitivity, tracking using a PLL, as

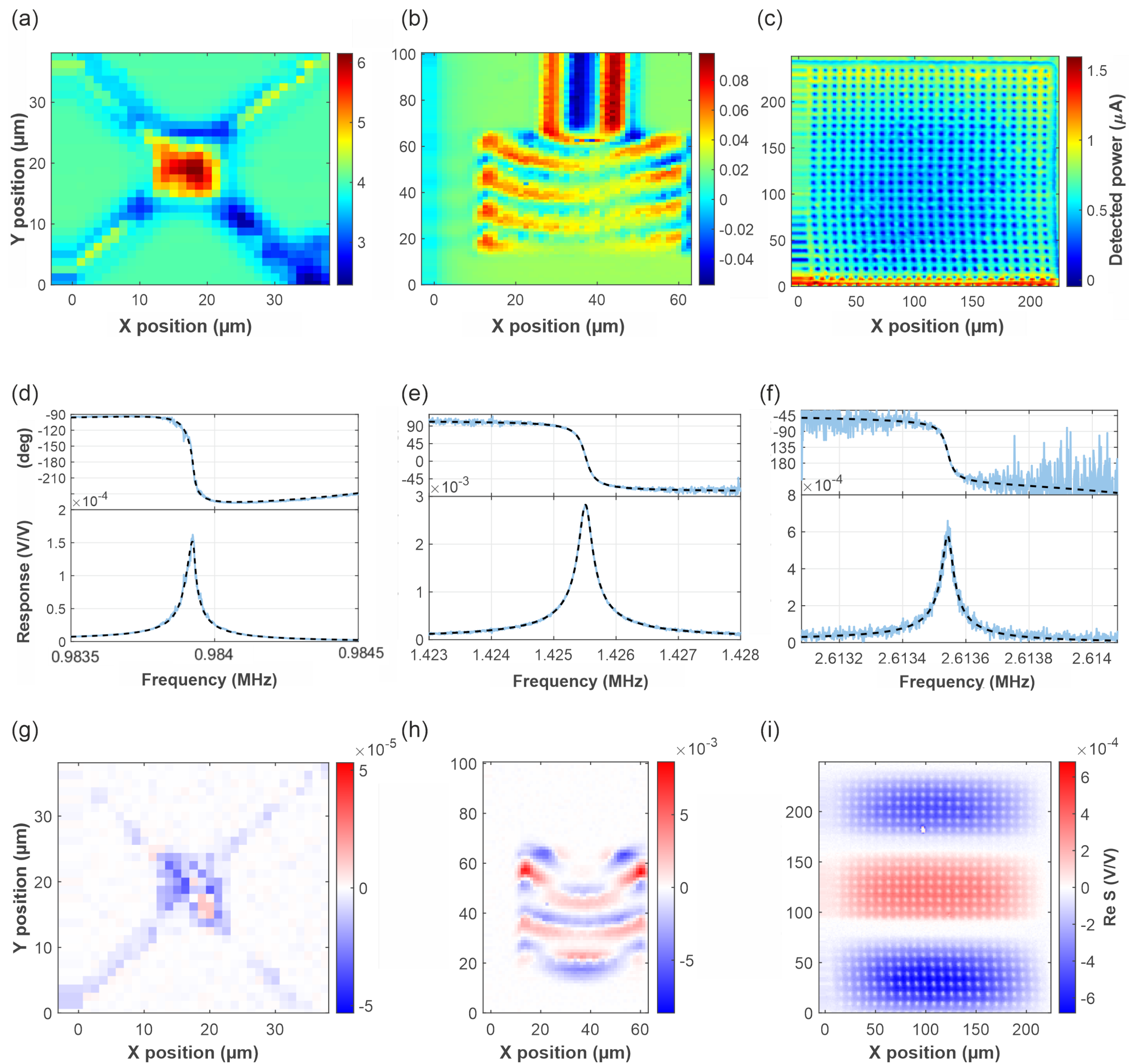

Figure 5.19: Measurements on a trampoline (a,d,g), cantilever (b,e,h) and AlN coated membrane (c,f,i). Top row: Reflectivity maps; middle row: frequency and phase response of the driven devices; bottom row: PLL maps of the respective modes shown in the middle row. Measurements taken by Timo Sommer (left), Julius Röwe (middle), and Aditya Yadav (right).

well as its robustness against sign changes of the mode shape when crossing nodal lines. I have illustrated the technique using a high-stress Si_3N_4 membrane, where degenerate modes were unambiguously identified. Up to six modes can be mapped simultaneously and from high-resolution mode maps the individual weights of superposition modes could be determined, and insights into the clamping loss mechanisms were obtained. Some examples for further measurements beyond the membranes were shown to show the broad spectrum of applications for this setup. Future plans are the study of one- and two-dimensional arrays of coupled micro-drums. Cantilevers with flakes of transition-metal dichalcogenides (TMDs) shall introduce strain into these flakes and reveal fascinating quantum effects. The setup is currently expanded for being capable of performing these quantum experiments.

CHAPTER 6

Geometric tuning of stress in pre-displaced silicon nitride resonators

This chapter covers the study of stress tuning in pre-displaced silicon nitride beams. I will introduce a novel method to geometrically tune the tension in pre-strained resonators by making Si_3N_4 strings with a designed pre-displacement. This enables us to e.g. study their dissipation mechanisms, which are strongly dependent on the stress. After release of the resonators from the substrate, their static displacement is extracted using scanning electron microscopy. The results match finite-element simulations, which allows us to quantitatively determine the resulting stress. The in- and out-of-plane eigenmodes are sensed using on-chip Mach-Zehnder interferometers and the resonance frequencies and quality factors are extracted. The geometrically-controlled stress not only enables tuning of the frequencies but also of the damping rate. We develop a model that quantitatively captures the stress dependence of the dissipation in the same SiN film. We show that the pre-displacement shape provides additional flexibility, including control over the frequency ratio and the quality factor for a targeted frequency.

This chapter is largely based on material published in Nano Letters.
David Hoch, Xiong Yao, and Menno Poot. Geometric tuning of stress in pre-displaced silicon nitride resonators. *Nanoletters, 2022* DOI:10.1021/acs.nanolett.2c00613 [16].
Reprinted with permission from Nano Lett. 2022, 22, 10, 4013–4019. Copyright 2022 American Chemical Society.
My personal contribution to the content of this chapter is the sample design and fabrication of some of the chips fabricated in the context of this chapter. I also performed many of the measurements discussed below and personally did a large share of the data processing and application of the model onto our results, which includes literature research and coding of the data processing scripts. Xiong Yao took over most of the FEM simulations, taking the SEM images and strongly assisted with taking the measurements under my supervision.

6 Geometric tuning of stress in pre-displaced silicon nitride resonators 87
6.1 Introduction 89
6.2 Sample and Setup 89
6.3 Beam shapes 93
6.4 Simulations 94
6.5 Relaxation and stress tuning 95

6.5.1 Stress relaxation in released beam 95
6.5.2 Influence of the beam parameters on the relaxation 95
6.6 Dynamic beam analysis 97
6.7 Dissipation 99
6.7.1 Dissipation mechanisms 99
6.7.2 Dissipation in stress-tuned Sbeams 100
6.7.3 Influence of D_0 on the dissipation 105
6.7.4 Influence of L on the dissipation 105
6.8 Influence of the beam shape 108
6.9 In- and out-of-plane Q_{bending} 109
6.10 Nonlinearity 110
6.11 Design considerations 113
6.12 Summary 114

6.1 Introduction

Micro- and nanomechanical devices are utilized in a huge variety for both applications and fundamental research, including sensing and detection [63, 184–186], phase shifting in the optical [144] or radio frequency [187] regime, and research in the quantum regime [2, 188–190]. There is a high demand for resonantly driven devices in the below and low MHz regime [120, 191], where SiN is an excellent choice of material due to its high intrinsic stress and therefore very high quality factors [89, 90, 140, 192]. The eigenfrequencies of SiN resonators are highly dependent on their stress. This typically can only be changed via the deposition process [193], for example by varying the silicon content from Si-rich SiN_x to stochiometric Si_3N_4 [136]. Every stress value would, however, need a different deposition run, making it expensive and inflexible as every batch of wafers is limited to one specific stress. Finally, different deposition parameters may result in different amounts of defects making a systematic study of the stress dependence of the dissipation challenging. To overcome these limitations, several techniques for stress engineering have been pursued [50], including bending of the chip [54], phononic crystal patterning [58], loss dilution [58], clamp widening [88], hierarchical structuring [51], clamp tapering [55], or altering the resonator design [53, 194]. Some of the ideas discussed in these publications are displayed in Fig. 6.1.

Here, I present a novel method to *geometrically* tune the stress of nanomechanical structures [122], adding a new degree of freedom for, e.g. applications demanding resonators with controllable resonance frequency. It also enables us to study damping as a function of stress under otherwise identical conditions. By design, our nanofabricated 'S'-shaped beams are pre-displaced and thus longer than the distance between the two clamping points L. The beams are pre-stretched because of the high tensile stress in the Si_3N_4 film. The displacement results in a net component of this stress pulling towards the center. Thus, when releasing them, they straighten and partially relax their stress [122] as illustrated in Fig. 6.2(a). This relaxation is studied quantitatively using scanning-electron microscopy, supported by simulations, which will be described in Sec. 6.5. The reduction in tension also strongly influences the dynamics of the resonators, such as their eigenfrequencies and quality factors (Q). To study this, we use integrated Mach-Zehnder interferometers to optically sense their driven motion, as described in Sec. 2.5.3. The observed change in Q with the stress is quantitatively explained by the model for the dissipation. Finally, we study the influence of different pre-displacement profiles on the dynamics.

Our devices provide valuable insight into the role of stress in the damping of SiN resonators, and add geometrically-tunable stress as a new degree of freedom for a variety of future experiments in the field of optomechanics, such as sensing [195], synchronization [196], and quantum optomechanics [197].

6.2 Sample and Setup

The dynamic measurements on the released devices were performed on two samples ("A" and "B") with 270 individual devices, which all contain a pre-displaced doubly-clamped beam. In addition, each chip contains 9 calibration MZIs without beams and 18 devices which directly connect the input and output grating coupler with a single waveguide to normalize over the transmission profile of the grating couplers (see Fig. 2.9 and explanation in Sec. 2.5.3) The design parameters including beam length (L), pre-displacement (D_0), and shape of the devices were systematically swept. As long as not stated otherwise, the data presented comes from beams following a double S-shape design, as described in detail in Section 6.3. The largest pre-displacement D_0 is located at the middle of the beams (see Fig. 6.2(a)) and is varied from 0 to 4 μm in steps of 0.5 μm. As illustrated by the micrograph of an individual device in Fig. 6.2(b), sensing its motion is done via integrated MZIs. A full overview of the chip design and the sweep parameters is provided

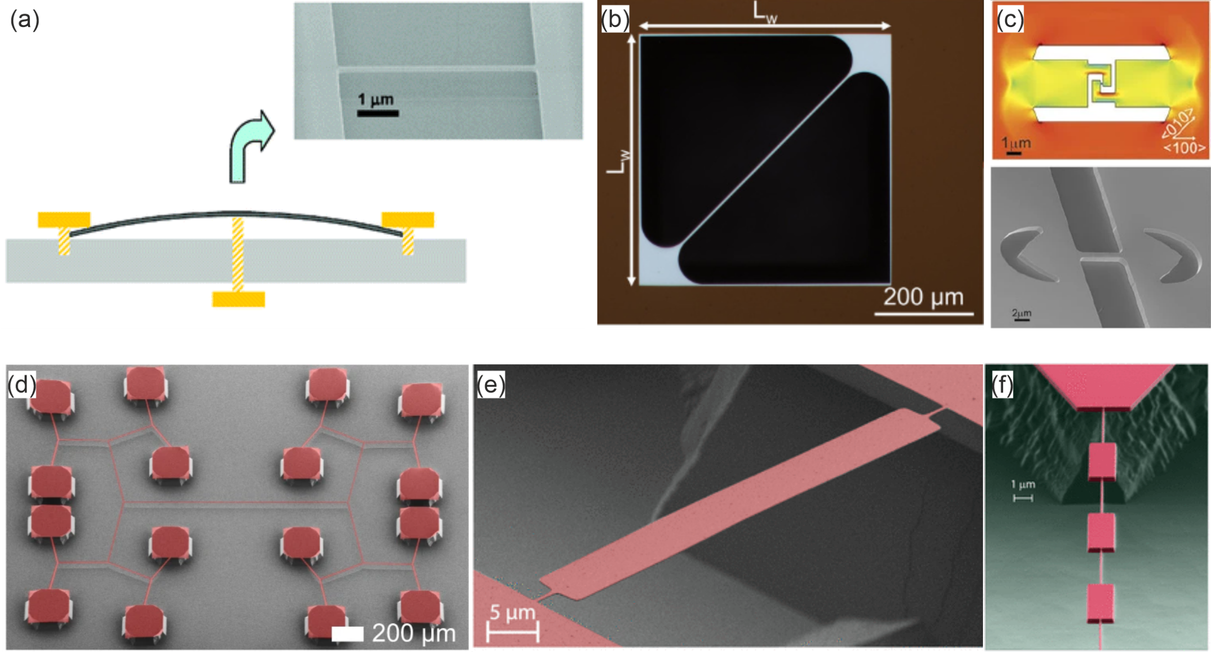

Figure 6.1: Various techniques of stress tuning: (a) Bending of the whole chip. Reprinted and adapted with permission from Verbridge *et al.* [54]. Copyright 2007 American Chemical Society. (b) Widening of the clamping points, as demonstrated by Sadeghi *et al.* [88], reprinted and adapted with permission from AIP Publishing. (c) Integration of structures into the bulk, close to the clamping points, as demonstrated by Zabel *et al.* [53], reprinted and adapted with permission from Springer Nature. (d) Hierarchical structuring of the resonator. Reprinted and adapted with permission from Bereyhi *et al.* [51] (Creative Commons Attribution 4.0), (e) Clamp tapering as demonstrated by Bereyhi *et al.* [55], Reprinted and adapted with permission from Nano Lett. 2019, 19, 4, 2329–2333. Copyright 2019 American Chemical Society. (f) Phononic crystal structuring. Reprinted and adapted with permission from Ghadimi *et al.* [58]. Copyright 2017 American Chemical Society.

in Fig. 6.3 together with Tab. 6.1. A third sample, identical to chip A, was used to extract D_0 and D via SEM images. This way, possible influences of charging and carbon deposition on the sample used for the dynamical measurements were avoided. The SEM images were taken on a ZEISS NVision® 40 a with 10 kV acceleration voltage. In Fig. 6.7, both the experimental and simulated D_0 and D before and after release will be shown.

sweep parameter (μm)	value 1	2	3	4	5	6	7	8	9
pre-displacement (H)	0.0	0.5	1.0	1.5	2.0	2.5	3.0	3.5	4.0
beam length (I)	50	59.5	73.5	96.2	138.9	250			
beam MZI distance (B)	0.1	0.15	0.2	0.3	0.5				

Table 6.1: Design parameters of the devices chip A. The pre-displacement is swept horizontally (H), the beam length is swept vertically within a block (I), and the beam-to-MZI distance is swept blockwise (B) (c.f. Fig. 6.3).

The devices are made of 330 nm thin high-stress stoichiometric silicon nitride (Si_3N_4), that was grown commercially using LPCVD on top 3300 nm silicon dioxide (SiO_2) on a silicon substrate [63] (Fig. 6.4(a)). Device patterning is performed by electron beam lithography using ZEP520A resist (Fig. 6.4(b,d)) and subsequent dry etching (Fig. 6.4(c,e)) with combined reactive-ion and inductively-coupled plasma etching (ICP-RIE). The fabrication of the devices with photonic Mach-Zehnder interferometers and the mechanical beams is done in two separate

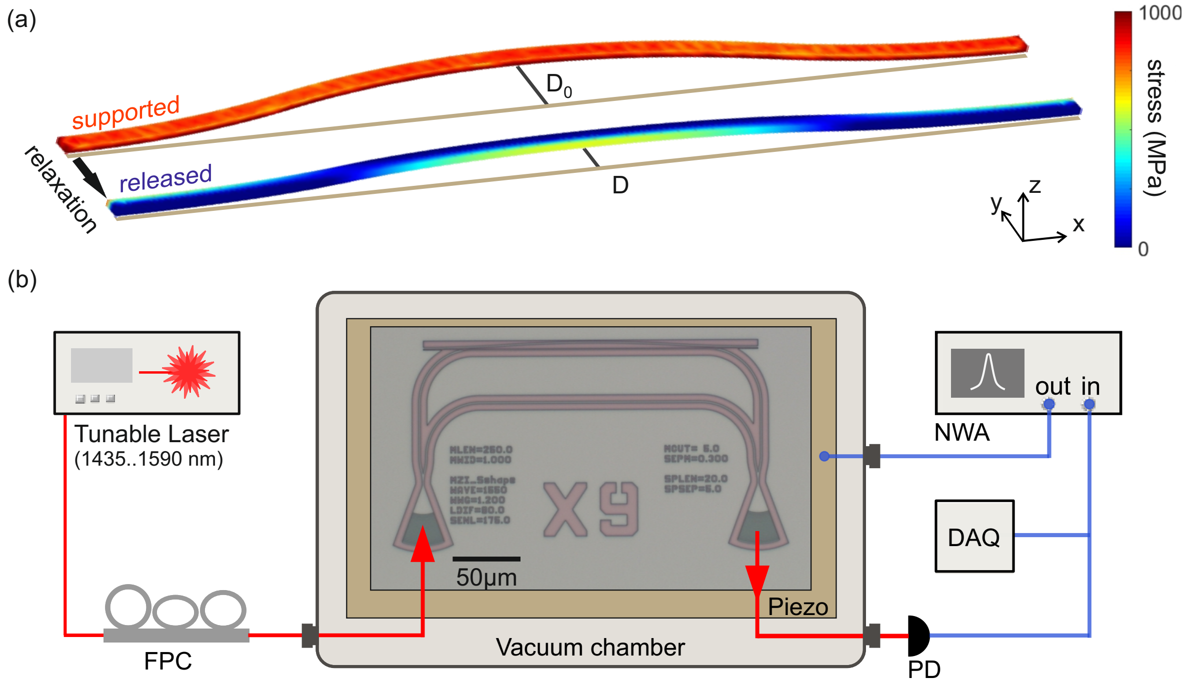

Figure 6.2: (a) Illustration of the stress distribution of a pre-displaced nanomechanical beam, before and after relaxation [122]. The beam straightens when being released and the stress relaxes, depending on the beam length and initial displacement. (b) Setup for the dynamic measurements. The chips are placed inside a vacuum chamber to avoid air damping. The probe laser is a tunable step laser and the polarization of the light is optimized with an FPC. The light is coupled on and off the chip with grating couplers and a fiber array placed above the sample. An NWA is driving the piezo element (ocher) underneath the sample, mechanically exciting the resonator. It also measures the signal coming from the photodetector (PD). For positioning the chip, the signal from the PD can also be read via a DAQ. A micrograph of a single device containing an integrated MZI with a 250-μm-long beam above the sensing waveguide of the interferometer is shown in the schematic. On each chip, there are many of these devices.

lithography steps where the SiN around the waveguides is etched such that a thin layer of a few 10s of nm remains (Fig. 6.4(e)) to protect these structures during release [144]. The mechanical parts, i.e. the beams under study, are fabricated by etching $\sim 70\,\text{nm}$ into the SiO_2 cladding layer (Fig. 6.4(c)) followed by a release through wet etching the underlying SiO_2 with buffered hydrofluoric acid (Fig. 6.4(f)) and subsequent critical point drying (Fig. 6.4(g)). A detailed description of the individual nanofabrication steps can be found in Chapter 3.

The finished chip is glued on a piezo-electric actuator and placed inside a vacuum chamber to reduce air damping, as described in Sec. 4.5. Then, as illustrated in Fig. 6.2(b), each device to be measured is positioned under an optical fiber array and light from a tunable laser is coupled into and out of the MZI using grating couplers. The transmitted light is detected by a photodetector which is read out with a data acquisition system and with a network analyzer which is also used to generate the driving signal that actuates the piezo, as detailed earlier in Sec. 2.5.3. The setup automatically locates and aligns the devices under the fiber array, steps the laser wavelength and determines its optimal value, and measures the driven response of the beam resonators [143]. This way, not just individual devices can be measured, but dependencies on device parameters, such as length, pre-displacement, or shape can be studied quantitatively.

As mentioned above, in this work, three chips were measured to cover all the presented beam parameters: two optically and one using the scanning electron microscope to extract D_0 and D (Sec. 6.5). The distance between the beam and sensing arm was also varied to make sure to

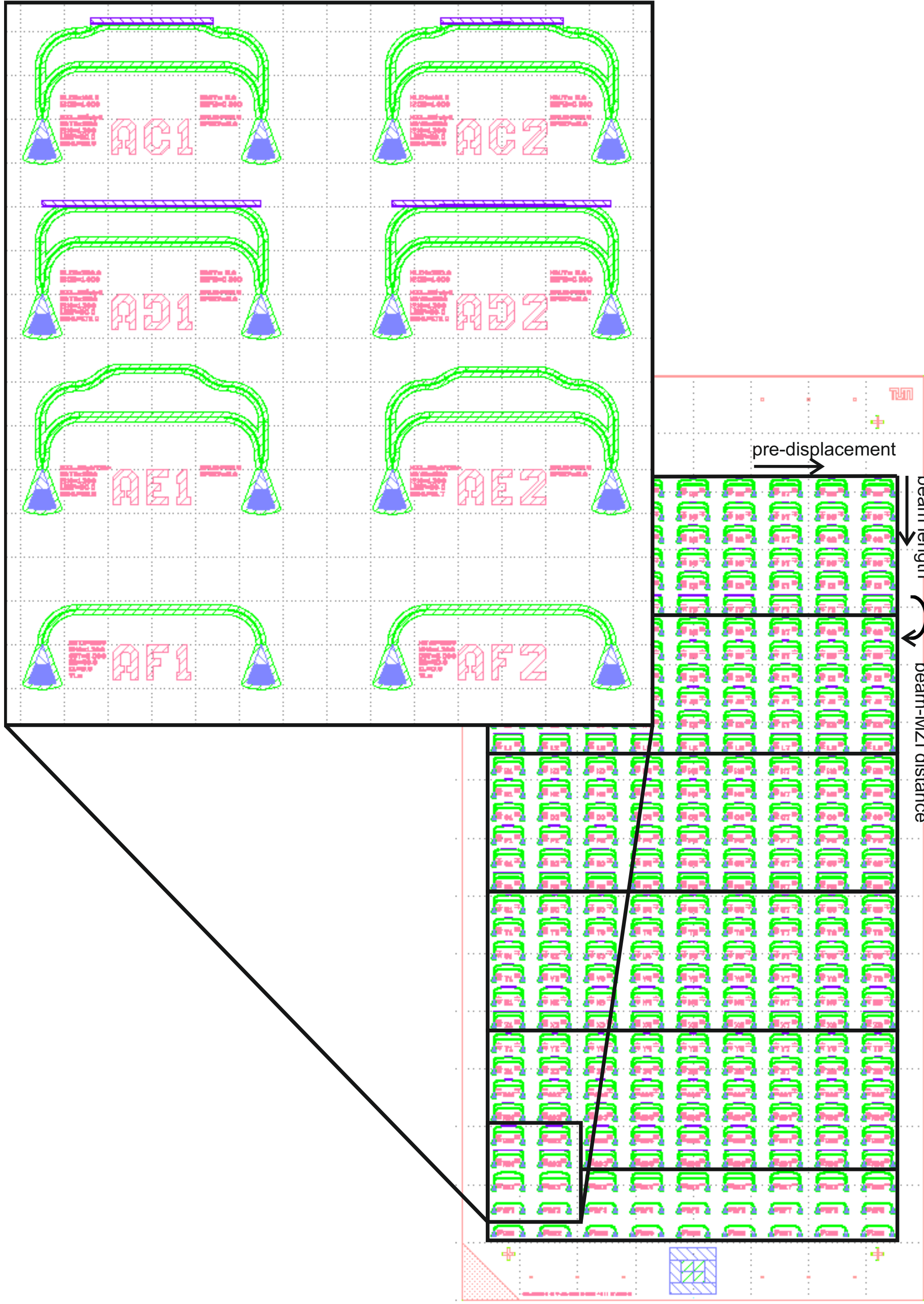

Figure 6.3: Chip design A as realized with the parameters listed in table 6.1. Horizontally the pre-displacement of the beams is swept. Vertically the design consists of five blocks as indicated by the black boxes. Within each block, the beam length is swept. The devices in the different blocks have the same parameters, only their distance to the MZI varies. At the bottom, three rows of calibration devices are placed: one row that only consists of a waveguide connecting the two grating couplers and two identical rows of MZIs without a beam. The inset shows a zoom into a part of the design with two rows of calibration devices and two rows of devices with beams.

include beams that are on the one hand fully released and far enough away from the sensing arm not to stick or to hit it when actuated, and on the other hand, still have a high enough signal to

detect the motion. The beam-to-sensing-arm distance is not expected to affect the dynamics of the beam, like frequency or damping rate, in any way, as long as the beam can resonate freely.

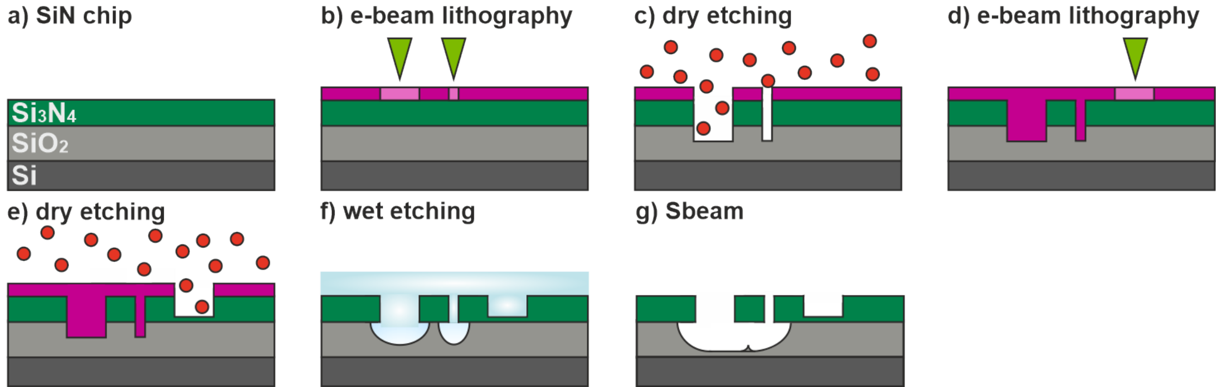

Figure 6.4: Nanofabrication steps for the Sbeam chip. (a) The blank chip consists of a 330 nm thin layer of Si_3N_4 (green) on a 3300 nm cladding layer of SiO_2 (light gray). The substrate is $\sim 525\,\mu$m silicon (dark gray). The Si_3N_4 and SiO_2 layers are on both sides of the double-sided polished chip. (b) The surface, covered with ZEP520A resist, is exposed in an electron-beam writer. In this first lithography step the structures that are going to be released later are defined. (c) The developed chip is dry-etched in an ICP-RIE. It is etched through the SiN layer, about 70 nm into the SiO_2. (d) In the second lithography step, the photonic structures are defined via electron-beam lithography. (e) In the second dry-etching step the photonic structures are etched such that about 30 nm of SiN remains. (f) The mechanical structures are released by wet-etching with buffered hydrofluoric acid. The photonic structures are protected from release by the remaining SiN layer. (g) The finished chip. The chip is critically point-dried to protect the mechanical structures from being destroyed by the surface tension of the liquid.

6.3 Beam shapes

The individual Sbeams are designed such that they follow a smooth shape with no sharp corners even with a displacement of few μm. The center line $y = u_0(x)$ of the Sbeam design consists of four circle segments - making up two S-shapes - that end perpendicular to the clamping points. For straight beams ($D_0 = 0$) the segments have no curvature, but the radius of curvature decreases with increasing center displacements: $R_c = ((L/4)^2 + (D_0/2)^2)/|D_0|$. This results in a curve length of $\ell = 4R_c\theta \approx L + \frac{1}{4}\pi^2 D_0^2/L \geq L$, where $\theta = \arccos(1 - |D/2R_c|)$ is the mid-angle of an "S". As an example, a Sbeam with $L = 96.2\,\mu$m and $D_0 = 4\,\mu$m would be 0.46% longer than a straight beam. The width of the Sbeam perpendicular to the center line is held constant at W by changing $R_c \to R_c \pm W/2$ for the two sides, keeping θ the same.

The other shapes were generated using (trigonometric) functions. In this case, the sides of the beam were defined by shifting the center $y = u_0(x)$ by $\pm W/2$ in the y-direction. The sine-shaped beams follow a sine function with half a period from 0 to π and thus have non-perpendicular edges at the clamping points. Likewise, the triangular beams have a sharp corner at the clamping points as well as at their center, whereas the cosine-shaped beams follow one (two, three) full periods of a shifted cosine function and do not have any kinks. In particular, the functions are:

$$u_0(\tilde{x}) = D_0 \times \begin{cases} 1 - 2|\tilde{x} - \frac{1}{2}| & \text{for "triangular"} \\ \sin(\pi\tilde{x}) & \text{for "sine"} \\ \frac{1}{2}(1 - \cos(2\pi\tilde{x})) & \text{for "cosine"} \\ \frac{1}{2}(1 - \cos(4\pi\tilde{x})) & \text{for "2 cosines"} \\ \frac{1}{2}(1 - \cos(6\pi\tilde{x})) & \text{for "3 cosines"} \end{cases} \tag{6.1}$$

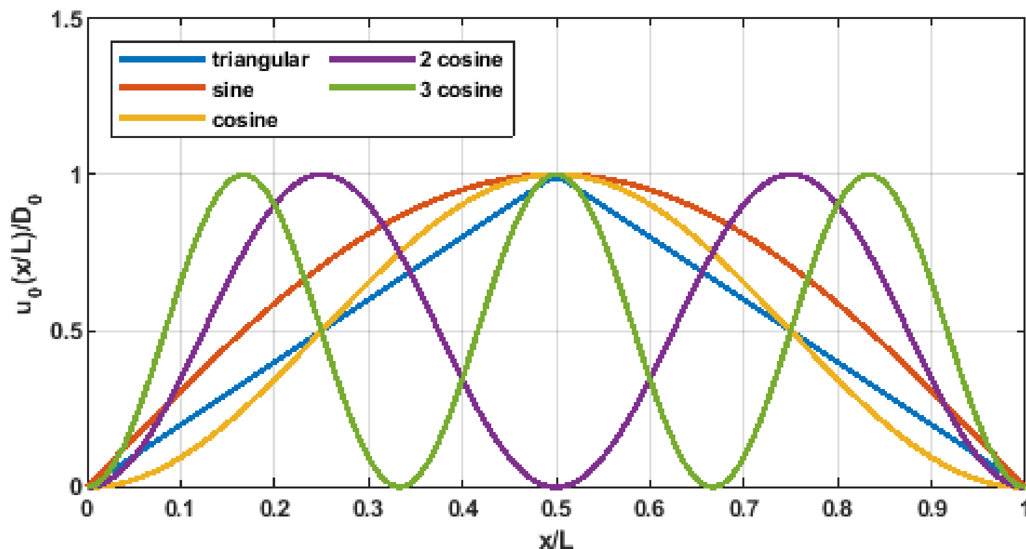

Figure 6.5: Normalized displacement $u_0(\tilde{x}/D_0)$ of each beam shape vs. the normalized position $\tilde{x} = x/L$. The shape of the Sbeam closely follows that of the cosine and is not plotted additionally.

where $\tilde{x} = x/L = 0..1$ is the normalized x-coordinate. Note that for all shapes $u_0(x) \geq 0$ for all x, i.e. everywhere they are pre-displaced away from the sensing waveguide, and that $\max\ u_0 = D_0 \geq 0$. These functiones are plotted in Fig. 6.5 as well as microscope images of each beam shape will be provided in Fig. 6.14.

6.4 Simulations

The beams with their individual shapes, defined above were realized on-chip as described in the previous section. For the analysis of the relaxation (Sec. 6.5), measured resonance frequencies (Sec. 6.6 & 6.8), and the study of the dissipation (Sec. 6.7), both the static and dynamic behavior of the beams was simulated. The FEM simulations were performed with COMSOL Multiphysics with Livelink™ for MATLAB®. The beams were simulated using the Solid Mechanics toolbox and the parameters (length L and initial displacement D_0) varied as in the chip design, but with more values in between to generate smooth simulated curves. The material parameters used are listed in Tab. 6.2. First, the static relaxation was computed with geometric nonlinearity included [198], followed by an eigenvalue analysis. In the simulations before release (i.e. "supported" in Fig. 6.2), the stress distribution and displacement profile are obtained while constraining the bottom of the beam (as if it is still supported by the substrate). For the simulations after the release, this constraint is disabled so that this boundary condition is also "free". The clamping points are fixed by constraining the end facets of the beam to have zero displacement. The stated stress σ is the xx-component of the stress tensor averaged over the entire beam. For more details on the stress distribution, see Ref. [122].

We have also used FEM to search for out-of-plane deformations such as vertical buckling or torsional deformations, but these were not observed. This is confirmed experimentally using SEM and OM, where out-of-plane deformations would appear as differences in focus heights between the substrate and the beam. By neither of these methods, we have found an indication of such deformations in our devices. The absence of out-of-plane deformations is discussed further in the next section as well in great detail in Yao *et al.* [122].

[1] As of the lateral etching of the beams while reactive ion etching the final width of 850 nm is smaller than the width of 1 μm defined during electron beam writing. The lateral and vertical etching during release is $\sim$ 5 nm

Table 6.2: Parameters used in simulations and modelling[1]

Parameter	Description	Value	Source
h	Thickness	330 nm	[16]
W	Width	850 nm	[16]
L	Length	$50 - 250\,\mu$m	[16]
σ_{film}	Film stress	1050.1 MPa	[63]
ρ	Density	3.10×10^3 kg/m^3	[86]
E	Young's modulus	250 GPa	[86]
ν	Poisson ratio	0.23	[86]

6.5 Relaxation and stress tuning

Before the above-mentioned release step, the beam is still constrained to its design shape as it is fixed to the cladding layer. The tensile stress, however, aims to straighten the beam. When the cladding layer below the beam is removed during release, this constraint falls away and the beam straightens. Straightening reduces the stress in the beam until it balances with the bending rigidity. The bending rigidity works against the deformation of the beam and competes with the tensile stress. The next section deals with the stress distribution in released beams followed by a discussion on the role of the design parameters on the resulting stress.

6.5.1 Stress relaxation in released beam

After relaxation, the average stress is constant over the full beam length. As in displaced beams bending rigidity and tension are concurring in keeping the beam bent or in straightening it, respectively. The stress distribution is not uniform. Figure 6.6 visualizes the stress distribution inside cut-planes at certain locations of the beam obtained by FEM as described in the previous section. The stress distribution in panel (a) actually is uniform due to the zero initial displacement. The situation in panel (b) now becomes more interesting. When there is curvature - the cut planes (i) and (ii) are placed at locations with maximum curvature in the respective segment - a strong transition of the stress from one side of the beam to the other is visible. The side the beam is bent to (orange regime), experiences stresses of about 800 MPa, as the relaxed straight beam of panel (a). Here, the stress could not relax further than estimated by the Poisson ratio. On the other side of the beam (blue regime), the stress relaxed down to about 30 MPa. Cut plane (iii) is located at a position with no curvature and thus displays a uniform stress distribution. Panel (c) shows a situation similar to the one in (b), however now D_0 is almost twice as much and the overall stresses relaxed much further. Especially at locations with large curvature, the stress distribution along y varies much less.

6.5.2 Influence of the beam parameters on the relaxation

As introduced above, the tensile stress in the pre-displaced beams will straighten them during release, thereby geometrically changing the stress [122]. Before focusing on the dynamics of the beams, in this section, we further explore the relaxation of the released beams.

The SEM images in Fig. 6.7 show how the maximum displacement of a particular beam is reduced from D_0 before (a) to D after (b) release. From images of different devices D_0 and D were extracted and plotted in Fig. 6.7(c) and (d). Before release, D_0 (filled symbols) is as designed (dashed line). After release, the beams relax, which results in a smaller center displacement (open symbols). As can be seen in Fig. 6.7(c) the beams do not straighten completely to $D = 0\,\mu$m. This can be explained by the bending rigidity working against a change of the beam shape [122]. The

and can safely be neglected in the analysis.

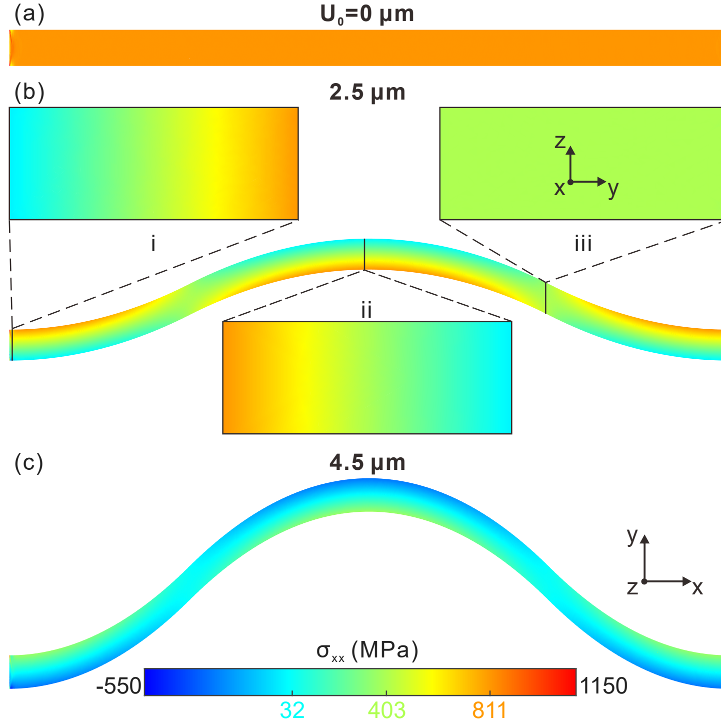

Figure 6.6: Simulated stress distribution inside a 100 μm long released beam. Displayed is the stress component σ_{xx}. The beams are displaced in the y-direction, shown is the x-y-plane. The displacement U_0 is (a) $0\,\mu$m, (b) $2.5\,\mu$m and (c) $4.5\,\mu$m. The average σ_{xx} over beam is 811, 403, and 32 MPa, respectively, as indicated in the color bar. In panel (b) also the stress distribution inside specific cut-planes (z-y) is shown. The positions of the cut-planes are (i) next to a clamping point, (ii) at the center, i.e. the maximum displacement, and (iii) at a quarter of the beam length, i.e. the minimum of the curvature. For clarity, the x and y directions are plotted on a different scale. Figure reprinted from [122] ©2022 American Physical Society.

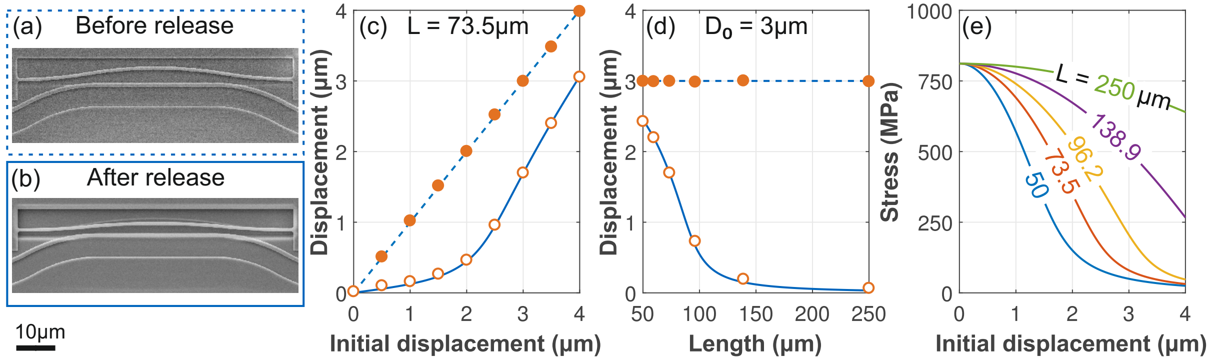

Figure 6.7: SEM images of a beam with $D_0 = 3\,\mu$m and $L = 73.5\,\mu$m before (a) and after (b) release. (c) Displacement D of $73.5\,\mu$m long beams with different D_0 before (filled circles, dashed line) and after (open circles, solid line) release. Data (circles) is extracted from SEM images like (a) and (b), and lines are FEM simulations. (d) Displacement D vs. length of beams initially displaced by $3\,\mu$m. Markers, lines, and colors as in (c). (e) Simulation of the stress after relaxation of the beam vs. D_0 for various lengths L.

change $D_0 - D$ grows for increasing initial displacement until $D_0 \sim 2\,\mu$m. From there the change in displacement starts to decrease, which is related to their potential to buckle [122]. Besides the initial displacement D_0, also the beam length L is varied on the chip: It is swept logarithmically from 50 to $250\,\mu$m. Note again that L denotes the distance between the two clamping points and

Table 6.3: Parameters of the modes shown in Fig. 6.8 as obtained from fitting the harmonic oscillator response with crosstalk, Eq. (2.10), to the data. Listed are the resonance frequencies f_0, linewidth w, quality factor Q, magnitude of the mechanical contribution Z_{mech}, and complex angle α. The listed uncertainty is the 95% confidence level for the fitted coefficients.

Mode	Freq. (MHz)	w (Hz)	Q (10^3)	Z_{mech} (V/V)	α (rad)
Z1	2.534785	22.28 ± 0.26	113.77 ± 1.30	$6.40 \cdot 10^{-4}$	-0.806 ± 0.008
Y1	2.772301	63.33 ± 0.10	43.78 ± 0.07	0.458	1.716 ± 0.001
Z2	5.095364	55.94 ± 5.40	91.08 ± 8.79	$3.21 \cdot 10^{-5}$	-1.486 ± 0.066
Y2	5.737229	189.43 ± 1.83	30.29 ± 0.29	$6.22 \cdot 10^{-5}$	0.331 ± 0.007
Z3	7.698305	127.24 ± 1.75	60.50 ± 0.83	$1.54 \cdot 10^{-4}$	2.376 ± 0.014
Y3	9.092569	445.68 ± 2.19	20.40 ± 0.10	$5.20 \cdot 10^{-4}$	1.817 ± 0.004

is, thus, smaller than the length of the center curve of the beam $\ell \approx L + \frac{1}{4}\pi^2 D_0^2/L$ (see Sec. 6.3). Figure 6.7(d) shows the initial and relaxed displacement for $D_0 = 3\,\mu$m as a function of L. For short beams, there is still a significant $D \sim D_0$, but longer beams straighten almost completely ($D \ll D_0$). For the latter, the length-to-displacement ratio is higher so that a bigger change in displacement is needed to get the same relative change in length $\Delta\ell/L$, i.e. the same amount of stress relaxation. Besides that, the bending rigidity, which is preventing the change in shape, is less important for longer resonators [199].

The relaxation of the beams is also studied using FEM simulations; as discussed in Sec. 6.4. The solid lines in Fig. 6.7(c) and (d) show the simulated displacement D. Both for the pre-displacement (Fig. 6.7(c)) and for the length dependence (Fig. 6.7(d)), the simulations match nicely with the data from the SEM images. The simulations not only give D but also provide quantities that are not easily accessible otherwise, importantly, the stress, as shown in Fig. 6.7(e). Initially, all curves start at the same point for $D_0 = 0$, which can be understood as follows [122]: The film stress in our chips is 1050 MPa [63], pulling isotropically in all in-plane directions. A straight beam will remain straight after the release process, but since it is then free in the y-direction, its width will shrink. Via the Poisson ratio $\nu \sim 0.23$ this relaxes the longitudinal stress [50] by a factor [122] $1 - \nu$, which is consistent with the value $\sigma(D_0 = 0) = 811$ MPa in the plot. Furthermore, the larger the initial displacement, the lower the stress after release. This trend continues until the beams almost fully relax. The pre-displacement for which this happens depends on L: long beams need a larger D_0 than shorter ones. Figure 6.7(e) also emphasizes that our geometric tuning of stress is not a small perturbation, but a drastic change: a $4\,\mu$m pre-displacement reduces the stress in a 50-μm-long beam by more than a factor 30. Still, the very good agreement between the observed relaxation and the simulations means that there is a direct way to determine the amount of stress remaining in the beams. This connection will be important when discussing the dynamics and dissipation of the beams in the following sections.

6.6 Dynamic beam analysis

When the released devices are excited via the piezo their eigenmodes become visible as sharp resonances in the obtained spectrum as introduced in Chapter 2 where the detection methods have been discussed. Figure 6.8(a) displays the overview spectrum of a typical device, displaying several sharp resonances (arrows) below 10 MHz. Note, that this measurement has already been introduced in Fig. 2.9.

In the displayed frequency range, both y- and z-polarized flexural modes are expected (in- and out-of-plane, respectively; coordinate system defined in Fig. 6.2(a)). The expected frequencies of the flexural modes as well as of other type of modes like longitudinal or torsional modes are

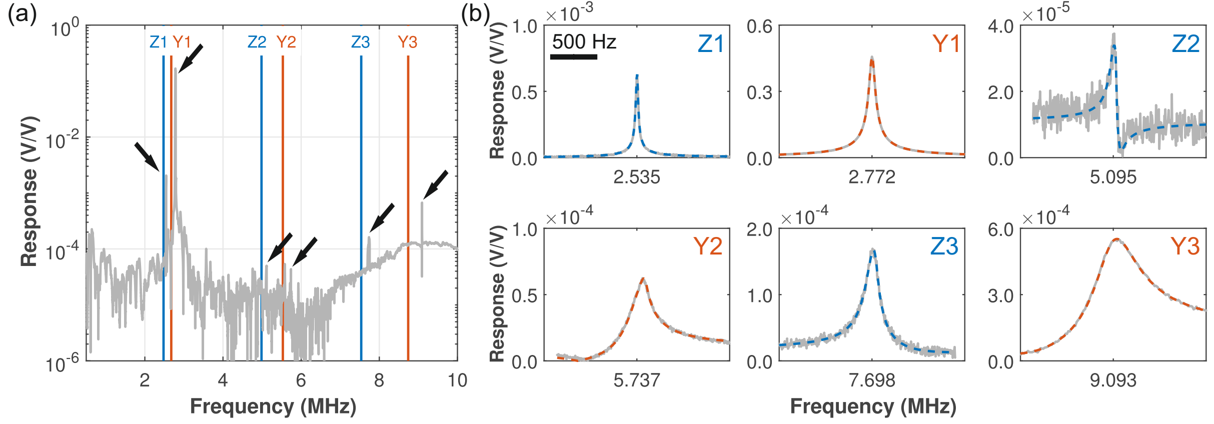

Figure 6.8: (a) Measured frequency response of a beam with $L = 96.2\,\mu$m and $D_0 = 1.5\,\mu$m (gray). The resonances are highlighted by arrows and the simulated flexural modes are indicated by the vertical lines, labeled by their polarization and mode number (in-plane in orange; out-of-plane in blue). (b) Zooms into the resonances observed in (a) together with the fitted standard harmonic oscillator response in the presence of crosstalk [145] (dashed lines). The span is 2 kHz in all sub-panels.

discussed in [151]. The two fundamental flexural modes (Z1, Y1) as well as their higher modes are close to the simulated frequencies (vertical lines) and hence can be identified. Both in the experiment and in the simulations, in-plane modes (orange) have a higher resonance frequency than the corresponding out-of-plane modes (blue). This is due to the higher bending rigidity in the y-direction, as the width of beam ($W \approx 850\,$nm) is larger than the thickness ($h = 330\,$nm). Figure 6.8(b) shows zooms of the observed modes together with the fitted responses which nicely fit the measured data. The extracted Qs range from 114,000 for the Z1 mode to about 20,000 for the 6th mode (Y3). Further details of theses modes on the parameters obtained by the fit can be found in Table 6.3.

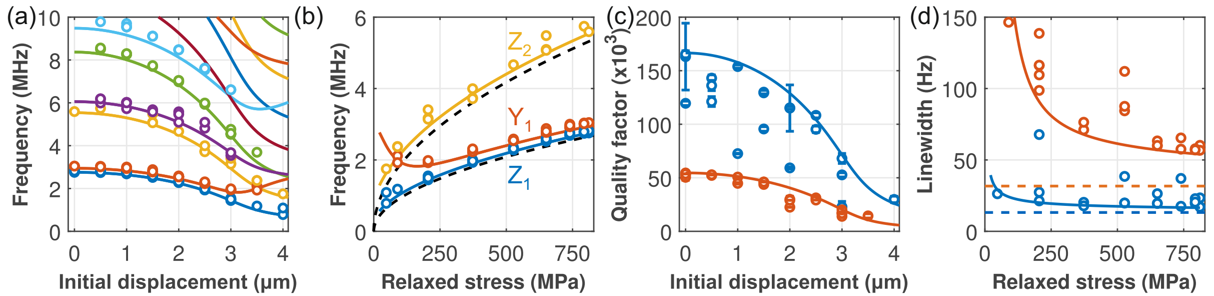

Figure 6.9: (a) Resonance frequencies of the flexural modes of beams with $L = 96.2\,\mu$m and D_0 varying from 0 to $4\,\mu$m, both measured (circles) and simulated (solid lines). (b) Resonance frequencies of the first three modes (same data as in (a)) vs. the stress after relaxation. The black dashed lines are the first two modes of strings (cf. Eq. (6.2)). (c) Quality factors of the first in-plane (orange) and out-of-plane (blue) mode. Solid lines: model of dissipation (Eq. (6.3)) with $Q_{\mathrm{bending,z}} = 6800$ and $Q_{\mathrm{bending,y}} = 7300$. (d) Linewidth of the fitted peaks of the first two modes shown in (b) vs. stress. The solid lines are the calculated linewidths for the respective Q_{bending} and the dashed lines indicate w_{edges}, the linewidth assigned to the damping contribution of the edges. The colors of the different modes are consistent between all panels.

As shown earlier, the static stress of the beams can be tuned drastically by increasing the curve length ℓ slightly beyond L. This strongly influences the dynamics of the resonators and to study this, the driven responses of the beams are measured as described above. Thus, resonance

frequencies f_0 and Qs are measured for a large number of devices. Figure 6.9(a) shows the resonance frequencies of the first flexural modes for $L = 96.2\,\mu$m. For all modes, f_0 decrease with increasing D_0. This is expected since initially higher displaced beams relax into lower stresses and therefore have lower resonance frequencies. Still, not all modes seem to decrease equally fast. Interestingly, for $D_0 \gtrsim 3\,\mu$m, the Y1 mode even seems to increase in frequency. Simulated eigenfrequencies (solid lines in Fig. 6.9(a)) nicely match the data and even reproduce this non-monotonic trend at high D_0. Analytical calculations hint that this increase may be related to buckling effects [122]. In any case, the pre-displacement of the beams can be used to tune their resonance frequencies in a predictable way. The question is, if - as intended - the resonators still act as strings, but now with a geometrically-tunable tension, or if the beams are more complex. For this, the eigenfrequencies are compared to that of a straight string under tension [2]:

$$f_0 = \frac{n}{2L} \times \sqrt{\frac{\sigma}{\rho}}, \tag{6.2}$$

where n is the mode number, $\rho = 3100\,\text{kg/m}^3$ is the density of Si_3N_4, and, importantly, σ is the stress in the string, which is now a function of D_0 and L. As shown in the previous section, using simulations, D_0 can be converted into stress. Figure 6.9(b) replots the resonance frequencies vs. σ for the first three modes. The dashed black lines show Eq. (6.2) (no free parameters). Especially the first (blue) and second (gold) z-polarized modes closely follow the frequency of a string. The small vertical offset between both the data and the simulations on one hand, and the string on the other hand, is attributed to the bending rigidity. Only for very low stress $\sigma \lesssim 200\,$MPa, Y1 starts to deviate from the string model. Note that this coincides with the upward trend in Fig. 6.9(a) and only occurs when the stress has been reduced by more than a factor of four. Thus, for most of the devices explored here, the pre-displaced beams simply act as strings under tension, but now with geometrically-tuned stress. How this impacts the dissipation will be discussed next.

6.7 Dissipation

It has already been mentioned before, that high-stressed SiN strings can reach exceptionally high Q [49, 89, 200], up to 10^9 [51, 201][2]. Such an enormous increase of Q in SiN resonators - that is these days reaching over 6 orders of magnitude more compared to unstressed single or two-sided clamped beams - have first been observed in 2006 by Verbridge *et al.* [49][3]. Since its discovery, this fascinating effect shall develop an enormous potential for the study of high-Q nano- and micromechanical devices as well as in industrial applications.

6.7.1 Dissipation mechanisms

Before we approach the concept of dissipation dilution, let us briefly look at the various sources of dissipation introduced in Sec. 2.4.4 and whether they have to be considered in the following discussion or if we can neglect them. As a reminder, the overall loss can be broken up into energy loss due to the surrounding *medium*, phonons traveling into the bulk via the *clamping* points, the for us most relevant *intrinsic* loss, and some *others* that shall not be of further interest in the context of this work. These sum up according to Eq. (2.9).

To build a model for the overall dissipation in our resonators we must know which of the individual mechanisms do and do not contribute. The measurements were performed at pressures of

[2]Very recently, quality factors above 10 billion have been reported in strained silicon, also by utilizing dissipation dilution [202]. Our approach is not limited to amorphous materials like SiN but should also be applicable to crystalline materials like strained silicon as long as it has tensile stress.

[3]Interestingly, the underlying physical principle, these days referred to as dissipation dilution, has already been discussed in the year 1994 for loaded wires [203].

$P < 10^{-5}$ mBar, making gas damping insignificant [204, 205]. Also clamping losses, i.e. acoustic waves radiating into the substrate are not expected to limit the Q for such narrow beams and low mode numbers [136]. The chip mounting can also influence the role of clamping losses [136]; here they are suppressed by the stiff mounting of our chips with silver paste. Clamping losses would also appear with an alternating behavior of Q with the mode number [192], which is also not the case here. Furthermore, from Schmid *et al.* [136] and Unterreithmeier *et al.* [192] it can be concluded that thermoelastic damping, Akhiezer damping, and surface losses are not limiting Q. This thus leaves the internal damping in the SiN as the dominant dissipation mechanism. This is always present and cannot be got rid of, however, there are ways to strongly reduce (or increase) it, e.g. by tuning of the stress (c.f. Fig. 6.1). A model of this *intrinsic* loss applied to our data in Fig. 6.9(c) and (d) as well as in Fig. 6.13 is introduced in the following.

6.7.2 Dissipation in stress-tuned Sbeams

As mentioned above, high-stressed SiN strings can reach exceptionally high Q. This is because in them a lot more tensile energy is stored compared to stress-less beams. With the same amount of energy lost per oscillation, high stress resonators thus exhibit very low relative losses, i.e. have a high Q, an effect known as dissipation dilution [50, 206]. Dynamic bending is, however, lossy and thus gives rise to internal material damping [50, 192]. Bending most notably occurs near the anti-nodes and near the clamping points of the beam. We derive a model for the dissipation including the mode shape calculated from the Euler-Bernoulli equation with tension included [122] to find Q_z[4]:

$$\frac{Q_z(\sigma)}{Q_{\mathrm{bending},z}} = 1 + \left[\frac{(\pi\tilde{n}_z)^2}{12}\frac{E}{\sigma}\left(\frac{h}{L}\right)^2 + a_n\sqrt{\frac{E}{\sigma}}\frac{h}{L}\right]^{-1}. \qquad (6.3)$$

Here, $\tilde{n}_z = 1.538$ is the effective mode number and $a_1 = 0.561$ is a dimensionless fit parameter. $E = 250$ GPa the Young's modulus and $h = 330$ nm the height of the beam. $Q_{\mathrm{bending},z} = Q_z(0)$ is the quality factor of an analogous singly-clamped, and hence tensionless, beam. The first term in the square brackets comes from the interior, i.e. away from the clamping points; the second term accounts for the bending near the edges. Remarkably, the quantity $\Sigma \equiv \frac{\sigma}{E}\left(\frac{L}{h}\right)^2$ appears in both. Σ is a measure for more string- ($\Sigma \gg 1$) or more beam-like ($\Sigma \ll 1$) behavior and we define it as the "stringness" of the resonator. The interior contribution scales as Σ^{-1} and the edge contribution as $\Sigma^{-1/2}$. Our geometric tuning of the stress allows us to vary $\Sigma \propto \sigma$ and to observe the impact of stress on the dissipation.

The model is inspired from Schmid *et al.* [136] and assumes that the dissipation in SiN is due to bending and that the stretching energy is stored without losses. As detailed above, other loss mechanisms are not expected to play a significant role here. In their model, building on the work of Unterreithmeier *et al.* [192] the ratio between bending $\mathcal{U}_{\mathrm{bending}}$ and stretching energy $\mathcal{U}_{\mathrm{str}}$ is a central quantity. They are related to the curvature and elongation of the beam, respectively [122]:

$$\mathcal{U}_{\mathrm{bending}} = \frac{1}{2}B\int_0^L \left(\frac{\partial^2 u}{\partial x^2}\right)^2 \mathrm{d}x \qquad (6.4)$$

$$\mathcal{U}_{\mathrm{str}} = \frac{1}{2}T\int_0^L \left(\frac{\partial u}{\partial x}\right)^2 \mathrm{d}x \qquad (6.5)$$

Here, B is the bending rigidity, and T is the tension. In a pure beam resonator (i.e. for $T = 0$) the stretching energy is zero, but with finite tension the total stored energy $\mathcal{U}_{\mathrm{bending}} + \mathcal{U}_{\mathrm{str}}$ increases. Since Q is related to the ratio of the energy lost per cycle to the total energy, the extra stored energy results in an increase in Q relative to that of a bending-only resonator such

[4]To obtain Q_y, replace $z \rightarrow y$ and $h \rightarrow W$.

as a cantilever [192]:

$$Q = Q_{\text{bending}} \frac{\mathcal{U}_{\text{bending}} + \mathcal{U}_{\text{str}}}{\mathcal{U}_{\text{bending}}} \tag{6.6}$$

Inserting Eqs. (6.4) and (6.5) into Eq.(6.6), yields

$$Q = Q_{\text{bending}} \left(1 + T_{\text{norm}} \frac{\langle u'^2 \rangle}{\langle u''^2 \rangle}\right), \tag{6.7}$$

where $'$ denoted a derivative w.r.t. the normalized position along the beam $\tilde{x} \equiv x/L$, $\langle \ldots \rangle$ is the value of the quantity at the position of the dots averaged over the length of the beam $1/L \int_0^L \ldots \, \mathrm{d}x$, and $T_{\text{norm}} \equiv TL^2/B$ is the tension normalized to the bending rigidity. The relation between the normalized tension and the stringness as defined above is $T_{\text{norm}} = 12\Sigma$.

To evaluate Eq. (6.7), the mode shape $u(x)$ is needed. In their model, Schmid and coworkers take far from the clamping points, i.e. in the interior, the mode shape of a string:

$$u(x) = U \sin\left(\frac{n\pi}{L} x\right) \tag{6.8}$$

where U is the amplitude. Especially near the n anti-nodes, the string's displacement has curvature, in other words: it bends there [2, 121]. Since $\partial^2 u/\partial x^2 = -(\pi n/L)^2 \times u(x)$, shorter beams and higher modes $n > 1$ will have larger curvature for the same amplitude U. Still, at the clamping points $x = 0, L$, Eq. (6.8) predicts that the curvature $\partial^2 u/\partial x^2 = 0$. However for a realistic beam, the boundary conditions $u|_{x=0,L} = \partial u/\partial x|_{x=0,L} = 0$ [121] imply that the beam has a curvature at the edges too. In their model, the mode shape near the clamping $x = 0, L$ follows the (static) shape of a singly clamped cantilever subjected to a point force.

Their original result (for bending in the z direction, where $B = EWh^3/12$ and for $\mathcal{U}_{\text{str}} \gg \mathcal{U}_{\text{bending}}$) is:

$$Q = \left[\frac{(\pi n)^2}{12} \frac{E}{\sigma} \left(\frac{h}{L}\right)^2 + 1.09 \sqrt{\frac{E}{\sigma}} \frac{h}{L}\right]^{-1} Q_{\text{bending}}, \tag{6.9}$$

Both the curvature of the ideal string (Eq. (6.8)) and the bending near the clamping points (derived from a cantilever-like shape) contribute to the dissipation in the stressed beam and these are the two terms in Eq. (6.9), respectively. Note that with the bending energy included in the numerator of Eq. (6.6), Eq. (6.9) can be written as

$$Q = \left(1 + \left[\frac{(\pi \tilde{n})^2}{T_{\text{norm}}} + a \sqrt{\frac{12}{T_{\text{norm}}}}\right]^{-1}\right) Q_{\text{bending}}, \tag{6.10}$$

with $a \approx 1.09$. The effective mode number $\tilde{n}$ is introduced as we will show it is different from n, which in Schmid's original model equals the actual mode number $n = 1, 2, 3, ...$ The term in the round brackets is the relative increase in Q, and is called the dissipation dilution factor DD [50, 206].

The exact profile of the flexural eigenmodes of a beam can be calculated using the Euler-Bernoulli equation with tension included (Eq. 2.4) [122,199,206]. The mode shape depends on the value of T_{norm}, as Fig. 6.10(a)-(c) shows for $T_{\text{norm}} = 10^{-2}$, 10^3, and 10^4, respectively. For small tension, the mode shapes are those of beams without tension, whereas for high T_{norm} the shape resembles that of Eq. (6.8). However, close to the clamping points, the curvature u'' increases strongly (green line), as also predicted by Schmid *et. al* [136]. By numerical integration, the different terms of Eq. (6.7) are obtained as a function of T_{norm}. Figure 6.10(d) and (e) show the stretching and bending contributions, respectively. Since the magnitude of the eigenmodes is not fixed, both are normalized to the maximum amplitude squared. From Fig. 6.10(d) it is clear that the difference in $\langle u'^2 \rangle$ between the pure bending (left) and the tension-dominated regime (right) is small. The value is also close to that of a string (Eq. (6.8)) (dashed line). For the curvature

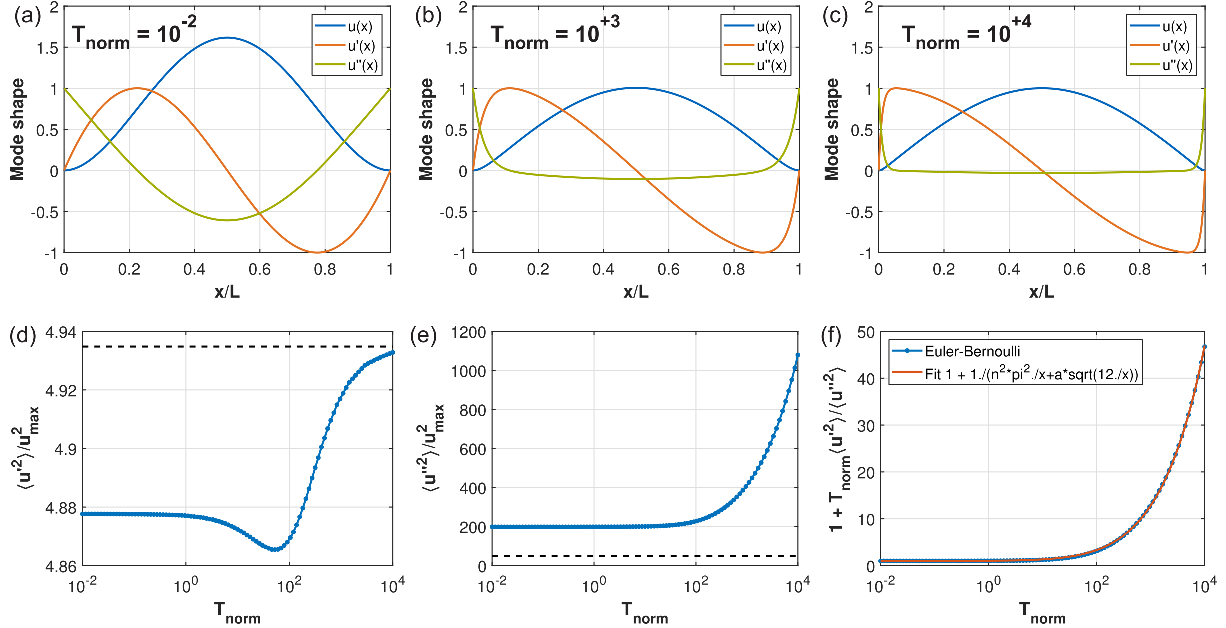

Figure 6.10: (a)-(c) Mode shapes $u(x)$ for the fundamental modes, and its first and second derivatives for the indicated values of the normalized tension. For clarity, the first and second derivatives have been normalized to their maximum value. (d) Mean-squared stretching $\langle u'^2 \rangle$ and (e) Mean-squared curvature $\langle u''^2 \rangle$ as obtained by (numerically) integrating the derivatives of the solutions to the Euler-Bernoulli equation. The dashed lines show the analytical results from the integration of Eq. (6.8), which are $\pi^2/2$ and $\pi^4/2$, respectively. (f) Dissipation dilution factor DD as function of the normalized tension, together with a fit by Eq. (6.10). The value of the fit parameters are $\tilde{n} = 1.538 \pm 0.018$ and $a = 0.561 \pm 0.003$.

$\langle u''^2 \rangle$ in Fig. 6.10(e), the situation is different: First of all, since the mode shape of a tensionless beam (Fig. 6.10(a)) is more curved than that of a string, the flat plateau is higher than the value $\pi^4/2$ for a string (dashed line). More importantly, is that the mean-squared curvature rises with increasing tension. This is due to the increased curvature near the edges, which is not resembled in Eq. 6.8, describing the mode shape of a string. This gives rise to a larger $\mathcal{U}_{\text{bending}}$, which partly cancels the increase in Q with tension due to the increased stretching energy $\mathcal{U}_{\text{str}}$ (see Eq. (6.6)). To quantify this, the dilution factor is calculated as shown in Fig. 6.10(f). Inspired by the model by Schmid, we fit Eq. (6.10) to the Euler-Bernoulli results. The fit function matches the dissipation dilution factor well, and yields $\tilde{n} = 1.538 \pm 0.018$ and $a = 0.561 \pm 0.003$. The coefficient to describe the clamping region is about a factor of two lower than in the original work of Ref. [136]. Although still widely used in the literature, it is important to note that this model was later improved by its author, and $a = 1/\sqrt{3} \approx 0.577$ was obtained [126], which is close to our value. We also find that the value of $\tilde{n}$ is different from the (integer) mode number n as can be seen in Tab. 6.4 for the values of $\tilde{n}$ for the first four modes. Since this contribution is important at modest values of T_{norm} where the mode shape (Fig. 6.10(a),(b)) is much more like a beam than a string (Fig. 6.10(c), Eq. (6.8))), it is reasonable that also here corrections appear. This discussion shows that it is not straight forward to find a description for the mode shape that is valid over a large range of T_{norm} and matches the actual mode shape for all x.

The different approaches to resembling the mode shape - essentially near the clamping points - are compared in Fig. 6.11. Panel (a) shows the overview of the full beam length. Plotted are the mode shape obtained via finite element simulation (light gray), the model introduced in this work, i.e. applying the solutions of the Euler-Bernoulli-equation with tension (dark gray), the pure string model (red), and the mode shape of a cantilever (yellow). The latter two combined form the model from reference [136] which our work is building on. From panel (a) it appears

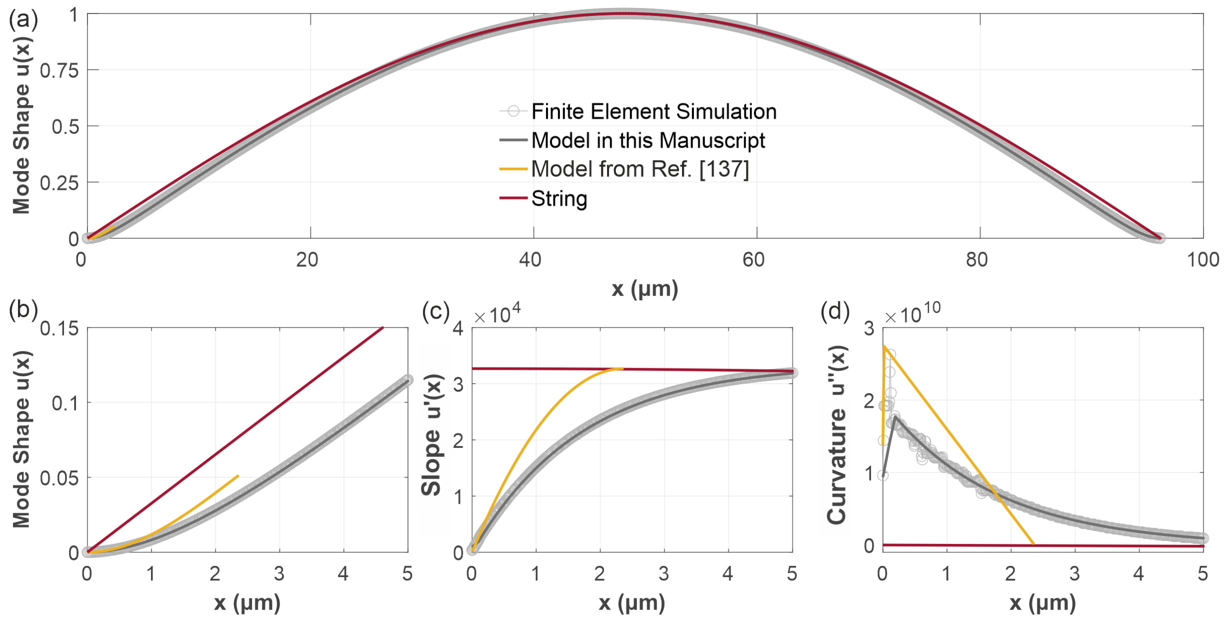

Figure 6.11: Comparison of different models for the mode shape: full mode profile (a) and zoom into the left clamping point for the mode (b) as well as the first (c) and second (d) derivative. FEM (light gray), Euler-Bernoulli with $T_{norm} = 3131.8$ (dark gray) (compare Fig. 6.10), cantilever with the length to match the slope a string (yellow) and string (red). Note that in panel (d) the y-scale starts slightly below 0 due to the negative curvature in the center region of the mode.

that all approaches roughly resemble the mode shape[5]. Panel (b), however, shows the zoom into the region next to one clamping point, where most deviations occur. Here, the differences are quite well visible. The FEM simulations can be viewed as a trusted reference as we already showed earlier that the results from the simulation nicely match our experimental data. As mentioned above, the model from Ref. [136] consists of the cantilever mode shape (yellow) near the clamping points combined with the sinusoidal shape (red) of a string away from the clamping points. The distance from the clamping point, where the latter displaces the first, is defined by the location where both have the same slope[6] - which is at the maximum length of the displayed cantilever. In the range below $1\,\mu m$ the cantilever matches indeed nicely with the simulation and is a clear improvement of the pure string model. Further away from the clamping points, however, the deviation increases. The Euler-Bernoulli (E-B) approach of our work (dark gray), however, almost perfectly follows the simulation. In panel (c) the first derivative of each approach is plotted. This goes with a squared contribution to the derivation of the tension energy. Again, the E-B approach is the best match to the simulation. The same can be seen in panel (d), where the second derivative of the mode shape is plotted. It contributes with its square to both the bending energy of the cantilever and the string part.

Table 6.4 shows the values for higher modes as well. The values of a depend only weakly on the mode number n, whereas the fitted $\tilde{n}$ roughly increases by one when going to the next higher mode n. The fitted values for a and $\tilde{n}$ are reproduced by finite-element simulations of straight beams with varying beam lengths. Here, the values differ slightly for the different polarizations: For the first z-polarized mode $a = 0.532 \pm 0.005$ and $\tilde{n} = 1.534 \pm 0.021$ and for the respective y-polarized mode $a = 0.498 \pm 0.025$ and $\tilde{n} = 1.731 \pm 0.037$ were obtained, but both are in agreement with the Euler-Bernoulli results. This thus confirms the validity of the model, which

[5]Note that all modes were normalized to a maximum value of 1.

[6]This is at $L_c = \sqrt{\frac{2EI_z}{\sigma A}}$, with Young's modulus E, the geometric moment of inertia I_z, where $EI_z = D_z$, stress σ and area of the cross-section of the beam A [136].

Table 6.4: Fit parameters obtained by fitting Eq. (6.10) to the dilution factor, using shapes calculated by the Euler-Bernoulli equation, for different modes, as was shown for the fundamental mode in Fig. 6.10(f). The indicated uncertainty is half the confidence interval returned by Matlab's fit function.

Mode	a	$\tilde{n}$
1	0.561 ± 0.003	1.538 ± 0.018
2	0.549 ± 0.003	2.429 ± 0.017
3	0.534 ± 0.004	3.418 ± 0.017
4	0.515 ± 0.005	4.437 ± 0.017

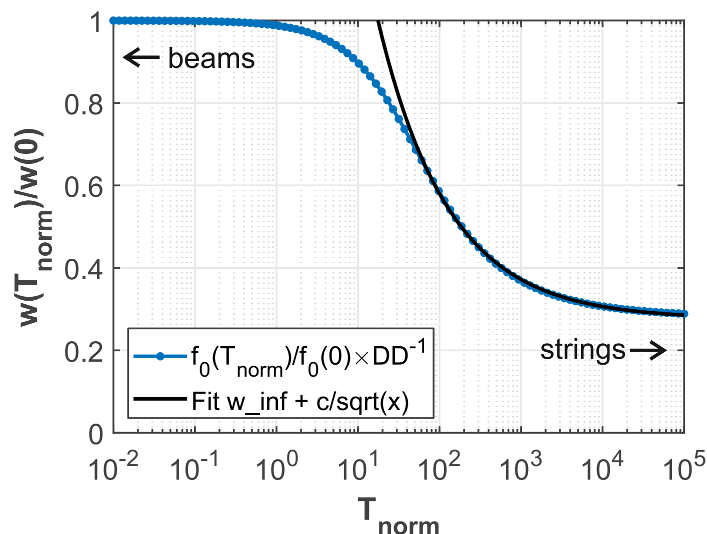

Figure 6.12: Normalized linewidth, i.e. the ratio of the linewidth of beams with varying amount of normalized tension T_{norm} to the linewidth with no tension at all, for the fundamental mode. Blue curve: linewidth obtained from Eq. (6.11), black curve: fit following the trend of Eq. (6.12).

is employed in this work. Note, that both results also match closely with the - mode independent - results for $a \approx 0.577$ reported by Sadeghi *et al.* [88].

The fast increase of DD with T_{norm} (Fig. 6.10(f)) leads to the large quality factors reported for high-stress resonators. However, at the same time, the frequency increases too. When discussing Fig. 6.9, we argued that it may be more insightful to quantify the dissipation using the damping rate $\gamma = 2\pi w$, or linewidth w. Equation 6.12 shows that for large stringness Σ, the linewidth approached the tension-independent w_{edges}. An interesting question is, how the limiting damping rate w_{edges} compares to that of a pure beam w_{bending}. Note that for the latter, $\Sigma = 0$ and that the assumptions underlying Eq. (6.12) are not satisfied anymore. Still, the results for the beams with tension presented in this section allow studying the entire evolution of w from zero to large stringness. The linewidth is given by:

$$\begin{aligned} w(T_{\text{norm}}) \equiv \frac{f_0(T_{\text{norm}})}{Q(T_{\text{norm}})} &= \frac{f_0(T_{\text{norm}})}{f_0(0)} \frac{f_0(0)}{Q_{\text{bending}}} \frac{Q_{\text{bending}}}{Q(T_{\text{norm}})} \\ &= w_{\text{bending}} \times \frac{f_0(T_{\text{norm}})}{f_0(0)} \frac{1}{DD(T_{\text{norm}})}. \end{aligned} \tag{6.11}$$

This shows that the ratio between $w(T_{\text{norm}})$ and $w_{\text{bending}} = f_0(0)/Q_{\text{bending}}$ is the relative increase in frequency divided by the dissipation dilution factor. Figure 6.12 shows how this quantity depends on the normalized tension for the fundamental mode $n = 1$. For pure beams, the ratio is, as expected, one. It decreases in a sigmoidal fashion with increasing T_{norm}, reaching a value

slightly below 0.3. This limit is equal to $\pi a_n/\beta_n^2$, where $\beta_n \approx 4.730, 7.853, 10.996\ldots$ are the roots corresponding to the solutions of the Euler-Bernoulli equation without tension [2]. The black curve shows how Eq. (6.12), that will be introduced below, matches $w(T_{\mathrm{norm}})$ well beyond $T_{\mathrm{norm}} \gtrsim 10^2$, and that it deviates for pure beams. The important point is, however, that not only the quality factor increases with increasing tension, but that also the damping rate is reduced beyond that of a pure bending beam.

6.7.3 Influence of D_0 on the dissipation

With that theoretical framework gained, I will discuss how actual design parameters, like D_0 and L do impact on the dissipation. Figure 6.9(c) shows the experimental Qs for the fundamental in- and out-of-plane mode as obtained from driven responses like in Fig. 6.8(b). The order of magnitude for the fundamental out-of-plane mode (z) of a non-displaced beam is around 10^5 and for the in-plane mode (y) around 10^4. These findings coincide with experiments found in the literature for beams with comparable design parameters [52, 136, 207]. $Q_z \approx 3Q_y$ and both decrease with increasing D_0. The solid lines are the predictions of Eq. (6.3) for $Q_{\mathrm{bending,z}} = 6800$ and $Q_{\mathrm{bending,y}} = 7300$, which were obtained by manually fitting to the highest Qs as these denote the limit of the device performance: it may always be possible to have additional dissipation, e.g. due to contamination or coupling to substrate modes, but never less [90]. Despite the factor three that we observe between Q_z and Q_y, the model matches the data with similar Q_{bending}. Interestingly, Q_{bending} appears to be slightly different for the two polarizations. This is discussed further below, but future work will have to determine whether this difference is significant, or not. In any case, the decrease in Q with D_0 is accompanied by the decrease in resonance frequency from Fig. 6.9(a). However, such dependence on f_0 is not immediately obvious from Eq. (6.3). To resolve this, we switch to the linewidth $w = f_0/Q$ to represent the damping. For strings (i.e. $\Sigma \gg 1$) one can use Eq. (6.2) to obtain:

$$w_z = \frac{n_z h}{2L^2} c_L \left[\frac{(\pi \tilde{n}_z)^2}{12} \Sigma^{-1/2} + a_n \right] Q_{\mathrm{bending},z}^{-1} = w_{z,\mathrm{interior}}(\Sigma) + w_{z,\mathrm{edges}}, \tag{6.12}$$

where $c_L = \sqrt{E/\rho}$ the speed of sound of the longitudinal vibrations [121]. Note that f_0 contains the regular mode number $n_z = 1, 2, 3, ...$ whereas $\tilde{n}_z$ is the effective mode number originating from Q. By switching to w, it becomes clear that $w_{z,\mathrm{edges}}$ is independent of the stress and that this contribution from the edges should dominate for high Σ. Figure 6.9(d) shows the measured linewidths together with the results from the model, which matches the data well. In this case, a generalization of Eq. (6.12) was used as the frequencies of the in-plane mode are not described perfectly by Eq. (6.2) for all stresses (see Fig. 6.9(b)) and, thus, the f_0 from the FEM simulations were used. As predicted by Eq. (6.12), the linewidth is indeed constant for high stresses. However, at low stress, Σ decreases, i.e. the resonator becomes more beam-like, and a higher linewidth is obtained, again in agreement with Eq. (6.12). This nicely illustrates that with our method, such a tension-dependent transition from string-like to beam-like behavior can now be studied.

6.7.4 Influence of L on the dissipation

So far we have looked at beams with a fixed length of $96.2\,\mu$m and varying D_0. As already mentioned, we fabricated and measured beams with various lengths: 50, 59.5, 73.5, 96.2, 138.9 and $250\,\mu$m. Still, most data points are available for the $96.2\,\mu$m long beams discussed so far and shown in Fig. 6.9. These beams have been realized on both chip designs used for the dynamic measurements and thus lots of devices turned out to be working properly and generating data. Devices with different lengths have been realized on just one of the chips for dynamic measurements, thus leading to fewer data points. In Fig. 6.13 the previously discussed model on

dissipation is applied to these beams focusing on the parameter regimes with good coverage by the data. The data of all the measured devices with the model applied to them can be found in Appendix A.

Figure 6.13(a) displays the trend of Q over the length L at the example of beams with D_0 of 2.5 μm. The model is applied with the same values for Q_{bending} as in Fig. 6.9. Longer beams exhibit significantly higher Q for a specific D_0 than shorter beams. This is as their remaining stress after relaxation is higher (see Fig. 6.7(e)) and so is the stored tensile energy. Also, a certain mode amplitude leads to less curvature near the clamping points and thus less internal losses. For both the in-plane (blue) and out-of-plane (green) fundamental modes the model nicely resembles the data.

Figure 6.13 (b) shows the Qs of the out-of-plane modes for all measured displacements over a range of lengths from 50 to 100 μm. Again, for all D_0 the quality factor rises with increasing beam length. However, the higher the displacement, the lower the overall Q because of the lower relaxed stresses. For low $D_0 \approx 0 - 1.5\,\mu$m the trend of Q over L appears linear for the full range of studied Ls. For larger D_0 a foot in the trend becomes visible. For lower lengths, Q rises slowly, for lengths beyond that foot, Q increases faster. The position in the plot at which this foot appears shifts to larger L with increasing D_0. These observed signatures in the trend become apparent in both the model and the data. These match well, even though it has to be mentioned that not for every D_0 a large number of data points is available and some data points show larger scattering. The argument applied above for the 96.2 μm long beams still is valid, that the relevant data points to compare the model to are the largest ones of a specific set of parameters as they denote the limit of the device performance. Panel (c) can be viewed and interpreted analog to panel (b), now displaying the in-plane modes. Again, the model and data match for varying D_0 and L.

One might argue, that Q_{bending} should be adjusted for different beam lengths individually as the cantilever contribution could differ. However, firstly, also in reference [136] the length for the cantilever contribution is $L_c = \sqrt{\frac{2EI_z}{\sigma A}}$ and thus independent of the overall beam length. And secondly, here it shall be specifically emphasized that the model works well over a broader range of beam parameters and is robust against changes in the design. It shows that no further tweaking of the fit values is needed to model the observed trends.

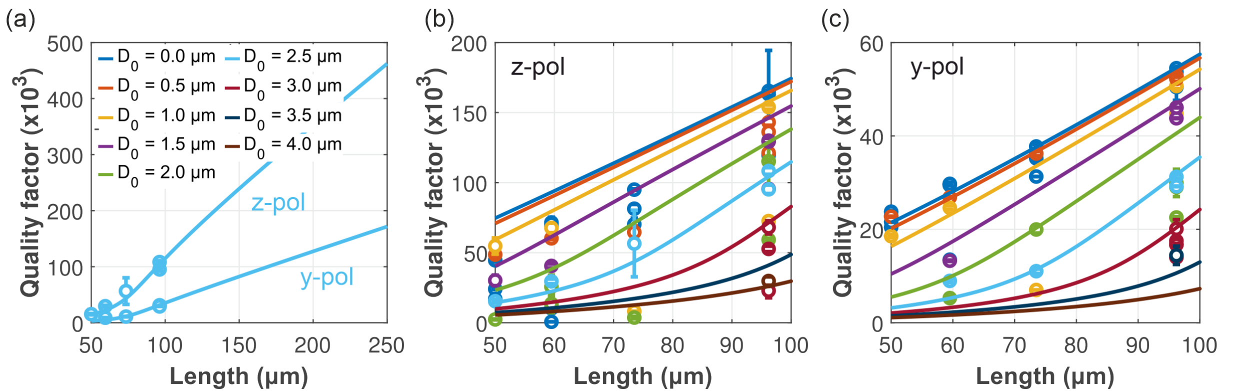

Figure 6.13: (a) Quality factor of the y- (lower curve) and z- (upper curve) polarized mode of beams with $D_0 = 2.5\ \mu$m and varying length. (b) Quality factor of the first (z-pol) mode of displaced beams vs. beam length. The different colors denote the different D_0 as displayed in the legend. (c) As (b) but shown is the second (y-pol) mode.

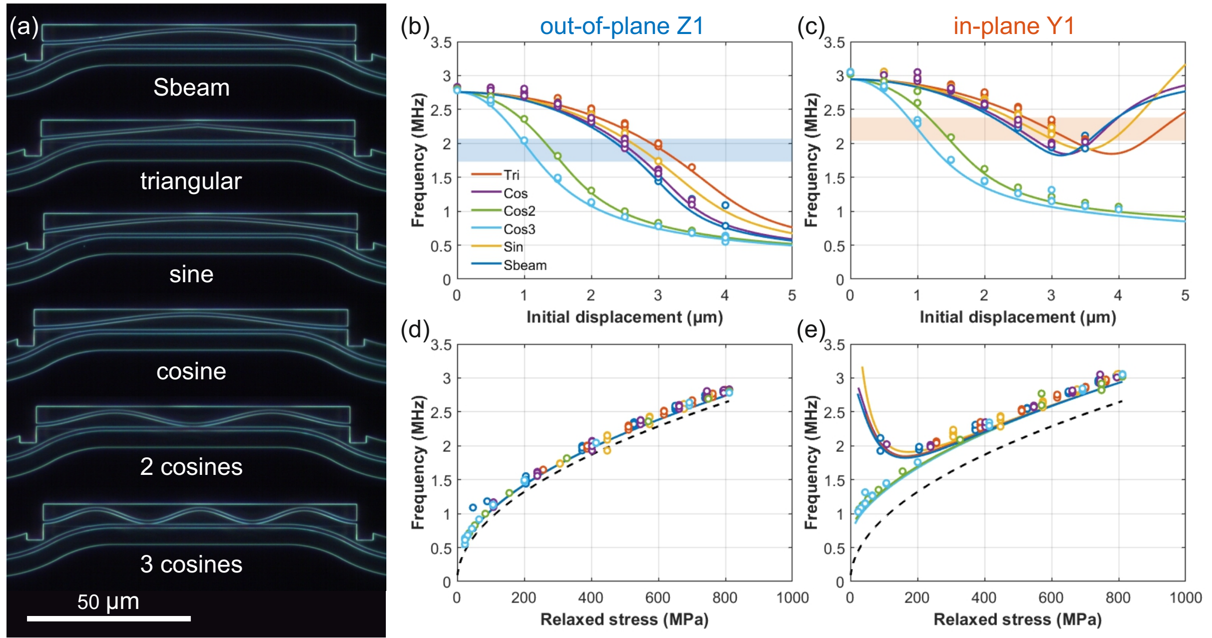

Figure 6.14: Study of different beam shapes (all with $L = 96.2\,\mu$m) and varying pre-displacement. (a) Optical micrographs of the different shapes: (top to bottom) Sbeam, triangular, sine-shaped with half a period, and cosine-shaped with one, two, and three periods, respectively. (b) Resonance frequency of the fundamental out-of-plane mode of each shape vs. D_0. Shown are both simulated (solid lines) and measured (circles) data. The shaded area marks a narrow band around 2 MHz containing a studied device of each shape. (c) Same as (b) but for the fundamental in-plane mode. (d) Plotted is the same data as in (b) but here vs. σ. The black dashed line denotes perfect strings of Eq. (6.2). (e) As (d) but for the fundamental in-plane mode.

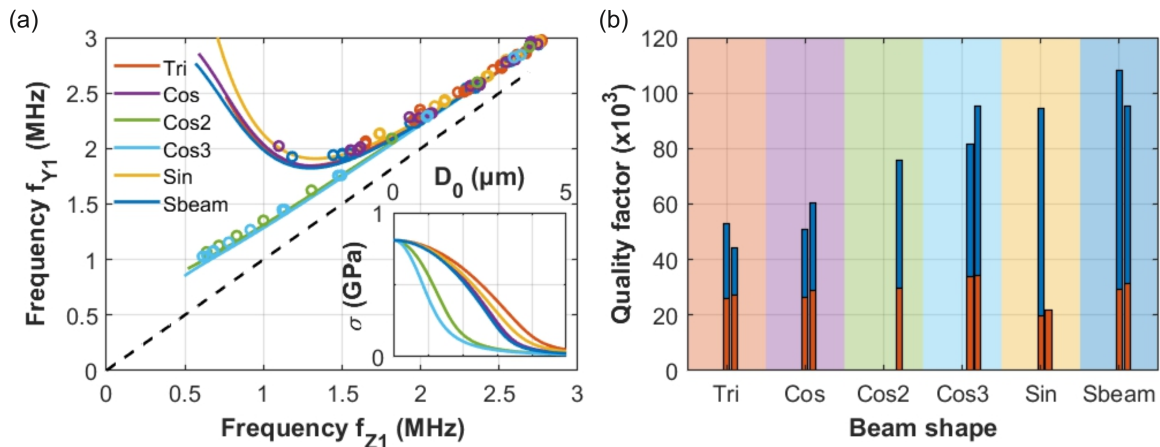

Figure 6.15: (a) Measured and simulated resonance frequencies of the in-plane mode (y-polarized) of each shape vs. the frequencies of the respective out-of-plane mode (z-polarized). Inset: Simulated stress in the beams vs. designed displacement. (b) Quality factors of the two fundamental flexural modes (orange: y-polarized, blue: z-polarized) of devices within the shaded frequency band indicated in Fig. 6.14(b,c) in the respective upper panels.

sweep parameter (μm)	value 1	2	3	4	5	6	7	8	9
pre-displacement (H)	0.0	0.5	1.0	1.5	2.0	2.5	3.0	3.5	4.0
beam shape (I)	Sbeam	tri	sin	1 cos	2 cos	3 cos			
beam MZI distance B	0.1	0.15	0.2	0.3	0.5				

Table 6.5: Design parameters of the devices on chip B. The pre-displacement is swept horizontally (H), the beam shape is swept vertically within a block (I), and the beam-to-MZI distance is swept blockwise (B). The beam length is fixed for all devices to 96.2 μm.

Table 6.6: Comparison of the dynamics of beams with different shapes with D_0 chosen such that f_0 is closest to 2 MHz. Displayed are the shape, displacement D_0, measured resonance frequency (f_{exp}) and quality factor (Q_{exp}), simulated resonance frequency (f_{sim}) and dissipation dilution factor ($\mathrm{DD}_{\mathrm{sim}}$), for both the out- and in-plane modes. For most shapes, two separate devices were measured and thus two experimental values are given.

Shape	**D_0 (μm)**	**f_{exp} (MHz)**	**Q_{exp} (x10^3)**	**f_{sim} (MHz)**	**$\mathrm{DD}_{\mathrm{sim}}$**	**f_{exp} (MHz)**	**Q_{exp} (x10^3)**	**f_{sim} (MHz)**	**$\mathrm{DD}_{\mathrm{sim}}$**
		out-of-plane mode (z)				in-plane mode (y)			
Tri	3.0	1.9558 1.9571	52.9 44.3	1.9366	13.0	2.2555 2.2620	25.8 27.2	2.1928	5.39
Cos1	2.5	1.9947 1.9284	60.5 50.7	1.9713	17.8	2.2790 2.2828	28.8 26.3	2.2123	5.33
Cos2	1.5	1.8163	75.9	1.7895	15.7	2.0901	29.7	2.0287	5.01
Cos3	1.0	2.0453 2.0376	95.3 81.5	1.9999	17.9	2.2961 2.2859	34.1 34.0	2.2148	5.67
Sin	3.0	1.7412	94.5	1.7324	14.9	2.1370 2.1328	19.8 21.9	2.0645	4.99
Sbeam	2.5	1.9327 1.9348	108.3 95.2	1.9017	17.0	2.2311 2.2209	29.2 31.2	2.1500	5.03

6.8 Influence of the beam shape

The question arises if our control over the beam dynamics and dissipation can be expanded beyond the “Sbeam”, e.g. to other pre-displacement profiles with features such as sharp edges or multiple periods. Such profiles have already been introduced in Sec. 6.3. Figure 6.14(a) shows fabricated beams with exactly these profiles, i.e. beams with triangular shape, sine shape with half a period, and cosine-shape with one, two, and three periods, respectively (as defined in Sec. 6.3). The distance between the clamping points is fixed at $L = 96.2\,\mu$m, while D_0 is swept from 0 to 4 μm - same as for the extensively studied Sbeams.

We have further used FEM, SEM, and OM to search for the appearance of nonlinear effects like out-of-plane deformations. In SEM and OM, out-of-plane deformations would appear as differences in focus heights between the substrate and the beam. By neither of these methods, we have found an indication of such deformations in our devices. The absence of these effects is further discussed by Yao *et al.* [122].

Figure 6.14(b) and (c) show both measured and simulated frequencies of the fundamental out-of-plane and in-plane modes for each shape vs. their initial design displacement, respectively. The different beam shapes display different tuning behavior of f_0 with D_0, forming two distinct groups with the Sbeam, cosine with one period, sine, and triangular shape forming one, and the cosine with two and three periods forming another. For the latter the curve length [122] ℓ is significantly longer for a given D_0 and L due to their multiple periods, resulting in a lower stress (inset of Fig. 6.17(a)). To reach a given frequency, there are thus multiple combinations of length, shape, and pre-displacement possible. The shaded area in each panel denotes a narrow

frequency band around 2 MHz containing a fabricated device of each shape; different shapes must have different D_0 to fall into this band. The panels (d) and (e) show the same data as (b) and (c), respectively, but plotted vs. the stress. Now, the data of the different shapes falls closely on top of each other. Thus it is the stress that matters and not the actual shape. Still, at low stresses, the in-plane mode separates into two different groups. The multiple-period shapes follow the string (dashed line) down to even lower stresses than the single-period shapes.

Next, the different tuning between Y1 and Z1, the relation between D_0 and σ, and the quality factors are discussed in more detail. Figure 6.15(a) shows the in-plane modes of Fig. 6.14(c) plotted over the respective out-of-plane modes (Fig. 6.14(b)). The two groups are still distinct but in this picture, the different trends in each group fall closely on top of each other. The cosines with higher periodicity follow an almost linear trend while the other shapes deviate from the linear behavior towards lower frequencies where they show a strong upward trend. Note, that the low-frequency regime here corresponds to larger displacements than for the beams with more periods.

Next, we discuss the effect of the shape on the dissipation. It is shown that the shape not only allows a fine-tuning of the ratio between the different eigenfrequencies but also provides control over the quality factor. The quality factor was shown to strongly depend on DD(T_{norm}) as well as the frequency. Hence to compare the dissipation between different shapes, devices with similar frequencies should be selected. As described above, we chose a narrow frequency band around 2 MHz (Fig. 6.14(b,c)) and selected devices of different shapes whose fundamental in- and out-of-plane modes lie within that band. As the stress of the different shapes relaxes differently the resulting devices correspond to different D_0. For most shapes and modes we were able to receive data from two individual devices on chip B with the same parameters, only differing in SEPM. The fitted Q as shown in Fig. 6.15(b) show little variation for the y-polarized mode but large differences for the z-polarized mode. To understand this behavior we compare the values obtained from the measurements with our simulations. Table 6.6 summarizes the results, such as the simulated and measured resonance frequencies ($f_{\text{sim}}, f_{\text{exp}}$), the experimentally obtained quality factors (Q_{exp}) and the simulated dissipation dilution factor (DD_{sim}). For both modes, the simulated and measured resonance frequencies match quite well. Q_{exp} of the in-plane mode does not show much variation, which is reflected by the hardly varying DD_{sim}. The sine shape has the lowest Q_{exp} which is accompanied by the lowest DD_{sim}. For the out-of-plane modes, the different shapes show significant differences in Q_{exp}. The obtained values are consistent for different measured beams with the same device parameters. Comparing this with DD_{sim} shows that the variation of the latter is smaller. Still, the triangular shape yielding the lowest Q_{exp} also shows the lowest DD_{sim}. Future research will have to give further insight into the exact mechanisms playing a role in the dissipation of complex shapes.

6.9 In- and out-of-plane Q_{bending}

As described earlier in the discussion, Q_{bending} can be understood as the quality factor of a cantilever with similar dimension and was fitted to our data. The Q_{bending} obtained by fitting Eq. (6.3) indeed match closely with our measurements on cantilevers of different samples as shown in Fig. 6.16 and with values from the literature [204]. However, we obtained slightly different values for the respective fit parameter Q_{bending} of Eq. (6.12) for the in-plane (7300) and out-of-plane (6800) modes. It is not obvious that Q_{bending} for the different polarizations has to be different at all. First, we confirm that this effect is reproducible by fitting the data of two individual chips separately, as shown in Fig. 6.17. The blue (orange) curves for the out-of-plane (in-plane) modes are generated using the same fit value $Q_{\text{bending}} = 6800$ (7300) for the two chips. The fits match well for both samples, indicating that the observed difference is reproducible between different fabrication runs. In gray, the curve with the fit value of the other mode is plotted, which clearly does not match the data. This confirms that different

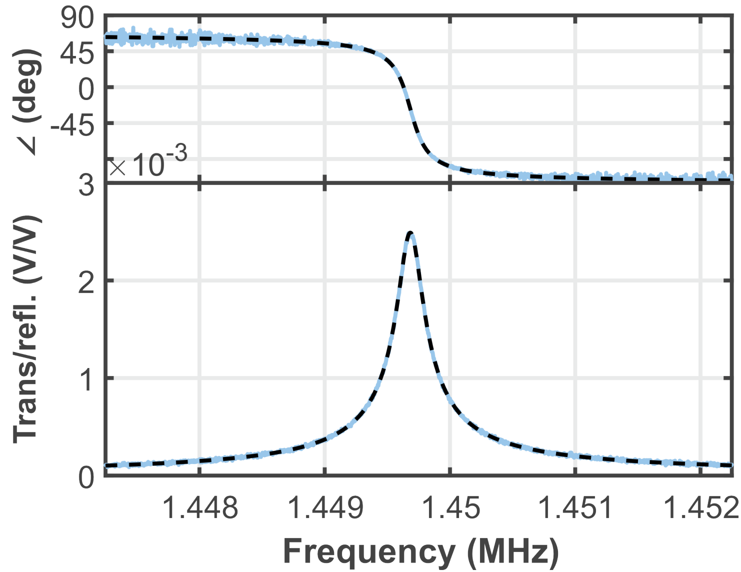

Figure 6.16: Frequency and phase response of the fundamental out-of-plane mode of a cantilever with 15 μm length and 2 μm width. The quality factor obtained by the standard harmonic oscillator fit including cross-talk (Eq. (2.11)) is 6985 ± 10. Measured by Julius Röwe [183]

modes do require a different Q_{bending}. It is thus very well possible that fundamental effects in damping become visible here. For example, the out-of-plane and in-plane modes have different polarization and thus defects feel different local strains. Also, surface losses start to play a role at low thicknesses and the vertical and top surfaces are fabricated differently. However, it should be pointed out that these are not yet expected in the range of thicknesses studied in this work [206]. Finally, although it was found to be not critical for the stress and eigenfrequency [122], it is not entirely ruled out that the undercut at the clamping points due to the release process may also play a role. By varying the thickness h and width W, it should be possible to distinguish these different hypotheses in the future.

6.10 Nonlinearity

So far we have focused on extracting values like the resonance frequencies and Quality factors from the measurements. This is done by fitting the data with Eq. 2.10. For the fit to be applicable to the data, the response needs to be in the linear or at least near the linear regime. The different types of nonlinearity that might appear in such systems have been described in Sec. 2.4.2. Here, we will focus on the geometric nonlinearity that becomes apparent when we increase the driving power sufficiently high.

Generally, we want to drive our devices as strongly as possible to obtain a good SNR. However, at some point increasing the excitation power further will result in mechanical nonlinearities and the resonator response deviates from the Lorentzian shape. The curves tilt to the right as can be seen in Fig. 6.18(a). This introduces bi-stability resulting in hysteresis. The obtained response thus depends on whether the frequency sweep is performed upwards or downwards. As discussed in Sec. 2.4.2 this is due to so-called spring-hardening, also known as duffing behavior. In panel (a) it can be seen that an increase in the driving power increases the duffing behavior. Panel (b) shows some of the traces of (a) together with the fit obtained by Eq. (2.12). Selected are traces with linear response and the appearance of light duffing nonlinearity that can still be resembled by the fit. It can be seen that the fit nicely recovering the Lorentzian shape in the linear regime is able to handle light nonlinearities well. Panel (c) shows the quality factors obtained from the

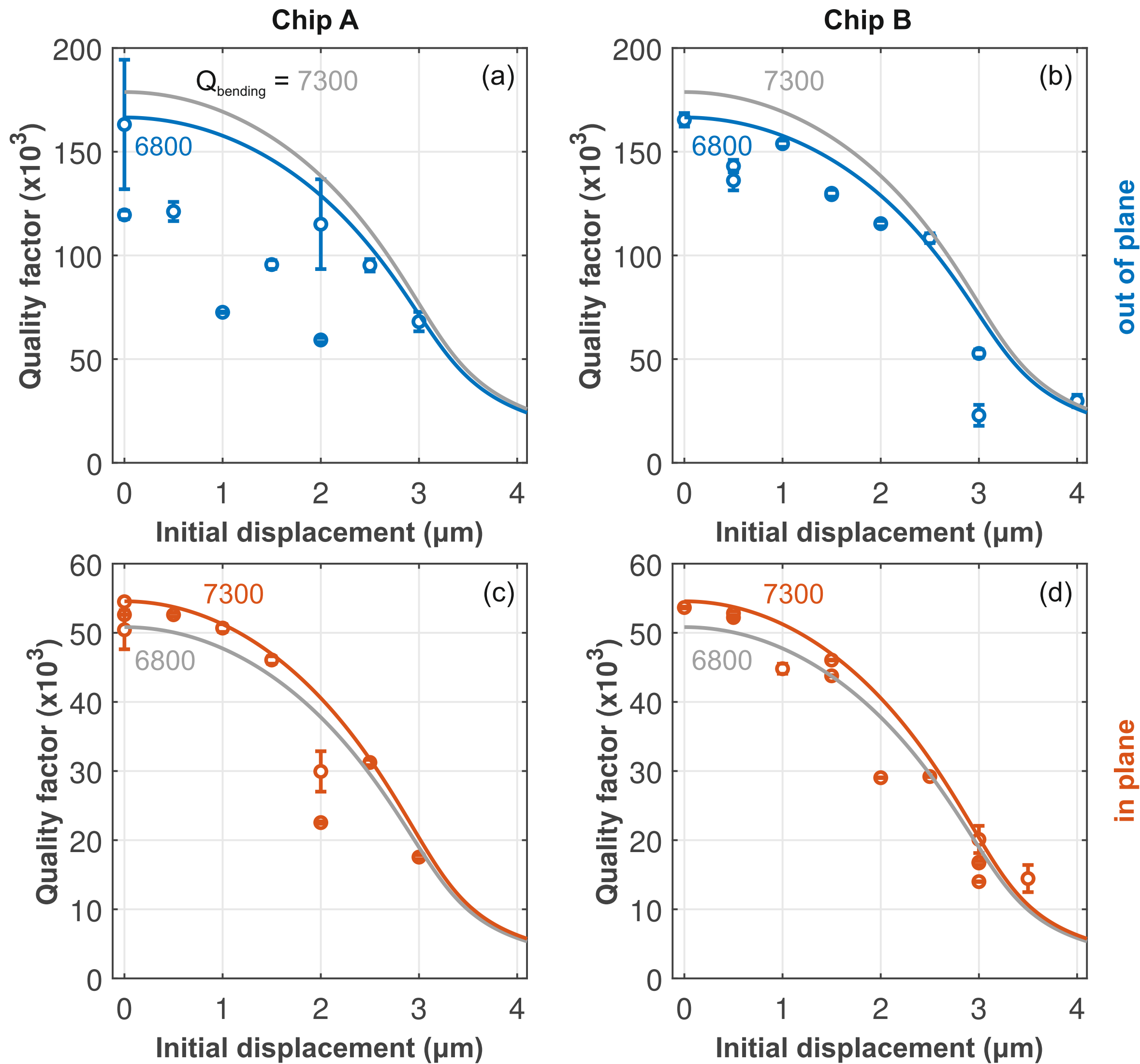

Figure 6.17: The two chips (A & B) measured for this work are analyzed individually with respect to the fitted curve. In (a),(b) blue ((c),(d) orange) the data and fit of the first out-of-plane (in-plane) mode as shown in Fig. 6.9(c). In gray the curve with fit parameter Q_{bending} of the respective other mode (cf. Eq. (6.3)). All Sbeams with $L = 96.2\,\mu$m.

fits from all traces of (a) that were properly fitted. The values of Q remain constant as long as the fit matches the data well, which is here up to a power of $-14\,$dBm. The uncertainty of Q even reduces with increasing power due to the better SNR. At even higher excitation powers above $-14\,$dBm, the fit does not resemble the measured mode anymore and the extracted Q cannot be trusted[7]. The strength of nonlinearity can be seen in panel (d) where the normalized duffing parameter $\alpha_n = \alpha/\alpha_c$ is plotted against the excitation power. α_c is the critical duffing parameter that denotes the onset of the hysteresis. This quadratic increase of α_n with higher powers is a measure of the duffing nonlinearity. Such trends were obtained on the vast majority of devices.

The picture in panel (e), however, shows a different scenario, measured on a different device.

[7]Note, that by tweaking of the initial conditions it is possible to properly fit even higher nonlinearities, but the situation remains that at some point the fit is eventually going to fail.

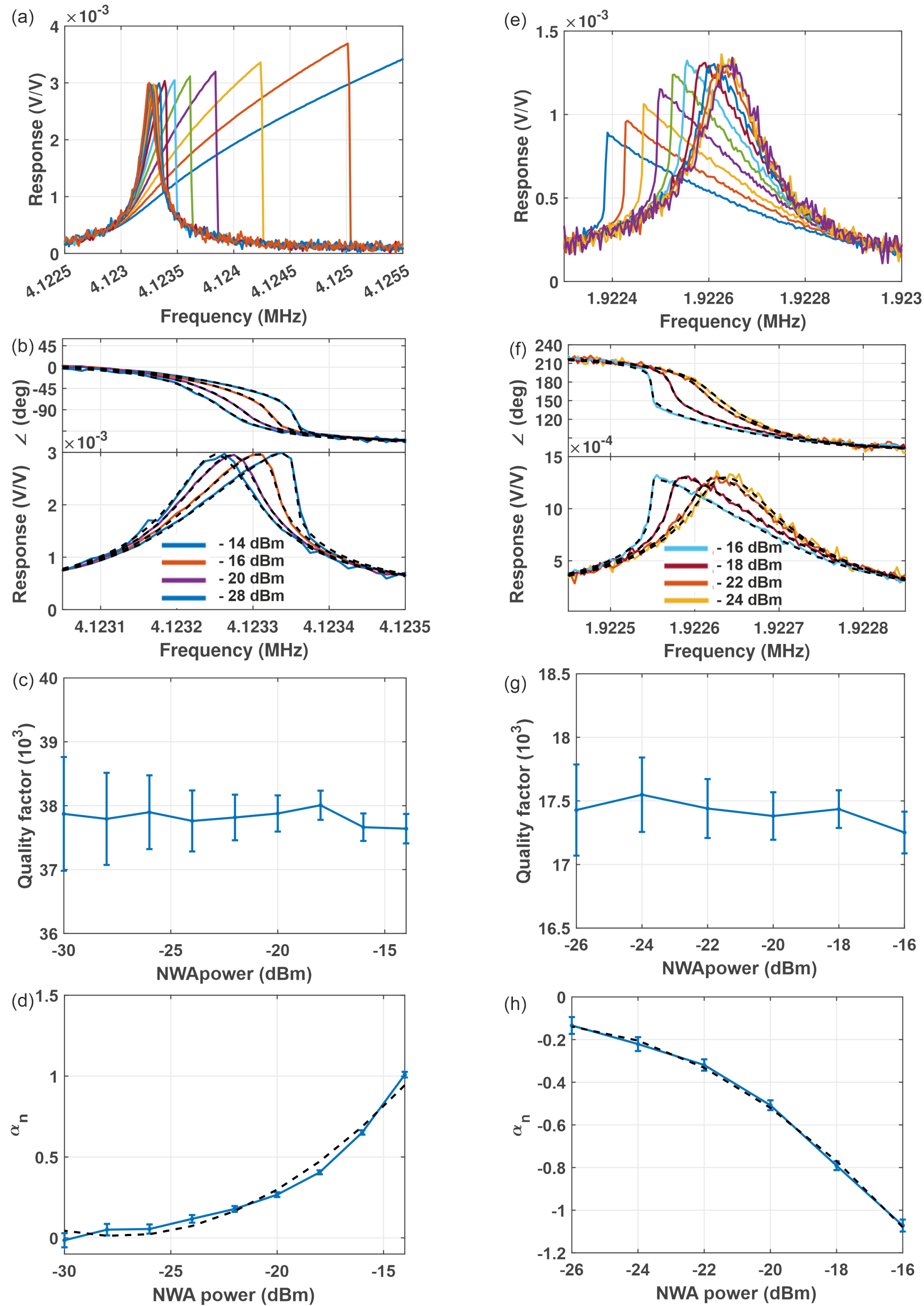

Figure 6.18: Network traces taken at different excitation powers on a Sbeam device showing positive duffing (a)-(d) and another Sbeam device showing negative duffing (e)-(h). (a) excitation from −30 dBm to −2 dBm and (e) excitation from −26 dBm to −6 dBm: Raw network traces. The traces show increasing deviation from Lorentzian behavior for increasing excitation powers. (b,f) Fitted response at selected excitations. (c,g) Fitted Q vs. excitation power. (d,h) Normalized duffing parameter α_n vs. excitation power. The black dashed line is a quardatic fit through the data. The device in the left column has a length of 73.5 μm and displacement of 0 μm. The device in the right column has a length of 96.2 μm and displacement of 3.0 μm.

The picture is quite similar to that in panel (a), however, the curves tilt to the left when the driving becomes nonlinear. This is a signature of so-called anti-duffing, also known as spring softening. Here, we see that the magnitude reduces with increasing excitation. Analog to panel (b), panel (f) displays some of the traces of (e) together with their fit. Panel (g) shows the quality factor which is again constant over the excitation power. In contrast to the case of positive duffing the duffing parameter (panel (h)) now reduces with increasing nonlinearity. Negative duffing was only observed on devices with very specific device parameters: a beam length of 96.2 μm and center displacement of 3.0 μm. This was observed on both chips, it is thus unlikely that it is a random appearance, resulting from the specific treatment during the fabrication of an individual chip. Interestingly, this was only observed on Sbeams and not on the cosine-shaped beams with the same length and initial displacement, even though they follow a very similar design curve. This might be related to the earlier described differences in Q between the Sbeams and cosine-shaped beams.

The question arises, under which conditions α is positive or negative. Elshurafa *et al.* found that in MEMS resonators spring hardening is generally dominating over spring softening [129]. However, from the theoretical analysis of the dynamics of our predisplaced resonators [122] we expect to see spring softening - which is closely related to the potential to buckle - more often than reflected by the experimental results. When in the regime of the potential to buckle, the strain for the straightened beam is negative. Due to the bending rigidity the beams actually do not necessarily fully straighten but keep a final displacement as discussed above. When driving the beams, they are deformed from their static shape - also against the bending rigidity - which can drive the beams through their negative strain regime for the in-plane modes as is the case for the measurement shown in the right column of Fig. 6.18, leading to spring softening. As mentioned earlier, we do not see any indication of buckling in our devices, still the appearance of spring softening or hardening is closely related to the potential to buckle. While there is no potential to buckle for beams with any studied length without predisplacement, increasing predisplacement leads into the buckling regime. For 25 μm long beams the regimes starts already at D_0 of 1 μm while 100 μm long beams need a $D_0 > 4$ μm. Interestingly, with a length of slightly below 100 μm and $D_0 = 3.0$ μm our only beam showing spring softening lies close to but not yet within the buckling regime while a large number of the shorter devices only exhibiting spring hardening behaviour does (c.f. Yao *et al.* [122]). However, with $D_0 = 3.0$ μm and $\alpha < 0$ this device lies close to the minimum in frequency for the in-plane mode (see Fig. 6.9(a)). In [122] it is discussed that here the mode shape becomes more complex with a local minimun at the center of the mode shape - an indication of buckling. Thus the observation of negative duffing here is not surprising. However, with the available chips and data, it was not possible to explain the measured appearance of negative duffing only on these specific devices. Further studies might resolve this fascinating effect. Suggestions to answering this question in the future are, e.g. the fabrication of a new chip with device parameters similar to those resulting in negative duffing. As the sweep steps of parameters like L and D_0 were rather large so far, it is recommended to sweep these parameters in very small steps this time. Also, small variations from the Sbeam shapes can be introduced to gain information about the onset of the negative duffing behavior.

6.11 Design considerations

The selection of the shape for specific performance goals adds another dimension to the parameter space of our geometric stress tuning approach. As discussed in the previous sections, the final design parameters are highly dependent on the specific performance goals: is one looking for a certain stress value, a certain frequency, or even a certain ratio between in- and out-of-plane modes? To provide an outline for an appropriate design strategy for geometrically-tuned stressed resonators we suggest, that if a large variance in stress for otherwise similar beams is desired, it is favorable to decide on shorter beams due to the steep stress-D_0 dependence (Fig. 6.7(e)).

To obtain a specific stress level for a given beam length, one can follow the respective stress-D_0 curve (c.f. Fig 6.7(e)) to retrieve the necessary pre-displacement. The same strategy can be used when a certain frequency is desired: in that case, Fig. 6.9(a) can be used. In either case, it can be advantageous to choose a shape with several periods to have the largest tuning in stress with relatively small D_0. Especially for small relaxed stresses, where the remaining tensile stress works against the bending rigidity, this results in straighter beams compared to beams with one period due to their lower initial bending. Figure 6.15 indicates, that this higher periodicity comes with only minimal reduction in Q. In general, narrow and thin beams shall be considered as they can acquire higher Qs [136]. Depending on the width-to-height ratio - our beams are typically designed much wider than high - it is recommended to utilize the out-of-plane modes as they exhibit significantly larger Qs than their corresponding in-plane modes. With all these parameters available, there is plenty of room to explore stress-tuned beams for almost any purpose.

6.12 Summary

We have demonstrated a novel method to geometrically tune the stress in double-clamped SiN strings and thus added a new degree of freedom in the design of nano- and micro-mechanical resonators. This was done by designing the beams with a pre-displacement instead of making them straight. When the beams are released from the substrate, their stress (partially) relaxes, depending on their length and displacement. Their resonance frequencies and dissipation depend on the remaining stress. We demonstrated that the beam relaxation and dynamics match with finite element simulations and with our method we were able to systematically study their damping. The developed model describes the stress-dependence of the dissipation in both the high and intermediate "stringness" regimes. By modifying the beam shape we further refine the control over stress and dynamics of our resonators.

By utilizing integrated Mach-Zehnder interferometers, we were able to study the relation of Q between both in-plane and out-of-plane modes and found remarkable variations between these in the low-stress regime - in the literature, typically only out-of-plane modes are studied (e.g. via Doppler vibrometers).

One can elaborate plenty of ideas on how to continue with the study of displaced beams and their incorporation into other projects. A suggestion for future questions to answer is the study of the potential influence of surface loss. This becomes relevant at very thin beams of only 100 nm. Fabricating thinner Sbeams and altering the aspect ratio of its cross-section should make this apparent. Whether this is the reason for slightly different values for Q_{bending} for differently polarized beams or if the underetch at the clamping points is having an influence here, is a question to be answered. In Sec. 6.10 we looked at measurements entering the nonlinear regime. Apart from the wide appearance of spring stiffening, we also observed the occurrence of spring softening at devices with very specific design parameters. Understanding the influence of these parameters on whether one or the other becomes apparent might be of great interest. Embedding a displaced beam into the racetrack designs, which have been mentioned in this work in the context of synchronization of beams is a parameter to tune the onset and strength of synchronization.

Overall, from basic research on damping mechanisms to applications in technology - one can think of frequency filters or quantum transmitters - displaced beams provide the opportunity to offer considerable contribution to larger frameworks.

CHAPTER 7

Conclusion and Outlook

In this thesis, three different setups for the study of integrated optomechanical devices and their physics questions are described. These setups were planned and built from scratch, only starting with an empty lab. This also accounts for the implementation and development of the nanofabrication methods in the clean room environment. Furthermore, I presented four research projects - two of these did already result in publications and were discussed in depth.

In chapter 2, I gave an introduction to the theoretical background specific to the projects discussed in this thesis. This covers the mathematical description of mechanical resonators and how information about their dynamics can be obtained with the specific setups in our labs. The various dissipation mechanisms that can potentially appear in micro-resonators are discussed together with their relevance in the context of this work. Also, the special properties of silicon nitride for optomechanical purposes are presented as well as how photonic circuitry and mechanical resonators are implemented into such a platform. Of course, this is far from being a thorough introduction to the broad field of optomechanics. For this, I recommend the reviews “Mechanical systems in the quantum regime” from M. Poot and H. van der Zant [2] and “Cavity optomechanics” from M. Aspelmeyer, T. Kippenberg, and F. Marquart [3].

In chapter 3, the nanofabrication techniques, that were used in the scope of this thesis and the development of the process parameters were explained. All steps and recipes had to be tested and optimized before they could be used for the device fabrication. This covers questions like dose tests, etch rates, or machine parameters. During the fabrication of chips already meant for measurements in the lab, unexpected issues can easily appear. Some designs require further tweaking of the process parameters, which have been successful for previous designs. An example is the beam current and beam alignment of the electron beam writer, which needed further attention when writing small structures like photonic crystals after they worked perfectly fine for simple waveguides. Other devices needed their masked layer written before the through layer and vice versa. Sometimes several machines had to be tested to find the perfect match for our needs. The successful steps are explained in the example of our currently most complex device, an optomechanical tunable directional coupler, the so-called H-directional. While establishing the steps for realizing the Hdirectional, many details were learned that are of help in improving the other devices in our portfolio as well. The design of the Hdirectional will now be improved in terms of the stability of its coupling ratio, its tuning range and the switching speed. For being able to fabricate even more complex devices the nanofabrication capabilities are currently expanded by my colleagues and will widen the available skill set. This includes back gate contacting for driving cantilevers capacitively and the fabrication of bridges over waveguides such that gold wires can cross photonic waveguides without physically touching them.

In chapter 4, I described the development and characterization of the three setups. The first is a setup for the optical characterization under ambient conditions of devices based on

integrated circuitry, such as Mach-Zehnder interferometers or ring resonators. The second setup is in principle very similar but placed inside a vacuum chamber to enable dynamic measurements on mechanical devices. The vacuum reduces air damping and allows for high quality factors. The third setup as well includes a vacuum chamber but uses a free space laser that is focused onto integrated optomechanical devices which form a cavity together with the chip substrate. Interferometry of the light reflected at the first and the latter, respectively, is utilized to sense the dynamics of the devices.

In chapter 5, a method to map the amplitude and phase of vibrational modes of optomechanical devices was presented. Its concept is based on a phase-lock loop with further improvements applied. Compared to traditional methods, it combines high resolution, sensitivity, and robustness against sign changes of the mode shape when crossing nodal lines. Up to six modes can be mapped simultaneously. With this method, a high-stress silicon nitride membrane was studied. The measured resonances could be assigned to the theoretically expected modes. From the high-resolution mode maps also ambiguous modes could be identified. Such modes are degenerate in theory but in the experiment a small splitting was recognized. Modes were found that did not only show such splitting but were the superposition of up to three individual modes. The individual weights of such superposition modes could be determined from the mode maps. Future plans are the analysis of these membranes when covered with a layer of aluminum nitride. Further ideas are the study of one- and two-dimensional drum arrays with certain overlap to learn more about the coupling of such devices. Besides drums and membranes, this setup is very well suited to take optomechanical measurements on trampoline or cantilever devices as well. Quantum experiments on strain-induced TMDs are currently being prepared [208, 209].

In chapter 6, a concept of the geometric tuning of stress in silicon nitride beam resonators was shown. The beams are pre-displaced by design, such that their stress partially relaxes when released from the substrate. Simulations of the relaxed beam shapes match nicely with the obtained experimental values and allow the extraction of the remaining stress. Beams with varying length and displacement, as well as with different shapes, were studied and dynamical measurements of their in- and out-of-plane modes were performed. Their quality factors strongly depend on their stress, thus the relation between stress and dissipation could be studied over a broad range from high to low stresses. A model from the literature was refined and matches nicely with the experimental results. It was shown that our predisplaced beams act as strings over a large range of the studied displacements. And further, more complex designed beams were fabricated and revealed that their resonance frequencies depend on their relaxed stressed and and not on their specific design. It was also shown that the in- and out-of-plane modes have different $Q_{bending}$. These findings are already of help in other projects, such as the development of the Hdirectional device for the dynamic tuning of coupling ratios in integrated circuitry. Here, the predisplacement of the resonator arms leads to lower stresses and thus can increase their tuning range for the same voltages applied. Predisplaced beams are also applied to our project with the goal to synchronize the motion of beams purely by an optical field. These beams are integrated into a racetrack cavity and undergo optomechanical coupling by the interaction of these beams with additional - photonic crystal patterned - beams in their vicinity. First characterization measurements on such racetrack devices are integrated into the scope of this thesis. Furthermore, negative duffing behavior was observed on a few of the pre-displaced beams with very specific device parameters. Getting more insight into this behavior will be an interesting challenge for the future.

The QMS described in chapter 4 is going to be expanded to perform spectroscopy and single-photon detection for the development and characterization of single photon sources. The ambient setup is accompanied by a similar setup, built by my colleagues, for redundancy but with further capabilities, such as the option to measure devices with opposing grating couplers. The measurement of light from second harmonic generation in aluminum nitride-covered ring resonators is under development. A further goal is the commissioning of a setup, based on the principle of

the large vacuum chamber for resonators integrated into photonic circuitry, which is currently underway. This is pushed by another team of members of the quantum technologies group. The great advancement will be that the chamber is located inside a cryostat that can be cooled down to 4 K and shall allow experiments, like the optomechanical measurement of the momentum of single photons.

Appendix A - Dissipation of beams

In Chapter 6 the dissipation of the beams is discussed for devices with a length of 96.2 μm. For completeness, this Appendix provides the data together with the obtained model for all lengths realized on the chips. Data is not available for all beam parameters, i.e. length and pre-displacement for the reasons discussed in the main text: as the beam-to-MZI distance was varied to ensure devices with the right balance between fully separated beams and MZIs and sufficiently strong coupling, not all devices will work out by design. When devices in the remaining ideal parameter regime are broken, no data is available. A larger batch of identical chips can lead to sufficient redundancy for obtaining a full data set in the future.

Figure A.1 shows the Quality factors of the first in- and out-of-plane modes versus the beam length. The panels (a) to (i) display the results for one specific pre-displacement each. Model and data match quite closely up to a length of 100 μm for all displacements. However, for $D_0 > 3\,\mu$m, not enough data is available to confirm that the trends match, still, the available data points coincide with the model. For $D_0 = 0$ and 0.5 μm data for lengths beyond 100 μm is available. For the y-polarized mode also in this range data and model match very well. Only for the z-polarized mode the measured Q lie below the expectation, and might indicate that the Qs of the real devices increase slower with L than the expectation. Still, it is as well possible that the measured devices do not meet their full potential Qs due to imperfections in fabrication.

Figure A.2 shows the beam dynamics of the first few modes plotted versus the pre-displacement and the directly related relaxed stress for each beam length realized on the chip. The panels in the first column display the resonance frequencies of the flexural modes of beams with $L = 96.2\,\mu$m and D_0 varying from 0 to 4 μm, both measured (circles) and simulated (solid lines). In column two the resonance frequencies of the first three modes (same data as in column one) vs. the stress after relaxation are shown. The black dashed lines are the first two modes of strings (cf. Eq. (6.2)). Note, that the second panel in (f) displays only a narrow stress regime which is due to the lower relaxation of longer beams for given pre-displacements (compare to Fig. 6.7(e)). Column three shows the Quality factors of the first in-plane (orange) and out-of-plane (blue) mode. Solid lines: model of dissipation (Eq. (6.3)) with $Q_{\mathrm{bending,z}} = 6800$ and $Q_{\mathrm{bending,y}} = 7300$. In column four the linewidth of the fitted peaks of the first two modes shown in column two vs. the stress is shown. The solid lines are the calculated linewidths for the respective Q_{bending} and the dashed lines indicate w_{edges}. The colors of the different modes are consistent between all panels (c.f. discussion in Sec. 6.6). Note, the data points between the second and the third mode in the left panel of (e). They can hardly be related to any of the displayed beam modes and their frequency stays constant over the variation of the sweep parameter. Their appearance might result from the dynamics of the partially released sensing arm of the MZI and can be further addressed in future studies. While data and model fit quite well for shorter beams, the studied devices with lengths of 138.9 μm and 250 μm show much larger deviations. For the reasons discussed in the main text the parameters $\mathrm{Q}_{\mathrm{bending,y,z}}$ optimized for the beam length of 96.2 μm are kept the same for all lengths and can lead to variations between data and model. Overall, the panels in column three and four indicate that the model matches the measured data well over a long range of beam lengths and is quite stable over a large range of device parameters.

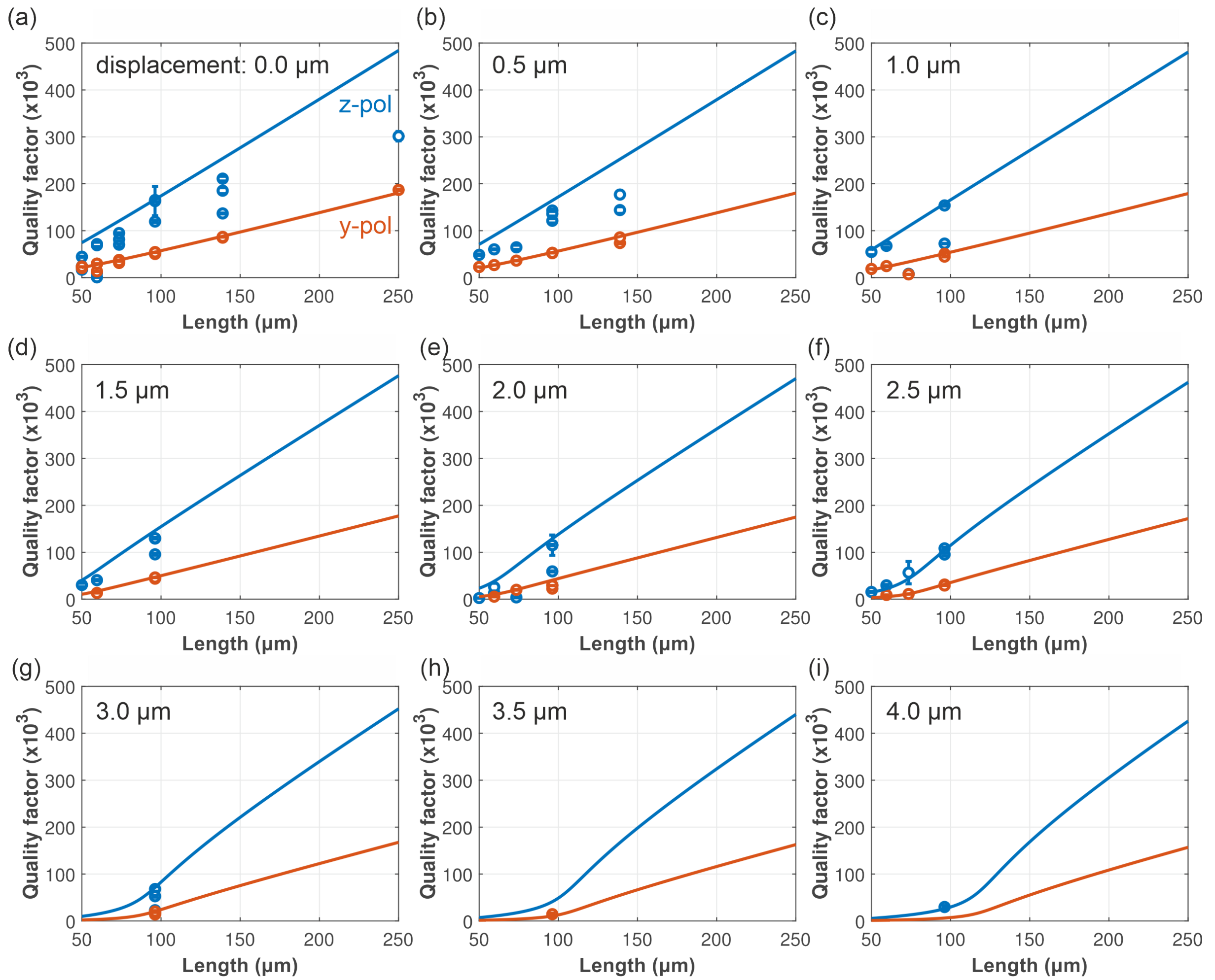

Figure A.1: Quality factors of the z-polarized (blue) and y-polarized (orange) modes vs. the beam length. (a)-(i) display the data for a specific displacement 0 μm to 4 μm, respectively.

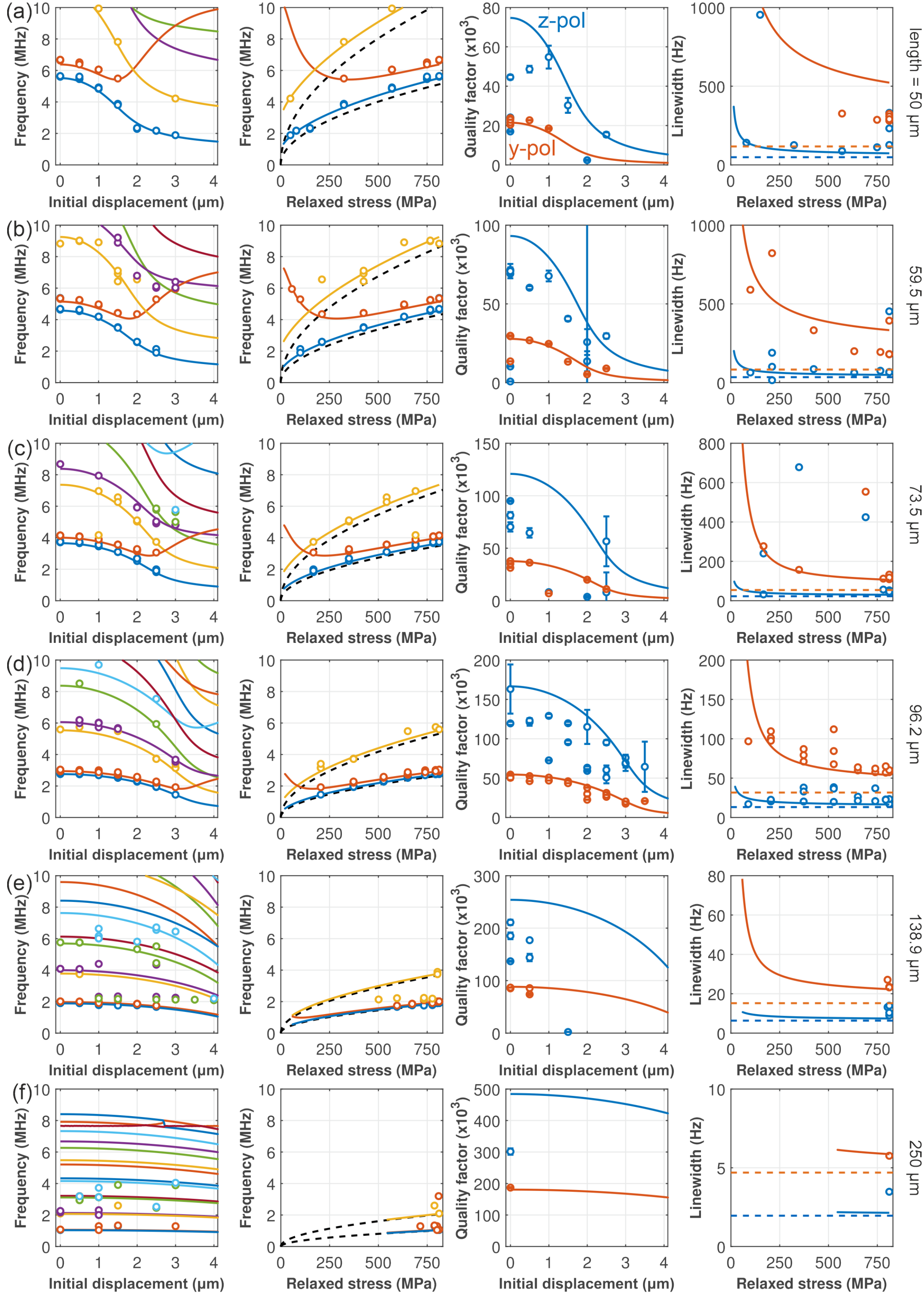

Figure A.2: Analysis of the beam dynamics of all beam lengths analogous to Fig. 6.9. In the individual rows from top to bottom, the beam lengths are 50, 59.5, 73.5, 96.2, 138.9, and 250 μm, respectively. More information can be found in the text.

Appendix B - Surface quality

Reflectometer measurements

Reflectometer measurements have been introduced in Chapter 3 Sec. 3.2.8 and later applied in Chapter 5 Sec. 5.2.1 when analyzing the surface quality and reflectivity of a membrane exposed to BOE. In this Appendix, more details are given about these measurements. Figure B.1 displays the full spectrum of the zoom-in measurements shown earlier. The individual measurements together with their fitted curves and measurement results are provided in Fig. B.2 to Fig. B.6. Details on the measured sample and fitting recipe can be found in the respective panels (a). Two measurements have been taken at different locations, each on the membrane and different locations off the membrane. The respective results match very well and show a high goodness of fit (gof), indicating good reliability.

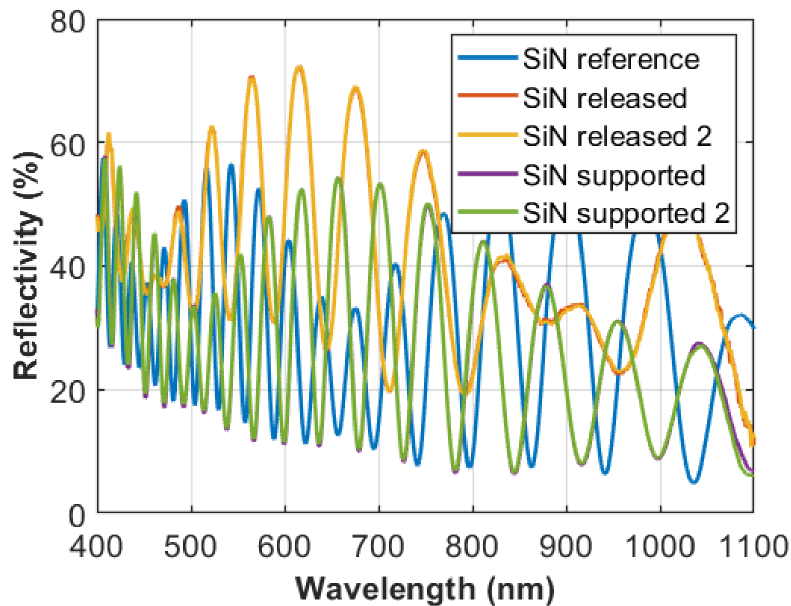

Figure B.3: Comparison of the reflectivity measurements taken on different sample surfaces. This is the same data as shown in Fig. 5.3(c), here plotted over the full wavelength range.

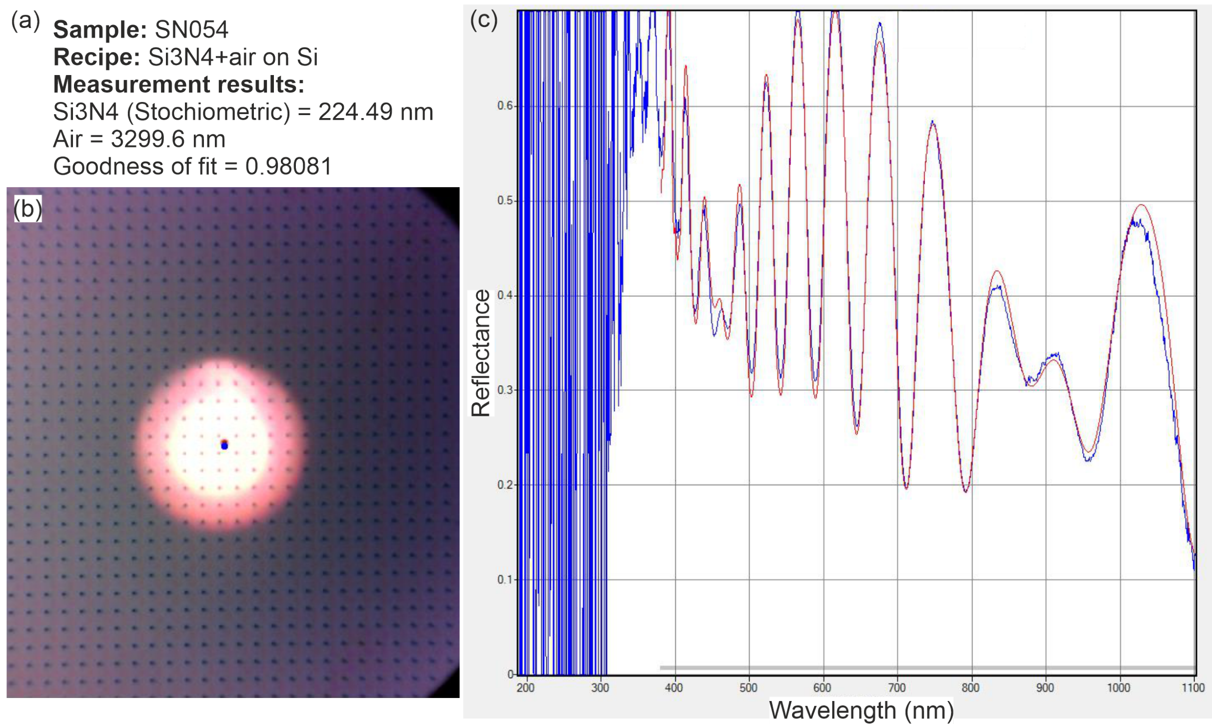

Figure B.4: Reflectometer measurement taken on the center of a membrane. (a) Listed are the sample name, the recipe used for fitting the data, and the measurement results. (b) Microscope image of the measured surface taken by the reflectometer when the measurement was taken. The black dot in the center denotes the spot where the reflectivity of the sample was measured. (c) Screenshot of the measurement result. Plotted is the reflectance over the wavelength. Blue: measured data, red: obtained fit.

(a) **Sample:** SN054
Recipe: Si3N4+air on Si
Measurement results:
Si3N4 (Stochiometric) = 225.22 nm
Air = 3300.6 nm
Goodness of fit = 0.98153

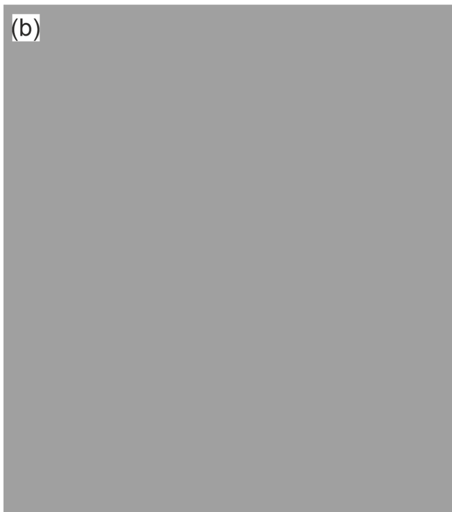

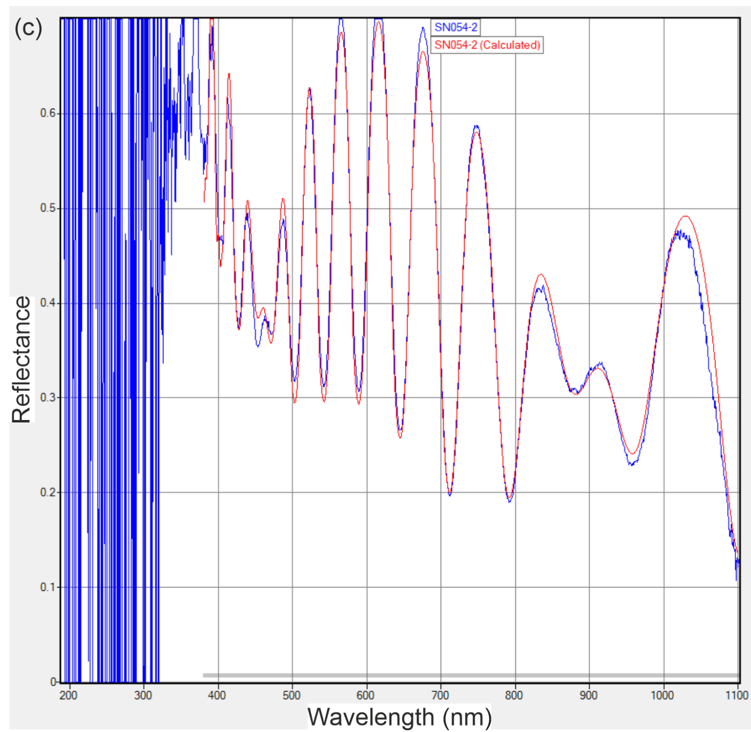

Figure B.5: Reflectometer measurement taken close to a corner of a membrane. (a) Listed are the sample name, the recipe used for fitting the data, and the measurement results. (b) No microscope image of the measured surface is available. (c) Screenshot of the measurement result. Plotted is the reflectance over the wavelength. Blue: measured data, red: obtained fit.

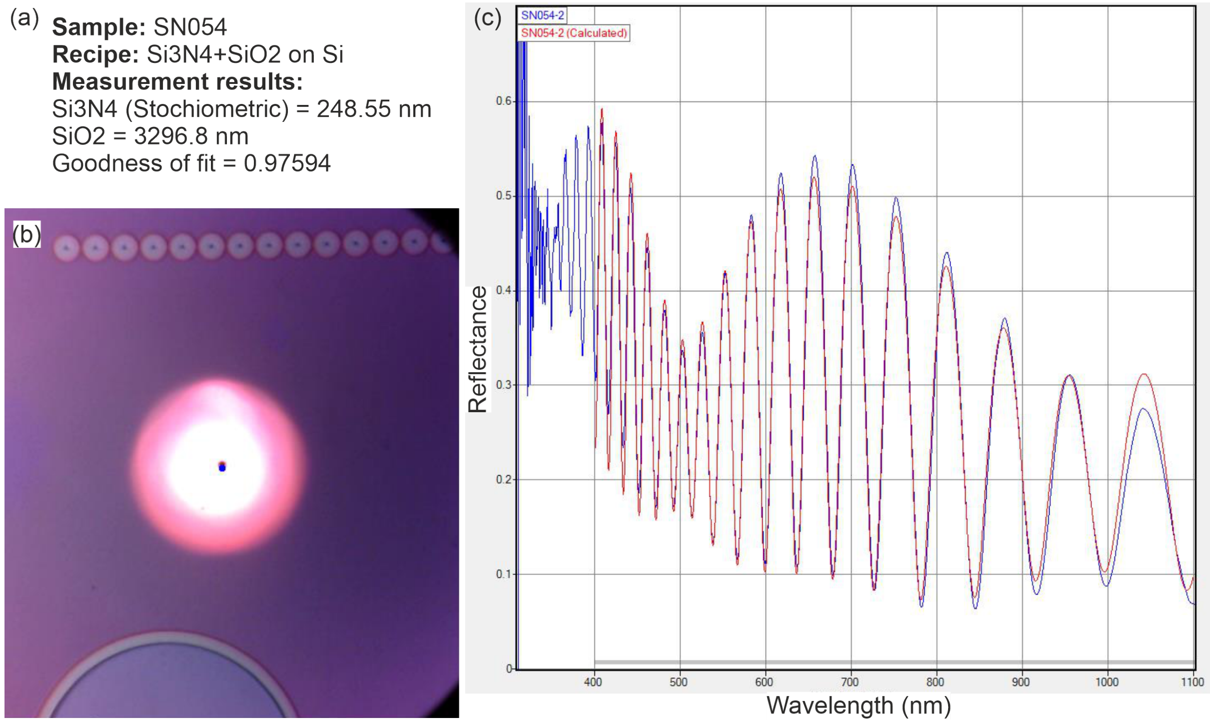

Figure B.6: Reflectometer measurement taken on the SiN surface on the same sample as the membrane shown above. The SiN is not underetched but as the membrane surface, it was exposed to BOE while etching. (a) Listed are the sample name, the recipe used for fitting the data, and the measurement results. (b) Microscope image of the measured surface taken by the reflectometer when the measurement was taken. The black dot in the center denotes the spot where the reflectivity of the sample was measured. (c) Screenshot of the measurement result. Plotted is the reflectance over the wavelength. Blue: measured data, red: obtained fit.

(a) **Sample:** SN054
Recipe: Si3N4+SiO2 on Si
Measurement results:
Si3N4 (Stochiometric) = 249.01 nm
SiO2 = 3294.5 nm
Goodness of fit = 0.94844

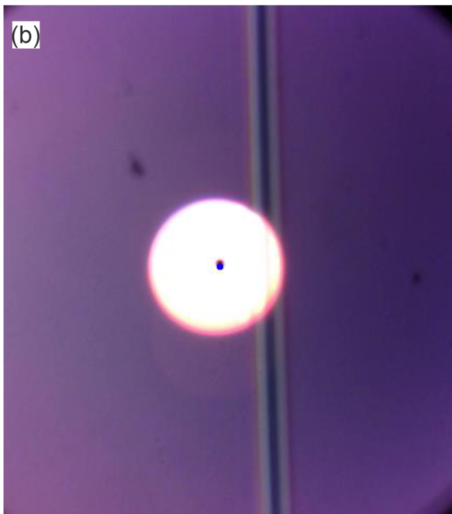

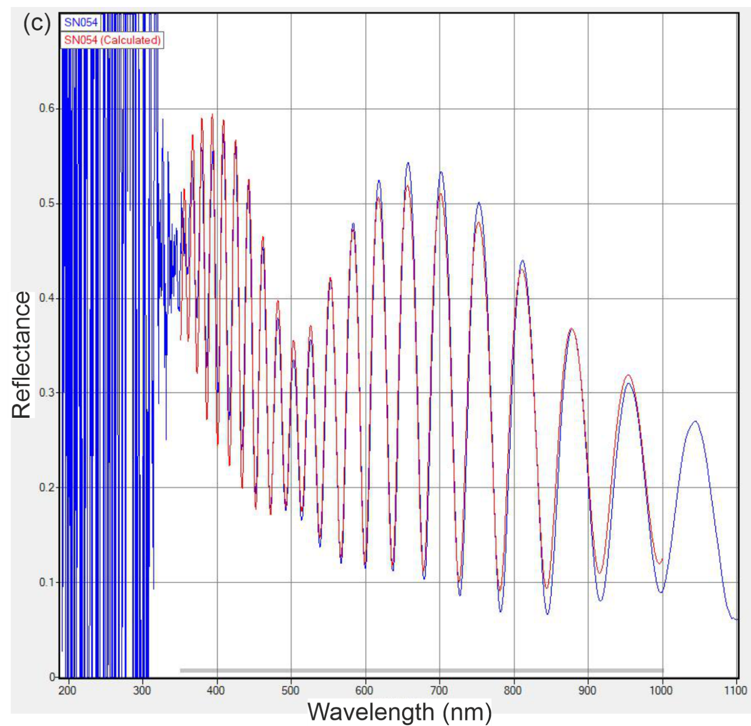

Figure B.7: Reflectometer measurement taken on the SiN surface on the same sample as the membrane shown above. The SiN is not underetched but as the membrane surface, it was exposed to BOE while etching. (a) Listed are the sample name, the recipe used for fitting the data, and the measurement results. (b) Microscope image of the measured surface taken by the reflectometer when the measurement was taken. The black dot in the center denotes the spot where the reflectivity of the sample was measured. (c) Screenshot of the measurement result. Plotted is the reflectance over the wavelength. Blue: measured data, red: obtained fit.

(a) **Sample:** WSN03_28
Recipe: Si3N4+air on Si
Measurement results:
Si3N4 (Stochiometric) = 329.32 nm
Air = 3291.4 nm
Goodness of fit = 0.97201

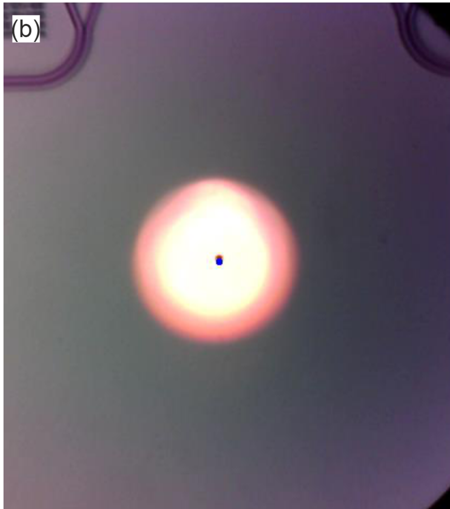

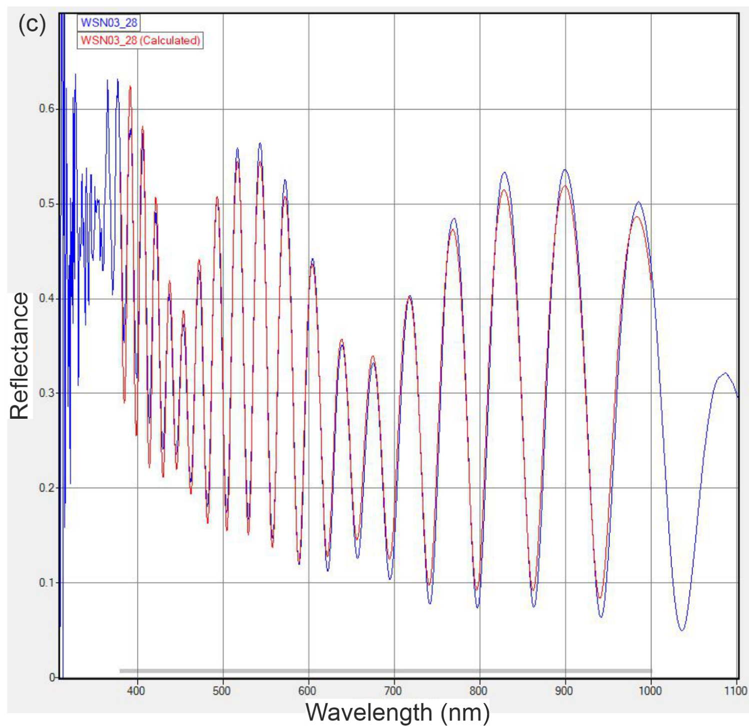

Figure B.8: Reflectometer measurement taken on the SiN surface on a different sample as the membrane shown above. The SiN is not underetched and in contrast to the membrane surface, it was not exposed to BOE. (a) Listed are the sample name, the recipe used for fitting the data, and the measurement results. (b) Microscope image of the measured surface taken by the reflectometer when the measurement was taken. The black dot in the center denotes the spot where the reflectivity of the sample was measured. (c) Screenshot of the measurement result. Plotted is the reflectance over the wavelength. Blue: measured data, red: obtained fit.

List of Figures

2.1 Implementations of optomechanical coupling. (a) Sketch of a Fabry-Pérot cavity with movable end mirror. (b) Microscope image of a racetrack cavity with integrated suspended beams. (c) Mach-Zehnder interferometer with a mechanical device - here, a H-resonator - next to one arm of the interferometer. 6

2.2 (a) Optical microscope image of a grating coupler. (b) Transmission profile of a calibration device over the wavelength. The individual measurements were done with different combinations of input and output fibers (sm: single-mode fiber, mm: multi-mode fiber). 10

2.3 Measurements on calibration devices, i.e. a single waveguide connecting the input and output grating coupler (similar to the device in Fig. 3.14(h)). The device parameters of the grating couplers are swept. (a) Maximum transmission versus the grating period and filling factor of the grating couplers. (b) The wavelength of maximum transmission versus the grating period and filling factor of the grating couplers. For the white data points no data is available. Measurements are taken by Giulio Terrassanta. 11

2.4 Top: maps of the detected power when scanning with the fiber array over a grating coupler. The input and output fibers are single-mode to single-mode (a) and single-mode to multi-mode (b). Bottom: detected power of wavelength scans when scanning from top to bottom over the grating coupler. The input and output fibers are single-mode to single-mode (c) and single-mode to multi-mode (d). Note that the x and y directions are swapped in the top panels for better comparison with the lower panels. These measurements were performed by Menno Poot. 12

2.5 Typical response of a MEMS resonator when the hardening behavior is dominant (the black traced segments are unstable regions): (a) The response when the resonator is in the linear region, (b) the response when the amplitude of oscillation is small but the hardening phenomenon is observed, (c) the response when the amplitude of oscillation is higher than that in (b) and softening just starts to occur over and above the hardening that is already there, and (d) the response when the amplitude of oscillation is very high and softening and hardening are clearly noticeable. Figure and caption adapted from [129] © 2011 IEEE. 16

2.6 (a) Sweep-up case. Note how a *jump* exists from point "B_{up}" to point "C_{up}" without passing by point "peak." (b) Sweep-down case. Note how a *jump* exists from point "peak" to point "C_{down}" spontaneously. Figures and captions adapted from [129] © 2011 IEEE. 17

2.7 Measurement on three different devices fitted with four different functions, each. Panels (a-d) display a measurement in the linear regime on the cantilever discussed later in Sec. 6.9. Panels (e-h) display the results of a measurement on a membrane also in the linear regime but with strong crosstalk described in Sec. 2.4.3. Panels (h-j) display a measurement in the nonlinear regime on the Sbeam discussed in Sec. 6.10. Column one is fitted with the pure standard harmonic oscillator function "SHO" (Eq. (2.10)), column two with the standard harmonic oscillator function including crosstalk "SHO crosstalk" (Eq. (2.11)), column three with the complex duffing fit including crosstalk "duffing crosstalk" (Eq. (2.12)), and column four is fitted with the complex duffing fit including delay "duffing delay" (Eq. (2.13)). . . 20

2.8 (a) Effect of a SiN object (arm) in the vicinity to the waveguide on the effective refractive index n_{eff} in dependence of its distance d_{opt}. The inset shows a sketch of the device. The light mode is symbolized by a change in color in an oval fashion in the waveguide. Adapted from [143]. (b) Principle of the detection mechanism of an integrated Mach-Zehnder interferometer. A small shift of the interference fringes (horizontal arrow) results in a high variation of transmission (vertical arrow) and enables high sensitivities. 22

2.9 (a) Network analyzer traces measured under different conditions. The green curve is measured on a regular Sbeam device with a mechanical resonator. The simulated flexural modes are indicated by the vertical lines, labeled by their polarization and mode number (in-plane in orange; out-of-plane in blue). The other curves are taken on a Mach-Zehnder interferometer device without a beam (light gray), a calibration device with a waveguide directly connecting the input and output grating couplers (gray), and one where the laser was off (dark gray), respectively. (b) Transmission through the devices (colors as in (a)) vs. wavelength. The markers in each curve denote the wavelength selected for the NWA measurements of (a). The overall transmission profile is similar for all devices and is that of the grating couplers. The dips visible in the MZI devices are the typical interference fringes expected in such devices. 23

2.10 Frequency response of the modes marked in Fig. 2.9(a), together with the respective phase $\angle S$. The span is 2 kHz in all panels. The dashed lines are the fits of Eq.(2.10) to the data. 24

2.11 Amplitude response of a string near 9.7 MHz for different excitation powers. . . . 25

2.12 (a) Network analyzer measurement of the fundamental mode of a racetrack device with integrated suspended beam. (b) Thermal motion measurements of the same mode with a spectrum analyzer. The resonance frequency has drifted by 55 kHz between these two measurements. 25

3.1 (a) Image of the full wafer in its transport box, ready to be sent out for dicing. The gold patterns defining the chips are visible. (b) Upper left corner of an empty chip with the gold pattern. Visible in this detail are the frame, square e-beam markers, an alignment cross, our group logo, and parts of the unique chip name. When looking closely, the SU8 covering the markers can be resolved as well. . . 30

3.2 (a) Gold marker unprotected during reactive ion etching. The five linear signatures crossing each edge result from the automatic marker search and focusing of the e-beam writer. (b) Unetched gold markers covered with SU8. The left marker was used to align the pattern, later used for evaporating the metal pattern, and is thus covered with gold in the exposed region. The right marker was not exposed in this lithography step and the gold (applied during this second evaporation step) lifted off completely. (c) Gold markers protected with SU8 during reactive ion etching. The left marker was not exposed to the electron beam and was additionally covered with ZEP resist. The right marker was used for alignment and only protected by the SU8, still, the gold is undamaged. Note that the alignment between SU8 and marker is not perfect, however within tolerance as the marker is fully covered. . 31

3.3 Schematics of the main nanofabrication steps for the Hdirectional. (a) The blank chip after being stripped from the protective resist with layers of 330 nm Si_3N_4 (green), 3300 nm SiO_2 (light gray) on Si substrate (dark gray). (b) Electron beam lithography on PMMA resist to create the mask for metallic structures. (c) Evaporation of gold to create metallic structures, e.g. electrodes. (d) Electron beam lithography on ZEP resist to create the etch mask of the simultaneously photonic and mechanical structures. (e) Dry etching with ICP assisted RIE through the 330 nm thin layer of Si_3N_4 around 70 nm into the SiO_2 cladding layer. (f) Electron beam lithography on ZEP resist to create the etch mask of the purely photonic structures. (g) Dry etching with ICP assisted RIE around 300 nm into the Si_3N_4 layer. (h) Optical lithography on AZ resist to create etch masks for the subsequent wet etch. (i) Wet etch with buffered oxide etch (BOE) to release the mechanical structures defined in step (e). (j) The finished sample, ready to be studied. . . . 32

3.4 Optical micrograph of a developed pattern. Shown are the structures of the two future electrodes of a H-directional device written on PMMA. 32

3.5 Gold structures after liftoff. (a) Wires sonicated too short: some gold is still sticking to the wires. (b) Broken wires, no electrical connection will be possible. (c) Unwanted gold that could not be removed during liftoff is remaining on the sample, covering the wires and electrodes. This is creating a short in the circuits and will prevent mechanical structures from proper release. (d) Electrodes and wires are properly lifted off, and no damage is visible. The width of the wires is 1 μm. 33

3.6 Scanning electron image of the cross-section of two adjacent waveguides out of SiN, here with a layer of AlN deposited on top. Figure taken by Timo Sommer. 35

3.7 Finished Hdirectional device. (a) The full device, (b) zoom into the directional coupler region. The distance between the grating couplers is 250 μm and the length of the coupling region is 168 μm. 36

3.8 Potential issues in electron beam writing. (a) Stitching errors between neighboring main fields result in a horizontal shift between the grating coupler and waveguide. (b) Non-circular photonic crystal holes due to too high beam currents. (c) Ridges in the grating coupler structure due to underexposure. (d) Missing subfields due to 1-dimensional structures in the pattern file, not corrected by the merge function. Insets: (top) One-dimensional structure as appearing in the gds file on the gap next to a waveguide. The features in this image have been enhanced for clarity. (bottom) Example of such a subfield written at a random location on the chip instead. 37

3.9 Sample analysis using different techniques. (a) Optical microscope image of an overview over several full scale devices. (b) AFM image zooming into a part of a grating coupler providing information of the height profile. (c) SEM image of the holes of a photonic crystal pattern of a Hdirectional device. (d) Reflectometer measurement of a SiN layer on SiO_2 on Si substrate. Displayed is the reflectivity of this layer stack over the wavelength. 39

3.10 Chip diced (a) manually with a diamond scribe and (b) with a wafer saw. 40

3.11 Alignment of the ring resonator and suspended beam (i.e. the through and masked layer) on our racetrack devices. (a) No mismatch of the layers is visible. The figure is taken with an optical microscope. (b) Large lateral shift between the layers. The figure is taken with an SEM. Both panels are taken from [137]. 42

3.12 Etch rates of our inductively coupled plasma-assisted reactive ion etching recipe optimized for optical and mechanical structures on a SiN platform. Plotted is the etch depth into the material versus time, measured with (a) an ellipsometer and (b) a profilometer. The trend is linear with a little offset, due to the strike step, having a higher etch rate for a few seconds in the beginning. The kink in the data appears when the SiN layer is fully etched through and the SiO_2 starts being etched. The measurements and analysis were performed by Burak Yildiz [148]. . 43

3.13 Profilometer measurements on a Hdirectional device covered with ZEP taken during fabrication. The electrodes are applied and the through etch is performed. Black: profile taken on the blank surface, blue: profile taken with ZEP applied at 3000 rpm (a) and 2000 rpm (b). The figure is taken from [149]. 44

3.14 Devices that will be mentioned throughout this thesis. (a) Hdirectional, (b) Hresonator, (c) Sbeam, (d) membrane, (e) two-dimensional drum array (top) and one-dimensional drum array (bottom), (f) trampoline, (g) cantilever, (h) photonic crystal beam, (i) racetrack. The bottom panels in (a,b,c,h) show a zoom into the functional region of the respective device. The device dimensions are described in the text. 45

4.1 Sketch of the QMS setup shown in Fig. 4.2. FPC: fiber polarization controller, yellow line: input fiber guiding the laser light onto the sample, blue lines: output fibers, collecting the light transmitted through the device. The output fibers end in photodetectors, connected to a DAQ. The motorized x-y stage and laser are Labview controlled. The data coming from the DAQ is also read by Labview. Figure adapted from [143]. 53

4.2 QMS setup. (a) Overview of the whole setup. (b) Sample holder and arm holding the fiber array. A sample is placed below the fiber array. At the top of the image, the camera objective for the observation optics is visible (black part). (c) Zoom towards the fiber array and sample. The devices on the sample are visible. The fiber array is reflected on the sample surface. (d) View through the observation camera onto the sample with devices on it. The red light is sent through one of the fibers and projected onto the sample. This is not the measurement laser (NIR) but a test laser in the visible regime used to align the grating couplers of the devices below the fibers. 54

4.3 Individual parts of the QMS. (a) Fiber polarization controller. (b) View into an opened FPC paddle with the winded fiber visible. (c) Electrical probe. 55

4.4 (a) Microscope image of the sample with devices on it. (b) Scanning electron micrograph of a grating coupler. (c) Histogram of the detected power for 100 optimizations of the chip position underneath the fiber array. Figure adapted from [143]. 55

4.5 (a) Outside view of the LVC. (b) View inside the chamber. (c) Close view of the PCB and fiber array. Inset: Bonded wires connecting the RF connector with the piezo. 56

4.6 (a) Pressure versus time during pump-down of the LVC. The pressure was obtained by gauges with different measurement ranges, a Pirani gauge (blue), and two AIM-S gauges (red and yellow). The purple dashed line is laid onto the data for the full range, combining the data of all three gauges in their respective measurement ranges. (b) Quality factor of a Hresonator device (c.f. Fig. 3.14(b)) versus the pressure inside the vacuum chamber. Panel taken from [143]. 57

4.7 (a) Photograph of the attenuator with control electronics. (1) Attenuator HP 33321SC, (2) Relais board, (3) Arduino. (b) Response of a Sbeam device at an excitation power of 10 dBm set by the NWA but different settings of the attenuator. Correction of the response for the attenuation is done during data processing. The legend displays the respective attenuator setting. 58

4.8 (b) Schematic overview of the measurement setup. BE: beam expander, (P)BS: (polarizing) beam splitter, QWP: quarter wave plate, PD: photodetector, LNA: low-noise amplifier, NWA: network analyzer, T: bias tee, +: combiner, LED: light emitting diode for illumination. 59

4.9 View on the SVC setup at an early stage, where calibrations were performed (here, an optical power meter is connected to a detector to measure and characterize the beam alignment). The optics are placed on the optical table with the HeNe laser placed inside the gray box (1) and the vacuum chamber (2) visible in the lower right corner of the image. The optical path is indicated by red lines, also visible are the photodetector (3), the observation camera (4), and the illumination source (5). The control electronics stand on the rack above (6). 60

4.10 (a) Main part of the beam path between laser, objective, and detector. (b) View inside the vacuum chamber through the viewport. Visible are the microscope objective mounted over the viewport and the sample mounted on a PCB inside the chamber. (c) PCB with the actuating piezo and sample mounted onto it. In the lower right corner, the connector for applying HF signals to the piezo is visible. 61

4.11 Magnitude (bottom panel) and phase (top panel) of the frequency response of a piezo element actuating the sample. Visible is the fundamental thickness mode of the piezo at about 20 MHz and its third higher harmonic close to 60 MHz. . . . 61

4.12 (a) Photograph of a Peltier element (side length: 40 mm) and (b) temperature sensor Pt1000 (the image of the Pt1000 is enlarged by a factor of 2 with respect to the Peltier element in panel (a)). (c) Measured temperature vs. current sent through the Peltier element. (d) Measured temperature vs. time in the measurement of (c). (e) Zoom into panel (d). 62

5.1 Optical micrographs of differently sized membranes. (a) Membrane with a side length of 275 μm, discussed in this work. (b) Zoom into the membrane of (a). The holes (gray dots) are dry etched through the SiN layer, each being the starting point for the 10 μm wet etch in a circular fashion. (c) Example of a small membrane realized on the chip. 68

5.2 Schematic illustration of the nanofabrication process flow of the sample. (a) The sample is diced from a wafer with 330 nm Si_3N_4 on 3300 nm SiO_2 on a Si substrate. (b) The holes of the membrane are patterned by electron beam lithography. (c) The holes are dry etched by reactive ion etching. (d) The membrane is released by wet etching with buffered hydrofluoric acid (light blue). (e) Under the released membrane a cavity is formed, resulting in the interference utilized for measuring the mode shapes. 69

5.3 Measurement of the surface properties of SiN after being exposed to BOE for about two hours. The measurements were taken by SEM (a), AFM (b), and reflectometry (c). The measurements were taken on different parts of the SiN surface, while (b) and (c) show measurements on a fully released membrane, is (a) showing a pattern where the holes have a larger distance and thus form coupled drums after the given time for the wet etch instead of a fully released membrane. The horizontal features next to the holes in panels (a) and (b) are artifacts, resulting from the horizontal scan direction. The inset in (b) shows a part of the SiN surface without holes and thus a much smaller range of the scale bar to make smaller features on the surface visible. (c) Shown are five measurements, one on an unetched reference sample (blue), two measurements on locations that were exposed to BOE only at the upper side (supported: purple, green), and two measurements on locations that were exposed to BOE both at the upper and lower side, i.e. a released membrane (released: red, yellow). The two supported (and the two released) measurements match very closely and can hardly be distinguished in the figure. The numbers indicate the reflectivity at the laser wavelength used in the setup, i.e. 632.8 nm. A figure showing the full wavelength range of this data can be found in Appendix B. 70

5.4 Measurement of the surface properties of the Si substrate after the SiO_2 layer has been etched away. The measurements were taken with an SEM (a), an AFM (b), and a reflectometer (c). The reflectometer measurements were taken on a polished reference Si sample (blue) and on the Si surface exposed to BOE (red). The black dot indicates the reflectivity of both samples at 632.8 nm, i.e. the laser wavelength of our setup. The measurements of (a), (b), and (c) were taken on close by, but not exactly the same parts of the Si surface. 71

5.5 (a) Sketch of the cross-section of a membrane device. The light green areas in the SiN layer indicate that the membrane includes a series of holes. As the underetching starts at the holes and continues until the full membrane is released, different parts on the bottom of the membrane are in contact with the etchant for different times and the thickness is thus not constant all over the membrane. If the light is partially or fully hitting a hole, the reflected signal becomes even more complex and differs from reflections at unperforated parts of the membrane. This becomes visible in both the reflectivity maps (Fig. 5.6) and mode maps (Fig. 5.12). (b) Interferometric principle of the measurement setup. When actuated, the distance between Si_3N_4 and Si changes dynamically. This results in a time-dependent interference pattern of the light reflected at the membrane and the light reflected at the substrate (red arrows). For clarity, the light path is drawn with an angle while the light is actually hitting the membrane perpendicular to its surface with a maximum angle of 16.3 degree due to its numerical aperture of 0.28. The layer stack is SiN on air on silicon. 72

5.6 Reflectivity map of a membrane with a side length of 275 μm. The data was taken in the same measurement as Fig 5.14. 72

5.7 Sketch of the overall system response. $V_{input}(\omega)$ is the driving voltage from the NWA or lock-in amplifier output, A is the response of the piezo transduction, R is the response of the photodector, G is the response of the amplifier, $\partial P/\partial U_{m,n}$ is the change of the reflected laser power with the displacement of the entire mode $U(\omega; x, y)$, and $V_{out}(\omega)$ is the voltage as measured by the NWA or lock-in amplifier. The "crosstalk" symbolizes possible pathways of the electical crosstalk in the setup. 73

5.8 Driven response of the membrane measured using the NWA (blue) with the calculated frequencies (Eq. (2.8)) as black dashed lines and the mode numbers indicated. The gray trace is the instrument background. 74

5.9 Driven responses of the modes described in this chapter. For the first 6 modes, the span is 200 Hz, whereas for the triplet the span is 500 Hz. The blue curves are measured using the LIA, whereas the black dotted lines are the fits of Eq. (5.1) to the data. The measurement settings and fit results are indicated in Table 5.1. 75

5.10 Network analyzer measurement of the driven response near the (3,1) and (1,3) eigenfrequencies. Two separate resonances with a spacing of 1.06 kHz can be seen. As discussed in the text, the left and right resonance correspond to the (3, 1) and (1,3) modes, respectively. 76

5.11 Line traces over the membrane for (i) constant frequency (dark blue), (ii) regular PLL (light blue), (iii) the modified PLL with mod 180° (orange), (iv) data measured using a network analyzer (green). (a) Reflected laser power. (b) The mode profile of the (1,3) mode near 3.26 MHz. Solid (dashed) lines indicate the real (imaginary) part. The curves are offset for clarity. (c) Frequency change during the measurement. For (i)-(iii), this was the actuation f, whereas for (iv) the resonance f_0 was extracted from the NWA traces. By definition, the frequency was constant in (i). (d) Elapsed time since the start of the trace. 77

5.12 Normalized mode maps (real part) of the first six modes of the square SiN membrane acquired in a single, simultaneous, measurement with the method described in this chapter. The release holes are visible as an array of dots across the entire surface of the structure. Starting frequencies are indicated in each map; further properties are listed in Table 5.1. 79

5.13 (a) Driven response near $f_{5,5} = f_{1,7} = f_{7,1}$. The triplet is fitted using three standard harmonic oscillator responses taking crosstalk into account (Sec. 5.3.2) [145] (black line). (b) Measured (top) and calculated (bottom) mode maps. The weights from the linear fitting are $\{w_{5,5}, w_{1,7}, w_{7,1}\} \propto \{0.561, -0.506, 0.656\}$, $\{0.817, 0.260, -0.515\}$, and $\{0.105, 0.694, 0.712\}$ for the left, middle, and right peak, respectively. The fit uncertainty in the weights is 0.002. 80

5.14 (a) Shift of the resonance frequencies of the first six modes over time (sweep steps). (b) Frequency shift of (a), relative to the shift of the first mode. 80

5.15 (a) Measurement of a fundamental membrane mode with the NWA. (b) Thermal motion measurement of the mode of (a) with a SPA. 81

5.16 Temperature sweep: Resonance frequency shift (top panels) and quality factor (bottom panels) of the fundamental mode when the temperature is changed. (a,c) The sample was cooled below ambient temperature and warmed up back to ambient. At each new setting of the current through the Peltier element, 500 traces were taken to let the temperature settle. In the plot, the result of the last trace at each setting is shown. The black arrows indicate the sweep direction. (b,d) The sample was heated above the ambient temperature and let to cool back to ambient. At each new setting of the current through the Peltier element, 300 traces were taken to let the temperature settle. In the plot, the result of the last trace at each setting is shown. 82

5.17 Overlay of the measurement of the temperature and the observed shift in resonance frequency versus time. (a) The stage was cooled below ambient temperature and heated up again with a zoom shown in (b). (c) The stage was heated above ambient temperature and cooled down again with a zoom shown in (d). The temperature was scaled with a factor of 0.34 kHz/° C. The data was obtained in the same measurements as that in Fig. 5.16. Panels made by Menno Poot. 83

5.18 Racetrack device with photonic crystal beam in the vicinity of the suspended beams integrated into the racetrack. (a) Frequency shift vs. laser power sent into the device (blue: photonic crystal beam, green: beam integrated into the racetrack). (b) Frequency shift measured during a temperature sweep, as in Fig. 5.16(b). The black arrows indicate the sweep direction. 84

5.19 Measurements on a trampoline (a,d,g), cantilever (b,e,h) and AlN coated membrane (c,f,i). Top row: Reflectivity maps; middle row: frequency and phase response of the driven devices; bottom row: PLL maps of the respective modes shown in the middle row. Measurements taken by Timo Sommer (left), Julius Röwe (middle), and Aditya Yadav (right). 85

6.1 Various techniques of stress tuning: (a) Bending of the whole chip. Reprinted and adapted with permission from Verbridge *et al.* [54]. Copyright 2007 American Chemical Society. (b) Widening of the clamping points, as demonstrated by Sadeghi *et al.* [88], reprinted and adapted with permission from AIP Publishing. (c) Integration of structures into the bulk, close to the clamping points, as demonstrated by Zabel *et al.* [53], reprinted and adapted with permission from Springer Nature. (d) Hierarchical structuring of the resonator. Reprinted and adapted with permission from Bereyhi *et al.* [51] (Creative Commons Attribution 4.0), (e) Clamp tapering as demonstrated by Bereyhi *et al.* [55], Reprinted and adapted with permission from Nano Lett. 2019, 19, 4, 2329–2333. Copyright 2019 American Chemical Society. (f) Phononic crystal structuring. Reprinted and adapted with permission from Ghadimi *et al.* [58]. Copyright 2017 American Chemical Society. 90

6.2 (a) Illustration of the stress distribution of a pre-displaced nanomechanical beam, before and after relaxation [122]. The beam straightens when being released and the stress relaxes, depending on the beam length and initial displacement. (b) Setup for the dynamic measurements. The chips are placed inside a vacuum chamber to avoid air damping. The probe laser is a tunable step laser and the polarization of the light is optimized with an FPC. The light is coupled on and off the chip with grating couplers and a fiber array placed above the sample. An NWA is driving the piezo element (ocher) underneath the sample, mechanically exciting the resonator. It also measures the signal coming from the photodetector (PD). For positioning the chip, the signal from the PD can also be read via a DAQ. A micrograph of a single device containing an integrated MZI with a 250-μm-long beam above the sensing waveguide of the interferometer is shown in the schematic. On each chip, there are many of these devices. 91

6.3 Chip design A as realized with the parameters listed in table 6.1. Horizontally the pre-displacement of the beams is swept. Vertically the design consists of five blocks as indicated by the black boxes. Within each block, the beam length is swept. The devices in the different blocks have the same parameters, only their distance to the MZI varies. At the bottom, three rows of calibration devices are placed: one row that only consists of a waveguide connecting the two grating couplers and two identical rows of MZIs without a beam. The inset shows a zoom into a part of the design with two rows of calibration devices and two rows of devices with beams. 92

6.4 Nanofabrication steps for the Sbeam chip. (a) The blank chip consists of a 330 nm thin layer of Si_3N_4 (green) on a 3300 nm cladding layer of SiO_2 (light gray). The substrate is $\sim 525\,\mu$m silicon (dark gray). The Si_3N_4 and SiO_2 layers are on both sides of the double-sided polished chip. (b) The surface, covered with ZEP520A resist, is exposed in an electron-beam writer. In this first lithography step the structures that are going to be released later are defined. (c) The developed chip is dry-etched in an ICP-RIE. It is etched through the SiN layer, about 70 nm into the SiO_2. (d) In the second lithography step, the photonic structures are defined via electron-beam lithography. (e) In the second dry-etching step the photonic structures are etched such that about 30 nm of SiN remains. (f) The mechanical structures are released by wet-etching with buffered hydrofluoric acid. The photonic structures are protected from release by the remaining SiN layer. (g) The finished chip. The chip is critically point-dried to protect the mechanical structures from being destroyed by the surface tension of the liquid. 93

6.5 Normalized displacement $u_0(\tilde{x}/D_0)$ of each beam shape vs. the normalized position $\tilde{x} = x/L$. The shape of the Sbeam closely follows that of the cosine and is not plotted additionally. 94

6.6 Simulated stress distribution inside a 100 μm long released beam. Displayed is the stress component σ_{xx}. The beams are displaced in the y-direction, shown is the x-y-plane. The displacement U_0 is (a) $0\,\mu$m, (b) $2.5\,\mu$m and (c) $4.5\,\mu$m. The average σ_{xx} over beam is 811, 403, and 32 MPa, respectively, as indicated in the color bar. In panel (b) also the stress distribution inside specific cut-planes (z-y) is shown. The positions of the cut-planes are (i) next to a clamping point, (ii) at the center, i.e. the maximum displacement, and (iii) at a quarter of the beam length, i.e. the minimum of the curvature. For clarity, the x and y directions are plotted on a different scale. Figure reprinted from [122] ©2022 American Physical Society. 96

6.7 SEM images of a beam with $D_0 = 3\,\mu$m and $L = 73.5\,\mu$m before (a) and after (b) release. (c) Displacement D of 73.5 μm long beams with different D_0 before (filled circles, dashed line) and after (open circles, solid line) release. Data (circles) is extracted from SEM images like (a) and (b), and lines are FEM simulations. (d) Displacement D vs. length of beams initially displaced by 3 μm. Markers, lines, and colors as in (c). (e) Simulation of the stress after relaxation of the beam vs. D_0 for various lengths L. 96

6.8 (a) Measured frequency response of a beam with $L = 96.2\,\mu$m and $D_0 = 1.5\,\mu$m (gray). The resonances are highlighted by arrows and the simulated flexural modes are indicated by the vertical lines, labeled by their polarization and mode number (in-plane in orange; out-of-plane in blue). (b) Zooms into the resonances observed in (a) together with the fitted standard harmonic oscillator response in the presence of crosstalk [145] (dashed lines). The span is 2 kHz in all sub-panels. 98

6.9 (a) Resonance frequencies of the flexural modes of beams with $L = 96.2\,\mu$m and D_0 varying from 0 to 4 μm, both measured (circles) and simulated (solid lines). (b) Resonance frequencies of the first three modes (same data as in (a)) vs. the stress after relaxation. The black dashed lines are the first two modes of strings (cf. Eq. (6.2)). (c) Quality factors of the first in-plane (orange) and out-of-plane (blue) mode. Solid lines: model of dissipation (Eq. (6.3)) with $Q_{\mathrm{bending,z}} = 6800$ and $Q_{\mathrm{bending,y}} = 7300$. (d) Linewidth of the fitted peaks of the first two modes shown in (b) vs. stress. The solid lines are the calculated linewidths for the respective Q_{bending} and the dashed lines indicate w_{edges}, the linewidth assigned to the damping contribution of the edges. The colors of the different modes are consistent between all panels. 98

6.10 (a)-(c) Mode shapes $u(x)$ for the fundamental modes, and its first and second derivatives for the indicated values of the normalized tension. For clarity, the first and second derivatives have been normalized to their maximum value. (d) Mean-squared stretching $\langle u'^2 \rangle$ and (e) Mean-squared curvature $\langle u''^2 \rangle$ as obtained by (numerically) integrating the derivatives of the solutions to the Euler-Bernoulli equation. The dashed lines show the analytical results from the integration of Eq. (6.8), which are $\pi^2/2$ and $\pi^4/2$, respectively. (f) Dissipation dilution factor DD as function of the normalized tension, together with a fit by Eq. (6.10). The value of the fit parameters are $\tilde{n} = 1.538 \pm 0.018$ and $a = 0.561 \pm 0.003$. 102

6.11 Comparison of different models for the mode shape: full mode profile (a) and zoom into the left clamping point for the mode (b) as well as the first (c) and second (d) derivative. FEM (light gray), Euler-Bernoulli with $T_{norm} = 3131.8$ (dark gray) (compare Fig. 6.10), cantilever with the length to match the slope a string (yellow) and string (red). Note that in panel (d) the y-scale starts slightly below 0 due to the negative curvature in the center region of the mode. 103

6.12 Normalized linewidth, i.e. the ratio of the linewidth of beams with varying amount of normalized tension T_{norm} to the linewidth with no tension at all, for the fundamental mode. Blue curve: linewidth obtained from Eq. (6.11), black curve: fit following the trend of Eq. (6.12). 104

6.13 (a) Quality factor of the y- (lower curve) and z- (upper curve) polarized mode of beams with $D_0 = 2.5$ μm and varying length. (b) Quality factor of the first (z-pol) mode of displaced beams vs. beam length. The different colors denote the different D_0 as displayed in the legend. (c) As (b) but shown is the second (y-pol) mode. 106

6.14 Study of different beam shapes (all with $L = 96.2\,\mu$m) and varying pre-displacement. (a) Optical micrographs of the different shapes: (top to bottom) Sbeam, triangular, sine-shaped with half a period, and cosine-shaped with one, two, and three periods, respectively. (b) Resonance frequency of the fundamental out-of-plane mode of each shape vs. D_0. Shown are both simulated (solid lines) and measured (circles) data. The shaded area marks a narrow band around 2 MHz containing a studied device of each shape. (c) Same as (b) but for the fundamental in-plane mode. (d) Plotted is the same data as in (b) but here vs. σ. The black dashed line denotes perfect strings of Eq. (6.2). (e) As (d) but for the fundamental in-plane mode. 107

6.15 (a) Measured and simulated resonance frequencies of the in-plane mode (y-polarized) of each shape vs. the frequencies of the respective out-of-plane mode (z-polarized). Inset: Simulated stress in the beams vs. designed displacement. (b) Quality factors of the two fundamental flexural modes (orange: y-polarized, blue: z-polarized) of devices within the shaded frequency band indicated in Fig. 6.14(b,c) in the respective upper panels. 107

6.16 Frequency and phase response of the fundamental out-of-plane mode of a cantilever with $15\,\mu$m length and $2\,\mu$m width. The quality factor obtained by the standard harmonic oscillator fit including cross-talk (Eq. (2.11)) is 6985 ± 10. Measured by Julius Röwe [183] 110

6.17 The two chips (A & B) measured for this work are analyzed individually with respect to the fitted curve. In (a),(b) blue ((c),(d) orange) the data and fit of the first out-of-plane (in-plane) mode as shown in Fig. 6.9(c). In gray the curve with fit parameter Q_{bending} of the respective other mode (cf. Eq. (6.3)). All Sbeams with $L = 96.2\,\mu$m. 111

6.18 Network traces taken at different excitation powers on a Sbeam device showing positive duffing (a)-(d) and another Sbeam device showing negative duffing (e)-(h). (a) excitation from -30 dBm to -2 dBm and (e) excitation from -26 dBm to -6 dBm: Raw network traces. The traces show increasing deviation from Lorentzian behavior for increasing excitation powers. (b,f) Fitted response at selected excitations. (c,g) Fitted Q vs. excitation power. (d,h) Normalized duffing parameter α_n vs. excitation power. The black dashed line is a quardatic fit through the data. The device in the left column has a length of 73.5 μm and displacement of 0 μm. The device in the right column has a length of 96.2 μm and displacement of 3.0 μm. 112

A.1 Quality factors of the z-polarized (blue) and y-polarized (orange) modes vs. the beam length. (a)-(i) display the data for a specific displacement $0\,\mu$m to $4\,\mu$m, respectively. 120

A.2 Analysis of the beam dynamics of all beam lengths analogous to Fig. 6.9. In the individual rows from top to bottom, the beam lengths are 50, 59.5, 73.5, 96.2, 138.9, and $250\,\mu$m, respectively. More information can be found in the text. . . . 121

B.3 Comparison of the reflectivity measurements taken on different sample surfaces. This is the same data as shown in Fig. 5.3(c), here plotted over the full wavelength range. 123

B.4 Reflectometer measurement taken on the center of a membrane. (a) Listed are the sample name, the recipe used for fitting the data, and the measurement results. (b) Microscope image of the measured surface taken by the reflectometer when the measurement was taken. The black dot in the center denotes the spot where the reflectivity of the sample was measured. (c) Screenshot of the measurement result. Plotted is the reflectance over the wavelength. Blue: measured data, red: obtained fit. 124

B.5 Reflectometer measurement taken close to a corner of a membrane. (a) Listed are the sample name, the recipe used for fitting the data, and the measurement results. (b) No microscope image of the measured surface is available. (c) Screenshot of the measurement result. Plotted is the reflectance over the wavelength. Blue: measured data, red: obtained fit. 125

B.6 Reflectometer measurement taken on the SiN surface on the same sample as the membrane shown above. The SiN is not underetched but as the membrane surface, it was exposed to BOE while etching. (a) Listed are the sample name, the recipe used for fitting the data, and the measurement results. (b) Microscope image of the measured surface taken by the reflectometer when the measurement was taken. The black dot in the center denotes the spot where the reflectivity of the sample was measured. (c) Screenshot of the measurement result. Plotted is the reflectance over the wavelength. Blue: measured data, red: obtained fit. 126

B.7 Reflectometer measurement taken on the SiN surface on the same sample as the membrane shown above. The SiN is not underetched but as the membrane surface, it was exposed to BOE while etching. (a) Listed are the sample name, the recipe used for fitting the data, and the measurement results. (b) Microscope image of the measured surface taken by the reflectometer when the measurement was taken. The black dot in the center denotes the spot where the reflectivity of the sample was measured. (c) Screenshot of the measurement result. Plotted is the reflectance over the wavelength. Blue: measured data, red: obtained fit. 127

B.8 Reflectometer measurement taken on the SiN surface on a different sample as the membrane shown above. The SiN is not underetched and in contrast to the membrane surface, it was not exposed to BOE. (a) Listed are the sample name, the recipe used for fitting the data, and the measurement results. (b) Microscope image of the measured surface taken by the reflectometer when the measurement was taken. The black dot in the center denotes the spot where the reflectivity of the sample was measured. (c) Screenshot of the measurement result. Plotted is the reflectance over the wavelength. Blue: measured data, red: obtained fit. . . . 128

List of Tables

5.1 Overview of the excitation power, setpoint, and fit parameters (see Fig. 5.9) for the modes discussed in this work. The fit uncertainty in the resonance frequency is below 3 Hz for all modes, but the exact value drifts over the course of time. . . 76

6.1 Design parameters of the devices chip A. The pre-displacement is swept horizontally (H), the beam length is swept vertically within a block (I), and the beam-to-MZI distance is swept blockwise (B) (c.f. Fig. 6.3). 90

6.2 Parameters used in simulations and modelling 95

6.3 Parameters of the modes shown in Fig. 6.8 as obtained from fitting the harmonic oscillator response with crosstalk, Eq. (2.10), to the data. Listed are the resonance frequencies f_0, linewidth w, quality factor Q, magnitude of the mechanical contribution Z_{mech}, and complex angle α. The listed uncertainty is the 95% confidence level for the fitted coefficients. 97

6.4 Fit parameters obtained by fitting Eq. (6.10) to the dilution factor, using shapes calculated by the Euler-Bernoulli equation, for different modes, as was shown for the fundamental mode in Fig. 6.10(f). The indicated uncertainty is half the confidence interval returned by Matlab's fit function. 104

6.5 Design parameters of the devices on chip B. The pre-displacement is swept horizontally (H), the beam shape is swept vertically within a block (I), and the beam-to-MZI distance is swept blockwise (B). The beam length is fixed for all devices to 96.2 μm. 108

6.6 Comparison of the dynamics of beams with different shapes with D_0 chosen such that f_0 is closest to 2 MHz. Displayed are the shape, displacement D_0, measured resonance frequency (f_{exp}) and quality factor (Q_{exp}), simulated resonance frequency (f_{sim}) and dissipation dilution factor ($\mathrm{DD}_{\mathrm{sim}}$), for both the out- and in-plane modes. For most shapes, two separate devices were measured and thus two experimental values are given. 108

List of Publications

Publications

- D. Hoch, T. Sommer, S. Mueller, and M. Poot, On-chip quantum optics and integrated optomechanics, *Turkish Journal of Physics, vol. 44, no. 3, pp. 239 – 246, 2020* DOI:10.3906/fiz-2004-20
- D. Hoch, K.-J. Haas, L. Moller, T. Sommer, P. Soubelet, J. J. Finley, and M. Poot, Efficient optomechanical mode-shape mapping of micromechanical devices, *Micromachines, vol. 12,no. 8, 2021* DOI:10.3390/mi12080880
- D. Hoch, X. Yao, and M. Poot, Geometric tuning of stress in silicon nitride beam resonators, *Nano Letters, vol. 22, issue 10, pp. 4013–4019, 2022* DOI:10.1021/acs.nanolett.2c00613
- X. Yao, D. Hoch, and M. Poot, Relaxation and dynamics of stressed predisplaced string resonators, *Physical Review B, vol. 106, issue 17, pp. 174109 2022* DOI:10.1103/PhysRevB.106.174109
- T. Sommer, D. Hoch, K.-J. Haas, L. Moller, J. Röwe, A. Yadav, P. Soubelet, J. J. Finley, and M. Poot, Optomechanical Mode-Shape Mapping in the Presence of Crosstalk, *Sensors & Transducers, vol. 258, issue 4, pp. 1-9, 2022*

Conference Contributions

- DPG summer school 2018, poster
- IAS General Assembly 2018, poster
- IAS General Assembly 2019, poster
- MCQST Munich Conference on QST 2019, poster
- MCQST-Technion Symposium 2019, poster
- IMPRS/MCQST/QST Meeting 2020, poster
- MCQST Munich Conference on QST 2020, poster
- APS March meeting 2021 Geometric tuning of stress in silicon nitride beam resonators, talk
- NMC 2021 Efficient optomechanical mode-shape mapping of micromechanical structures, pitch talk and poster
- ICFO-IMPRS Joint Workshop 2021, poster
- IMPRS-MPHQ-BeyondC Summer School 2021, talk
- IMPRS-ETH Zurich Quantum Workshop 2021, poster

Acknowledgements

Any success is never the success of only one person. So many people supported me on my path in life that did lead me to the decision to start the so far greatest project of my life, my dissertation. And numerous people supported me during the time until I finally finished that project.

Thank you, Prof. Dr. Menno Poot for the opportunity to work in your group. The very first time we met and you told me about your many ideas I was convinced that these are the projects I want to work on in the coming years. Being the first member of your Quantum Technologies Group and seeing it grow from empty labs to a vital environment with noisy vacuum pumps, shiny lasers, and busy measurement devices, that (almost) always create data makes me very proud. A group is more than just cool equipment, it is the people that are part of it and make everything possible. The real growth lies in the many people that joined and accompanied the EQT group in the past years. I am grateful for witnessing this growth. Thank you for your support and the many many things I learned from you in the past years.

Thank you, Prof. Dr. Rudi Hackl for being my mentor not only during my time as a Ph.D. student but also in the years before. Very early in my studies, I joined your group as a working student and got the chance to write both my Bachelor's and Master's theses about the Tip-enhanced Raman spectroscopy setup. These were my first steps in a real scientific environment and have cleared my path for many years. I have always felt welcome in your office and enjoyed the extensive discussions far beyond the field of science. Whenever the Ramanators received a guest, you invited the whole group to your home or "Biergarten", from the working to the Ph.D. student, which built a strong relationship within the group and a great feeling of appreciation.

Thank you, Prof. Dr. Alexander Holleitner for being my mentor when I had the chance to join the International Max Planck Research School. I felt very welcome and very much appreciate your advice and your perspective from outside the EQT group.

Thank you, Prof. Dr. Rudolph Gross, Prof. Dr. Alexander Holleitner, and Prof. Dr. Stefan Philipp for the courtesy to allow the usage of the clean room environment on campus. Together with the numerous Ph.D. students keeping all the machines up and running, this outstanding setting provides plenty of room to create cool stuff at the bottom.

Thank you, Timo, for bringing Hamburg vibes to the still small but growing team. You brought a fresh drive into the group with your many ideas and commitment. We spent endless hours together in the clean room and it was great to have you at my side.

Thank you, all the great and motivated students, having joined the team. Without you, none of the projects would have been nearly as successful as they have been. And working on them would have been much less fun. Special thanks to Burak, you have been my first colleague who joined for a full year and you doubled the number of EQT people in the clean room. I appreciate your enthusiasm and support. I am not any less grateful to the Master's students that followed you, Evgeny, Sebastian, Giulio, Xiong, Julius, Nirav, Sarath, Agnes, Aditya, and Kevin, as well as the Bachelor's, working, and exchange students Julia, Christopher, Xiaohe, Luis, Kevin (yes, you again), Leopold, Sebastian, Raphael, Peter, Filip, and Chiun. Your dedication and enthusiasm made this team a team, a room a lab, and a coffee break a recreative discussion. Special thanks to you, Xiong and Kevin, your contribution to the projects discussed in this thesis was extraordinary.

Thank you, Susanne Tillich and Dr. Sonya Gzyl for your support and help with the administrative tasks, and thank you, Mareike Stoller-Häfele for your help with any of our IT-related wishes and problems.

Many thanks to you, Ralf Lang, Hubert Riedl, Peter Weiser, Marcus Altzschner, and Sebastian Kammerer for your help with the technical support, and your dedication to helping us with our many ideas and solving our problems. It was a pleasure to work with you. Many thanks as well to the people from the TUM mechanical workshop, the physics department staff, WSI-ZNN staff, and the WMI staff. Special thanks to you, Simon, I wish you had joined us a couple of years earlier. Thank you for your engagement with our setups, and your ideas, and I cannot thank you enough for your help with the Reactive Ion Etcher and for finally taking over the full responsibility for the machine. Speaking of the RIE, many thanks to Ralf Oelmann from Oxford Instruments for his great support. He knew all the ins and outs of this machine and called me back during his breaks and even after a long day from his hotel room. Thank you, Daniel Ruhstorfer and Daniel Schwienbacher for your help and the many discussions about the RIE and Nanobeam.

Finally, I want to thank my parents, my whole family, and my close friends, who always supported me on my path of life, during good and hard times, and made me the person I am today. Without you, I would not have made it up to this point.

Accomplishing the present work has been my job, my education, and my passion.

If not stated otherwise, images, i.e. microscope images or SEM images, in this work are taken by myself or by the students I was supervising.

Bibliography

[1] F. Marquardt and S. Girvin, "Optomechanics," *Physics*, vol. 2, p. 40, may 2009.

[2] M. Poot and H. S. van der Zant, "Mechanical systems in the quantum regime," *Phys. Rep.*, vol. 511, pp. 273–335, feb 2012.

[3] M. Aspelmeyer, T. J. Kippenberg, and F. Marquardt, "Cavity optomechanics," *Rev. Mod. Phys.*, vol. 86, pp. 1391–1452, dec 2014.

[4] M. Metcalfe, "Applications of cavity optomechanics," *Appl. Phys. Rev.*, vol. 1, p. 031105, sep 2014.

[5] M. Aspelmeyer, P. Meystre, and K. Schwab, "Quantum optomechanics," *Phys. Today*, vol. 65, pp. 29–35, jul 2012.

[6] M. Hossein-Zadeh and K. Vahala, "An optomechanical oscillator on a silicon chip," *IEEE Journal of Selected Topics in Quantum Electronics*, vol. 16, no. 1, pp. 276–287, 2010.

[7] U. Akram, W. P. Bowen, and G. J. Milburn, "Entangled mechanical cat states via conditional single photon optomechanics," *New J. Phys.*, vol. 15, p. 093007, sep 2013.

[8] X. Liu, W. Liu, Z. Ren, Y. Ma, B. Dong, G. Zhou, and C. Lee, "Progress of optomechanical micro/nano sensors: a review," *Int. J. Optomechatronics*, vol. 15, pp. 120–159, jan 2021.

[9] P. Lebedew, "Untersuchungen über die druckkräfte des lichtes," *Annalen der Physik*, vol. 311, no. 11, pp. 433–458, 1901.

[10] A. Ashkin, "Trapping of atoms by resonance radiation pressure," *Phys. Rev. Lett.*, vol. 40, pp. 729–732, mar 1978.

[11] B. Abbott *et al.*, "Observation of gravitational waves from a binary black hole merger," *Phys. Rev. Lett.*, vol. 116, p. 061102, feb 2016.

[12] K. Y. Fong, M. Poot, and H. X. Tang, "Nano-optomechanical resonators in microfluidics," *Nano Lett.*, vol. 15, pp. 6116–6120, aug 2015.

[13] T. S. Fanse, "Micro-electro-mechanical system (mems) application and prospects in automobile," *IOSR J. Mech. Civ. Eng. (IOSR-JMCE)*, vol. 19, no. 1, pp. 17–21, 2022.

[14] G. Shi, C. S. Chan, W. J. Li, K.-S. Leung, Y. Zou, and Y. Jin, "Mobile human airbag system for fall protection using MEMS sensors and embedded SVM classifier," *IEEE Sens. J.*, vol. 9, pp. 495–503, may 2009.

[15] L. Mercadé, M. Morant, A. Griol, R. Llorente, and A. Martínez, "Optical up/down-conversion of OFDM wireless signals based on ultracompact silicon optomechanical cavities," in *2021 Optical Fiber Communications Conference and Exhibition (OFC)*, pp. 1–3, 2021.

[16] D. Hoch, X. Yao, and M. Poot, "Geometric tuning of stress in predisplaced silicon nitride resonators," *Nano Lett.*, vol. 22, no. 10, pp. 1530–6984, 2022.

[17] G. S. Agarwal, *Quantum optics.* Cambridge University Press, 2012.

[18] A. L. Schawlow and C. H. Townes, "Infrared and optical masers," *Physical Review*, vol. 112, pp. 1940–1949, dec 1958.

[19] Z. Chen and M. Segev, "Highlighting photonics: looking into the next decade," *eLight*, vol. 1, jun 2021.

[20] R. P. Feynman, "Quantum mechanical computers.," *Found. Phys.*, vol. 16, no. 6, pp. 507–532, 1986.

[21] E. Oh, X. Lai, J. Wen, and S. Du, "Distributed quantum computing with photons and atomic memories." arXiv:2207.02350v1, 2022.

[22] M. H. Devoret and R. J. Schoelkopf, "Superconducting circuits for quantum information: An outlook," *Science*, vol. 339, pp. 1169–1174, mar 2013.

[23] D. S. Weiss and M. Saffman, "Quantum computing with neutral atoms," *Phys. Today*, vol. 70, pp. 44–50, jul 2017.

[24] C. D. Bruzewicz, J. Chiaverini, R. McConnell, and J. M. Sage, "Trapped-ion quantum computing: Progress and challenges," *Appl. Phys. Rev.*, vol. 6, p. 021314, jun 2019.

[25] P. Kok, W. J. Munro, K. Nemoto, T. C. Ralph, J. P. Dowling, and G. J. Milburn, "Linear optical quantum computing with photonic qubits," *Rev. Mod. Phys.*, vol. 79, pp. 135–174, jan 2007.

[26] B. Qi, W. Zhu, L. Qian, and H.-K. Lo, "Feasibility of quantum key distribution through a dense wavelength division multiplexing network," *New J. Phys.*, vol. 12, p. 103042, oct 2010.

[27] D. Huang, Y. Zhao, T. Yang, S. Rahman, X. Yu, X. He, and J. Zhang, "Quantum key distribution over double-layer quantum satellite networks," *IEEE Access*, vol. 8, pp. 16087–16098, 2020.

[28] L. Gyongyosi and S. Imre, "Advances in the quantum internet," *Communications of the ACM*, vol. 65, pp. 52–63, aug 2022.

[29] J. Mower, N. C. Harris, G. R. Steinbrecher, Y. Lahini, and D. Englund, "High-fidelity quantum state evolution in imperfect photonic integrated circuits," *Phys. Rev. A*, vol. 92, p. 032322, sep 2015.

[30] C. P. Dietrich, A. Fiore, M. G. Thompson, M. Kamp, and S. Höfling, "GaAs integrated quantum photonics: Towards compact and multi-functional quantum photonic integrated circuits," *Laser & Photonics Reviews*, vol. 10, pp. 870–894, sep 2016.

[31] C. Errando-Herranz, A. Y. Takabayashi, P. Edinger, H. Sattari, K. B. Gylfason, and N. Quack, "MEMS for photonic integrated circuits," *IEEE Journal of Selected Topics in Quantum Electronics*, vol. 26, pp. 1–16, mar 2020.

[32] M. Yano, F. Yamagishi, and T. Tsuda, "Optical MEMS for photonic switching-compact and stable optical crossconnect switches for simple, fast, and flexible wavelength applications in recent photonic networks," *IEEE Journal of Sel. Top. Quantum Electron.*, vol. 11, pp. 383–394, mar 2005.

[33] X. Ma and G.-S. Kuo, "Optical switching technology comparison: optical MEMS vs. other technologies," *IEEE Commun. Mag.*, vol. 41, pp. 50–57, nov 2003.

[34] P. Toliver, R. Runser, T. Chapuran, J. Jackel, T. Banwell, M. Goodman, R. Hughes, C. Peterson, D. Derkacs, J. Nordholt, L. Mercer, S. McNown, A. Goldman, and J. Blake, "Experimental investigation of quantum key distribution through transparent optical switch elements," *IEEE Photon. Technol. Lett*, vol. 15, pp. 1669–1671, nov 2003.

[35] S. Gyger, J. Zichi, L. Schweickert, A. W. Elshaari, S. Steinhauer, S. F. C. da Silva, A. Rastelli, V. Zwiller, K. D. Jöns, and C. Errando-Herranz, "Reconfigurable photonics with on-chip single-photon detectors," *Nat Commun*, vol. 12, mar 2021.

[36] D. Vitali, S. Gigan, A. Ferreira, H. R. Böhm, P. Tombesi, A. Guerreiro, V. Vedral, A. Zeilinger, and M. Aspelmeyer, "Optomechanical entanglement between a movable mirror and a cavity field," *Phys. Rev. Lett.*, vol. 98, p. 030405, jan 2007.

[37] P. Sekatski, M. Aspelmeyer, and N. Sangouard, "Macroscopic optomechanics from displaced single-photon entanglement," *Phys. Rev. Lett.*, vol. 112, p. 080502, feb 2014.

[38] H. Molinares, V. Eremeev, and M. Orszag, "High-fidelity synchronization and transfer of quantum states in optomechanical hybrid systems," *Phys. Rev. A*, vol. 105, p. 033708, mar 2022.

[39] G. Kurizki, P. Bertet, Y. Kubo, K. Mølmer, D. Petrosyan, P. Rabl, and J. Schmiedmayer, "Quantum technologies with hybrid systems," *Proceedings of the National Academy of Sciences*, vol. 112, pp. 3866–3873, mar 2015.

[40] J. Bochmann, A. Vainsencher, D. D. Awschalom, and A. N. Cleland, "Nanomechanical coupling between microwave and optical photons," *Nat. Phys.*, vol. 9, pp. 712–716, sep 2013.

[41] R. W. Andrews, R. W. Peterson, T. P. Purdy, K. Cicak, R. W. Simmonds, C. A. Regal, and K. W. Lehnert, "Bidirectional and efficient conversion between microwave and optical light," *Nat. Phys.*, vol. 10, pp. 321–326, mar 2014.

[42] M. Mirhosseini, A. Sipahigil, M. Kalaee, and O. Painter, "Superconducting qubit to optical photon transduction," *Nature*, vol. 588, pp. 599–603, dec 2020.

[43] T. Kaur, M. Kaur, Arvind, and B. Arora, "Generating sustained coherence in a quantum memory for retrieval at times of quantum revival," *Atoms*, vol. 10, p. 81, aug 2022.

[44] S. G. Hofer, W. Wieczorek, M. Aspelmeyer, and K. Hammerer, "Quantum entanglement and teleportation in pulsed cavity optomechanics," *Phys. Rev. A*, vol. 84, p. 052327, nov 2011.

[45] S. Gröblacher, K. Hammerer, M. R. Vanner, and M. Aspelmeyer, "Observation of strong coupling between a micromechanical resonator and an optical cavity field," *Nature*, vol. 460, pp. 724–727, aug 2009.

[46] D. E. Chang, K.-K. Ni, O. Painter, and H. J. Kimble, "Ultrahigh-Q mechanical oscillators through optical trapping," *New J. Phys.*, vol. 14, p. 045002, apr 2012.

[47] Y. Tsaturyan, A. Barg, E. S. Polzik, and A. Schliesser, "Ultracoherent nanomechanical resonators via soft clamping and dissipation dilution," *Nat. Nanotechnol.*, vol. 12, pp. 776–783, jun 2017.

[48] R. Singh and T. P. Purdy, "High-Q nanomechanical resonators for optomechanical sensing beyond the standard quantum limit," in *2020 Conference on Lasers and Electro-Optics (CLEO)*, pp. 1–2, IEEE, 2020.

[49] S. S. Verbridge, J. M. Parpia, R. B. Reichenbach, L. M. Bellan, and H. G. Craighead, "High quality factor resonance at room temperature with nanostrings under high tensile stress," *J. Appl. Phys.*, vol. 99, p. 124304, jun 2006.

[50] L. Sementilli, E. Romero, and W. P. Bowen, "Nanomechanical dissipation and strain engineering," *Adv. Funct. Mater.*, vol. 32, p. 2105247, aug 2021.

[51] M. J. Bereyhi, A. Beccari, R. Groth, S. A. Fedorov, A. Arabmoheghi, T. J. Kippenberg, and N. J. Engelsen, "Hierarchical tensile structures with ultralow mechanical dissipation," *Nat Commun*, vol. 13, jun 2022.

[52] M. J. Bereyhi, A. Arabmoheghi, A. Beccari, S. A. Fedorov, G. Huang, T. J. Kippenberg, and N. J. Engelsen, "Perimeter modes of nanomechanical resonators exhibit quality factors exceeding 10^9 at room temperature," *Phys. Rev. X*, vol. 12, p. 021036, may 2022.

[53] T. Zabel, R. Geiger, E. Marin, E. Müller, A. Diaz, C. Bonzon, M. J. Süess, R. Spolenak, J. Faist, and H. Sigg, "Top-down method to introduce ultra-high elastic strain," *J. Mater. Res.*, vol. 32, pp. 726–736, feb 2017.

[54] S. S. Verbridge, D. F. Shapiro, H. G. Craighead, and J. M. Parpia, "Macroscopic tuning of nanomechanics: substrate bending for reversible control of frequency and quality factor of nanostring resonators," *Nano Lett.*, vol. 7, pp. 1728–1735, may 2007.

[55] M. J. Bereyhi, A. Beccari, S. A. Fedorov, A. H. Ghadimi, R. Schilling, D. J. Wilson, N. J. Engelsen, and T. J. Kippenberg, "Clamp-tapering increases the quality factor of stressed nanobeams," *Nano Lett.*, vol. 19, pp. 2329–2333, feb 2019.

[56] M. Eichenfield, J. Chan, R. M. Camacho, K. J. Vahala, and O. Painter, "Optomechanical crystals," *Nature*, vol. 462, pp. 78–82, oct 2009.

[57] G. Madiot, R. C. Ng, G. Arregui, O. Florez, M. Albrechtsen, S. Stobbe, P. D. Garcia, and C. M. Sotomayor-Torres, "Optomechanical generation of coherent GHz vibrations in a phononic waveguide." arXiv:2206.06913v1, 2022.

[58] A. H. Ghadimi, D. J. Wilson, and T. J. Kippenberg, "Radiation and internal loss engineering of high-stress silicon nitride nanobeams," *Nano Lett.*, vol. 17, pp. 3501–3505, apr 2017.

[59] J. D. Thompson, B. M. Zwickl, A. M. Jayich, F. Marquardt, S. M. Girvin, and J. G. E. Harris, "Strong dispersive coupling of a high-finesse cavity to a micromechanical membrane," *Nature*, vol. 452, pp. 72–75, mar 2008.

[60] J. C. Sankey, C. Yang, B. M. Zwickl, A. M. Jayich, and J. G. E. Harris, "Strong and tunable nonlinear optomechanical coupling in a low-loss system," *Nat. Phys.*, vol. 6, pp. 707–712, jun 2010.

[61] W.-W. Liu and C.-L. Zhang, "Fast excitation fluctuation transfer between two membranes based on transitionless quantum driving," *Laser Phys. Lett.*, vol. 19, p. 035202, jan 2022.

[62] Y. Liu, J. Zhou, L. M. de Lépinay, and M. A. Sillanpää, "Quantum backaction evading measurements of a silicon nitride membrane resonator," *New J. Phys.*, vol. 24, p. 083043, aug 2022.

[63] D. Hoch, K.-J. Haas, L. Moller, T. Sommer, P. Soubelet, J. J. Finley, and M. Poot, "Efficient optomechanical mode-shape mapping of micromechanical devices," *Micromachines*, vol. 12, no. 8, p. 880, 2021.

[64] G. Conte, L. Vicarelli, S. Zanotto, and A. Pitanti, "Mechanical mode engineering with orthotropic metamaterial membranes," *Adv. Mater. Technol.*, vol. 7, p. 2200337, jul 2022.

[65] A. Barg, Y. Tsaturyan, E. Belhage, W. H. P. Nielsen, C. B. Møller, and A. Schliesser, "Measuring and imaging nanomechanical motion with laser light," *Appl. Phys. B*, vol. 123, no. 1, p. 8, 2016.

[66] X. Zhang, R. Waitz, F. Yang, C. Lutz, P. Angelova, A. Gölzhäuser, and E. Scheer, "Vibrational modes of ultrathin carbon nanomembrane mechanical resonators," *Appl Phys Lett*, vol. 106, no. 6, 2015.

[67] D. Davidovikj, J. J. Slim, S. J. Cartamil-Bueno, H. S. J. van der Zant, P. G. Steeneken, and W. J. Venstra, "Visualizing the motion of graphene nanodrums," *Nano Lett.*, vol. 16, pp. 2768–2773, Apr. 2016.

[68] Z. Shen, X. Han, C.-L. Zou, and H. X. Tang, "Phase sensitive imaging of 10 GHz vibrations in an AlN microdisk resonator," *Rev. Sci. Instrum.*, vol. 88, Dec. 2017.

[69] E. Romero, R. Kalra, N. Mauranyapin, C. Baker, C. Meng, and W. Bowen, "Propagation and imaging of mechanical waves in a highly stressed single-mode acoustic waveguide," *Phys. Rev. Applied*, vol. 11, p. 064035, June 2019.

[70] R. Singh and T. P. Purdy, "Detecting acoustic blackbody radiation with an optomechanical antenna," *Phys. Rev. Lett.*, vol. 125, p. 120603, Sept. 2020.

[71] T. Hesjedal, E. Chilla, and H.-J. Fröhlich, "High resolution visualization of acoustic wave fields within surface acoustic wave devices," *Appl Phys Lett*, vol. 70, no. 11, pp. 1372–1374, 1997.

[72] D. Garcia-Sanchez, A. M. van der Zande, A. S. Paulo, B. Lassagne, P. L. McEuen, and A. Bachtold, "Imaging mechanical vibrations in suspended graphene sheets," *Nano Lett.*, vol. 8, pp. 1399–1403, May 2008.

[73] D. Garcia-Sanchez, A. S. Paulo, M. J. Esplandiu, F. Perez-Murano, L. Forró, A. Aguasca, and A. Bachtold, "Mechanical detection of carbon nanotube resonator vibrations," *Phys. Rev. Lett.*, vol. 99, no. 8, p. 085501, 2007.

[74] S. Etaki, M. Poot, I. Mahboob, K. Onomitsu, H. Yamaguchi, and H. S. J. van der Zant, "Motion detection of a micromechanical resonator embedded in a d.c. SQUID," *Nat. Phys.*, vol. 4, pp. 785–788, Oct. 2008.

[75] B. Abbott *et al.*, "Observation of a kilogram-scale oscillator near its quantum ground state," *New J. Phys.*, vol. 11, p. 073032, jul 2009.

[76] A. Schliesser, R. Rivière, G. Anetsberger, O. Arcizet, and T. J. Kippenberg, "Resolved-sideband cooling of a micromechanical oscillator," *Nat. Phys.*, vol. 4, pp. 415–419, apr 2008.

[77] Z. Chen, Q. Lin, and B. He, "Cooling effect and cooling speed for a membrane-in-middle optomechanical system," *Photonics*, vol. 9, p. 400, jun 2022.

[78] M. Eichenfield, R. Camacho, J. Chan, K. J. Vahala, and O. Painter, "A picogram- and nanometre-scale photonic-crystal optomechanical cavity," *Nature*, vol. 459, pp. 550–555, may 2009.

[79] Q. Lin, J. Rosenberg, X. Jiang, K. J. Vahala, and O. Painter, "Mechanical oscillation and cooling actuated by the optical gradient force," *Phys. Rev. Lett.*, vol. 103, p. 103601, aug 2009.

[80] M. Poot, C. Schuck, X. song Ma, X. Guo, and H. X. Tang, "Design and characterization of integrated components for SiN photonic quantum circuits," *Opt. Express*, vol. 24, p. 6843, mar 2016.

[81] M. Group, "Siliziumnitrid." https://www.moeschter-group.com/de/werkstoffe/siliziumnitrid/. accessed 09.09.2022.

[82] F. L. Riley, "Silicon nitride and related materials," *J. Am. Ceram. Soc.*, vol. 83, pp. 245–265, dec 2004.

[83] V. A. Gritsenko, "Electronic structure of silicon nitride," *Phys.-Uspekhi*, vol. 55, pp. 498–507, may 2012.

[84] T. Gisler, M. Helal, D. Sabonis, U. Grob, M. Héritier, C. L. Degen, A. H. Ghadimi, and A. Eichler, "Soft-clamped silicon nitride string resonators at millikelvin temperatures," *Phys. Rev. Lett.*, vol. 129, p. 104301, aug 2022.

[85] W.-H. Chuang, T. Luger, R. Fettig, and R. Ghodssi, "Mechanical property characterization of LPCVD silicon nitride thin films at cryogenic temperatures," *J Microelectromech S*, vol. 13, pp. 870–879, oct 2004.

[86] COMSOL material library, Si3N4 - Silicon nitride, COMSOL Multiphysics v5.6.

[87] B. Merle and M. Göken, "Fracture toughness of silicon nitride thin films of different thicknesses as measured by bulge tests," *Acta Mater.*, vol. 59, pp. 1772–1779, feb 2011.

[88] P. Sadeghi, M. Tanzer, S. L. Christensen, and S. Schmid, "Influence of clamp-widening on the quality factor of nanomechanical silicon nitride resonators," *J. Appl. Phys.*, vol. 126, p. 165108, oct 2019.

[89] R. Norte, J. Moura, and S. Gröblacher, "Mechanical resonators for quantum optomechanics experiments at room temperature," *Phys. Rev. Lett.*, vol. 116, p. 147202, apr 2016.

[90] D. Høj, F. Wang, W. Gao, U. B. Hoff, O. Sigmund, and U. L. Andersen, "Ultra-coherent nanomechanical resonators based on inverse design," *Nat. Commun.*, vol. 12, pp. 1–8, oct 2021.

[91] D. M. Knotter and T. J. J. D. Denteneer, "Etching mechanism of silicon nitride in HF-based solutions," *J Electrochem Soc*, vol. 148, no. 3, p. F43, 2001.

[92] T. Longjuan, Z. Yinfang, Y. Jinling, L. Yan, Z. Wei, X. Jing, L. Yunfei, and Y. Fuhua, "Dependence of wet etch rate on deposition, annealing conditions and etchants for PECVD silicon nitride film," *J. Semicond.*, vol. 30, p. 096005, sep 2009.

[93] A. Gondarenko, J. S. Levy, and M. Lipson, "High confinement micron-scale silicon nitride high Q ring resonator," *Opt. Express*, vol. 17, p. 11366, jun 2009.

[94] M.-C. Tien, J. F. Bauters, M. J. R. Heck, D. T. Spencer, D. J. Blumenthal, and J. E. Bowers, "Ultra-high quality factor planar Si_3N_4 ring resonators on Si substrates," *Opt. Express*, vol. 19, p. 13551, jun 2011.

[95] J. Liu, G. Huang, R. N. Wang, J. He, A. S. Raja, T. Liu, N. J. Engelsen, and T. J. Kippenberg, "High-yield, wafer-scale fabrication of ultralow-loss, dispersion-engineered silicon nitride photonic circuits," *Nat Commun*, vol. 12, apr 2021.

[96] G. Terrasanta, M. Müller, T. Sommer, S. Geprägs, R. Gross, M. Althammer, and M. Poot, "Growth of aluminum nitride on a silicon nitride substrate for hybrid photonic circuits," *Mater. Quantum Technol.*, vol. 1, p. 021002, June 2021.

[97] G. Terrasanta, T. Sommer, M. Müller, M. Althammer, R. Gross, and M. Poot, "Aluminum nitride integration on silicon nitride photonic circuits: a hybrid approach towards on-chip nonlinear optics," *Opt. Express*, vol. 30, pp. 8537–8549, mar 2022.

[98] D. J. Blumenthal, R. Heideman, D. Geuzebroek, A. Leinse, and C. Roeloffzen, "Silicon nitride in silicon photonics," *Proceedings of the IEEE*, vol. 106, pp. 2209–2231, dec 2018.

[99] J. T. Boyd, R. W. Wu, D. E. Zelmon, A. Naumaan, H. A. Timlin, and H. E. Jackson, "Planar and channel optical waveguides utilizing silicon technology," in *SPIE Proceedings* (D. B. Ostrowsky and S. Sriram, eds.), SPIE, jan 1985.

[100] J. F. Bauters, M. J. R. Heck, D. D. John, J. S. Barton, C. M. Bruinink, A. Leinse, R. G. Heideman, D. J. Blumenthal, and J. E. Bowers, "Planar waveguides with less than 01 dB/m propagation loss fabricated with wafer bonding," *Opt. Express*, vol. 19, p. 24090, nov 2011.

[101] T. A. Huffman, G. M. Brodnik, C. Pinho, S. Gundavarapu, D. Baney, and D. J. Blumenthal, "Integrated resonators in an ultralow loss si3n4/sio2 platform for multifunction applications," *IEEE Journal of Selected Topics in Quantum Electronics*, vol. 24, pp. 1–9, jul 2018.

[102] K. Wörhoff, R. G. Heideman, A. Leinse, and M. Hoekman, "TriPleX: a versatile dielectric photonic platform," *Advanced Optical Technologies*, vol. 4, pp. 189–207, apr 2015.

[103] D. T. Spencer, J. F. Bauters, M. J. R. Heck, and J. E. Bowers, "Integrated waveguide coupled si_3n_4 resonators in the ultrahigh-q regime," *Optica*, vol. 1, p. 153, sep 2014.

[104] P. J. Winzer, D. T. Neilson, and A. R. Chraplyvy, "Fiber-optic transmission and networking: the previous 20 and the next 20 years [invited]," *Opt. Express*, vol. 26, p. 24190, aug 2018.

[105] K. Ikeda, R. E. Saperstein, N. Alic, and Y. Fainman, "Thermal and kerr nonlinear properties of plasma-deposited silicon nitride/ silicon dioxide waveguides," *Opt. Express*, vol. 16, p. 12987, aug 2008.

[106] K. Okamoto, *Fundamentals of optical waveguides.* Elsevier, 2021.

[107] N. Mange, "Quantum optics on chip: Adiabatic couplers for integrated photonics SWAP operations and waveguide crossings," Master's thesis, TU Munich, OTH Regensburg, 2022.

[108] K. Alexander, N. A. Savostianova, S. A. Mikhailov, D. V. Thourhout, and B. Kuyken, "Gate-tunable nonlinear refraction and absorption in graphene-covered silicon nitride waveguides," *ACS Photonics*, vol. 5, pp. 4944–4950, nov 2018.

[109] G. Terrasanta, "Aluminum nitride integration on silicon nitride substrate: a new approach towards on-chip nonlinearities," Master's thesis, TU Munich, EPFL, 2020.

[110] A. Juarez and L. Zimmermann, "Laboratory manuskript: integrated grating couplers." https://www.hft.tu-berlin.de/fileadmin/fg154/HFT/Labor/Grating_coupler.pdf, Jan. 2010. accessed: 21.08.2022.

[111] X. Bai, "Modelling single-photon sources for optical quantum circuits," Bachelor's thesis, TU Munich, 2019.

[112] J. L. O'Brien, A. Furusawa, and J. Vučković, "Photonic quantum technologies," *Nat. Photonics*, vol. 3, pp. 687–695, dec 2009.

[113] J.-S. Xu and C.-F. Li, "Quantum integrated circuit: classical characterization," *Science Bulletin*, vol. 60, p. 141, jan 2015.

[114] B. Lounis and M. Orrit, "Single-photon sources," *Rep. Prog. Phys.*, vol. 68, pp. 1129–1179, apr 2005.

[115] X. Guo, C. ling Zou, C. Schuck, H. Jung, R. Cheng, and H. X. Tang, "Parametric down-conversion photon-pair source on a nanophotonic chip," *Light Sci. Appl.*, vol. 6, pp. e16249–e16249, nov 2016.

[116] R. H. Hadfield, "Single-photon detectors for optical quantum information applications," *Nat. Photonics*, vol. 3, pp. 696–705, dec 2009.

[117] A. N. McCaughan, Y. Zhai, B. Korzh, J. P. Allmaras, B. G. Oripov, M. D. Shaw, and S. W. Nam, "The thermally coupled imager: A scalable readout architecture for superconducting nanowire single photon detectors," *Appl. Phys. Lett.*, vol. 121, p. 102602, sep 2022.

[118] L. Cheng, S. Mao, Z. Li, Y. Han, and H. Fu, "Grating couplers on silicon photonics: Design principles, emerging trends and practical issues," *Micromachines*, vol. 11, p. 666, jul 2020.

[119] G. Maire, L. Vivien, G. Sattler, A. Kazmierczak, B. Sanchez, K. B. Gylfason, A. Griol, D. Marris-Morini, E. Cassan, D. Giannone, H. Sohlström, and D. Hill, "High efficiency silicon nitride surface grating couplers," *Opt. Express*, vol. 16, no. 1, p. 328, 2008.

[120] M. Poot, K. Y. Fong, and H. X. Tang, "Classical non-gaussian state preparation through squeezing in an optoelectromechanical resonator," *Phys. Rev. A*, vol. 90, p. 063809, dec 2014.

[121] A. Cleland, *Foundations of Nanomechanics.* Springer, 2003.

[122] X. Yao, D. Hoch, and M. Poot, "Relaxation and dynamics of stressed predisplaced string resonators," *Phys. Rev. B*, vol. 106, p. 174109, nov 2022.

[123] B. Witkamp, M. Poot, and H. S. J. van der Zant, "Bending-mode vibration of a suspended nanotube resonator," *Nano Lett.*, vol. 6, pp. 2904–2908, nov 2006.

[124] W. A. Strauss, *Partial differential equations - an introduction.* John Wiley and Sons, Inc., 1992.

[125] D. R. Lide, ed., *Handbook of Chemistry and Physics.* GRC press, 1974.

[126] S. Schmid, L. G. Villanueva, and M. L. Roukes, *Fundamentals of nanomechanical resonators*, vol. 49. Springer, 2016.

[127] D. A. Hall, "Review nonlinearity in piezoelectric ceramics," *J. Mater. Sci.*, vol. 36, no. 19, pp. 4575–4601, 2001.

[128] A. H. Nayfeh and D. T. Mook, *Nonlinear Oscillations.* Wiley-vch Verlag GmbH & Co. KGaA, 1995.

[129] A. M. Elshurafa, K. Khirallah, H. H. Tawfik, A. Emira, A. K. S. A. Aziz, and S. M. Sedky, "Nonlinear dynamics of spring softening and hardening in folded-MEMS comb drive resonators," *J Microelectromech S*, vol. 20, pp. 943–958, aug 2011.

[130] U. Fano, “Effects of configuration interaction on intensities and phase shifts,” *Phys. Rev.*, vol. 124, pp. 1866–1878, dec 1961.

[131] T. Sommer, D. Hoch, K.-J. Haas, L. Moller, J.Röwe, A. Yadav, P. Soubelet, J. J. Finley, and M. Poot, “Optomechanical mode-shape mapping in the presence of crosstalk,” *Sensors & Transducers*, vol. 258, pp. 1–9, July 2022.

[132] M. Barton, “Dissipation dilution,” 2008. Private communication LIGO DCC T070101-00.

[133] M. I. A. Asri, M. N. Hasan, M. R. A. Fuaad, Y. M. Yunos, and M. S. M. Ali, “MEMS gas sensors: A review,” *IEEE Sens. J.*, vol. 21, pp. 18381–18397, sep 2021.

[134] M. Najmzadeh, S. Haasl, and P. Enoksson, “A silicon straight tube fluid density sensor,” *J. Micromech Microeng.*, vol. 17, pp. 1657–1663, jul 2007.

[135] L. Arana, S. Schaevitz, A. Franz, M. Schmidt, and K. Jensen, “A microfabricated suspended-tube chemical reactor for thermally efficient fuel processing,” *J Microelectromech S*, vol. 12, pp. 600–612, oct 2003.

[136] S. Schmid, K. D. Jensen, K. H. Nielsen, and A. Boisen, “Damping mechanisms in high-Q micro and nanomechanical string resonators,” *Phys. Rev. B*, vol. 84, p. 165307, oct 2011.

[137] X. Yao, “Geometric tuning of stress in silicon nitride resonators and integration into ring cavities for synchronization,” Master’s thesis, TU Munich, 2021.

[138] A. M. Zinth, “Optomechanical racetrack cavities - towards the synchronization of mechanical resonators using light,” Master’s thesis, TU Munich, 2022.

[139] D. N. Hao and N. D. Anh, “Response of duffing oscillator with time delay subjected to combined harmonic and random excitations,” *Math Probl Eng*, vol. 2017, pp. 1–8, 2017.

[140] M. Poot, K. Y. Fong, and H. X. Tang, “Deep feedback-stabilized parametric squeezing in an opto-electromechanical system,” *New J. Phys.*, vol. 17, p. 043056, apr 2015.

[141] K. P. Zetie, S. F. Adams, and R. M. Tocknell, “How does a mach-zehnder interferometer work?,” *Phys. Educ.*, vol. 35, pp. 46–48, jan 2000.

[142] Y. Ji, Y. Chung, D. Sprinzak, M. Heiblum, D. Mahalu, and H. Shtrikman, “An electronic mach–zehnder interferometer,” *Nature*, vol. 422, pp. 415–418, mar 2003.

[143] D. Hoch, T. Sommer, S. Müller, and M. Poot, “On-chip quantum optics and integrated optomechanics,” *Turk. J. Phys.*, vol. 44, pp. 239 – 246, 2020.

[144] M. Poot and H. X. Tang, “Broadband nanoelectromechanical phase shifting of light on a chip,” *Appl. Phys. Lett.*, vol. 104, p. 061101, feb 2014.

[145] M. Poot, S. Etaki, H. Yamaguchi, and H. S. J. van der Zant, “Discrete-time quadrature feedback cooling of a radio-frequency mechanical resonator,” *Appl. Phys. Lett.*, vol. 99, p. 013113, jul 2011.

[146] D. James, “TSMC’s 7nm, 5nm, and 3nm “are just numbers… it doesn’t matter what the number is”.” https://www.pcgamesn.com/amd/tsmc-7nm-5nm-and-3nm-are-just-numbers. Accessed: 2022-05-25.

[147] L. L. Cheng Ting-Fang, “Apple and Intel become first to adopt TSMC’s latest chip tech.” https://asia.nikkei.com/Business/Tech/Semiconductors/Apple-and-Intel-become-first-to-adopt-TSMC-s-latest-chip-tech. Accessed: 2022-05-25.

[148] B. Yildiz, "High frequency optomechanical devices for quantum optomechanics," Master's thesis, TU Munich, 2019.

[149] S. Chandran, "Quantum optics on a chip: Design, fabrication, and optimization of tuneable MEMS H directional couplers," Master's thesis, Hochschule München, 2022.

[150] S. Müller, "Optimization and advancement of on-chip beam splitters for integrated optics quantum computing," Master's thesis, TU Munich, 2020.

[151] J. Lamprich, "Designing and modeling high frequency optomechanical devices," Bachelor's thesis, TU Munich, 2018.

[152] K.-J. Haas, "2d optomechanics," Bachelor's thesis, TU Munich, 2020.

[153] L. Bellon, "Thermal noise of microcantilevers in viscous fluids," *J. Appl. Phys.*, vol. 104, p. 104906, nov 2008.

[154] L. Rosendahl, "2D optomechanics," Bachelor's thesis, TU Munich, 2019.

[155] E. Lebedev, "Vibrational and optical properties of freestanding atomically thin nanomaterials," Master's thesis, TU Munich, 2020.

[156] S. Bhagavantam and D. Suryanarayana, "A note on the even, odd and half-overtones in piezo-electric crystal plates," in *Proceedings of the Indian Academy of Sciences-Section A*, vol. 21, pp. 19–23, Springer India, 1945.

[157] C. Waas, "Set-up and analysis of a two-dimensional translation stage for integrated optics experiments," Bachelor's thesis, TU Munich, 2018.

[158] A. Venkatasubramanian, V. T. K. Sauer, S. K. Roy, M. Xia, D. S. Wishart, and W. K. Hiebert, "Nano-optomechanical systems for gas chromatography," *Nano Lett.*, vol. 16, no. 11, pp. 6975–6981, 2016.

[159] A. K. Naik, M. S. Hanay, W. K. Hiebert, X. L. Feng, and M. L. Roukes, "Towards single-molecule nanomechanical mass spectrometry," *Nat Nano*, vol. 4, pp. 445–450, July 2009.

[160] S. J. McKeown, X. Wang, X. Yu, and L. L. Goddard, "Realization of palladium-based optomechanical cantilever hydrogen sensor," *Microsyst Nanoneng*, vol. 3, 2017.

[161] J. Melcher, J. Stirling, F. G. Cervantes, J. R. Pratt, and G. A. Shaw, "A self-calibrating optomechanical force sensor with femtonewton resolution," *Appl. Phys. Lett.*, vol. 105, 2014.

[162] A. C. Bleszynski-Jayich, W. E. Shanks, B. Peaudecerf, E. Ginossar, F. von Oppen, L. Glazman, and J. G. E. Harris, "Persistent currents in normal metal rings," *Science*, vol. 326, pp. 272–275, Oct. 2009.

[163] K. Y. Fong, H.-K. Li, R. Zhao, S. Yang, Y. Wang, and X. Zhang, "Phonon heat transfer across a vacuum through quantum fluctuations," *Nature*, vol. 576, no. 7786, pp. 243–247, 2019.

[164] I. E. Rosłoń, A. Japaridze, P. G. Steeneken, C. Dekker, and F. Alijani, "Probing nanomotion of single bacteria with graphene drums," *Nat. Nanotechnology*, vol. 17, p. 637–642, apr 2022.

[165] M. D. LaHaye, O. Buu, B. Camarota, and K. C. Schwab, "Approaching the quantum limit of a nanomechanical resonator," *Science*, vol. 304, pp. 74–77, Apr. 2004.

[166] G. Anetsberger, O. Arcizet, Q. P. Unterreithmeier, R. Riviere, A. Schliesser, E. M. Weig, J. P. Kotthaus, and T. J. Kippenberg, “Near-field cavity optomechanics with nanomechanical oscillators,” *Nat Phys*, vol. 5, pp. 909–914, Dec. 2009.

[167] V. P. Adiga, B. Ilic, R. A. Barton, I. Wilson-Rae, H. G. Craighead, and J. M. Parpia, “Modal dependence of dissipation in silicon nitride drum resonators,” *Appl. Phys. Lett.*, vol. 99, no. 25, p. 253103, 2011.

[168] K. Williams and R. Muller, “Etch rates for micromachining processing,” *Microelectromechanical Systems, Journal of*, vol. 5, pp. 256–269, Dec. 1996.

[169] Unless stated otherwise, images and measurements regarding the surface quality are performed on sample SN054.

[170] These values were measured on sample WSN04_71.

[171] The reference measurement was taken on sample WSN03_28.

[172] D. Miller and B. Alemán, “Spatially resolved optical excitation of mechanical modes in graphene NEMS,” *Appl. Phys. Lett.*, vol. 115, no. 19, p. 193102, 2019.

[173] P. Rohse, J. Butlewski, F. Klein, T. Wagner, C. Friesen, A. Schwarz, R. Wiesendanger, K. Sengstock, and C. Becker, “A cavity optomechanical locking scheme based on the optical spring effect,” *Rev. Sci. Instrum.*, vol. 91, no. 10, p. 103102, 2020.

[174] M. J. Jhung and K. H. Jeong, “Free vibration analysis of perforated plate with square penetration pattern using equivalent material properties,” *Nucl Eng Technol*, vol. 47, no. 4, pp. 500–511, 2015.

[175] L. Moller, “2D optomechanics,” Bachelor’s thesis, TU Munich, 2021.

[176] G. D. Cole, I. Wilson-Rae, K. Werbach, M. R. Vanner, and M. Aspelmeyer, “Phonon-tunnelling dissipation in mechanical resonators,” *Nat Commun*, vol. 2, no. 1, p. 231, 2011.

[177] X. Sun, J. Zheng, M. Poot, C. W. Wong, and H. X. Tang, “Femtogram doubly clamped nanomechanical resonators embedded in a high-Q two-dimensional photonic crystal nanocavity,” *Nano Lett.*, vol. 12, no. 5, pp. 2299–2305, 2012.

[178] The chip is WSN05_47.

[179] T. Larsen, S. Schmid, L. Grönberg, A. O. Niskanen, J. Hassel, S. Dohn, and A. Boisen, “Ultrasensitive string-based temperature sensors,” *Appl. Phys. Lett.*, vol. 98, p. 121901, mar 2011.

[180] Y. Okada and Y. Tokumaru, “Precise determination of lattice parameter and thermal expansion coefficient of silicon between 300 and 1500 K,” *J. Appl. Phys.*, vol. 56, pp. 314–320, jul 1984.

[181] S. Schmid, *Electrostatically actuated all-polymer microbeam resonators: Characterization and application*, vol. 6. ETH Zurich, 2009.

[182] Accuratus, “Fused silica, SiO2 glass properties.” `http://accuratus.com/fused.html`. Accessed: 2022-05-20.

[183] J. Röwe, “2D optomechanics,” Master’s thesis, TU Munich, 2022.

[184] W. J. Westerveld, M. Mahmud-Ul-Hasan, R. Shnaiderman, V. Ntziachristos, X. Rottenberg, S. Severi, and V. Rochus, “Sensitive, small, broadband and scalable optomechanical ultrasound sensor in silicon photonics,” *Nat. Photonics*, vol. 15, no. 5, pp. 341–345, 2021.

[185] M. Calleja, P. M. Kosaka, Á. S. Paulo, and J. Tamayo, "Challenges for nanomechanical sensors in biological detection," *Nanoscale*, vol. 4, no. 16, p. 4925, 2012.

[186] P. S. Waggoner and H. G. Craighead, "Micro- and nanomechanical sensors for environmental, chemical, and biological detection," *Lab Chip*, vol. 7, no. 10, p. 1238, 2007.

[187] G. Rebeiz, G.-L. Tan, and J. Hayden, "RF MEMS phase shifters: design and applications," *IEEE Microw*, vol. 3, pp. 72–81, jun 2002.

[188] A. D. O'Connell, M. Hofheinz, M. Ansmann, R. C. Bialczak, M. Lenander, E. Lucero, M. Neeley, D. Sank, H. Wang, M. Weides, J. Wenner, J. M. Martinis, and A. N. Cleland, "Quantum ground state and single-phonon control of a mechanical resonator," *Nature*, vol. 464, pp. 697–703, Apr. 2010.

[189] N. Fiaschi, B. Hensen, A. Wallucks, R. Benevides, J. Li, T. P. M. Alegre, and S. Gröblacher, "Optomechanical quantum teleportation," *Nat. Photonics*, vol. 15, no. 11, pp. 817–821, 2021.

[190] H. Yu *et al.*, "Quantum correlations between light and the kilogram-mass mirrors of LIGO," *Nature*, vol. 583, no. 7814, pp. 43–47, 2020.

[191] X. M. H. Huang, M. Manolidis, S. C. Jun, and J. Hone, "Nanomechanical hydrogen sensing," *Appl. Phys. Lett.*, vol. 86, p. 143104, apr 2005.

[192] Q. P. Unterreithmeier, T. Faust, and J. P. Kotthaus, "Damping of nanomechanical resonators," *Phys. Rev. Lett.*, vol. 105, p. 027205, jul 2010.

[193] J. M. Olson, "Analysis of LPCVD process conditions for the deposition of low stress silicon nitride. Part I: preliminary LPCVD experiments," *Mater. Sci. Semicond. Process.*, vol. 5, pp. 51–60, feb 2002.

[194] R. Zhang, C. Ti, M. I. Davanço, Y. Ren, V. Aksyuk, Y. Liu, and K. Srinivasan, "Integrated tuning fork nanocavity optomechanical transducers with high fMQM product and stress-engineered frequency tuning," *Appl. Phys. Lett.*, vol. 107, p. 131110, sep 2015.

[195] Y.-W. Hu, Y.-F. Xiao, Y.-C. Liu, and Q. Gong, "Optomechanical sensing with on-chip microcavities," *Front Phys-beijing*, vol. 8, pp. 475–490, oct 2013.

[196] M. Bagheri, M. Poot, L. Fan, F. Marquardt, and H. X. Tang, "Photonic cavity synchronization of nanomechanical oscillators," *Phys. Rev. Lett.*, vol. 111, p. 213902, nov 2013.

[197] K. Y. Fong, D. Jin, M. Poot, A. Bruch, and H. X. Tang, "Phonon coupling between a nanomechanical resonator and a quantum fluid," *Nano Lett.*, vol. 19, pp. 3716–3722, apr 2019.

[198] "Structural mechanics module user's guide." COMSOL v3.5.

[199] M. Poot, B. Witkamp, M. A. Otte, and H. S. J. van der Zant, "Modelling suspended carbon nanotube resonators," *Phys. Stat. Sol. (b)*, vol. 244, no. 11, pp. 4252–4256, 2007.

[200] A. H. Ghadimi, S. A. Fedorov, N. J. Engelsen, M. J. Bereyhi, R. Schilling, D. J. Wilson, and T. J. Kippenberg, "Elastic strain engineering for ultralow mechanical dissipation," *Science*, vol. 360, pp. 764–768, apr 2018.

[201] M. J. Bereyhi, A. Arabmoheghi, S. A. Fedorov, A. Beccari, G. Huang, T. J. Kippenberg, and N. J. Engelsen, "Nanomechanical resonators with ultra-high-Q perimeter modes," *arXiv:2108.03615v2*, Aug. 2021.

[202] A. Beccari, D. A. Visani, S. A. Fedorov, M. J. Bereyhi, V. Boureau, N. J. Engelsen, and T. J. Kippenberg, "Strained crystalline nanomechanical resonators with quality factors above 10 billion," *Nat. Phys.*, vol. 18, p. 436–441, feb 2022.

[203] G. I. González and P. R. Saulson, "Brownian motion of a mass suspended by an anelastic wire," *J. Acoust. Soc. Am.*, vol. 96, pp. 207–212, jul 1994.

[204] K. B. Gavan, J. van der Heijden, E. W. J. M. van der Drift, and H. S. J. van der Zant, "Effect of pressure on the Q factor and the resonance frequency of SiN microcantilevers," in *2009 4th IEEE International Conference on Nano/Micro Engineered and Molecular Systems*, pp. 380–384, 2009.

[205] A. L. Alter, D. D. Gerrard, H.-K. Kwon, G. D. Vukasin, and T. W. Kenny, "Quality factor extraction and enhancement across temperature in ring resonators," *J Microelectromech S*, vol. 29, pp. 1124–1126, oct 2020.

[206] S. A. Fedorov, N. J. Engelsen, A. H. Ghadimi, M. J. Bereyhi, R. Schilling, D. J. Wilson, and T. J. Kippenberg, "Generalized dissipation dilution in strained mechanical resonators," *Phys. Rev. B*, vol. 99, p. 054107, feb 2019.

[207] Q. P. Unterreithmeier, E. M. Weig, and J. P. Kotthaus, "Universal transduction scheme for nanomechanical systems based on dielectric forces," *Nature*, vol. 458, pp. 1001–1004, apr 2009.

[208] S. Ruffert, "Improving an optomechanical setup towards characterization of semiconductor "transition metal dichalcogenides"," Bachelor's thesis, TU Munich, 2021.

[209] R. Maier, "Electrostatic force modelling of a cantilever shape platform for single photon sources," Bachelor's thesis, TU Munich, 2021.